Multinuclear Solid-State Magnetic Resonance Studies on 'Exotic' Quadrupolar Nuclei: Acquisition Methods, High-Order Effects, Quantum Chemical Computations, and NMR Crystallography

Cory Widdifield

A thesis submitted to the Faculty of Graduate and Postdoctoral Studies at the University of Ottawa in partial fulfillment of the requirements for the degree of

Doctor of Philosophy in Chemistry

Ottawa-Carleton Chemistry Institute
Department of Chemistry
Faculty of Science
University of Ottawa

uOttawa

Multinuclear Solid-State Magnetic Resonance Studies on 'Exotic' Quadrupolar Nuclei:

Acquisition Methods, High-Order Effects, Quantum Chemical Computations, and NMR

Crystallography

by

Cory Widdifield

APPROVED BY:

_____

Dr. William P. Power, Associate Professor of Chemistry, External Examiner
Department of Chemistry, University of Waterloo

_____

Dr. John A. Ripmeester, Adjunct Research Professor
Department of Chemistry, Carleton University

_____

Dr. Natalie K. Goto, Associate Professor of Chemistry
Department of Chemistry, University of Ottawa

_____

Dr. Tom K. Woo, Professor of Chemistry
Department of Chemistry, University of Ottawa

_____

Dr. David L. Bryce, Associate Professor of Chemistry, Advisor
Department of Chemistry, University of Ottawa

_____

Chair of Defence
Faculty of Graduate and Postdoctoral Studies, University of Ottawa

Abstract

This dissertation attempts to extend the classes of halogen-containing systems which may be studied using solid-state nuclear magnetic resonance (SSNMR). As line shape broadening due to the quadrupolar interaction (QI) scales inversely with the applied field, high-field magnet technology is indispensable for this research. Combining advanced radiofrequency pulse sequences with high-field wideline data acquisition allowed for the collection of very broad SSNMR signals of all quadrupolar halogen nuclei (i.e., $^{35/37}Cl$, $^{79/81}Br$ and ^{127}I) within a reasonable amount of experimental time. The initial systems for study were of the MX_2 variety (M = Mg, Ca, Sr, Ba; X = Cl, Br, I). In total, 9 anhydrous compounds were tested. The effects of hydrate formation were tested on 7 additional compounds. Systematic trends in the observed δ_{iso} values (and to a lesser extent, Ω and C_Q) were found to be diagnostic of the extent of hydration in these materials. Resolving power was successfully tested using $SrBr_2$, which possesses 4 magnetically unique sites. The composition of $CaBr_2 \cdot xH_2O$ was convincingly determined using SSNMR data and the hydration trends noted above. The sensitivity of the QI to the local bonding environment (e.g., bond distance changes of less than 0.05 Å) was used to refine (when coupled with gauge-including projector augmented-wave density functional theory (GIPAW DFT) quantum chemical computations) the structure of $MgBr_2$, and was used to correct prior NMR data for $CaCl_2$ (earlier accounts had been performed upon a $CaCl_2$ hydrate). During NMR data analysis of certain iodine-containing materials, it was found that standard fitting software (which uses perturbation theory) could not reproduce the observations. Proper analysis required the use of exact simulation software and allowed for the observation of high-order quadrupole-induced effects (HOQIE). This motivated further studies using rhenium-185/187 nuclei, where it was expected that HOQIE would be more dramatic. The observed rhenium SSNMR spectra

possessed additional fine structure that had never been observed before experimentally, nor would be expected from currently-available perturbation theory analysis software. Lastly, preliminary results are shown where ^{127}I SSNMR is used to study important supramolecular systems, and the composition of the popular synthetic reagent 'GaI' is elucidated.

Acknowledgements

acknowledged, although I must confess that I did not get to know them very well: Omar Anjum, Prisca Hendarsa, Ritesh Kumar, Aurore Lebrun, Melanie Mastronardi, Elisabeth Messner-Henning, Mélanie Ouellette, Nuiok Dicaire, (she is also thanked for the computer monitor which I stole), Devon Fyson, Sophie Leclerc, and Matthew Leclerc (no relationship between those last two). Brittany Franchuk is thanked for continually being 'super', 'awesome', and 'cool': I am sure you will be one of the most enthusiastic pharmacists on this planet. Rob Attrell is thanked for occasionally listening to my well-intentioned advice.

I now turn my attention to the people I find currently in this lab, including: Kevin Burgess (a.k.a. 'static'), Frédéric Perras (a.k.a. 'MAS'), and Jasmine Viger-Gravel (a.k.a. no comment). Kevin: I would like to thank you for your 'full-on' interest in pursuing bromine and calcium SSNMR, as this should surely increase my h-index. As well, I acknowledge and am grateful for your mastery and great successes in the synthesis of a variety of low-valent cobalt materials and calcium-containing amino acids. I hope we can turn all of these above-mentioned systems into publications, although I apologize for perhaps not being on top of things. Fred (a.k.a. 'FSolids'): I am greatly impressed by your ability and rapid development. Your attention to the correct details (and inattention to that which is not important) should be practiced by more people, including myself. Your sense of humour is unique. Jasmine: I congratulate you on 'beating' Rob for the first halogen-bonding paper from the group. Hopefully it is the first of many more.

To Prof. Se-Woung Oh (a.k.a. 'Dr. Oh'): I admire your seemingly insatiable attention to detail, astute observations of certain things which others may miss, and I wish you success upon your return to South Korea. I hope that your visit to the Bryce lab has been fruitful. To Joseph 'Manischewitz' Weiss: I reflect fondly upon our enjoyment of many tubs full of 'extraordinary' beverages, trips to the SAQ, playing Rock Band®, and the Jew jokes. I also enjoyed the

perpetual stream of Facebook posts pertaining to the terrible public transit options in Toronto. I am saddened by the fact that I will be unable to have you read my thesis while you are on holiday. Thanks finally also for the instant coffee and the 500-pack of dry and tasteless crackers.

I thank now some additional people who had more of a social, as opposed to academic, impact on my time at Ottawa. Titel Jurca: I hope your muffins are always moist, and your fantasy hockey teams remain terrible. Chemické Listy surely awaits us…someday. Po-Heng Lin: to Taipei 101! Ian Mallov: while the Flames may suck, you sure can grow an interesting mustache. By the way, I am holding you to our bet. Jessica Harris: I think you hold the record for the number of coincidental run-ins while I was at Ottawa. Elyse Bernard: you were always a gracious co-host at many gatherings; thanks for the cooking pot and those stuffing tips. Best of luck during the remainder of your Ph.D. and all your future T_1 measurements! Jessica Priem: thanks for being a great CGSA president, social catalyst, party host, and for being excited by the fact that I went to Jackson Square. I would have respected you more if you didn't always have your father pick your fantasy hockey teams. Dave Blair: thanks for trying your best to keep the Townsend in stock, for picking up my slack at trivia, and for giving me a ride home on numerous occasions. Bryan Lucier: while you are technically at Windsor, you visited Ottawa so many times that it felt like you were always here. Thanks also for the 10 million status updates, MSN chats, and for being the greatest beer mile champion of all time. No brokeback.

I acknowledge all the members of my Ph.D. dissertation examination committee: Prof. Tom K. Woo, Prof. Natalie K. Goto, Dr. John A. Ripmeester, and Prof. William P. Power (Waterloo) for reading my dissertation and I thank them all for taking time out from their doubtlessly very busy schedules on the day of my defence. I additionally thank Prof. Paul M. Mayer for being on my first comprehensive examination committee.

Statement of Originality

I certify that this dissertation, and the research to which it refers, are the products of my own efforts, and that any ideas or quotations from the works of others, be it those which are published or otherwise, are fully acknowledged in accordance with the standard referencing practices of the scientific community. I acknowledge the helpful guidance and support of my supervisor, Prof. David L. Bryce. Prof. Alex D. Bain (McMaster University) is acknowledged for developing the software used for some of the line shape analysis in Chapters 4 and 5. Mr. T. Maris (Université de Montréal) acquired the powder X-ray data for $MgBr_2$, which was used to generate Figure 6.5. The group of Prof. Darrin S. Richeson (University of Ottawa) is acknowledged for providing samples of 'GaI', which were used for the magnetic resonance experiments presented in Chapter 7. The group of Prof. Pierangelo Metrangolo (Politecnico di Milano, Italy) is acknowledged for providing several iodine-containing samples, used for the SSNMR experiments presented in Section 9.3.

Chapter 3 is based upon the following publication:

C. M. Widdifield and D. L. Bryce, Solid-State $^{79/81}$Br NMR and Gauge-Including Projector-Augmented Wave Study of Structure, Symmetry, and Hydration State in Alkaline Earth Metal Bromides, *J. Phys. Chem. A*, **2010**, *114*, 2102 – 2116.

Chapter 4 and parts of Chapter 5 are based upon the following publication:

C. M. Widdifield and D. L. Bryce, Solid-State ^{127}I NMR and GIPAW Study of Metal Iodides and Their Hydrates: Structure, Symmetry, and Higher-Order Quadrupole-Induced Effects, *J. Phys. Chem. A*, **2010**, *114*, 10810 – 10823.

Parts of Chapter 5 are based upon the following publication:

C. M. Widdifield, Alex D. Bain and D. L. Bryce, Definitive solid-state $^{185/187}$Re NMR spectral evidence for and analysis of the origin of high-order quadrupole-induced effects for $I = 5/2$, *Phys. Chem. Chem. Phys.*, **2011**, *13*, 12413 – 12420.

Chapter 6 is based upon the following publications:

C. M. Widdifield and D. L. Bryce, Crystallographic structure refinement with quadrupolar nuclei: a combined solid-state NMR and GIPAW DFT example using $MgBr_2$, *Phys. Chem. Chem. Phys.*, **2009**, *11*, 7120 – 7122.

C. M. Widdifield and D. L. Bryce, A multinuclear solid-state magnetic resonance and GIPAW DFT study of anhydrous calcium chloride and its hydrates, *Can. J. Chem.*, **2011**, *89*, 754 – 763.

Chapter 7 is based upon the following publication:

C. M. Widdifield, T. Jurca, D. S. Richeson and D. L. Bryce, Using $^{69/71}$Ga solid-state NMR and ^{127}I NQR as probes to elucidate the composition of 'GaI', *Polyhedron*, **2012**, *35*, 96 – 100.

Contents

6   *Aspects of 'NMR Crystallography' Using Quadrupolar Halogen Nuclei*

Appendices

List of Tables

List of Figures

List of Abbreviations

a.u.   atomic units

CASTEP   Cambridge Serial Total Energy Package

CCD   charge-coupled device

CS   chemical shift

CSA   chemical shift anisotropy

CT   central transition (i.e., $m = +1/2 \leftrightarrow -1/2$)

CW   continuous-wave

DEISM   direct enhancement of integer spin magnetization

DFT   density functional theory

EFG   electric field gradient

FFT   fast-Fourier transformation

GGA   generalized gradient approximation

GIAO   gauge-including atomic orbitals

GIPAW   gauge-including projector augmented-wave

HDI   hexadecapole interaction

HOMO   highest occupied molecular orbital

HOQIE   high-order quadrupole-induced effects

ICP-MS   inductively coupled plasma mass spectrometry

IR   infrared

IUPAC   International Union of Pure and Applied Chemistry

LUMO   lowest unoccupied molecular orbital

MAS   magic-angle spinning

mb	millibarn (1 mb = 1×10^{-31} m^2)
MG	Meiboom-Gill
MO	molecular orbital (plural: MOs)
MS	magnetic shielding
N/A	not applicable
NMR	nuclear magnetic resonance
NN	nearest neighbours
NNN	next-nearest neighbours
NOE	nuclear Overhauser Effect
NQR	nuclear quadrupole resonance
o.d.	outer diameter
otfg	on-the-fly generation
PAS	principal axis system
PAW	projector augmented-wave
PBE	Perdew-Burke-Ernzerhof exchange-correlation functional
POV	persistence of vision
ppm	parts per million
PW91	Perdew-Wang exchange-correlation functional developed in 1991
pXRD	powder X-ray diffraction
QCPMG	quadrupolar Carr-Purcell Meiboom-Gill
QI	quadrupolar interaction
QIE	quadrupole-induced effects
QIS	quadrupole-induced shift
QUEST	Quadrupolar Exact Software

ref.	reference
RF	radiofrequency
rmsd	root-mean-squared difference
S/N	signal-to-noise ratio
SR	spin-rotation
SSNMR	solid-state nuclear magnetic resonance
ST	satellite transition(s) (i.e., $m = \pm1/2 \leftrightarrow \pm3/2$, and/or $\pm3/2 \leftrightarrow \pm5/2$, $|\Delta m| = 1$)
STMAS	satellite transition magic-angle spinning
STREAQI	slow turning reveals enormous quadrupolar interactions
usp	ultrasoft pseudopotential
vdW	van der Waals
VOCS	variable-offset cumulative spectrum
WURST	wideband uniform-rate and smooth truncation
XC	exchange-correlation
XRD	X-ray diffraction

List of Symbols

$\hat{1}$ identity operator

a, b, c values associated with unit cell dimensions

a_i, b_i generic weighting coefficients

a_0 atomic Bohr radius ($0.529\ 177\ 210\ 92(17) \times 10^{-10}$ m)

$|A\rangle$ generic eigenstate label

B_0 applied external magnetic field component (traditionally, the z-component)

B_1 magnetic field associated with an applied oscillating radiofrequency pulse

B_{eff} effective magnetic field due to a near-resonance radiofrequency pulse

$\mathbf{B}_{ind}$ induced magnetic field

$\mathbf{B}_{nuc}$ total magnetic field experienced at the nucleus (for magnetic shielding)

$\mathbf{B}_0$ applied external magnetic field

C_n n-fold rotational axis

C_Q nuclear quadrupole coupling constant

e elementary electric charge ($1.602\ 176\ 565(35) \times 10^{-19}$ C)

E energy (arbitrary units)

E_{cut} plane wave basis set energy cutoff

E_{xtal} energy associated with the accepted crystal structure (GIPAW DFT)

h Planck constant ($6.626\ 069\ 57(29) \times 10^{-34}$ J s)

$\hbar$ reduced Planck constant ($1.054\ 571\ 726(47) \times 10^{-34}$ J s)

$\hat{\mathcal{H}}_{1e}, \hat{\mathcal{H}}_Q$ internal one spin electric Hamiltonian, quadrupolar Hamiltonian

$\hat{\mathcal{H}}_{1m}$ internal one spin magnetic Hamiltonian

$\hat{\mathcal{H}}_{2e}$	internal two spin electric Hamiltonian
$\hat{\mathcal{H}}_{2m}$	internal two spin magnetic Hamiltonian
$\hat{\mathcal{H}}_{CS}^1$	chemical shift Hamiltonian under the secular approximation, first-order perturbation
$\hat{\mathcal{H}}_{CS}^{iso}$	isotropic chemical shift Hamiltonian
$\hat{\mathcal{H}}_{D}$	direct dipole-dipole Hamiltonian
$\hat{\mathcal{H}}_{e}$	total electric spin Hamiltonian
$\hat{\mathcal{H}}_{e\text{-ext}}$	external electric spin Hamiltonian
$\hat{\mathcal{H}}_{int}$	total internal spin Hamiltonian
$\hat{\mathcal{H}}_{J}$	indirect dipole-dipole Hamiltonian (a.k.a. the J Hamiltonian)
$\hat{\mathcal{H}}_{m}$	total magnetic spin Hamiltonian
$\hat{\mathcal{H}}_{m\text{-ext}}$	external magnetic spin Hamiltonian
$\hat{\mathcal{H}}_{Q}^1$	quadrupolar Hamiltonian under the secular approximation, first-order perturbation
$\hat{\mathcal{H}}_{RF}(t)$	on-resonance RF Hamiltonian
$\hat{\mathcal{H}}_{spin}$	total spin Hamiltonian (time-independent contributions only)
$\hat{\mathcal{H}}_{SR}$	spin-rotation Hamiltonian
$\hat{\mathcal{H}}_{Z}$	Zeeman Hamiltonian
I	nuclear spin angular momentum quantum number
$\mathbf{I}$	nuclear spin angular momentum vector

$\hat{I}_X,\ \hat{I}_Y,\ \hat{I}_Z$	nuclear spin angular momentum operators (X, Y, and Z components, respectively)
J	isotropic indirect spin-spin coupling constant
k_B	Boltzmann constant ($1.380\ 6488(13) \times 10^{-23}$ J K^{-1})
m	nuclear spin angular momentum quantum number, z-component
$\mathbf{M}$	bulk nuclear spin magnetic moment vector (a.k.a. magnetization vector)
$\mathbf{M'}$	bulk nuclear spin magnetic moment vector after an applied RF pulse
N_B	number of basis set functions (used in cluster methods)
$\tilde{p}_i$	projector functions (PAW method)
$q(X)$	partial ionic charge value associated with ionic species 'X'
Q	nuclear electric quadrupole moment
r	generic distance parameter
$r_{A\text{-}B}$	internuclear distance between arbitrary atoms 'A' and 'B'
R	correlation coefficient parameter
R_{core}	core region distance
$\left\langle 1/r^3 \right\rangle_{np}$	average value of $1/r^3$ over the valence p electrons for a free atom
$\overline{r(M-X)}$	average internuclear metal-halogen first-coordination sphere distance
T	temperature (in K)
T_1	spin-lattice relaxation parameter (a.k.a. longitudinal relaxation parameter)
T_2	spin-spin relaxation parameter (a.k.a. transverse relaxation parameter)
T_2^*	spin-spin relaxation parameter due to the QI and B_0-inhomogeneity
$\hat{T}_{PAW}$	PAW wave function transformation operator
V	unit cell volume

V_{ij}	electric field gradient tensor matrix elements ($i, j = x, y, z$)
V_{11}, V_{22}, V_{33}	eigenvalues (principal components) of the electric field gradient tensor
$\mathbf{V}_{11}, \mathbf{V}_{22}, \mathbf{V}_{33}$	eigenvectors of the electric field gradient tensor
$\ddot{V}$	electric field gradient tensor
$\ddot{V}_{\mathrm{PAS}}$	electric field gradient tensor in its principal axis system
$^A X$	mass number 'A' associated with nuclear species 'X'
Z	integer point charge value
α, β, γ	Euler angles
$\alpha_{\mathrm{C}}, \beta_{\mathrm{C}}, \gamma_{\mathrm{C}}$	values associated with unit cell angles
$\alpha_{\mathrm{D}}, \beta_{\mathrm{D}},$	angles associated with the direct dipolar coupling tensor
$|\alpha\rangle$	label for Zeeman eigenstate: $I = 1/2$, $m = +1/2$
$|\beta\rangle$	label for Zeeman eigenstate: $I = 1/2$, $m = -1/2$
γ	gyromagnetic / magnetogyric ratio
γ_∞	Sternheimer antishielding factor
Δc	displacement along the c-axis of a unit cell
ΔC_{Q}	error in the C_{Q} value when comparing exact and second-order perturbation theory simulations
Δc_{xtal}	displacement along the c-axis of a unit cell for the accepted crystal structure
Δ_{HL}	HOMO–LUMO gap
$\Delta \delta_{\mathrm{iso}}$	error in the isotropic chemical shift value when comparing exact and second-order perturbation theory simulations
Δv	offset frequency from some reference point
Δv_{CT}	breadth of the central transition under second-order perturbation theory

Δv_{NMR}	breadth of an NMR line shape (transition not specified)
δ	chemical shift value (general)
δ^{K}_{ij}	Kronecker Delta function
δ_{iso}	isotropic chemical shift
δ_{cg}	centre of gravity of the central transition
δ^+	partial positive electric charge
δ^-	partial negative electric charge
δ_{ij}	chemical shift tensor matrix elements ($i, j = x, y, z$)
$\delta_{11}, \delta_{22}, \delta_{33}$	eigenvalues (principal components) of the chemical shift tensor
$\delta_{zz}(\Theta)$	portion of the chemical shift tensor which is retained under the secular (i.e., high-field) approximation
δ^2_{QIS}	second-order quadrupole-induced shift
$\boldsymbol{\delta}_{11}, \boldsymbol{\delta}_{22}, \boldsymbol{\delta}_{33}$	eigenvectors of the chemical shift tensor
$\ddot{\delta}$	chemical shift tensor (generic Cartesian reference frame)
$\ddot{\delta}_{\text{PAS}}$	chemical shift tensor in its principal axis system
ε_0	electric constant ($8.854\ 187\ 817 \times 10^{-12}$ F m^{-1})
η_{Q}	asymmetry parameter of the electric field gradient tensor
2θ	goniometer axis value (for X-ray apparatus)
θ, φ	polar angles (defined in the usual sense)
Θ	angular dependence symbol (generic)
κ	skew of the chemical shift / magnetic shielding tensor
λ	wavelength (for X-ray source)

μ	nuclear spin magnetic moment value
$\boldsymbol{\mu}\ (\boldsymbol{\mu}_i)$	nuclear spin magnetic moment vector (same, but for an individual spin)
$\rho_{|\alpha\rangle},\ \rho_{|\beta\rangle}$	eigenstate populations of eigenstates α and β, respectively
v_i	fractional unit cell coordinate labels ($i = a, b, c$)
v_0	Larmor frequency of precession (in units of Hz)
v_1	frequency of precession induced by an applied radiofrequency pulse (on-resonance, in units of Hz)
v_{Q1}, v_{Q2}	quadrupolar resonance frequencies for $I = 5/2$, ordered such that $v_{Q2} > v_{Q1}$
v_{iso}	isotropic nuclear spin precession frequency (for shift calculations)
$v_{iso,\,ref}$	isotropic nuclear spin precession frequency for a reference sample
$v_{CT,\,high}$	frequency associated with the high-frequency CT discontinuity (second-order perturbation theory)
$v_{CT,\,low}$	frequency associated with the low-frequency CT discontinuity (second-order perturbation theory)
$v^2_{CT,\,axial}$	frequency shift of central transition Zeeman eigenstates under second-order perturbation theory for an axial EFG
v_{MAS}	sample rotation frequency under magic-angle spinning conditions
v_Q	quadrupolar frequency (in units of Hz)
v_{RF}	frequency of an applied oscillating radiofrequency pulse (in units of Hz)
σ	magnetic shielding value (general)
σ_{ij}	magnetic shielding tensor matrix elements ($i, j = x, y, z$)
σ_{iso}	isotropic magnetic shielding value
$\sigma_{iso,\,ref}$	isotropic magnetic shielding value for a reference sample

$\boldsymbol{\sigma}_{11}, \boldsymbol{\sigma}_{22}, \boldsymbol{\sigma}_{33}$	eigenvectors of the magnetic shielding tensor
$\hat{\sigma}_X, \hat{\sigma}_Y, \hat{\sigma}_Z$	Pauli matrices (X, Y, and Z components, respectively)
$\ddot{\sigma}$	magnetic shielding tensor
$\tau_1, \tau_2, \tau_3, \tau_4$	interpulse delays for echo and multiple-echo pulse sequences
τ_{RF}	pulse width (i.e., duration of applied oscillating radiofrequency pulse)
φ_{RF}	phase of an applied radiofrequency pulse
$\hat{\varphi}_i$	pseudo partial wave functions (PAW method)
$\psi(r)$	true electronic wave function
$\tilde{\psi}(r)$	auxiliary electronic wave function
Ω	span of the chemical shift / magnetic shielding tensor
ω_0	Larmor frequency of precession (in units of rad s^{-1})
ω_1	frequency of precession induced by an applied oscillating radiofrequency pulse (on-resonance, in units of rad s^{-1})
ω_Q	quadrupolar frequency (in units of rad s^{-1})
ω_{RF}	frequency of an applied oscillating radiofrequency pulse (in units of rad s^{-1})

Chapter One

General Introduction and Objectives

1.1   The Ubiquity of Nuclear Magnetic Resonance in Chemistry

The spectroscopic technique of nuclear magnetic resonance (NMR) is used every day in academic, industrial, and governmental research laboratories around the world. From the time the first commercially-available NMR spectrometer was introduced in 1952 (Figure 1.1),[1] there has been considerable growth in the field (certain advances are outlined in Chapter 2): nowadays nearly every modern chemistry department has at least one NMR spectrometer,[2] and many have dedicated NMR facilities coordinated by one or more individuals (Figure 1.2).[3]
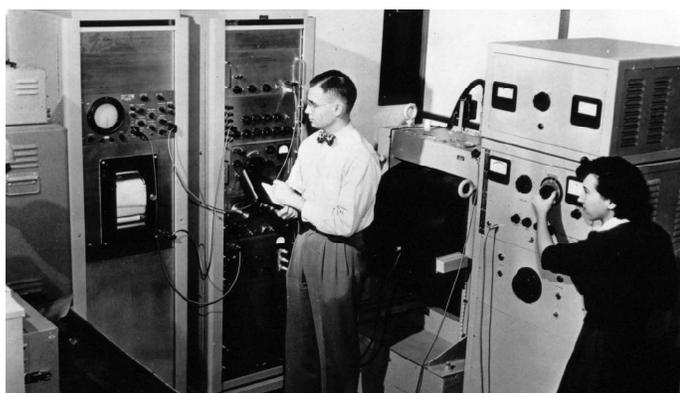
Figure 1.1 James Shoolery (left) and Virginia Royden (right) operating the HR-30 prototype (the first commercial NMR spectrometer). From ref. 4.

From a fundamental physical science perspective, the continuing advances in NMR spectroscopy benefit not only those directly associated with the field, but also a great many others. For example, when synthetic chemists perform chemical reactions, they will usually have a desired product in mind. To establish the identity of the product material, it is subjected to a number of characterization tests. Liquid-state NMR experiments are often performed during

this characterization phase, as they are sensitive to the local electronic structure about a particular nucleus. While liquid-state NMR experiments can provide a great deal of information through observables such as the isotropic chemical shift (δ_{iso}), the isotropic indirect spin-spin (J) coupling constant, and the nuclear Overhauser Effect (NOE), these experiments are relatively insensitive from a signal-to-noise ratio (S/N) standpoint when compared to other forms of spectroscopy (as will be discussed further in Chapter 2).[5] This low sensitivity has somewhat limited the typical applications of NMR to relatively sensitive nuclides such as ^{1}H, ^{19}F, and ^{31}P.[6] Due primarily to the prevalence of carbon and nitrogen in synthetic chemistry and biochemistry, there also exists a great deal of information on the very insensitive methods of liquid-state ^{13}C and ^{15}N NMR spectroscopy.[7,8]

Figure 1.2 Solid-state NMR spectrometers available at the University of Ottawa, as of 2011. Clockwise from upper left: B_0 = 21.1 T; B_0 = 11.75 T; B_0 = 9.4 T; B_0 = 4.7 T. All photos were taken by C. M. Widdifield during the period from April 2008 to August 2011.

In comparison to liquid-state NMR, solid-state NMR (SSNMR) spectroscopy is less developed due to the presence of a variety of anisotropic line shape broadening effects in microcrystalline powder samples (some of these effects will be detailed in Chapter 2). Many of the anisotropic effects could be removed by performing single-crystal NMR experiments; however, the crystal sizes required are an order of magnitude larger than what is required for X-ray diffraction (XRD) experiments, which generally makes this approach impractical. While liquid-state ^{1}H NMR experiments are considered routine, even 'simple' ^{1}H SSNMR experiments are typically not of substantial utility because the anisotropic line shape broadening mechanisms oftentimes lead one to record broad and somewhat featureless line shapes.[9] As could be anticipated, the poor resolution of SSNMR experiments makes subsequent line shape analysis difficult. At the same time, while the resolution and sensitivity of SSNMR suffers, these anisotropic interactions are also dense in valuable information. In favourable scenarios, this additional information may be used to paint a very detailed picture of the electronic (and therefore structural) environment about the probe nucleus. It is therefore of significant general importance to further explore and develop SSNMR methods for a variety of nuclei.

1.2   Quadrupolar Nuclei

Due to the potential wealth of structural information that may be extracted from accurately modeled SSNMR line shapes, a great number of techniques have been developed over the past half-century to enhance both the resolution and the sensitivity of SSNMR experiments (some of which are discussed in detail in Section 2.4). Even with the substantial improvements that have been made over the past 50 years, many nuclei are still thought of as being 'inaccessible' to observation using SSNMR. Of these inaccessible nuclei, many possess a nonspherical distribution of electric charge, which leads to a measurable nuclear electric

quadrupole moment (Q). The Q associated with these nuclei can couple to the external electric field gradient (EFG), resulting in a quadrupolar interaction (QI). Unless dictated otherwise by the molecular or lattice symmetry, the QI will produce additional SSNMR signal broadening. Of course, this broadening further decreases the sensitivity of the SSNMR experiment and requires additional techniques to be applied to acquire high-quality SSNMR spectra in a timely manner.

1.3   Objectives and Overview

In this dissertation, modern SSNMR techniques are employed and developed in an effort to characterize the local environments at a variety of insensitive quadrupolar nuclei. Primarily, the quadrupolar halogen nuclei (i.e., $^{35/37}$Cl, $^{79/81}$Br, and ^{127}I) have been selected here for observation, as SSNMR methods for these probe nuclei are relatively underdeveloped (especially the $^{79/81}$Br and ^{127}I nuclides). It is envisioned that the observations, analyses, and discussions provided in Chapters 3, 4, and 6 will motivate further studies using the quadrupolar halogen nuclei as sensitive local probes of electronic structure and of crystallographic symmetry. Particular halide-containing systems are chosen to provide a framework for the discussion of effects such as hydration and lattice symmetry upon the various SSNMR observables. One particular aim herein (detailed in Chapter 6) is the use of the observed SSNMR tensor parameters as restraints in 'NMR crystallography' structural refinements, as the QI is expected to be sufficiently sensitive to the local arrangement of atoms/ions near the probe nucleus.[10]

Due to the rather large Q values associated with the $^{79/81}$Br and ^{127}I nuclides, it might be expected that the QI would rival the familiar Zeeman interaction, and lead to unforeseen complications in modeling the observed SSNMR line shapes using standard techniques. As accurate line shape modeling in this regime has not appeared in the literature for powdered samples, investigations were performed in order to test the limitations of currently-accepted line

shape simulation methods. An exact method for the simulation of these line shapes is also tested using experimental data. The above tests are the primary focus of Chapter 5, where nuclear quadrupole resonance (NQR) and SSNMR observations using ^{127}I and $^{185/187}$Re nuclei are presented (NMR experiments using rhenium nuclei are particularly rare). It is also desirable to see if the accurate treatment of the rhenium QI would allow for the observation of more subtle effects, such as isotropic chemical shifts, which could then be related to rhenium oxidation states (this is of substantial value, since rhenium can exist in a variety of oxidation states).

Chapter 7 outlines efforts towards understanding the composition of 'GaI', which is an important synthetic precursor for low-valent gallium-containing products, and whose composition is ambiguous based upon earlier powder XRD (pXRD) and Raman spectroscopy studies. For the 'GaI' study, multiple-field $^{69/71}$Ga SSNMR and ^{127}I NQR experiments were chosen. As part of an ongoing project to more generally understand strong QI effects in SSNMR spectra, Chapter 9 describes current research progress on additional systems where the SSNMR spectra are greatly influenced by the QI. Brief discussions include $^{185/187}$Re SSNMR experiments on additional rhenium-containing materials, ^{181}Ta SSNMR of tantalum oxides, and moderate-field ^{81}Br SSNMR on $CaBr_2$. As well, ^{127}I SSNMR experiments on industrially-important iodine-containing materials are briefly discussed in order to comment on the utility of these experiments at detecting weak solid-state intermolecular interactions, such as halogen bonding.

1.4   References

1   J. N. Shoolery, *Anal. Chem.*, **1993**, *65*, 731A-741A.

2   J. Ginsberg, *NMR and MRI: Applications in Chemistry and Medicine*, accessed August 25th, 2011, http://portal.acs.org/portal/PublicWebSite/education/whatischemistry/landmarks/about/CNBP_026831.

3   W. P. Niemczura, *ammrl*, accessed September 1st, 2011, http://www.ammrl.org/.

4   Varian Corporation, *NMR History According to Varian Associates*, accessed August 17th, 2011, http://www.varianinc.com/image/vimage/docs/products/nmr/spectromet/inova_brochure/shared/NMR_history.pdf.

5   V. Sablinskas, G. Steiner and M. Hof, Optical Spectroscopy - Applications In *Handbook of Spectroscopy*, 1st edn., G. Gauglitz and T. Vo-Dinh, Eds., Wiley: Weinheim, **2003**, 89-168.

6   D. L. Rabenstein, *Anal. Chem.*, **2001**, *73*, 214A-223A.

7   C. Dominguez, M. Schubert, O. Duss, S. Ravindranathan and F. H.-T. Allain, *Prog. Nucl. Magn. Reson. Spectrosc.*, **2011**, *58*, 1-61.

8   D. S. Wishart, *Prog. Nucl. Magn. Reson. Spectrosc.*, **2011**, *58*, 62-87.

9   A. Lesage, *Phys. Chem. Chem. Phys.*, **2009**, *11*, 6876-6891.

10   R. K. Harris, Crystallography & NMR: an Overview In *NMR Crystallography*, R. K. Harris, R. E. Wasylishen and M. J. Duer, Eds., John Wiley & Sons: Chichester, United Kingdom, **2009**, 3-18.

Chapter Two

Introduction to Nuclear Magnetic Resonance

2.1   The Discovery of Spin

On March 12th 1862, Michael Faraday attempted to detect a change in the frequency of the light emitted from a sample due to the presence of a large magnetic field.[1] Unfortunately, his experiment produced a negative result, and it was therefore believed for many years that applied forces (of any nature) could not alter the frequency of the light emitted from a particle. This remained so until Pieter Zeeman (Nobel Prize in physics, 1902) detected a spectral broadening in the light emitted from a sample of sodium once it was subjected to a magnetic force.[2] In a time that preceded the formal discovery of the electron as a particle, the broadening mechanism was quickly explained (although incompletely) by Hendrik Lorentz (Nobel Prize in physics, 1902) as being due to the electric charge of this 'hypothetical' entity. After further studies by Zeeman, however, it was apparent that the Lorentz theory could not fully explain all of the experimental observations (e.g., the 'anomalous' Zeeman effects).[3,4]

The concept of (electron) spin was put forward publically by Wolfgang Pauli (Nobel Prize in physics, 1945) in 1925 in an effort to fully explain the additional absorption or emission lines that appeared when a sample was placed within a sufficiently strong magnetic field.[5] Very striking experimental evidence for the existence of electron spin had actually already been provided by Otto Stern (Nobel Prize in physics, 1943) and Walther Gerlach (although the splitting was originally thought to be due to orbital angular momentum),[6] as well as George Uhlenbeck and Samuel Goudsmit (who appear to have correctly interpreted prior experimental observations).[7] Otto Stern would subsequently observe the same behaviour using protons (and

hence demonstrate the existence of nuclear spin).[8,9] Paul Dirac (Nobel Prize in physics, 1933) illustrated (via a four component wave function) how spin emerged naturally when applying special relativity to the quantum mechanics of the electron.[10,11] Amazingly, Dirac's treatment also predicted solutions for a particle exactly analogous to the electron, but which carried a positive electric charge (although out of "pure cowardice"[12] he did not explicitly state this finding). Spin angular momentum appears to be a fundamental property of all (non-hypothetical) elementary particles, and has influenced development in a variety of areas, such as quantum physics, analytical chemistry, structural biology, cognitive neuroscience, and information storage.[13]

2.2   Initial Accounts and Observations of NMR

In 1938, the NMR phenomenon was first illustrated by Isidor I. Rabi (Nobel Prize in physics, 1944) *et al.* using the nuclei from a beam of LiCl molecules.[14] At this time, NMR was envisioned as a method to accurately measure the value of nuclear spin magnetic moments (μ). While the initial attempts to detect NMR in bulk materials did not lead to favourable outcomes,[15,16] improvements in technology and experimental design led to two research groups observing a bulk NMR effect in late 1945.[17,18] By 1951, experimental resolution had improved to the point that the measured NMR values for a given ground state nucleus appeared to be sample-dependent.[19-23] This 'sample-dependent shift' was later termed the isotropic chemical shift (δ_{iso}), which is the parameter most often quoted when reporting the results of NMR measurements.

2.3   Introduction to Nuclear Spin Dynamics

The spin dynamics which are believed to govern NMR experiments have been outlined in detail numerous times;[24-28] hence, only the most relevant topics will be considered here. Specific theoretical background discussions will be included in subsequent Chapters, as required.

2.3.1   The Classical Motion of Isolated*Nuclear Spins

A nucleus which possesses nonzero nuclear spin angular momentum ($\mathbf{I}$) can be associated with a nuclear spin magnetic moment ($\boldsymbol{\mu}$). Classically, both may be described as vector quantities, and they are linearly related through the gyromagnetic (or magnetogyric) ratio (γ), as $\boldsymbol{\mu} = \gamma\mathbf{I}$. Under this classical vector model, both quantities can be pictured as in Figure 2.1.

$\gamma > 0$ $\gamma < 0$
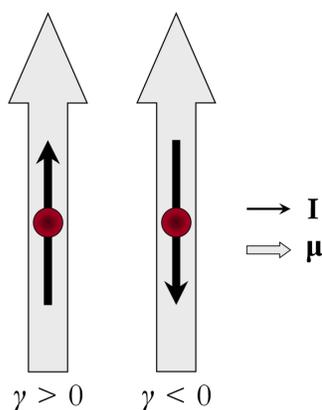
Figure 2.1 Vector representations of $\mathbf{I}$ and $\boldsymbol{\mu}$. If these two vectors are collinear, then γ is positive, while if they are antiparallel, then γ is negative.

If an electronically diamagnetic sample is not within an externally applied magnetic field ($\mathbf{B}_0$), each $\boldsymbol{\mu}$ may individually direct along any spatial direction (i.e., they are randomly distributed), and the sample does not possess a bulk nuclear spin magnetic moment ($\mathbf{M}$). When an ensemble of nuclear spins are subjected to $\mathbf{B}_0$, contrary to popular belief,[28] there is no re-

---

* Isolated will be taken as nuclei which are interacting with, at most, a constant external magnetic field ($\mathbf{B}_0$).

orientation of the magnetic moments of the individual spins into spatial states. Rather, they begin to precess about the applied field. The sense of the precession is determined by the sign of γ (Figure 2.2).

$\gamma > 0$ $\qquad$ $\gamma < 0$
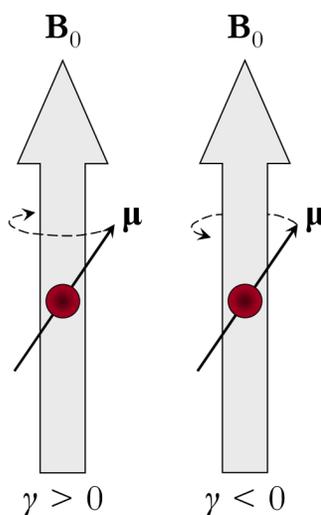
Figure 2.2 The precession of $\boldsymbol{\mu}$ about $\mathbf{B}_0$. The sense of this precession about $\mathbf{B}_0$ may be either clockwise ($\gamma > 0$) or counterclockwise ($\gamma < 0$).

The frequency of precession (the Larmor frequency, ω_0) for a given nuclide may be specified by the negative of the product of the gyromagnetic ratio and a spatial component of the applied field (i.e., $\omega_0 = -\gamma B_0$). Note that ω_0 is an angular frequency and therefore carries units of rad s^{-1}, so in order to determine the frequency value in Hz (i.e., v_0), the value of ω_0 must be divided by 2π rad.

2.3.2 The Quantum Mechanical Description of Nuclear Spin Interactions

The previous section discussed using a classical vector model to describe the motion of isolated nuclear spins when they interact with $\mathbf{B}_0$, (it is traditionally assumed that $\mathbf{B}_0$ is parallel to the z-axis, and this will be represented using B_0 in all subsequent discussions). This subsection

uses quantum mechanics to determine the nuclear spin state eigenvalues for both the isolated situation, as well as when the nuclear spins are subjected to additional coupling interactions.

2.3.2.1 Coupling to an External Magnetic Field

While the quantum mechanical treatments for spin angular momentum and orbital angular momentum are somewhat similar,[29,30] they should not be thought of in the same sense. This is because spin angular momentum is usually described as an intrinsic property of a wide array of particles, including the electron and many nuclei, which contrasts with the conventional understanding of orbital angular momentum. When isolated nuclear spins of arbitrary nuclear spin angular momentum quantum number (I) experience an external B_0, there are $2I + 1$ possible eigenstates. These are often referred to as Zeeman (or hyperfine) eigenstates. The case when $I = 1/2$ is the most commonly encountered, has been treated in numerous introductory texts,[31-35] and will serve as the starting point here. The nuclear spin eigenstates projected along the axis in which the magnetic field is applied may be reported according to the convention of Dirac:[36]

$$|\text{state}\rangle = |I, m\rangle,$$

$$|\alpha\rangle = \left|\frac{1}{2}, \frac{1}{2}\right\rangle = \begin{bmatrix} 1 \\ 0 \end{bmatrix}, \qquad |\beta\rangle = \left|\frac{1}{2}, -\frac{1}{2}\right\rangle = \begin{bmatrix} 0 \\ 1 \end{bmatrix}, \tag{2.1}$$

where m is the nuclear spin angular momentum quantum number projected along z, and $|\alpha\rangle$ and $|\beta\rangle$ serve as arbitrary Zeeman eigenstate labels. The Zeeman Hamiltonian ($\hat{\mathcal{H}}_Z$) describes the dynamics of the nuclear spin states under the conditions outlined above (in this dissertation, a caret ($\hat{\ }$) will denote quantum mechanical operators, and $\hbar$ is the reduced Planck constant):

$$\hat{\mathcal{H}}_Z = \omega_0 \hat{I}_Z = \frac{\hbar}{2} \omega_0 \hat{\sigma}_Z, \tag{2.2}$$

with $\hat{I}_Z$ as the nuclear spin angular momentum operator along the direction of B_0 and where $\hat{\sigma}_Z$ is one of the conventional Pauli matrices,[37] the set of which together with the identity operator ($\hat{1}$) forms the basis of the spin space. As an example, for $I = 1/2$, the spin space basis appears as below:

$$\hat{\sigma}_X = \begin{bmatrix} 0 & 1 \\ 1 & 0 \end{bmatrix}, \quad \hat{\sigma}_Y = \begin{bmatrix} 0 & -i \\ i & 0 \end{bmatrix}, \quad \hat{\sigma}_Z = \begin{bmatrix} 1 & 0 \\ 0 & -1 \end{bmatrix}, \quad \hat{1} = \begin{bmatrix} 1 & 0 \\ 0 & 1 \end{bmatrix}. \tag{2.3}$$

When the Zeeman Hamiltonian operates upon the spin states in (2.1), the relative energies of these states may be obtained:

$$\hat{\mathcal{H}}_Z|\alpha\rangle = \omega_0 \hat{I}_Z|\alpha\rangle = \frac{\hbar}{2}\omega_0|\alpha\rangle = -\frac{\hbar}{2}\gamma B_0|\alpha\rangle, \tag{2.4}$$

$$\hat{\mathcal{H}}_Z|\beta\rangle = \omega_0 \hat{I}_Z|\beta\rangle = -\frac{\hbar}{2}\omega_0|\beta\rangle = \frac{\hbar}{2}\gamma B_0|\beta\rangle. \tag{2.5}$$

It is therefore observed that for $I = 1/2$, there exists two eigenstates, each of which depends upon γ and B_0. Since the value for γ is a constant for a given nuclide, the energy separation between the two states will increase with increasing magnetic field strength (Figure 2.3):
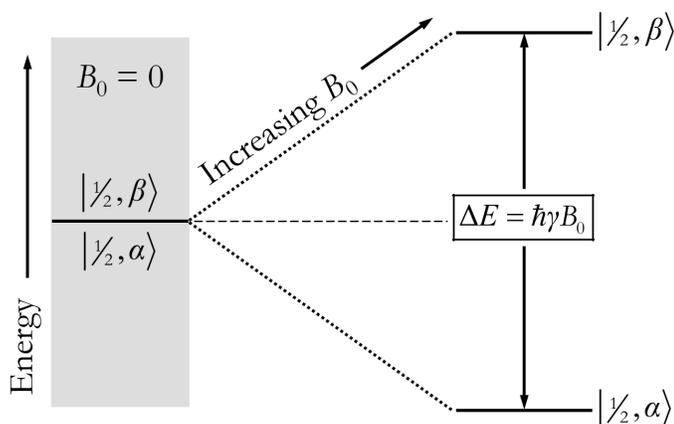
Figure 2.3 The interaction between **μ** and B_0 leads to spin states which are no longer degenerate. The number of available states equals $2I + 1$, and the energy difference between adjacent states is $\hbar\gamma B_0$. This Figure depicts $I = 1/2$ and $\gamma > 0$. For $\gamma < 0$, the state ordering would be reversed.

As hinted at earlier when using the classical vector model to describe the motion of isolated nuclear spins, a given nuclear spin where $I = 1/2$ is not restricted to being either 'pure $|\alpha\rangle$' or 'pure $|\beta\rangle$'; rather, the state is described by the superposition of the Zeeman eigenstates:

$$|A\rangle \;=\; a_i|\alpha\rangle \;+\; b_i|\beta\rangle, \tag{2.6}$$

where a_i and b_i are generic weighting coefficients. The above methodology (with appropriate modifications to the spin space basis for a given I value) can also be used to determine eigenstate energies for nuclides where $I > 1/2$, in each case leading to $2I + 1$ states (Figure 2.4):
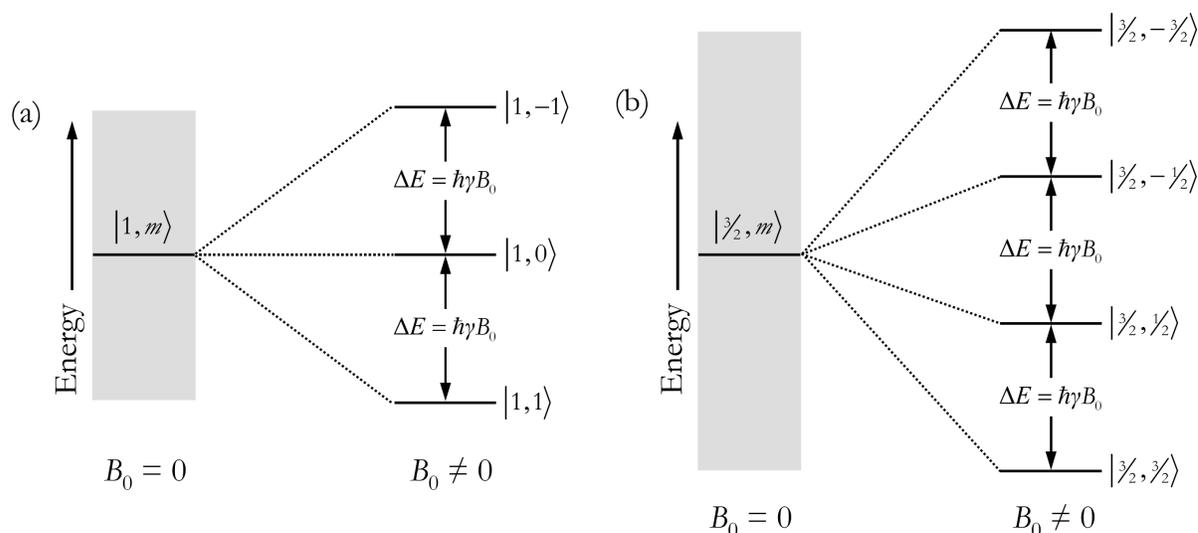
Figure 2.4 Nuclear spin state energy levels for the cases where (a) $I = 1$ and (b) $I = 3/2$ are coupled to B_0 (γ is taken as positive).

2.3.2.2 The Establishment of Thermal Equilibrium Populations

While the preceding discussions considered isolated nuclear spins, NMR spectroscopy on condensed matter involves the presence of an ensemble of spins which interact with one another. If one again considers the case where $I = 1/2$ and $\gamma > 0$, the relative population of eigenstate α ($\rho_{|\alpha\rangle}$) is often described using a Boltzmann distribution:[28]

$$\rho_{|\alpha\rangle} \;\cong\; \rho_{|\beta\rangle} \left(\frac{2 \;+\; \hbar\omega_0 / k_B T}{2 \;-\; \hbar\omega_0 / k_B T} \right), \tag{2.7}$$

where $\rho_{|\beta\rangle}$ is the population of spin state β, k_B is the Boltzmann constant, and T is the temperature (in K). The above equation assumes that the high-temperature approximation is valid. As touched on in Section 1.1, relative to other forms of spectroscopy, the energy separation between adjacent spin states is very small, which leads to very similar populations and corresponding low experimental sensitivity. Although not featured predominantly in this dissertation, under certain conditions, these populations can be manipulated using appropriate radiofrequency (RF) pulses.[38,39] At this point, the effect of these pulses on the bulk magnetization vector is briefly considered.

2.3.2.3 Response of the Magnetization to RF Pulses

The bulk nuclear spin magnetic moment (or magnetization, **M**) is determined by summing the ensemble of $\boldsymbol{\mu}_i$ (i.e., $\mathbf{M} = \sum \boldsymbol{\mu}_i$). When the α state is lower in energy and therefore of higher population relative to the β state, it is understood that **M** points along the applied field. If the populations of these two levels are inverted, **M** would direct anti-parallel to B_0.

The NMR signal for the nuclide under study is typically prepared (i.e., transformed into a state whose evolution may be monitored) by applying an oscillating RF pulse. This pulse produces its own magnetic field (B_1), which is usually substantially smaller in magnitude than B_0. When the frequency of the oscillating RF pulse (ω_{RF}) matches ω_0, the RF field is said to be 'on-resonance'. In a frame of reference rotating at ω_0, B_0 is constant, which leaves only B_1 to interact with **M**. As a result, **M** begins to precess about the B_1 axis with a frequency of ω_1 (Figure 2.5a). While it is unlikely that the resonance condition will always be precisely matched

(for reasons outlined in the sections below), it is the case that as long as $\omega_0 \approx \omega_{RF}$, **M** will interact meaningfully with B_1, but will instead precess about an effective field (B_{eff}) (Figure 2.5b):

$$B_{eff} = \left(B_0 + \omega_{RF}/\gamma \right) + B_1. \tag{2.8}$$

The amount of precession is determined by B_1, as well as the duration of the applied pulse (the pulse width, τ_{RF}). The resonant and time-dependent RF Hamiltonian ($\hat{\mathcal{H}}_{RF}(t)$) is as follows:[37]

$$\hat{\mathcal{H}}_{RF}(t) = -\hbar\gamma B_1 \left[\cos(\omega_{RF}t + \varphi_{RF})\hat{I}_X \pm \sin(\omega_{RF}t + \varphi_{RF})\hat{I}_Y \right], \tag{2.9}$$

where φ_{RF} is the phase of the RF pulse. The Hamiltonian in **(2.9)** represents the component of the applied RF field which is circularly polarized in the same sense as the Larmor precession frequency of a given nuclide. Note that during the pulse, another (non-resonant) circularly polarized component rotates with a frequency of $-\omega_0$. The component which interacts with **M** clearly depends upon the sign of γ and in fact some sources suggest that **(2.9)** should be multiplied by a factor of $1/2$, since half of the RF energy does not interact with the system.[28]
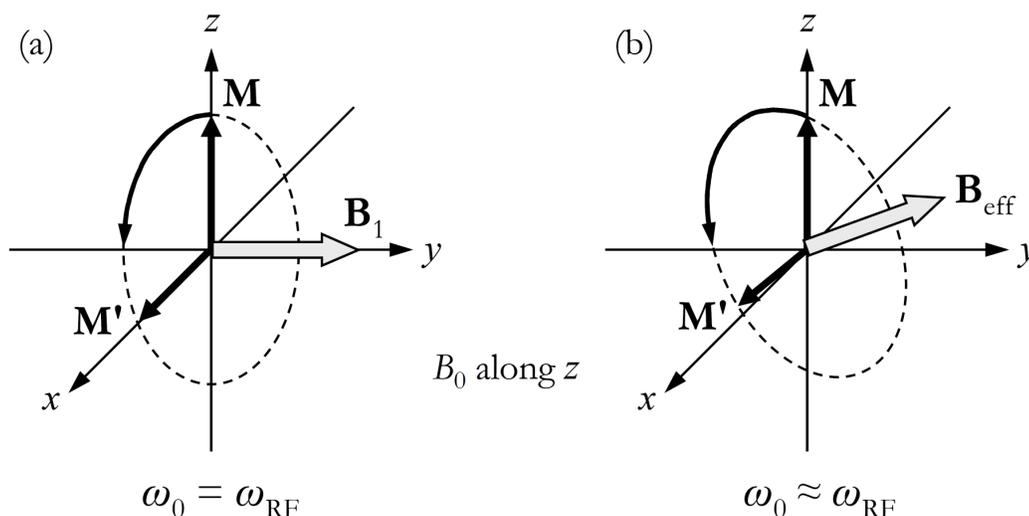
Figure 2.5 Effect of applied RF fields upon **M**. If $\omega_0 = \omega_{RF}$, as in (a), the application of an RF pulse along the y-axis will result in **M** precession about B_1. If $\omega_0 \approx \omega_{RF}$, as in (b), the RF pulse will still interact with **M**, but the precession will be about B_{eff}, according to **(2.8)**. If $\omega_0 \neq \omega_{RF}$, then **M** will not interact with the applied RF field.

2.3.2.4 Magnetic Shielding (MS)

In addition to the external interactions outlined in the preceding sections, there exists an array of internal nuclear spin interactions (although they are not always relevant or measurable). The magnetic shielding (MS) interaction results from the coupling between the nuclear spin angular momentum and the local magnetic field which is produced by B_0-induced electron circulation. This additional field augments the total field experienced at the nucleus ($\mathbf{B}_{nuc}$) such that it is not equal to B_0. The MS effect is commonly observed when studying molecules, with the local and applied fields being related via a magnetic shielding value (σ):

$$\mathbf{B}_{nuc} = (1 - \sigma)B_0. \tag{2.10}$$

The value which σ assumes is usually small for diamagnetic samples, and is therefore typically denoted in 'units' of parts per million (ppm) of B_0. Although useful from a theoretical standpoint, MS is not often measured experimentally,[40] but rather, a chemical shift (CS) value (δ) is measured. The CS values for samples in isotropic media (δ_{iso}) can be expressed relative to a well-characterized (i.e., reference) sample:[27]

$$\delta_{iso} = \frac{v_{iso} - v_{iso,\,ref}}{v_{iso,\,ref}}, \tag{2.11}$$

where v_{iso} and $v_{iso,\,ref}$ are the isotropic nuclear spin precession frequencies (in Hz) of the sample under study, and the reference sample, respectively. Any measured δ_{iso} value may be related to an isotropic MS (σ_{iso}) value if an absolute shielding scale has been established for that nuclide:[41]

$$\delta_{iso} = \frac{\sigma_{iso,\,ref} - \sigma_{iso}}{1 - \sigma_{iso,\,ref}} \cong \sigma_{iso,\,ref} - \sigma_{iso}. \tag{2.12}$$

If $\delta_{iso} > 0$, the sample under study is said to be deshielded (or downfield) relative to the standard, while if $\delta_{iso} < 0$, the sample is shielded (or upfield) relative to the standard. The Hamiltonian for an isotropic chemical shift ($\hat{\mathcal{H}}_{CS}^{iso}$) is defined as:

$$\hat{\mathcal{H}}_{CS}^{iso} \quad = \quad -\hbar\gamma\delta_{iso}B_0\hat{I}_Z. \tag{2.13}$$

Thus, it is clear that the amount that the CS Hamiltonian alters the eigenvalue of a given spin state will depend (to a first approximation, as justified below) linearly on both γ and B_0, and that the change in the energy is small based upon the usual magnitude of δ_{iso}. Hence, the effects of $\hat{\mathcal{H}}_{CS}^{iso}$ may be treated as a first-order perturbation upon the $\hat{\mathcal{H}}_Z$ eigenstates and there is little evidence that any additional corrections are required for essentially all relevant systems studied to date (although attempts have been made to determine the magnitude of such corrections).[42,43]

2.3.2.5 The Quadrupolar Interaction

If $I > 1/2$, then the electric charge distribution within the nucleus is no longer uniform and it can no longer be adequately described using a sphere. Commonly, an ellipsoid is used instead (Figure 2.6).
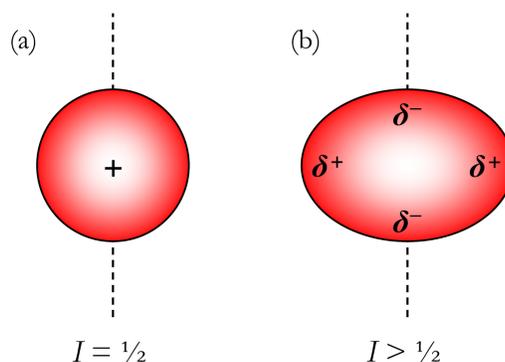
Figure 2.6 Qualitative comparison of the nuclear charge distribution between nuclides where $I = 1/2$ (a), and where $I > 1/2$ (b). Nuclei which possess $I = 1/2$ do not interact with an EFG, while the non-spherical charge distribution in (b) leads to a Q, which can interact with the local EFG. Regions of partial positive and partial negative electric charge are denoted using δ^+ and δ^-, respectively.

Nuclei where $I > 1/2$ are often called quadrupolar (or quadrupoles). Each quadrupolar nucleus possesses a Q, which interacts with the EFG at the nuclear site. Due to this

quadrupolar interaction (QI), the set of quadrupolar nuclei serve as sensitive probes of both local magnetic and electric environments. In the context of SSNMR, the magnitude of the QI is useful when it is on the order of kHz to MHz, however many cases are known where this interaction can be hundreds of MHz.[44]

For the more useful cases, the Zeeman interaction remains the dominant interaction and hence the QI is treated as a perturbation on $\hat{\mathcal{H}}_Z$. The quadrupolar Hamiltonian under the first-order secular approximation ($\hat{\mathcal{H}}_Q^1$) is:[26,45]

$$\hat{\mathcal{H}}_Q^1 \quad = \quad \frac{h\omega_Q}{8\pi}\left(3\hat{I}_Z^2 \quad - \quad I(I+1)\hat{1}\right), \tag{2.14}$$

with ω_Q representing the quadrupolar frequency, and h being the Planck constant. The first-order energy augmentation of the Zeeman eigenstates is thus linearly proportional to ω_Q. For small molecules in isotropic media, $\hat{\mathcal{H}}_Q^1$ is averaged to zero (indeed, so too are higher-order terms); however, the QI will still contribute to nuclear spin relaxation processes. Efficient spin relaxation results in signals which decay rapidly in the time-domain and in many cases additional RF pulses must be applied to compensate for these effects.

2.3.2.6 Additional Interactions and the Total Spin Hamiltonian

There exists a variety of other interactions which can be observed using NMR experiments. At this time they are simply enumerated here for completeness, but most of them will not be the focus of subsequent discussions (Figure 2.7). These additional interactions include: (i) direct dipole-dipole ($\hat{\mathcal{H}}_D$), which is derived from the through space coupling between the nuclear spin angular moments of proximate nuclei; (ii) indirect (J) dipole-dipole ($\hat{\mathcal{H}}_J$), which represents the coupling of the nuclear spin angular moments of two nuclei, as

mediated via bonding electrons; and (iii) spin-rotation ($\hat{\mathcal{H}}_{SR}$), which is the coupling between $\mathbf{I}$ and the magnetic field generated by molecular rotation. All of these additional interactions can be thought of as perturbations upon the Zeeman Hamiltonian, and therefore the total spin Hamiltonian ($\hat{\mathcal{H}}_{spin}$) can be generated by forming a linear combination of all the time-independent Hamiltonian terms within the Zeeman frame of reference:

$$\hat{\mathcal{H}}_{spin} \;=\; \hat{\mathcal{H}}_{Z} \;+\; \hat{\mathcal{H}}_{Q} \;+\; \hat{\mathcal{H}}_{CS} \;+\; \hat{\mathcal{H}}_{D} \;+\; \hat{\mathcal{H}}_{J} \;+\; \hat{\mathcal{H}}_{SR}. \qquad (2.15)$$
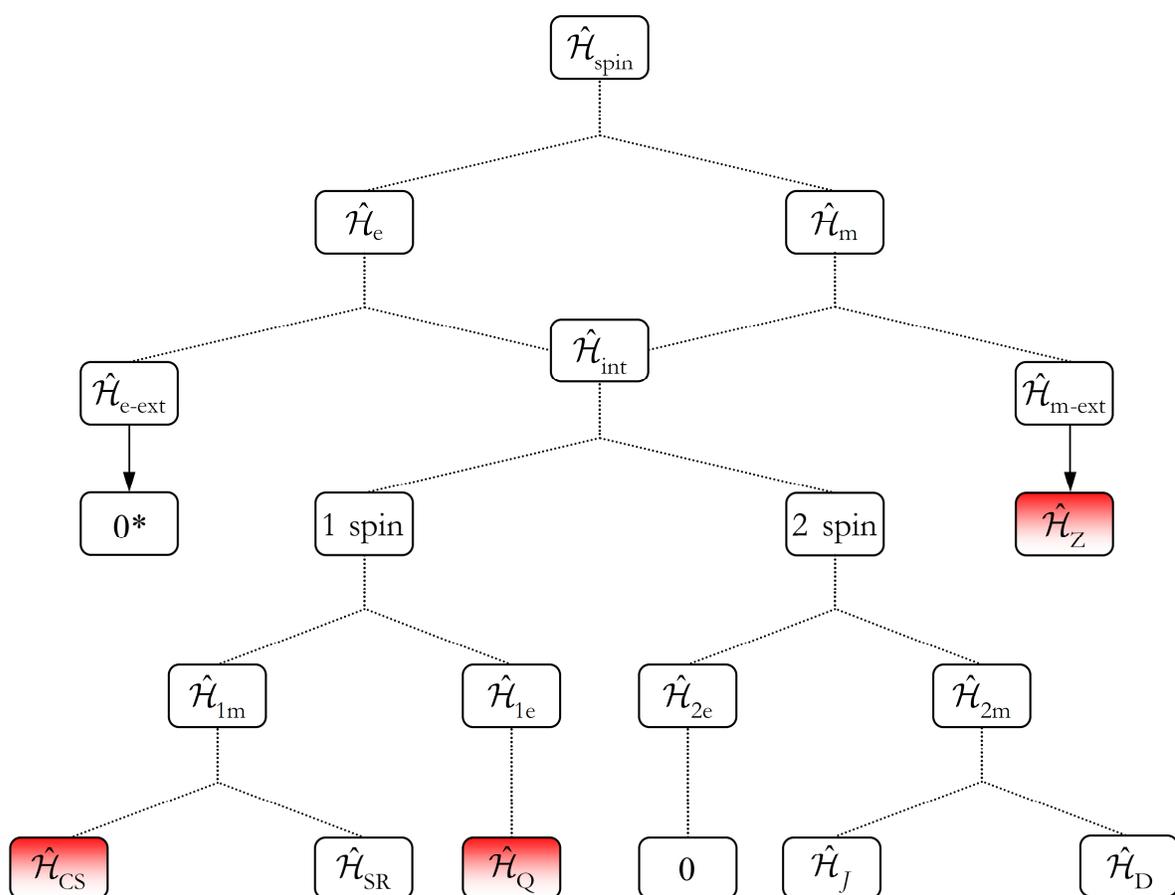
Figure 2.7 Contributions to the total nuclear spin Hamiltonian.[28] Definitions for any undefined Hamiltonian terms can be found in the List of Symbols. *Assumes the system is diamagnetic. The terms shaded in red are of relevance for the systems studied within this dissertation.

2.3.3 Anisotropic NMR Interactions

As noted earlier, NMR experiments which are performed on solid-state systems suffer from reduced sensitivity and resolution when compared to NMR experiments performed on liquid-state media. The origin of these reductions stems from the orientation-dependence of many of the NMR interactions noted above. Within a powdered sample, each crystallite will typically orient randomly with respect to the applied magnetic field, which leads to a distribution of the total NMR signal over a range of frequencies (Figure 2.8).
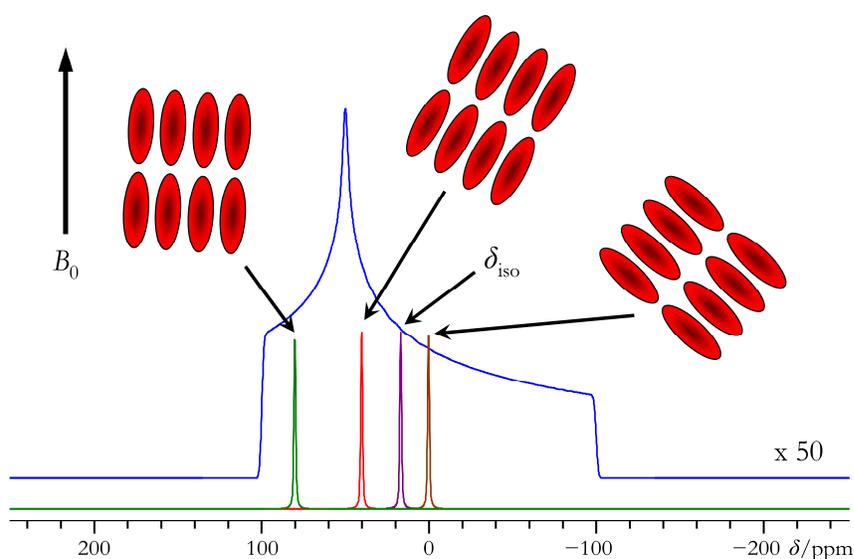
Figure 2.8 Magnetic shielding, one example of an orientation-dependent NMR interaction, manifests as chemical shift anisotropy (CSA) in solids. Each microcrystalline region (represented above as an octet of ovals; the ovals themselves being two-dimensional representations of tensors, *vide infra*) gives rise to a narrow resonance; however, since each crystallite is randomly oriented in a powdered sample, the total SSNMR signal is broad as it is a composite of many of these resonances. The vertical scale of the broad signal, known as a powder pattern, has been increased by a factor of 50.

2.3.3.1 Chemical Shift Anisotropy (CSA)

Unless the chemical environment is of very high symmetry, such as in a tetrahedron or octahedron, a single δ_{iso} value is no longer adequate to describe the observed NMR powder

pattern for a solid-state sample (analogously, a single σ_{iso} value is also insufficient to describe MS in these situations). When this is the case, a Cartesian tensor is sufficient (in this dissertation, tensor quantities will be indicated using the diaeresis ($\ddot{\ }$) above the symbol), which itself may be represented using a 3×3 matrix:[46]

$$\ddot{\delta} = \begin{bmatrix} \delta_{xx} & \delta_{xy} & \delta_{xz} \\ \delta_{yx} & \delta_{yy} & \delta_{yz} \\ \delta_{zx} & \delta_{zy} & \delta_{zz} \end{bmatrix}, \tag{2.16}$$

where each matrix element (δ_{ij}, $i, j = x, y, z$) describes the shift which results when an external magnetic field is applied along the j-axis and induces a magnetic field which possesses a component along the i-axis of the lab frame. A corresponding magnetic shielding tensor ($\ddot{\sigma}$) may be generated by the application of (2.12) for each δ_{ij} (where δ_{ij} and σ_{ij} replace δ_{iso} and σ_{iso}, respectively). As $\mathbf{B}_0$ is assumed to lie entirely along the z-axis (i.e., $\mathbf{B}_0 \rightarrow B_0$) and is very much stronger than the other interactions, things are simplified when one wishes to determine the induced magnetic field vector ($\mathbf{B}_{ind}$) using the CS tensor specified in (2.16):

$$\mathbf{B}_{ind} = \ddot{\delta} \cdot \mathbf{B}_0 = \begin{bmatrix} \delta_{xx} & \delta_{xy} & \delta_{xz} \\ \delta_{yx} & \delta_{yy} & \delta_{yz} \\ \delta_{zx} & \delta_{zy} & \delta_{zz} \end{bmatrix} \cdot \begin{bmatrix} 0 \\ 0 \\ B_0 \end{bmatrix} = \begin{bmatrix} \delta_{xz} B_0 \\ \delta_{yz} B_0 \\ \delta_{zz} B_0 \end{bmatrix}, \tag{2.17}$$

where the lab frame of reference has been chosen in order to evaluate the right hand terms. The induced magnetic field is therefore fully described using a three component column vector, where each element is proportional to B_0. Under the secular approximation (i.e., that the Zeeman interaction is very much larger than all other interactions), only the element containing δ_{zz} is retained. An appropriate re-casting of (2.13) is thus produced, which is valid for use with solid-state samples:[28]

$$\hat{\mathcal{H}}_{CS}^1 = -\hbar\gamma\left(\delta_{zz}(\Theta)\right)B_0\hat{I}_Z, \tag{2.18}$$

where Θ indicates that the value for δ_{zz} in the first-order shift Hamiltonian (i.e., $\hat{\mathcal{H}}_{CS}^1$) is orientation-dependent. In order to understand the full expression for the $\delta_{zz}(\Theta)$ term, further discussion is now provided. The matrix which represents the observable part of the CS tensor is symmetric (i.e., $\delta_{ij} = \delta_{ji}$) and is diagonalizable. Upon completion of the diagonalization process, one gains information pertaining to the relative orientation between the Cartesian frame of the molecule and the principal axis system (PAS) of $\ddot{\delta}$. When specified within its PAS, only the diagonal elements of the CS tensor are nonzero (i.e., the eigenvalues), and these elements are known as the principal components, as shown:

$$\ddot{\delta}_{PAS} = \begin{bmatrix} \delta_{11} & 0 & 0 \\ 0 & \delta_{22} & 0 \\ 0 & 0 & \delta_{33} \end{bmatrix}, \tag{2.19}$$

where popular conventions (detailed below) dictate that $\delta_{11} \geq \delta_{22} \geq \delta_{33}$. The δ_{iso} value is necessarily invariant to the reference frame of choice, and therefore the isotropic chemical shift may be calculated using any set of CS tensor diagonal matrix elements:

$$\delta_{iso} = \frac{1}{3}(\delta_{11} + \delta_{22} + \delta_{33}) = \frac{1}{3}(\delta_{xx} + \delta_{yy} + \delta_{zz}) = \frac{1}{3}\mathbf{Tr}(\ddot{\delta}), \tag{2.20}$$

where $\ddot{\delta}$ is a CS tensor in a general Cartesian reference frame, and $\mathbf{Tr}(\ddot{\delta})$ denotes that the matrix trace of the CS tensor is being evaluated. With this in mind, the $\delta_{zz}(\Theta)$ term may be specified:[26]

$$\delta_{zz}(\Theta) = \delta_{iso} + \left(\frac{\delta_{33} - \delta_{iso}}{2}\right)\left[(3\cos^2\theta - 1) + \left(\frac{\delta_{11} - \delta_{22}}{\delta_{33} - \delta_{iso}}\right)(\sin^2\theta\cos 2\varphi)\right]. \tag{2.21}$$

Where θ and φ correspond to the polar angles (defined in the usual sense), and specify the orientation between the fixed B_0-frame and the moving CS tensor PAS frame. Alternative

specifications of **(2.21)** are known, where the CS tensor frame is fixed, while the B_0-frame is rotated.[41]

The parameterization of a given CS (or MS) powder pattern is not unique, and three conventions are often used in the current literature.[47] The Maryland convention (sometimes referred to as the Herzfeld-Berger convention),[48,49] which uses three parameters to specify the magnitude of a CS tensor, will be used exclusively herein. Beyond the above-mentioned δ_{iso} value, the two additional parameters are:

$$\Omega \cong \delta_{11} - \delta_{33}; \qquad \kappa = \frac{3(\delta_{22} - \delta_{iso})}{\Omega}, \qquad (2.22)$$

where Ω is the span, which specifies the breadth of the CS tensor (in ppm) in the frequency domain, and κ is the skew, which is unitless, ranges between -1 to $+1$, and can offer insight into the degree of axial symmetry of the CS tensor. A general CS tensor powder pattern according to the Maryland convention is provided in Figure 2.9.
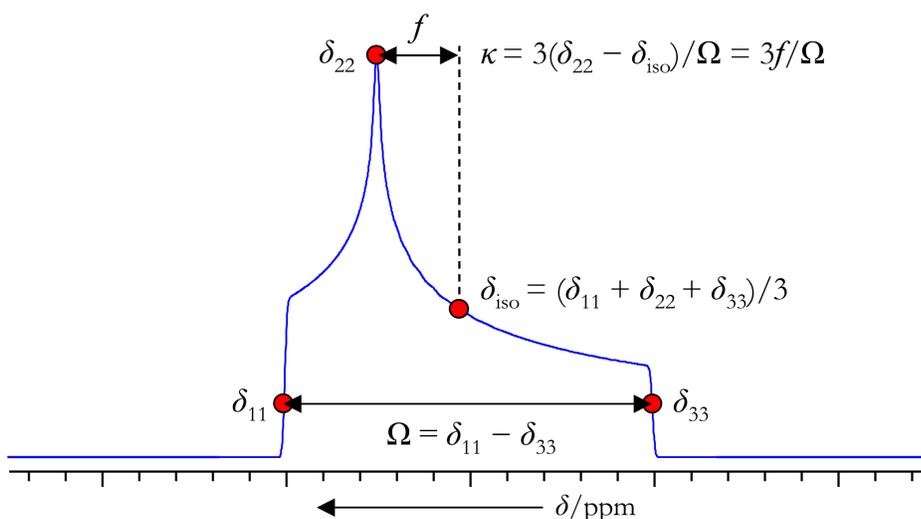
Figure 2.9 A schematic highlighting the CS tensor convention used herein.[50] In the particular example considered here, $I = 1/2$ is assumed, and other potential perturbing interactions are ignored.

2.3.3.2 The Quadrupolar Interaction in Solids

Unless the probe nucleus is within a highly symmetric environment, the local EFG will couple with the Q to produce a QI. In solids, the EFG tensor can be expressed using a traceless and symmetric 3×3 matrix ($\ddot{V}$):

$$\ddot{V} = \begin{bmatrix} V_{xx} & V_{xy} & V_{xz} \\ V_{yx} & V_{yy} & V_{yz} \\ V_{zx} & V_{zy} & V_{zz} \end{bmatrix}, \tag{2.23}$$

where V_{ij} $(i, j, = x, y, z)$ are the elements of the EFG tensor. As the matrix represents a traceless quantity, the sum of the diagonal elements must evaluate to zero in any chosen frame of reference. The EFG tensor may be diagonalized, which allows for one to determine the relative orientation of the EFG tensor PAS with respect to the frame of the molecule. When within its own PAS, the EFG tensor matrix is specified as:

$$\ddot{V}_{PAS} = \begin{bmatrix} V_{11} & 0 & 0 \\ 0 & V_{22} & 0 \\ 0 & 0 & V_{33} \end{bmatrix}, \tag{2.24}$$

where it is defined such that $|V_{33}| \geq |V_{22}| \geq |V_{11}|$. Regardless of the reference frame, under the secular approximation, the $\ddot{V}$ component along B_0 (i.e., V_{zz}) is related to the quadrupolar frequency (ω_Q):[28]

$$\omega_Q(\Theta) = \frac{3eQ}{2I(2I-1)\hbar} V_{zz}(\Theta), \tag{2.25}$$

where e is the electric charge of the proton, and Θ again specifies that this interaction bears an orientation dependence. As the QI is not averaged in many solid-state samples, the quadrupolar Hamiltonian ($\hat{\mathcal{H}}_Q$) will augment the eigenvalues of the system[45] (Figure 2.10 highlights this effect to first-order). It is important to note here that the central transition (CT) for half-integer

quadrupolar nuclei (i.e., $m = +1/2 \leftrightarrow -1/2$) is not affected to first-order by the QI, and that the

value of ω_Q may be determined from the spacing between the critical points associated with one

of the satellite transitions (ST) (for the systems considered here: $m = \pm1/2 \leftrightarrow \pm3/2$ and/or

$\pm3/2 \leftrightarrow \pm5/2$, $|\Delta m| = 1$) and the CT in a given spectrum. Once ω_Q is known, it can be

related to the nuclear quadrupole coupling constant (C_Q):

$$\omega_Q = \frac{3\pi C_Q}{I(2I-1)} = 2\pi\nu_Q, \tag{2.26}$$

where ν_Q is the quadrupolar frequency in Hz units (which will be used preferentially in most

subsequent discussions), and where C_Q is directly related to the largest component of the EFG

tensor in its own PAS:

$$C_Q = \frac{eQV_{33}}{h}. \tag{2.27}$$
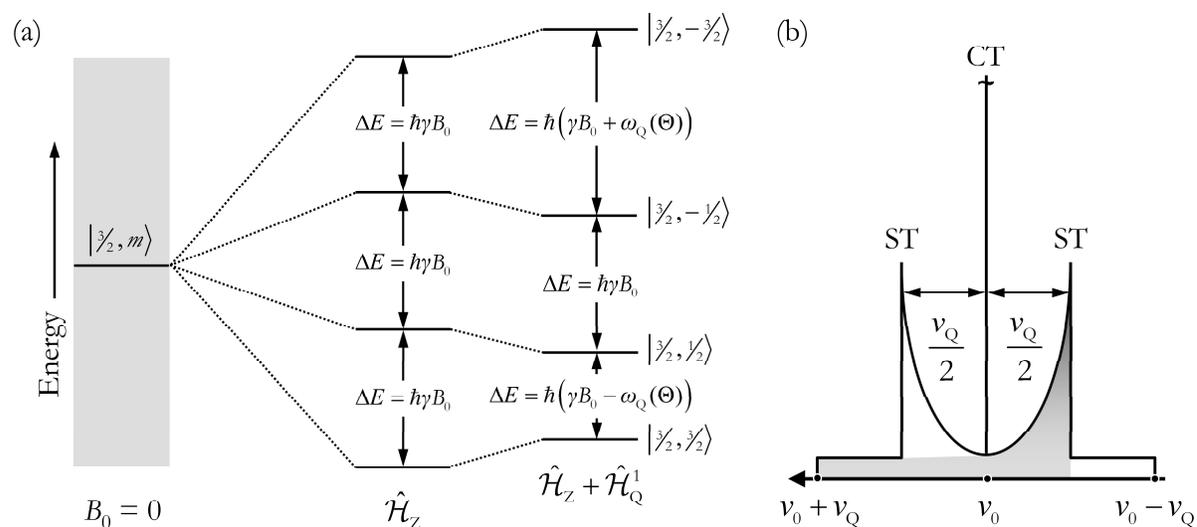
Figure 2.10 (a) The effect of the first-order QI upon the Zeeman eigenstates for $I = 3/2$ and $\omega_Q > 0$. When this description is valid, the resulting NMR spectrum will possess three transitions. The outer two ST carry an angular dependence, but the CT is unaffected to first-order. (b) Schematic showing the distribution of the CT and ST under first-order perturbation theory and $\eta_Q = 0$ for a powdered sample. The full extent of one ST is highlighted in grey. Note that the CT has been vertically truncated (~).

In order to fully specify the EFG tensor, an additional parameter is required, which is the EFG tensor asymmetry parameter (η_Q):

$$\eta_Q = \frac{V_{11} - V_{22}}{V_{33}}. \qquad (2.28)$$

Note that the use of first-order perturbation theory is valid for the regime where $v_0 \gg v_Q$, but many situations have been reported where this is not the case.[44,45,51] When this occurs, expansion of the $\hat{\mathcal{H}}_Q$ must be done to second-order, which produces a more complicated expression, but allows C_Q and η_Q to be determined via analysis of the CT only (Figure 2.11).

(a)

$\eta_Q = 0$

vertical scale

$C_Q = 1.0$ MHz   × 1

$C_Q = 2.0$ MHz   × 2

$C_Q = 3.0$ MHz   × 3

$C_Q = 4.0$ MHz   × 5

$C_Q = 5.0$ MHz   × 6

30   20   10   0   −10   −20 $\Delta v/$kHz

(b)

$C_Q = 3.0$ MHz

$\eta_Q = 1.0$

$\eta_Q = 0.8$

$\eta_Q = 0.6$

$\eta_Q = 0.4$

$\eta_Q = 0.2$

30   20   10   0   −10   −20 $\Delta v/$kHz
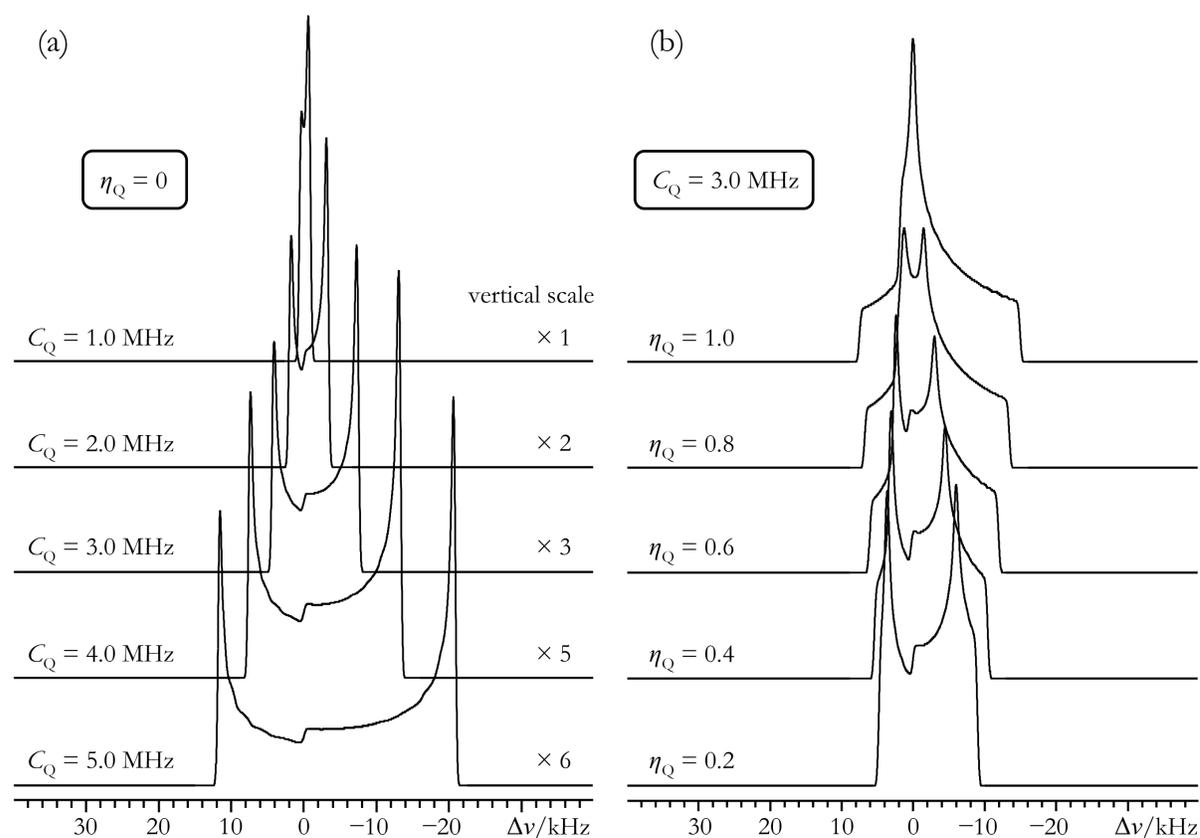
Figure 2.11 Analytical (WSolids1)[50] simulations (including second-order effects) of theoretical $I = 3/2$ SSNMR CT powder patterns under static (i.e., stationary sample) conditions, which serve to highlight the effects that changing C_Q (a) and η_Q (b) values have upon the resulting SSNMR line shapes. For all simulations, $v_0 = 100$ MHz and 500 Hz of Gaussian line-broadening was used. The vertical scales of the powder patterns in (a) have been augmented according to the factors shown.

This potential is of key importance, since it is typically very difficult (or at the very least, exceptionally time-consuming) to completely observe the ST in this regime, while observation of the CT is significantly more facile. All analytical line shape simulations in this dissertation used the program WSolids1,[50] which treats the QI as a perturbation up to second-order.

In certain situations,[52] it is possible to perform SSNMR experiments within a regime where the Zeeman and QI are similar to one another. When this occurs, even perturbation theory to second-order is no longer suitable to simulate the observed 'NMR' line shape. A variety of methods have been proposed to analyse spectra of this nature.[53-58] As the observation and analysis of these sorts of spectra comprise much of the results and discussion in Chapter 5 of this dissertation, further comments will be postponed until then.

2.3.3.3 Euler Angles

As both the CS and EFG tensors can be diagonalized, the orientation of each interaction tensor PAS with respect to the molecular frame may be determined, at least in principle. Most simply, this information may be determined directly by using a large single-crystal and performing many SSNMR experiments at a variety of crystal orientations with respect to B_0.[59,60] If certain knowledge about the system is known *a priori*, microcrystalline samples coupled with multidimensional double-quantum filtered experiments may be used in favourable cases.[61] More generally, when performing SSNMR experiments upon microcrystalline samples where both CSA and the QI contribute significantly to the total powder pattern, it is often only possible to determine the relative orientation between the CS and EFG tensor PASs.[62] This relative orientation is specified using three parameters (α, β, γ), which are collectively known as the Euler angles.[63] These three angles specify the degree of positive (i.e., counterclockwise) rotation about certain rotational axes, and depend upon the convention chosen. For all scenarios

considered herein, the 'ZYZ' convention is used.[64] Under a popular NMR implementation of this convention, the EFG PAS is chosen as the static frame of reference, while the CS tensor frame is actively subjected to a series of three successive rotations, the end result of which produces coincident CS and EFG tensor frame PASs (Figure 2.12).
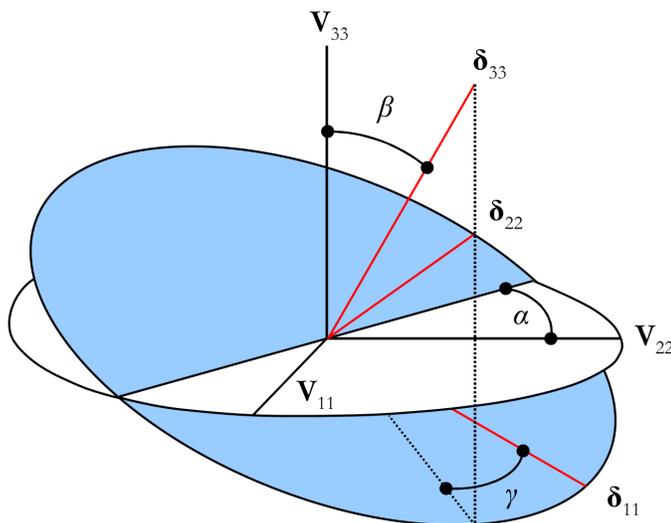
Figure 2.12 Schematic highlighting the relationship between the Euler angles (i.e., α, β, γ), and the relative orientation between the CS and EFG tensor PASs (illustration inspired by Eichele[50]). The angle of each rotation is determined by the value of each of the Euler angles and occurs in the order $\alpha \rightarrow \beta \rightarrow \gamma$. The convention used here assumes the EFG tensor PAS is static, while the CS tensor PAS is active. The eigenvectors shown (i.e., V_{11}, δ_{11}, etc.,) are associated with the tensor eigenvalues defined earlier.

2.3.4 Nuclear Quadrupole Resonance (NQR)

For any system that possesses a QI, in principle it is possible to perform an NQR experiment. Within the context of the systems studied herein, NQR experiments are performed to confirm, or to give greater confidence to, the SSNMR measurements. As no B_0 is applied, all effects due to the Zeeman interaction and CSA are absent. While this greatly simplifies data analysis, much of the useful NMR data are lost. Depending upon the value of I, the magnitude of the EFG tensor (i.e., C_Q, η_Q) may be fully determined. In the specific case of $I = 3/2$, NQR

experiments alone are unable to provide information regarding C_Q and η_Q, as there exists only one NQR transition (Figure 2.13a). For other I values, the presence of multiple allowed single quantum transitions enables unambiguous measurements of both $\ddot{V}$ parameters (Figure 2.13b).
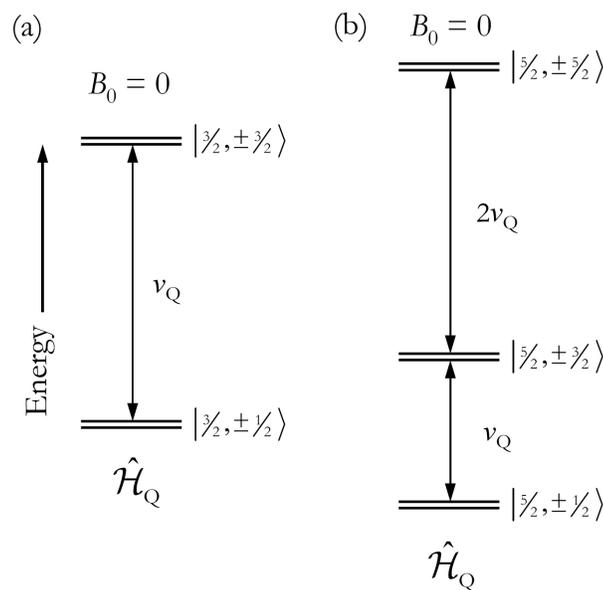
Figure 2.13 Spacing of the nuclear spin eigenstates under only the QI for (a) $I = 3/2$, and for (b) $I = 5/2$. For simplicity, the EFG tensor in (b) has been assumed to possess axial symmetry (i.e., $\eta_Q = 0$), and $C_Q > 0$. For cases where $C_Q < 0$, the ordering of the eigenstates is reversed (e.g., the $\pm 5/2$ eigenstates would be the lowest in energy in (b)).

2.3.5 NMR/NQR Line Shape Fitting and Parameter Determination

The SSNMR spectra were typically modeled (i.e., unless specified otherwise) using analytical simulation software (WSolids1),[50] and included contributions from the QI to second-order and CSA under the high-field approximation. Other contributions (i.e., J, dipole-dipole, etc.) can be safely ignored for all of the systems studied herein. In cases where the high-field approximation was not obviously valid (*vide infra*), line shape analysis was performed using a simulation program that incorporates QI effects exactly.[58] In nearly all cases, the observed SSNMR signals primarily correspond to the CT (i.e., $m = +1/2 \leftrightarrow -1/2$), but effects due to the

ST ($m = \pm 3/2 \leftrightarrow \pm 1/2$ and $\pm 5/2 \leftrightarrow \pm 3/2$, $|\Delta m| = 1$, as appropriate) were included in all static line shape simulations. While the observation of the full ST is generally time consuming, portions were collected in certain cases. As magnetic shielding and QI effects on the SSNMR line shape scale differently with B_0, SSNMR spectra were often acquired at multiple fields, when possible, to improve the accuracy of the extracted parameters. In many cases considered in this dissertation, there existed two NMR-active isotopes for a particular atomic species (e.g., $^{35/37}$Cl, $^{69/71}$Ga, $^{79/81}$Br, $^{185/187}$Re). As each nuclide possesses unique values for Q and γ, SSNMR spectra were recorded using both isotopes, when possible, to enhance accuracy.

Due to the large spectral regions sampled (often, many MHz), the spectra were simulated heuristically, without automated iteration, with special emphasis placed on fitting the positions of the spectral discontinuities, rather than the intensities. Estimation of the errors in the spectral parameters was performed by systematically altering, in turn, each of the parameters derived from the best-fit, until the point where the simulated spectrum deviated from the experimental spectrum at one of the discontinuities by an amount comparable to the inherent point-by-point resolution of the spectrum. Additional aspects of SSNMR line shape fitting (e.g., inclusion of CSA, justification of nonzero Euler angles, etc.) are outlined over the course of this dissertation, as deemed relevant.

To determine the $\ddot{V}$ parameters using NQR data for $I = 5/2$ nuclides, the closed-form solutions to the secular equations, recently outlined by Semin,[65] were employed. The values obtained via this procedure were shown to produce results identical to numerical simulations.[66]

2.4   *Experimental Background*

As in any scientific discipline, SSNMR has many specialized experimental procedures which may be used in order to efficiently collect data. As noted before, the most substantial

challenges to the further development of SSNMR are poor experimental sensitivity and resolution. A number of techniques have been developed in order to enhance experimental efficiency, sensitivity and resolution: only those that were used within the studies discussed herein are outlined at this time. In addition to these enhancement techniques, when acquiring the SSNMR spectra of quadrupolar nuclei, it is often the case that broad line shape data acquisition techniques are required, and one such approach will be discussed.

2.4.1 The Utility of Echo Experiments

When performing SSNMR experiments upon quadrupolar nuclei, the initial time-domain signal decay produced after appropriate preparation will lose coherence (T_2* decay) rather rapidly due to the QI and (to a much smaller extent) B_0-inhomogeneity. In certain cases, the NMR signal will decay in such an efficient manner that it cannot be meaningfully analyzed. Although a variety of advanced pulse sequences now exist to acquire SSNMR data, it is often the case that traditional echo experiments (especially when the experiments are performed in very high B_0) are acceptable to produce high S/N spectra in a reasonable amount of time. This is even generally true in the case of exceedingly broad ($\Delta\nu_{NMR} > 1$ MHz) line shapes, as long as the nuclei under observation are not substantially dilute. Pulse sequences such as the quadrupolar Carr–Purcell–Meiboom–Gill (QCPMG) may be of use (see Section 2.4.5.1) in those particular cases. The general echo sequence is rather straightforward: after a $\pi/2$ pulse, **M** is allowed to evolve for a period of time (τ_1), after which a refocusing pulse is applied. Subsequently, an additional delay (τ_2) is used to wait until the echo has completely refocused. The 90/90 or 'solid/Solomon echo' experiment[67,68] (Figure 2.14a) may be used in situations where a somewhat strong NMR signal is being observed, as it can produce more uniform excitation for a given B_1 field relative to the Hahn echo (or 90/180) experiment (Figure 2.14b).[69] The relative increase in

the uniform signal excitation afforded by using the solid echo experiment comes at the expense of reduced signal intensity (by roughly a factor of 2) relative to the Hahn echo experiment; it is important to note that the exact factor will depend on the phase cycling and coherence pathway selection. A theoretical and experimental discussion of the optimal conditions for echo pulse sequences for various half-integer quadrupolar nuclei has been provided by Bodart *et al.*[70] Recently, these echo sequences have been thoroughly discussed and classified according to their transition pathway symmetries.[71]
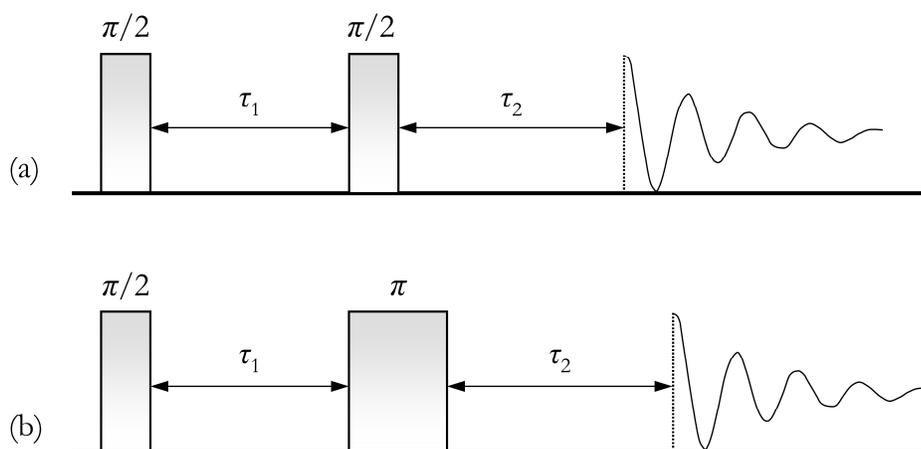
Figure 2.14 Pulse sequence diagrams of the solid/Solomon echo (a), and Hahn echo (b) experiments. Under a simple vector model, the pulse lengths are such that $\pi/2$ causes a 90 degree rotation of **M**, while the π pulse causes a 180 degree rotation. Interpulse delays (τ_1/τ_2) are selected such that the echo top (i.e., the point of maximum signal amplitude, as shown) may be experimentally observed.

2.4.2 Variable-Offset Cumulative Spectrum (VOCS) Data Acquisition

To acquire meaningful SSNMR spectra for many quadrupolar nuclei, data acquisition will often be carried out using multiple RF transmitter settings. Failure to uniformly excite the entire CT powder pattern (recall **(2.8)**) may potentially result in incorrect spectral analysis and erroneous CS/EFG tensor parameters. Unless high site symmetry (e.g., tetrahedral, octahedral) at the nucleus of interest is known *a priori*, it is advisable to obtain two SSNMR spectra using at

least two different transmitter frequencies to confirm that the entire CT has been acquired. To observe the full CT powder pattern when it is clearly broadened beyond what can be uniformly excited using a single transmitter frequency, the variable-offset cumulative spectrum (VOCS) method is useful.[44,72] This protocol involves collecting a set of SSNMR spectra, with each individual spectrum (sometimes referred to as a 'sub-spectrum') being acquired at a unique, but uniformly offset, transmitter frequency (Figure 2.15). Each sub-spectrum is to be collected using the same number of scans and should be processed individually. Once the entire set of SSNMR spectra has been processed, they are co-added in the frequency domain, thereby producing the final VOCS spectrum.
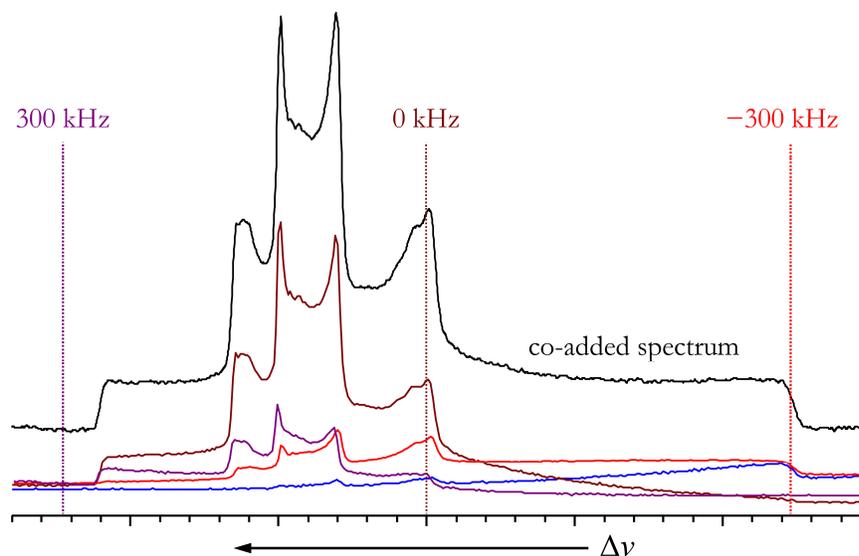
Figure 2.15 Example of VOCS data acquisition and co-addition for an arbitrary sample (partial ^{81}Br SSNMR spectrum of SrBr$_2$ acquired at B_0 = 21.1 T) using a uniform offset value of 300 kHz. The transmitter frequency offset values (Δv) are displayed for three of the sub-spectra (i.e., purple, brown, and red traces), while the transmitter location for the blue trace is located outside of the current spectral window (Δv = −600 kHz). After the completion of the data acquisition, each sub-spectrum is processed individually, and then co-added in the frequency domain to yield the final VOCS spectrum (black trace).

2.4.3 Using Multiple-Field Data Acquisition

As noted above, many of the SSNMR interactions relevant to this dissertation are anisotropic. In addition to this, the line shape broadening contributions from CSA and the second-order QI (the dominant perturbing interactions considered herein) scale differently with B_0. In units of Hz, the scaling of the CSA interaction is linear with B_0, while the second-order QI effects on the CT will scale inversely with B_0 (since $v_0 \propto B_0$):[26]

$$\Delta v_{CT} = \left[\frac{3C_Q}{2I(2I-1)}\right]^2 \frac{\left(\eta_Q^2 + 22\eta_Q + 25\right)\left(I(I+1) - 3/4\right)}{144v_0}, \qquad (2.29)$$

where Δv_{CT} specifies the breadth of the CT line shape due solely to the second-order QI on a stationary powdered sample. Because of these drastically different B_0-dependent scaling behaviours, multiple-field data acquisition can greatly facilitate the quantitative line shape analysis for a great variety of half-integer quadrupolar nuclides.

2.4.4 Resolution Enhancement Methods

2.4.4.1 Magic-Angle Spinning (MAS)

In liquid-state NMR experiments, isotropic molecular tumbling will render unobservable the anisotropic portion of the interactions that are observed in SSNMR experiments. Several of these interactions, including MS, direct dipole-dipole, and the first-order QI, possess the same orientation dependence[73] and can therefore be averaged to their isotropic values via the rapid mechanical rotation of a solid-state sample at the so-called 'magic-angle' (Figure 2.16). The value for this angle is found by solving for the root of $3\cos^2\theta = 1$, where θ represents the angle between the direction associated with the secular component of a given interaction tensor (e.g., σ_{zz} for magnetic shielding) and B_0. Thus, if θ can be set to 54.74°, the corresponding anisotropy will average and result in significant line shape narrowing.[74-76]
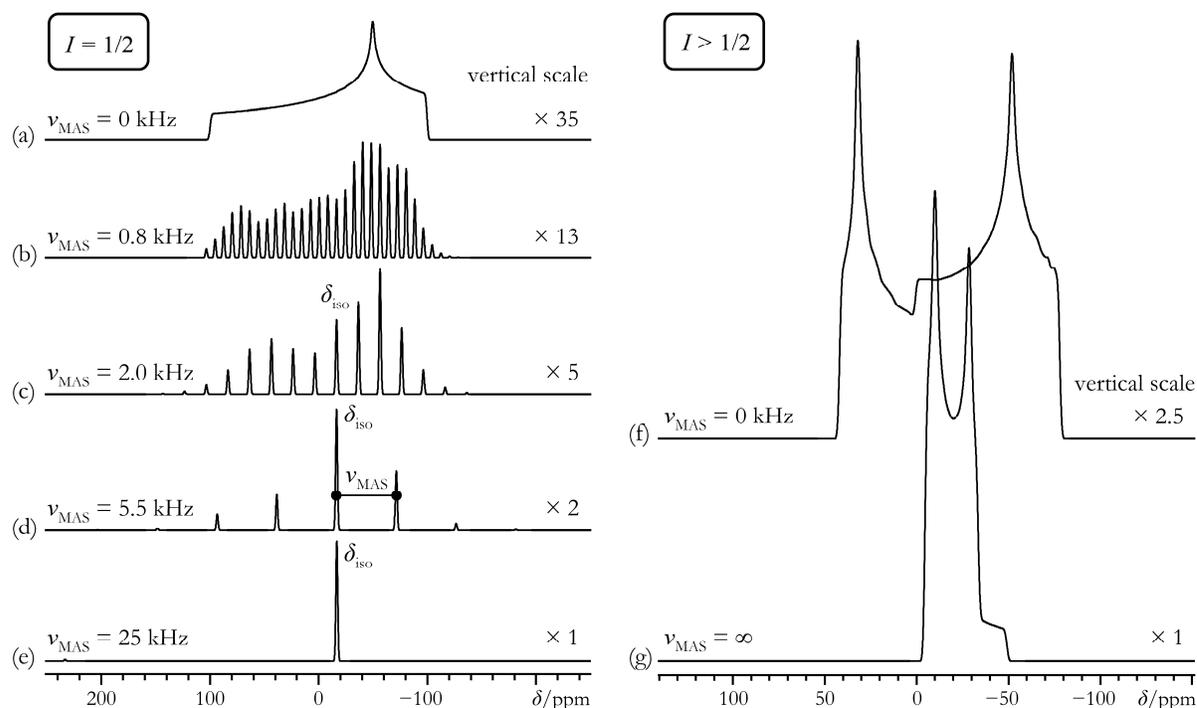
Figure 2.16 Analytical simulations highlighting the effect of MAS conditions on CSA-dominated (a – e), and QI-dominated (f – g) spectra. If $I = 1/2$, the low resolution static powder pattern that is produced due to CSA (a) is partitioned into an isotropic peak, plus a number of spinning sidebands (b – d), assuming MAS conditions and $v_{MAS} < \Omega$. These sidebands flank the isotropic peak at integer multiples of v_{MAS} (highlighted in (d)). If $v_{MAS} \gg \Omega$, a liquid-like peak is observed (e). When the QI is significant and cannot be truncated at first-order, MAS will only narrow the CT powder pattern by a factor of about 2 – 3 (f – g). This is due to the complex angular dependence of the second-order QI under MAS conditions. Note the various vertical scale enhancements used in the above spectra. Parameters used in the simulations: (a – e) $I = 1/2$, $v_0 = 100$ MHz, $\delta_{iso} = -16.7$ ppm, $\Omega = 200$ ppm, $\kappa = -0.5$; (f – g) $I = 3/2$, $v_0 = 100$ MHz, $C_Q = 2.8$ MHz, $\eta_Q = 0.2$. All simulations include 200 Hz of Gaussian line-broadening.

Unfortunately, due to the microcrystalline nature of powdered samples, it is not possible to simultaneously set θ to the magic-angle for all crystallites. Rather, the rotation axis of the entire sample is set to the magic-angle, and the rapid mechanical rotation causes the secular portion of the interaction to become time-dependent. Likewise, rotation causes the tensor components perpendicular to the rotation axis to time-average to zero, while only the tensor component

parallel to the rotation axis remains. As the parallel component is fixed at the magic-angle, it will necessarily equal zero.[73] Most conventional SSNMR probe designs can achieve sample rotation frequencies (ν_{MAS}) of approximately $10 - 25$ kHz,[77] although a number of more specialized probes have been able to realize frequencies of 70 and even 80 kHz.[78,79]

2.4.4.2 Heteronuclear Decoupling

In most of the systems considered here, the QI and CSA contribute nearly all of the observed line shape broadening. In certain cases (i.e., somewhat small QIs), the effects of heteronuclear dipole-dipole coupling (where one of the spins is ^{1}H) may become important. Although very advanced heteronuclear ^{1}H decoupling solutions are known,[80,81] due to the relatively weak nature of this interaction for the samples studied in this dissertation, only the simple 'continuous-wave' (CW) decoupling method is used presently. Briefly, heteronuclear CW ^{1}H decoupling involves the application of a fixed phase RF field at the ^{1}H Larmor frequency while a second channel is used for the detection of the desired quadrupolar nuclide NMR signal.[82]

2.4.5 Sensitivity Enhancement Methods

2.4.5.1 The QCPMG Experiment

While the echo sequences outlined in Section 2.4.1 allow for the acquisition of a variety of broad SSNMR signals, a number of situations exist where those solutions are not terribly useful. The lack of utility is generally due to poor experimental sensitivity, perhaps as would be expected.

The QCPMG pulse sequence was first presented in the 1950's, and is a modified variant of the Hahn echo sequence that includes additional acquisition and delay periods (Figure

2.17).[83,84] While the (Q)CPMG pulse sequence was initially used to measure spin-spin relaxation (T_2) values, and to address such issues as homonuclear dipolar couplings[85-87] and dynamics,[88-92] it was not expressly applied with the goal of experimental sensitivity enhancement in mind. This changed when Larsen *et al.* presented very convincing QCPMG-based SSNMR signal enhancement studies near the turn of the last century.[93] This sequence will increase sensitivity if the individual T_2^* decays are much shorter than the natural T_2 decay of the sample. Additional details regarding this sequence may be found elsewhere,[83,84] but it enhances sensitivity by acquiring what is often referred to as an echo 'train', as opposed to a single echo (as is the case in the solid/Solomon/Hahn echo pulse sequences) during each recycle delay.
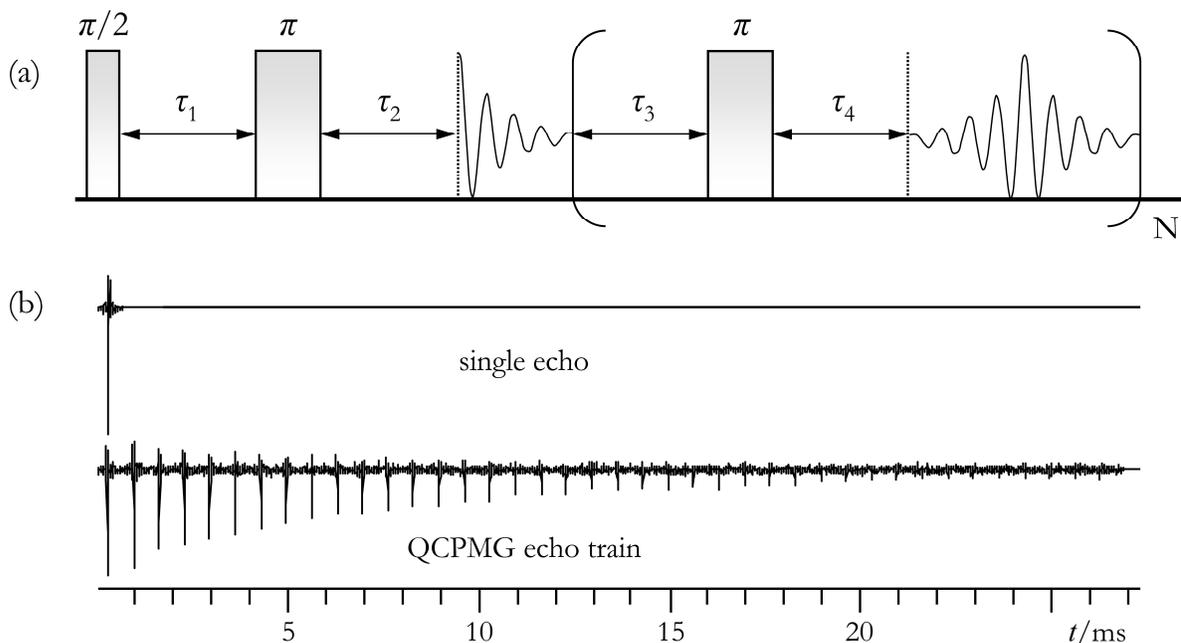
Figure 2.17 (a) The QCPMG pulse sequence is a modified Hahn echo experiment that includes additional delays (i.e., τ_3 and τ_4), π pulses, and acquisition periods. The portion within the brackets is termed a Meiboom-Gill (MG) loop, and is repeated N times. (b) Qualitative illustration of single echo and QCPMG system responses in the time-domain. The single echo sequence collects one system response (determined by T_2^*), while the QCPMG sequence collects many (shown by the number of spikelets and determined by T_2).

2.5   Quantum Chemical Computations

The use of calculation methods which are based on some flavour of *ab initio* quantum mechanics principles is well-established in the field of SSNMR, as well as in spectroscopy in general.[94] In the context of the calculation of NMR parameters, it has usually been the case that atom-centered basis sets or molecular orbitals (MOs) were employed as part of a cluster model approach.   In microcrystalline solids, where lattice effects are generally non-negligible, these local methods can suffer in the calculation of properties which possess non-local character, such as EFGs (i.e., they possess a $1/r^3$ dependence, where r is the distance from a given probe nucleus).   In addition, the scaling behaviour of the more popular cluster models is polynomial (roughly N_B^3 to N_B^4, where N_B is the number of basis set functions), which means that a modest increase in the number of atoms considered in the calculation can lead to order of magnitude increases in the computational resources required.   Thankfully, quantum chemical calculations using plane wave basis set expansions (which are valid electronic wave function expansions according to Bloch's theorem,[95] who later shared in the 1946 Nobel Prize for the demonstration of condensed phase NMR) with periodic boundary conditions and pseudopotentials have recently appeared in the literature.   Calculations of this class can thus mimic the infinite crystal lattice, and have shown great promise in the calculation of NMR tensor properties for a diverse range of solid-state systems.[96-99]

2.5.1   Gauge-Including Projector Augmented-Wave Density Functional Theory (GIPAW DFT)

All of the quantum chemical calculations presented herein utilize a non-local plane wave basis set with pseudopotentials being used to model the core electron states.   While the computational resources required when using a plane wave basis scale linearly with the unit cell

volume,[100] it was noted many years ago that properties which were sensitive to the core electron wave functions would not be adequately modeled using a computationally feasible number of plane waves (i.e., magnetic shielding).[101] One solution to this problem was found by removing the core electrons, replacing them with an effective potential, which when combined with the nuclear potential, generates a core region pseudopotential function.[102] This procedure, however, resulted in the loss of the 'true' electronic wave function ($\psi(r)$).[103] In order to regain $\psi(r)$, an additional approach was to use atomic-like 'augmented-waves' to treat the core, while using plane waves to treat the valence regions.[104] The augmented-wave method allowed for the regeneration of the core $\psi(r)$. The combination of certain aspects of both solutions (i.e., one for the core electrons and one for the valence) resulted in the projector augmented-wave (PAW) method, which is used exclusively for the quantum chemical results presented in this dissertation.

Very briefly, the PAW method introduces a wave function transformation operator ($\hat{T}_{PAW}$), which can relate the true wave function to an auxiliary wave function ($\tilde{\psi}(r)$) that is smooth in the core region (Figure 2.18). Beyond a defined core region distance (R_{core}), the auxiliary wave function is identical to the true wave function. A set of projector functions ($\tilde{p}_i$) are then defined, which, when combined with an appropriate set of pseudo partial wave functions ($\hat{\varphi}_i$), allows one to relate $\tilde{\psi}(r)$ to expansions within the core:[105]

To calculate the total electronic energy of a particular system, the $\psi(r)$ are calculated at a finite number of so-called k-points within reciprocal lattice space.[100] This operates under the assumptions that the $\psi(r)$ is locally continuous and rather similar between very proximate k-points, and therefore the electronic wave function over a region of k space is assumed to be well-represented by the $\psi(r)$ at a single k-point. In order to obtain an accurate approximation of

the true electronic potential, the electronic states are calculated at certain special sets of k-points in what is known as 'the Brillouin zone' (i.e., a primitive cell within reciprocal space).[106,107]
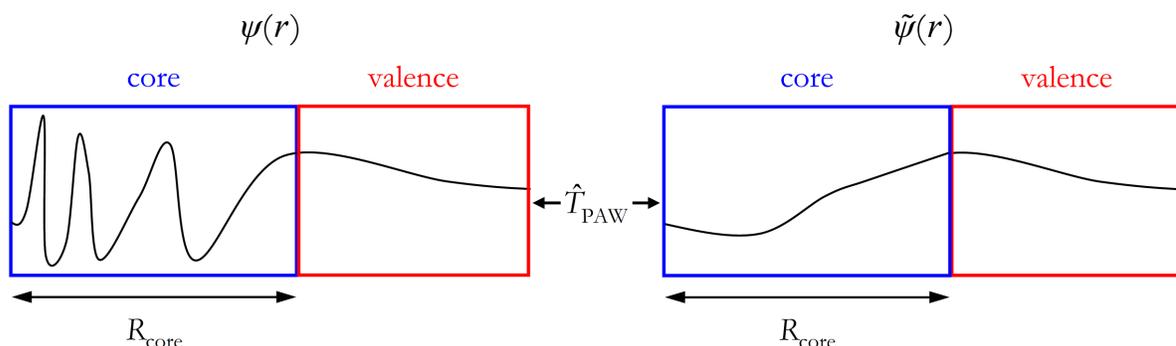
Figure 2.18 Qualitative description of the relationship between $\psi(r)$ and the auxiliary wave function, as related via the PAW transformation operator. The design of the operation is to yield a smooth core region wave function, and to match the true wave function beyond a given cutoff distance (i.e., R_{core}).

The sampling algorithm used by the Cambridge Serial Total Energy Package (CASTEP) quantum chemical software (the software used herein) works well for systems with nonzero Fermi gaps (e.g., insulators and semiconductors), but will often fail if metallic systems are considered, as metallic systems require a very dense set of k-points to be sampled. Errors in the total energy may be simply overcome by choosing a denser array of k-points. Once the total electronic energy of the system is known, many of the relevant properties for the system under consideration may be calculated (such as $\ddot{V}$). This does not extend to the computation of $\ddot{\sigma}$, however, and it was long thought that pseudopotential methods would never be able to calculate MS.[94] For the computation of $\ddot{\sigma}$, the GIPAW method is used, which extends the PAW methodology by including magnetic field dependent phase factors in a fashion similar to other approaches, such as the gauge-including atomic orbitals (GIAO) method.[108] In effect, this allows for the restoration of the spatial translational invariance, which was lost upon the application of a magnetic field.

2.6 References

1   A. Trabesinger, *Nature Phys.*, **2008**, *4*, S5.

2   P. Zeeman, *Nature*, **1897**, *55*, 347.

3   P. Zeeman, *Phil. Mag., Ser. 5*, **1897**, *44*, 55-60.

4   P. Zeeman, *Phil. Mag., Ser. 5*, **1897**, *44*, 255-259.

5   W. Pauli, *Z. Phys.*, **1925**, *31*, 373-385.

6   W. Gerlach and O. Stern, *Z. Phys.*, **1922**, *9*, 349-352.

7   G. E. Uhlenbeck and S. Goudsmit, *Naturwiss.*, **1925**, *13*, 953-954.

8   R. Frisch and O. Stern, *Z. Phys.*, **1933**, *85*, 4-16.

9   I. Estermann and O. Stern, *Z. Phys.*, **1933**, *85*, 17-24.

10 P. A. M. Dirac, *Proc. R. Soc. London, Ser. A*, **1928**, *117*, 610-624.

11 P. A. M. Dirac, *Proc. R. Soc. London, Ser. A*, **1928**, *118*, 351-361.

12 R. Webb, *Nature Phys.*, **2008**, *4*, S7.

13 A. Trabesinger and A. Wright, *Nature Phys.*, **2008**, *4*, S3.

14 I. I. Rabi, J. R. Zacharias, S. Millman and P. Kusch, *Phys. Rev.*, **1938**, *53*, 318.

15 C. J. Gorter, *Physica*, **1936**, *3*, 995-998.

16 C. J. Gorter and L. J. F. Broer, *Physica*, **1942**, *9*, 591-596.

17 E. M. Purcell, H. C. Torrey and R. V. Pound, *Phys. Rev.*, **1946**, *69*, 37-38.

18 F. Bloch, W. W. Hansen and M. Packard, *Phys. Rev.*, **1946**, *69*, 127.

19 W. G. Proctor and F. C. Yu, *Phys. Rev.*, **1950**, *77*, 717.

20 W. C. Dickinson, *Phys. Rev.*, **1950**, *77*, 736-737.

21 G. Lindström, *Phys. Rev.*, **1950**, *78*, 817-818.

22 H. A. Thomas, *Phys. Rev.*, **1950**, *80*, 901-902.

23　J. T. Arnold, S. S. Dharmatti and M. E. Packard, *J. Chem. Phys.*, **1951**, *19*, 507.

24　A. Abragam, *The Principles of Nuclear Magnetism*, Oxford University Press: New York, **1961**.

25　C. P. Slichter, *Principles of Magnetic Resonance*, 3rd edn., M. Cardona, P. Fulde, K. von Klitzing, H. J. Queisser and H. K. V. Lotsch, Eds., Springer-Verlag: New York, **1990**.

26　K. J. D. MacKenzie and M. E. Smith, *Multinuclear Solid-State NMR of Inorganic Materials*, Pergamon: Amsterdam, **2002**.

27　J. Mason, *Multinuclear NMR*, Plenum Press: New York, **1987**.

28　M. H. Levitt, *Spin Dynamics: Basics of Nuclear Magnetic Resonance*, Wiley: Chichester, **2003**.

29　A. R. Edmonds, *Angular Momentum in Quantum Mechanics*, Princeton University Press: Princeton, **1957**.

30　E. Feenberg and G. E. Pake, *Notes on the Quantum Theory of Angular Momentum*, Stanford University Press: Stanford, **1959**.

31　C. H. Yoder and C. D. Schaeffer, *Introduction to Multinuclear NMR: Theory and Application*, Benjamin/Cummings: Menlo Park, CA, **1987**.

32　J. B. Lambert, H. F. Shurvell, D. Lightner and R. G. Cooks, *Introduction to Organic Spectroscopy*, Macmillan: New York, **1987**.

33　T. D. W. Claridge, *High-Resolution NMR Techniques in Organic Chemistry*, 1st edn., Pergamon: New York, **1999**.

34　P. Atkins and J. de Paula, *Physical Chemistry*, 7th edn., W. H. Freeman and Company: New York, **2002**.

35　J. H. Nelson, *Nuclear Magnetic Resonance Spectroscopy*, Prentice Hall: Upper Saddle River, **2003**.

36　P. A. M. Dirac, *The Principles of Quantum Mechanics*, 4th edn., Oxford University Press: Oxford, **1958**.

37　M. Mehring and V. A. Weberruβ, *Object-Oriented Magnetic Resonance: Classes and Objects, Calculations and Computations*, Academic Press: New York, **2001**.

38　Z. Yao, H.-T. Kwak, D. Sakellariou, L. Emsley and P. J. Grandinetti, *Chem. Phys. Lett.*, **2000**, *327*, 85-90.

39　R. W. Schurko, I. Hung and C. M. Widdifield, *Chem. Phys. Lett.*, **2003**, *379*, 1-10.

40　K. Jackowski, M. Jaszuński and M. Wilczek, *J. Phys. Chem. A*, **2010**, *114*, 2471-2475.

41 C. M. Widdifield and R. W. Schurko, *Concept. Magn. Reson. A*, **2009**, *34A*, 91-123.

42 D. M. Doddrell, D. T. Pegg and M. R. Bendall, *Aust. J. Chem.*, **1979**, *32*, 1-10.

43 M. R. Bendall and D. M. Doddrell, *J. Magn. Reson.*, **1979**, *33*, 659-663.

44 R. W. Schurko, S. Wi and L. Frydman, *J. Phys. Chem. A*, **2002**, *106*, 51-62.

45 E. A. C. Lucken, *Nuclear Quadrupole Coupling Constants*, Academic Press: London, **1969**.

46 M. Mehring, *Principles of High Resolution NMR in Solids*, 2nd edn., Springer-Verlag: New York, **1983**.

47 D. M. Grant, Chemical Shift Tensors In *Encyclopedia of Magnetic Resonance*, D. M. Grant and R. K. Harris, Eds., Wiley: New York, **1996**, 1298.

48 J. Herzfeld and A. E. Berger, *J. Chem. Phys.*, **1980**, *73*, 6021-6030.

49 J. Mason, *Solid State Nucl. Magn. Reson.*, **1993**, *2*, 285-288.

50 K. Eichele and R. E. Wasylishen, *WSolids1: Solid-State NMR Spectrum Simulation Package*, v. 1.19.11, Universität Tübingen: Tübingen, **2009**.

51 M. E. Smith and E. R. H. van Eck, *Prog. Nucl. Magn. Reson. Spectrosc.*, **1999**, *34*, 159-201.

52 M. Khasawneh, J. S. Hartman and A. D. Bain, *Mol. Phys.*, **2004**, *102*, 975-983.

53 R. B. Creel, H. R. Brooker and R. G. Barnes, *J. Magn. Reson.*, **1980**, *41*, 146-149.

54 R. B. Creel and D. A. Drabold, *J. Mol. Struct.*, **1983**, *111*, 85-90.

55 R. B. Creel, *J. Magn. Reson.*, **1983**, *52*, 515-517.

56 B. C. Sanctuary, T. K. Halstead and P. A. Osment, *Mol. Phys.*, **1983**, *49*, 753-784.

57 G. M. Muha, *J. Magn. Reson.*, **1983**, *53*, 85-102.

58 A. D. Bain, *Mol. Phys.*, **2003**, *101*, 3163-3175.

59 S. Kroeker, K. Eichele, R. E. Wasylishen and J. F. Britten, *J. Phys. Chem. B*, **1997**, *101*, 3727-3733.

60 T. Vosegaard, J. Skibsted and H. J. Jakobsen, *J. Phys. Chem. A*, **1999**, *103*, 9144-9149.

61 M. Edén, *Chem. Phys. Lett.*, **2009**, *470*, 318-324.

62   W. P. Power, R. E. Wasylishen, S. Mooibroek, B. A. Pettitt and W. Danchura, *J. Phys. Chem.*, **1990**, *94*, 591-598.

63   R. N. Zare, *Angular Momentum: Understanding Spatial Aspects in Chemistry and Physics*, John Wiley & Sons: Toronto, **1988**.

64   G. B. Arfken and H. J. Weber, Euler Angles In *Mathematical Methods for Physicists*, 6th edn., Academic Press: New York, **2005**, 202-203.

65   G. K. Semin, *Russ. J. Phys. Chem. A*, **2007**, *81*, 38-46.

66   R. Livingston and H. Zeldes, *Table of Eigenvalues for Pure Quadrupole Spectra, Spin 5/2,* ORNL-1913, **1955**, 26 pages.

67   I. Solomon, *Phys. Rev.*, **1958**, *110*, 61-65.

68   I. D. Weisman and L. H. Bennett, *Phys. Rev.*, **1969**, *181*, 1341-1350.

69   E. L. Hahn, *Phys. Rev.*, **1950**, *80*, 580-594.

70   P. R. Bodart, J.-P. Amoureux, Y. Dumazy and R. Lefort, *Mol. Phys.*, **2000**, *98*, 1545-1551.

71   P. J. Grandinetti, J. T. Ash and N. M. Trease, *Prog. Nucl. Magn. Reson. Spectrosc.*, **2011**, *59*, 121-196.

72   D. Massiot, I. Farnan, N. Gautier, D. Trumeau, A. Trokiner and J. P. Coutures, *Solid State Nucl. Magn. Reson.*, **1995**, *4*, 241-248.

73   S. P. Brown and L. Emsley, Solid-State NMR In *Handbook of Spectroscopy*, 1st edn., G. Gauglitz and T. Vo-Dinh, Eds., Wiley: Weinheim, **2003**, 269-326.

74   H. S. Gutowsky and G. E. Pake, *J. Chem. Phys.*, **1950**, *18*, 162-170.

75   E. R. Andrew, A. Bradbury and R. G. Eades, *Nature*, **1958**, *182*, 1659.

76   I. J. Lowe, *Phys. Rev. Lett.*, **1959**, *2*, 285-287.

77   D. L. Bryce, G. M. Bernard, M. Gee, M. D. Lumsden, K. Eichele and R. E. Wasylishen, *Can. J. Anal. Sci. Spect.*, **2001**, *46*, 46-82.

78   A. Samoson, T. Tuherm, J. Past, A. Reinhold, T. Anupõld and I. Heinmaa, *Top. Curr. Chem.*, **2005**, *246*, 15-31.

79   Y. Nishiyama, J. Trébosc, O. Lafon, X. Lu, Z. Gan, P. K. Madhu and J.-P. Amoureux, *A Simple Scheme for High Resolution ¹H Solid-State NMR Measurements at Ultra-Fast MAS of 80 kHz*, ENC Conference, Asilomar, California, **2011**.

80   A. E. Bennett, C. M. Rienstra, M. Auger, K. V. Lakshmi and R. G. Griffin, *J. Chem. Phys.*, **1995**, *103*, 6951-6958.

81   M. Carravetta, M. Edén, X. Zhao, A. Brinkmann and M. H. Levitt, *Chem. Phys. Lett.*, **2000**, *321*, 205-215.

82   F. Bloch, *Phys. Rev.*, **1958**, *111*, 841-853.

83   H. Y. Carr and E. M. Purcell, *Phys. Rev.*, **1954**, *94*, 630-638.

84   S. Meiboom and D. Gill, *Rev. Sci. Instrum.*, **1958**, *29*, 688-691.

85   A. N. Garroway, *J. Magn. Reson.*, **1977**, *28*, 365-371.

86   M. Engelsberg and C. S. Yannoni, *J. Magn. Reson.*, **1990**, *88*, 393-400.

87   M. J. Lizak, T. Gullion and M. S. Conradi, *J. Magn. Reson.*, **1991**, *91*, 254-260.

88   A. J. Vega, *J. Magn. Reson.*, **1985**, *65*, 252-267.

89   P. S. Marchetti, L. Bhattacharyya, P. D. Ellis and C. F. Brewer, *J. Magn. Reson.*, **1988**, *80*, 417-426.

90   J. T. Cheng and P. D. Ellis, *J. Phys. Chem.*, **1989**, *93*, 2549-2555.

91   S. Bank, J. F. Bank and P. D. Ellis, *J. Phys. Chem.*, **1989**, *93*, 4847-4855.

92   K. Müller, R. Poupko and Z. Luz, *J. Magn. Reson.*, **1990**, *90*, 19-39.

93   F. H. Larsen, H. J. Jakobsen, P. D. Ellis and N. C. Nielsen, *J. Phys. Chem. A*, **1997**, *101*, 8597-8606.

94   M. Kaupp, M. Bühl and V. G. Malkin, *Calculation of NMR and EPR Parameters: Theory and Applications*, Wiley: Chichester, **2004**.

95   F. Bloch, Z. *Phys. A: Hadrons Nucl.*, **1929**, *52*, 555-600.

96   J. W. Zwanziger and M. Torrent, *Appl. Magn. Reson.*, **2008**, *33*, 447-456.

97   R. P. Chapman and D. L. Bryce, *Phys. Chem. Chem. Phys.*, **2009**, *11*, 6987-6998.

98   A. L. Webber, L. Emsley, R. M. Claramunt and S. P. Brown, *J. Phys. Chem. A*, **2010**, *114*, 10435-10442.

99   A. L. Webber, B. Elena, J. M. Griffin, J. R. Yates, T. N. Pham, F. Mauri, C. J. Pickard, A. M. Gil, R. Stein, A. Lesage, L. Emsley and S. P. Brown, *Phys. Chem. Chem. Phys.*, **2010**, *12*, 6970-6983.

100 M. C. Payne, M. P. Teter, D. C. Allan, T. A. Arias and J. D. Joannopoulos, *Rev. Mod. Phys.*, **1992**, *64*, 1045-1097.

101 J. C. Phillips, *Phys. Rev.*, **1958**, *112*, 685-695.

102 M. T. Yin and M. L. Cohen, *Phys. Rev. B*, **1982**, *25*, 7403-7412.

103 D. R. Hamann, M. Schlüter and C. Chiang, *Phys. Rev. Lett.*, **1979**, *43*, 1494-1497.

104 O. K. Andersen, *Phys. Rev. B*, **1975**, *12*, 3060-3083.

105 P. E. Blöchl, *Phys. Rev. B*, **1994**, *50*, 17953-17979.

106 D. J. Chadi and M. L. Cohen, *Phys. Rev. B*, **1973**, *8*, 5747-5753.

107 H. J. Monkhorst and J. D. Pack, *Phys. Rev. B*, **1976**, *13*, 5188-5192.

108 R. Ditchfield, *J. Chem. Phys.*, **1972**, *56*, 5688-5691.

Chapter Three

Solid-State $^{79/81}$Br NMR and GIPAW DFT Study of Structure, Symmetry, and Hydration State in Alkaline Earth Metal Bromides

3.1   Introduction

Bromine is found naturally in seawater, brines, and various bromide salts.[1] In addition to their ubiquitous presence in synthetic organic chemistry, organic bromine-containing materials are applied as flame retardants, dyes, drilling fluids, fuel additives, nematocides, and fumigants. Silver bromide is the most commonly applied inorganic bromide-containing compound, primarily in photography. While the above are important applications, recent evidence suggests that there is a negative environmental impact associated with using certain bromine-containing materials, and their future use is being reduced.[2] Similarly, a recent editorial has noted the negative effects that halides have during the production of biomass fuels, as they corrode the steam lines of production facilities.[3] In light of these accounts, methods must be further developed to (i) quantify the presence of bromine and bromides and (ii) comment upon bromine/bromide chemical environments. As will be detailed in Chapter 6, it has been demonstrated that $^{79/81}$Br SSNMR line shapes are very sensitive to the local environment about the bromide ions in MgBr$_2$. Presently, the power of $^{79/81}$Br SSNMR in the characterization and understanding of additional bromide-containing systems is established and demonstrated, with a particular emphasis on the extraction of structural information.

Both naturally occurring isotopes of bromine (^{79}Br and ^{81}Br) possess NMR-active quadrupolar nuclei ($I(^{79}$Br$) = I(^{81}$Br$) = 3/2$)), that are present in high natural abundance (~ 50 %). However, recent literature reviews report that $^{79/81}$Br SSNMR data are sparse.[4,5] Considering the

relatively large Q values[6] and Sternheimer antishielding factors (γ_∞, *vide infra*)[7,8] possessed by the $^{79/81}$Br nuclei, it is clear why $^{79/81}$Br SSNMR spectroscopy is underdeveloped (recall that when a quadrupolar nucleus experiences a nonzero EFG, the EFG will couple with the Q, leading to a QI which can produce substantial SSNMR line shape broadening in powdered samples, often to the extent that the SSNMR signal cannot be detected).

Most of the $^{79/81}$Br SSNMR literature accounts involve alkali metal bromides or other cubic salts (e.g., AgBr, CuBr, and TlBr), as the QI in these compounds is zero by symmetry and therefore the spectral acquisition is straightforward.[9-15] Over the past 20 years, a few $^{79/81}$Br SSNMR studies have been carried out on systems where the bromide experiences a small but nonzero QI. For example, inquiries using microcrystalline samples include perbromates,[16-19] oxygen-doped BaFBr,[20] and bromide-containing sodalites.[21-24] Investigations using single crystals have characterized bromide environments with more substantial QIs, such as in K$_2$Pt(CN)$_4$Br$_{0.3}$·3.2H$_2$O,[25,26] *tris*-sarcosine CaBr$_2$,[27,28] and deuterated glycyl-L-alanine HBr·H$_2$O.[29] Recently, the 'slow turning reveals enormous quadrupolar interactions' (STREAQI) method was applied to measure the bromine QIs in L-leucine HBr and L-tyrosine HBr,[30] and ^{14}N and ^{81}Br SSNMR was used to study several polycrystalline C$_x$H$_{2x+1}$(CH$_3$)$_3$NBr samples.[31,32]

Current reviews pertaining to the NMR-active quadrupolar halogen nuclides[4,5,33] underscore the significant ongoing advances in $^{35/37}$Cl SSNMR spectroscopy. Recent progress is primarily due to the increasing availability of ultrahigh magnetic fields (i.e., $B_0 > 18.8$ T) and the development of advanced pulse sequences.[34-41] Prior to these developments, $^{35/37}$Cl SSNMR studies were limited to systems where the chlorine environment was known to be nearly octahedral or tetrahedral.[14,42-50] Hence, the chlorine environments in the systems traditionally investigated using $^{35/37}$Cl SSNMR are similar to the bromine environments of those studied using $^{79/81}$Br SSNMR. In the last several years, new insights into the relationship between $^{35/37}$Cl

SSNMR parameters and local molecular and electronic structure have been obtained for a range of interesting compounds, including amino acid hydrochlorides,[51-54] alkaline earth metal chlorides,[55-57] hydrochloride pharmaceuticals,[58] group 4 and 13 metal chlorides,[59-61] halide-containing ionic liquids,[62,63] and antiferromagnetic/superconducting materials.[64-68] Most of these recent studies featured chlorides that were not present at a position of high symmetry; hence, these characterizations were made for systems where the QI is nonzero. It is therefore believed that $^{79/81}$Br SSNMR spectroscopy may be developed in a similar fashion as $^{35/37}$Cl SSNMR.

To provide an experimental basis for understanding the relationship between local structure and symmetry at the bromine and the observable $^{79/81}$Br SSNMR parameters, a systematic $^{79/81}$Br SSNMR study of several alkaline earth metal bromides and corresponding stable hydrates is presented in this Chapter. While these systems possess relatively simple structures, a variety of bromide environments are represented. These compounds (i) contain different numbers of magnetically unique bromide sites, ranging from 1 to 4; (ii) exhibit distinct bromine QIs, both in terms of magnitude and symmetry; and (iii) form stable hydrates, which allows for an investigation of the relationship between hydration (sometimes incorrectly referred to as 'pseudopolymorphism') and the $^{79/81}$Br SSNMR parameters. These systems are also more than simply of academic interest: CaBr$_2$ is used in oil drilling brine solutions, as a desiccant, a food preservative, and a fire retardant. Eu(III)-doped CaBr$_2$-based aluminoborate glasses are candidate materials for use in lasers, optical amplifiers and optical storage devices.[69] Strontium bromide has been used as a vapour-phase laser.[70] Barium bromide single-crystals are excellent X-ray storage phosphors when doped with lanthanide ions such as Eu(II)[71] or Ce(III)[72] and have recently been proposed for use in X- and γ-ray scintillation applications.[73,74] By combining multiple field $^{79/81}$Br SSNMR experiments with GIPAW DFT quantum chemical computations, it is shown that significant insight is available regarding the bromide environments in the alkaline

earth metal bromides and corresponding hydrates. It will also be shown that hydration may be easily distinguished and characterized, and that the composition of a simple mixture may be determined using $^{79/81}$Br SSNMR experiments.

3.2   Experimental Details

3.2.1   Sample Preparation

CaBr$_2$ (99.98 %), SrBr$_2$ (99.995 %), and BaBr$_2$ (99.999 %) were purchased from Aldrich as anhydrous beads. All the above compounds are hygroscopic and were stored and prepared for use under either dry N$_2$ or Ar. MgBr$_2$·6H$_2$O (99 %), SrBr$_2$·6H$_2$O (99 %), and CaBr$_2$·xH$_2$O (98 %) were purchased from Aldrich in either polycrystalline or microcrystalline powder form. BaBr$_2$·2H$_2$O (99.3 %) was purchased from Alfa Aesar as a microcrystalline powder. All of the hydrates are air stable. For all $^{79/81}$Br SSNMR experiments, the samples were powdered and tightly packed into 4 mm outer diameter (o.d.) Bruker MAS zirconia rotors.

3.2.2   Solid-State $^{79/81}$Br NMR

Bromine-79/81 SSNMR data were acquired at the University of Ottawa using a Bruker AVANCE spectrometer operating at B_0 = 11.75 T (v_0(^{1}H) = 500.13 MHz) and at the National Ultrahigh-field NMR facility for Solids in Ottawa using a Bruker AVANCEII spectrometer operating at B_0 = 21.1 T (v_0(^{1}H) = 900.08 MHz). At 11.75 T, all experiments used a Bruker 4 mm HXY MAS probe (v_0(^{81}Br) = 135.076 MHz; v_0(^{79}Br) = 125.310 MHz). At 21.1 T, experiments performed on stationary samples used a Bruker 4 mm HX MAS probe (v_0(^{81}Br) = 243.093 MHz; v_0(^{79}Br) = 225.519 MHz), while MAS NMR experiments on BaBr$_2$·2H$_2$O used Bruker 3.2 mm and 2.5 mm HX MAS probes for the detection of ^{81}Br and ^{79}Br SSNMR signals,

respectively. Due to the known heating effect of MAS on the sample, and as the loss of H_2O in powdered $BaBr_2 \cdot 2H_2O$ occurs upon heating above 323 K,[75] all MAS experiments were carried out while passing cooled N_2 gas through the probe. Bromine $\pi/2$ pulse widths were determined using the $^{79/81}$Br NMR signal of KBr powder. The same compound also served as the chemical shift reference (δ_{iso}(KBr(s) = 0.00 ppm). The values reported in this Chapter may be converted to the suggested IUPAC standard scale, which is relative to 0.01 mol/dm^3 NaBr in D_2O, by adding 54.51 ppm.[76] As the ion lattice of solid KBr is cubic, the CT selective (i.e., 'solid $\pi/2$') pulse widths used for the alkaline earth metal bromides were scaled by $1/(I + 1/2) = 1/2$. Bromine-79/81 SSNMR signals were primarily acquired using the Solomon echo pulse sequence[77,78] with the phase cycling suggested by Kunwar et $al.$[79] For all samples except $BaBr_2 \cdot 2H_2O$ and $SrBr_2 \cdot 6H_2O$, long T_2 values (estimated using the QCPMG pulse sequence, $vide$ $infra$) allowed for whole echo data acquisition, thus increasing the S/N of the echo experiment by $\sqrt{2}$ per scan. Typical $^{79/81}$Br Solomon echo parameters (for full details, see Appendix A, Table A.1) were the following: $\pi/2$ = 1.0 to 3.0 μs, spectral window = 250 to 2000 kHz, τ_1 = 100 to 500 μs (whole echo acquisition) or 26 μs to 100 μs (half echo acquisition), recycle delay = 0.3 to 0.8 s, collection of 1 024 to 4 096 data points per transient and 1 000 to 65 536 transients. MAS NMR data were acquired under rotor-synchronized conditions. The QCPMG pulse sequence[34,80,81] was used at B_0 = 11.75 T to enhance the $^{79/81}$Br SSNMR signals and thus reduce experiment times. For typical QCPMG parameters, see Appendix A, Table A.1. For all hydrates of known composition, the effects of CW ^{1}H decoupling were tested. Typical $\nu_1(^1H)$ values were 40 to 100 kHz.

For most of the samples studied, the VOCS data acquisition method[82-84] was used to collect the very broad $^{79/81}$Br CT SSNMR signals. Offsets varied from 200 to 400 kHz for

Solomon echo experiments, and from 86.31 to 95.90 kHz for QCPMG experiments. Each sub-spectrum was processed normally and then combined in the frequency-domain by co-addition.

3.2.3 Quantum Chemical Computations

GIPAW DFT computations were carried out using the NMR module associated with version 4.1 of the CASTEP program,[85-88] and input files were generated from Materials Studio 3.2. Bromine on-the-fly generation (otfg) pseudopotential files were obtained directly from Accelrys Inc. (San Diego, CA). Geometry optimizations, as well as NMR calculations (i.e., of the $\ddot{V}$ and $\ddot{\sigma}$ tensors), used the Perdew-Burke-Ernzerhof (PBE) exchange-correlation (XC) functional,[89,90] under the generalized gradient approximation (GGA). Additional NMR parameter computations employed the Perdew-Wang-91 (PW91) XC functional,[91-95] and yielded computed values that were similar to the PBE calculations. NMR parameter convergence was tested by varying both the Monkhorst-Pack[96] k-point sampling of the Brillouin zone and the plane wave basis set energy cutoff (E_{cut}). All NMR calculations used the 'precise' setting, as defined by Materials Studio, for the fast-Fourier transformation (FFT) grid, except $MgBr_2 \cdot 6H_2O$, where the 'standard' FFT grid setting was used due to computational resource limitations. All geometry optimizations used the standard FFT grid setting. Conversions of calculated MS tensor element values (σ_{ij}) into δ_{ij} values used the following procedure: the bromine σ_{iso} value for the secondary reference compound KBr (i.e., $\sigma_{iso, ref}$) was computed using E_{cut} = 800 eV, a 6 × 6 × 6 k-point grid, and the same XC functional as for a given sample. This was followed by application of **(2.12)**. The E_{cut} and k-point grid used for each system are in the footnotes to Tables 3.5 and 3.7. Computed energies, structure references, and additional computational input

details are in Appendix A, Table A.2. The crystal structure parameters used for NMR computations are in Appendix A, Table A.3.

For $MgBr_2 \cdot 6H_2O$ and $SrBr_2 \cdot 6H_2O$, two structural models were used for subsequent NMR parameter computations, and are labeled as 'model A' and 'model B'. For model A of $MgBr_2 \cdot 6H_2O$, the heavy atom positions from Andress and Gundermann[97] and the unit cell from Sorrell and Ramey[98] were used. Hydrogen atoms were added using Gaussview 3.0 and then optimized using CASTEP. For model B, the heavy atom positions were adjusted slightly, while remaining within the error bounds of the structural parameters reported in the original sources. For $SrBr_2 \cdot 6H_2O$, model A, the heavy atom positions and unit cell from Abrahams and Vordemvenne were used.[99] Hydrogen positions were initially placed according to those of $SrCl_2 \cdot 6H_2O$,[100] whose structure was determined using neutron diffraction and should be isomorphic to $SrBr_2 \cdot 6H_2O$. The hydrogen positions were then optimized computationally. For model B, the procedure used was nearly identical, but the c unit cell position values of the bromides were changed to $-c$ in order to agree with the halogen atom positions in the isomorphic $SrCl_2 \cdot 6H_2O$, $CaBr_2 \cdot 6H_2O$, and $CaCl_2 \cdot 6H_2O$ compounds.[101] After computational optimization of the hydrogen positions, NMR parameter calculations were performed.

3.2.4 Point Charge Model Calculations

Calculations were semi-automated using Microsoft Excel, using full integer charges for the ions in the lattice. For all anhydrous compounds, the point charge lattices corresponded to an $8 \times 8 \times 8$ super cell (except for $SrBr_2$, where a $6 \times 6 \times 6$ super cell was used). This amounted to 3 435, 6 792, and 6 143 point charges and super cell volumes of 100.57 nm^3, 208.77 nm^3, and 208.30 nm^3 for $CaBr_2$, $SrBr_2$, and $BaBr_2$, respectively. Calculations included Sternheimer

antishielding effects by using $(1 - \gamma_\infty) = 81$.[102] To assess the influence of ionic charge on $C_Q(^{81}Br)$, the partial ionic charge values (i.e., $q(Ca)$ and $q(Br)$) for $CaBr_2$ were also varied.

3.3   Results and Discussion

3.3.1   Bromine-79/81 SSNMR Experiments

3.3.1.1 Anhydrous Alkaline Earth Metal Bromides

The measured $^{79/81}Br$ SSNMR parameters for the anhydrous alkaline earth metal bromides $CaBr_2$, $SrBr_2$, and $BaBr_2$ are presented in Tables 3.1 and 3.2. As these systems are highly ionic, the EFG at the Br nuclei, while nonzero, is not so large that it renders $^{79/81}Br$ SSNMR experiments impossible: $C_Q(^{79}Br)$ values range from a low of 12.3 MHz for one site in $SrBr_2$ to a high of 75.1 MHz for $CaBr_2$.

Table 3.1 Experimental $^{79/81}Br$ EFG tensor parameters: alkaline earth metal bromides[a]

compound	site label	$\lvert C_Q(^{81}Br)\rvert$[b] / MHz	$\lvert C_Q(^{79}Br)\rvert$ / MHz	η_Q	$\nu_Q(^{79}Br)$[c] / MHz
$CaBr_2$	—	62.8(4)	75.1(5)	0.445(20)	38.76(0.08)
$SrBr_2$	Br(1)	10.3(3)	12.3(3)	0.07(4)	—
	Br(2)	18.10(10)	21.65(20)	0.03(2)	—
	Br(3)	25.6(2)	30.6(2)	0.695(15)	16.54(0.10)
	Br(4)	53.7(6)	64.2(6)	0.33(2)	32.90(0.12)
$BaBr_2$	Br(1)	23.5(3)	28.1(4)	0.17(2)	13.96(0.3)/23.36(0.35)
	Br(2)	27.2(3)	32.5(3)	0.070(15)	

[a] Error bounds are in parentheses (e.g., 0.445(20) $\leftrightarrow$ 0.445 $\pm$ 0.020). Parameter definitions are in Section 2.3.3.2.
[b] While C_Q may take any real value, $\lvert C_Q\rvert$ is measured using conventional SSNMR experiments.
[c] From literature.[103] All ^{79}Br NQR measurements were at T = 300 K, except for $BaBr_2$, which was at T = 209 K.

3.3.1.1.1   CaBr₂: An Example of a Significant Bromine QI and CSA

The static $^{79/81}Br$ SSNMR spectra acquired at $B_0 = 21.1$ T are broadened due to a nonzero EFG at the bromine, as the signals span several MHz and feature line shapes that are

characteristic of second-order quadrupolar broadening (Figure 3.1). While the [79/81]Br SSNMR signals are distributed over a large frequency range, they were acquired using the Solomon echo pulse sequence[77] and VOCS data acquisition methods[82-84] in about 8 hours. Data acquisition was facilitated by efficient [79/81]Br quadrupole-dominated spin-lattice (T_1) relaxation.[104] A [81]Br SSNMR spectrum of $CaBr_2$ was also acquired at 11.75 T under static conditions (see Appendix A, Figure A.1); however, the QCPMG pulse sequence[34,80,81] and about two days of experiment time were required to obtain a spectrum with a reasonable S/N ratio (74 sub-spectra).

Table 3.2 Experimental bromine CS tensor parameters: alkaline earth metal bromides[a]

compound	site label	δ_{iso}[b] / ppm	Ω / ppm	κ	α, β, γ / °
$CaBr_2$	—	280(50)	250(150)	0	270[c], 90(20), 180[c]
$SrBr_2$	Br(1)	422(5)	50(20)	−1[d]	90[c], 90(15), 180(5)
	Br(2)	410(8)	85(25)	−1[d]	90[c], 90(10), 180(8)
	Br(3)	320(10)	110(30)	0.3(4)	42(8), 90(10), 235(20)
	Br(4)	300(50)	—	—	—
$BaBr_2$	Br(1)	280(10)	200(20)	−0.6(2)	0[c], 47(7), 180[c]
	Br(2)	480(15)	170(30)	0.1(2)	180[c], 18(7), 180[c]

[a] Includes Euler angle values. Error bounds are in parentheses. Parameter definitions are in Sections 2.3.2.4, 2.3.3.1, and 2.3.3.3.
[b] With respect to solid KBr (δ_{iso} = 0.00 ppm).
[c] Simulated NMR line shape is insensitive to parameter variation; the value is assigned based on computational results.
[d] Assumed based on crystallographic site symmetry.

The ambient temperature and pressure structure of $CaBr_2$ is believed to be isomorphic to $CaCl_2$,[105] and belongs to the orthorhombic *Pnnm* space group.[106,107] The bromide ions are located at *m* symmetry sites and coordinate to three Ca^{2+} ions in a distorted trigonal planar fashion (Figure 3.2). The shortest Br-Br distance is 3.79 Å, which is slightly greater than twice the accepted value for the bromine van der Waals (vdW) radius (i.e., 3.66 Å).[108,109] Calcium-43 MAS SSNMR measurements exist for this compound,[110] and while [79]Br NQR data collected at

300 K determined the ν_Q value to be 38.76 MHz,[103] insight into the $\ddot{V}$ tensor symmetry (as well as any comment on the $\ddot{\sigma}$ tensor) was not obtained, as standard [79]Br NQR experiments are insensitive to this property.
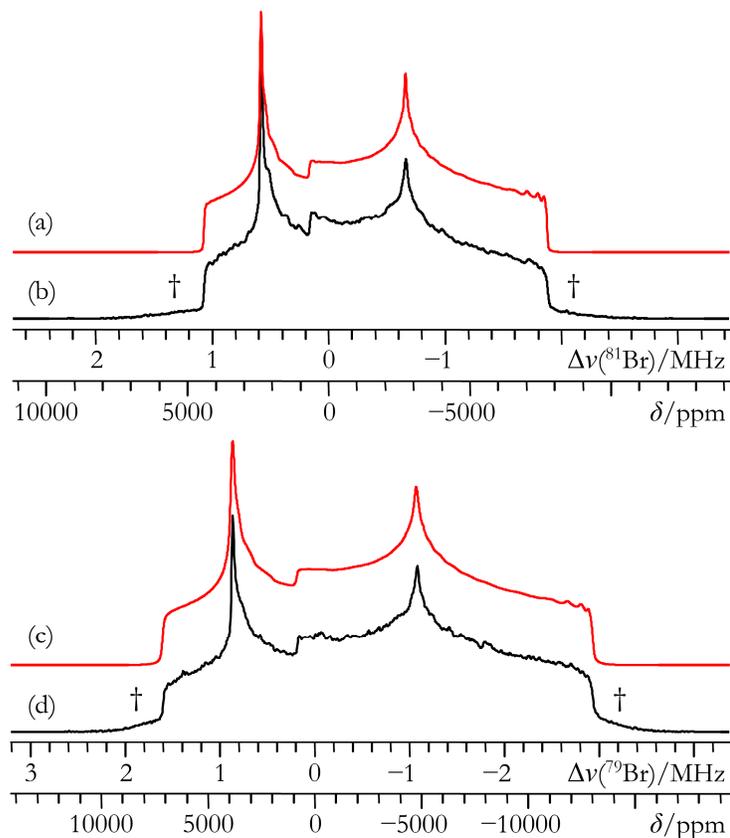
Figure 3.1 Best-fit analytical simulations (a, c), and experimental static VOCS Solomon echo [79/81]Br SSNMR spectra of powdered $CaBr_2$ acquired at $B_0 = 21.1$ T (b, d). Partially excited ST are denoted using '†'.

The line widths of the [79/81]Br SSNMR spectra in Figure 3.1 imply a substantial QI at the bromide ions. The measured values of C_Q([81]Br) = 62.8(4) MHz and C_Q([79]Br) = 75.1(5) MHz are by far the largest measured using [79/81]Br SSNMR spectroscopy.[4,5,33] The nonaxial $\ddot{V}$ tensor (η_Q = 0.445(20)) underscores the low site symmetry at the bromide, and restricts the rotational symmetry at this point to a maximum of C_2, in agreement with the accepted site symmetry.
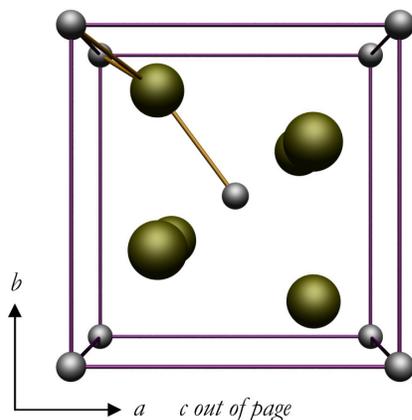
Figure 3.2 POV-ray rendering of the CaBr$_2$ unit cell. The calcium ions are denoted in grey. Solid lines denote ions within the sum of the Ca and Br vdW radii (i.e., $r_{\text{Ca-Br}} < 4.14$ Å).[108,109]

The value of ν_Q measured using NQR spectroscopy may be related to C_Q when η_Q and I are also known:[111]

$$\nu_Q = \frac{3C_Q\sqrt{1+\left(\eta_Q^2/3\right)}}{2I(2I+1)}. \tag{3.1}$$

Using the ^{79}Br EFG tensor parameters measured with SSNMR, $\nu_Q(^{79}$Br$)$ is calculated to be 38.8 MHz, in perfect agreement with the earlier NQR data. Quantitative agreement between NQR and NMR observations provides an experimental basis for an earlier assertion,[4] based on exact QI theoretical modeling,[112,113] that substantial $C_Q(^{79/81}$Br$)$ values may be accurately measured while remaining within the high-field approximation (often stated as when $10\nu_Q < \nu_0$). Further testing of the high-field approximation is discussed more thoroughly in Chapter 5.

Using a series of M[BPh$_4$] salts (M = Na, K, Rb, Cs), Wu and Terskikh illustrated a linear relationship between measured C_Q(M) values and the quantity $eQ(1-\gamma_\infty)/V$, where V is the unit cell volume and other terms have been defined previously (note that the γ_∞ are empirical corrections attributed to core electron polarization due to external EFGs. They may be applied to estimate the true EFG at a nuclear site, relative to the EFG which would be produced by the

ionic charges themselves).[114] In the present context, it is interesting to compare the $C_Q(^{81}Br)$ value for CaBr$_2$ measured here with the $C_Q(^{35}Cl)$ value measured for CaCl$_2$.[55] Using the parameters in Table A.4 of Appendix A, it is calculated that $|C_Q(^{81}Br)/C_Q(^{35}Cl)|$ should be 7.12. This is in severe disagreement with the value established from experimental SSNMR data, which is 29.9. Indeed, Sandland *et al.* seemed rightfully surprised that the CaCl$_2$ structure, with its distorted trigonal planar geometry about the chloride and relatively short Cl-Ca distances, should exhibit such a small $C_Q(^{35}Cl)$. It is emphasized that CaBr$_2$ possessed the *largest* $C_Q(^{81}Br)$ value measured in the current study (*vide infra*). During their $^{35/37}$Cl SSNMR study of alkaline earth metal chloride compounds, Bryce and Bultz[57] noted that among the anhydrous compounds, the accepted $C_Q(^{35}Cl)$ value[55] for CaCl$_2$ was the *smallest*, if one neglected the cubic SrCl$_2$ system. Further discussion on this topic will be provided in Chapter 6.

The bromine chemical shift of solid CaBr$_2$ (δ_{iso} = 280(50) ppm) lies between the alkali metal bromides and the perbromates (although it is much closer to the bromides). Precise line shape analysis (see Figures A.2 and A.3 in Appendix A) allows for the first determination of bromine CSA in a powdered sample using a multiple field and multiple nuclide data set, Ω = 250(150) ppm. Prior accounts of bromine CSA are limited to a single-crystal study on NaBrO$_3$ (Ω = 90 ppm)[115] and a recent study of several powdered C$_x$H$_{2x+1}$(CH$_3$)$_3$NBr systems.[31] This recent account reported ^{81}Br MAS SSNMR data at a single magnetic field and multiple MAS frequencies, followed by numerical line shape fitting routines which incorporate QI/CSA interplay under MAS. The values of Ω were found to range from 23 to 80 ppm; however, error bounds were not reported. Modest $C_Q(^{81}Br)$ values (6.03 to 8.08 MHz) were also measured.

The simulated $^{79/81}$Br SSNMR line shapes for CaBr$_2$ were relatively insensitive to the κ value, which is assumed to be near 0 as a result of GIPAW DFT computations (*vide infra*). The simulations shown in Figure 3.3 clearly demonstrate the presence of bromine CSA, as well as the

noncoincidence of the $\ddot{V}$ and $\ddot{\sigma}$ tensor PASs. These present findings are consistent with the known m site symmetry at the bromide ion, which only restricts one principal axis of $\ddot{V}$ and $\ddot{\sigma}$ to be collinear. The $^{79/81}$Br NMR line shape is also found to be sensitive to β, while α and/or γ variation leads to very subtle line shape changes.
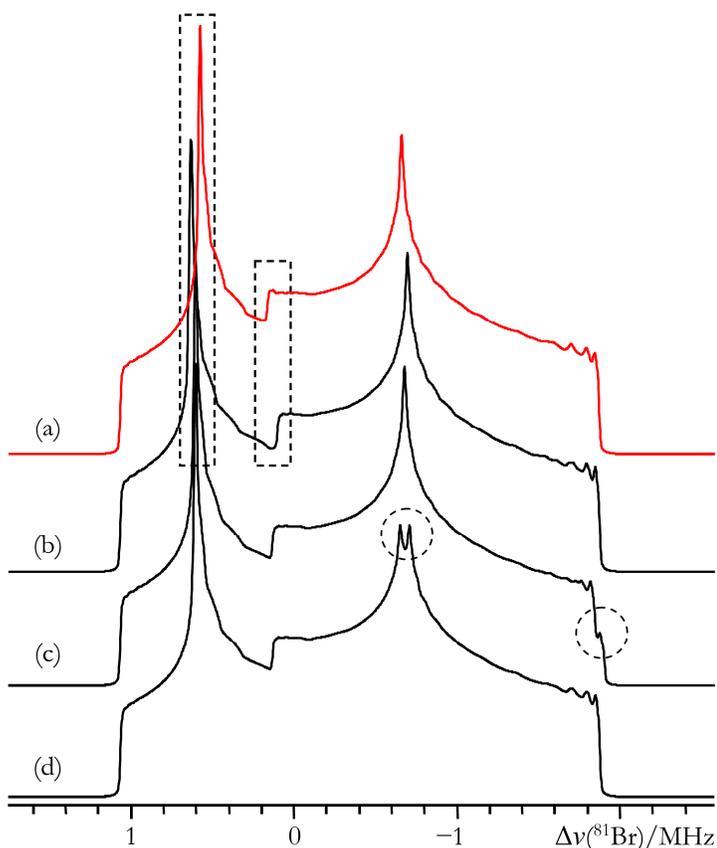
Figure 3.3 Illustration of the necessity of considering the effects of noncoincident bromine $\ddot{V}$ and $\ddot{\sigma}$ tensor frames for CaBr$_2$. Analytical simulations are provided and use identical values as the best-fit simulation in Figure 3.1a (reproduced here as (a)) except: (b) $\beta = 0°$; (c) $\beta = 45°$; (d) $\beta = 45°$ and $\alpha = 0°$. In each case (b – d), there exists additional fine structure (regions within the dashed boxes or circles), which disagree with the best-fit spectrum in (a).

3.3.1.1.2   *SrBr₂: A Test of the Resolving Power of $^{79/81}$Br SSNMR*

The static $^{79/81}$Br SSNMR spectra of SrBr$_2$ are complex (Figures 3.4 and 3.5) due to several overlapping signals. Accurate line shape simulations were enabled by having four

experimental data sets from which to draw. The measured $^{79/81}$Br SSNMR parameters are reported above, in Tables 3.1 and 3.2.
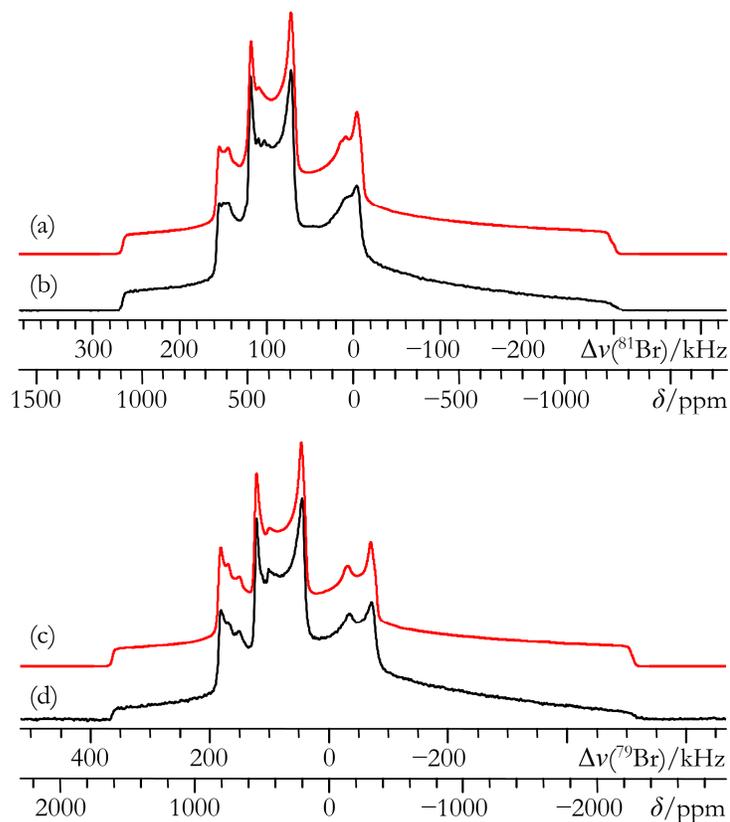
Figure 3.4 Best-fit analytical simulations (a, c), and experimental static VOCS Solomon echo $^{79/81}$Br SSNMR spectra of three of the four unique bromine sites in powdered SrBr$_2$ acquired at B_0 = 21.1 T (b, d).

Preliminary accounts regarding the ambient crystal structure of SrBr$_2$[106,116,117] appeared in the literature prior to it being established that the structure belongs to the tetragonal space group $P4/n$.[118] The four crystallographic bromine sites in SrBr$_2$ offer a clear test of the resolving power of $^{79/81}$Br SSNMR spectroscopy. Two of the sites, labeled as Br(1) and Br(2) (Figure 3.6) occupy $\overline{4}$ lattice sites, while the remaining two sites (Br(3) and Br(4)) are found at 1 lattice positions. Bromine-79 NQR data exist,[103] albeit for only two of the four sites (Table 3.1). After de-convoluting the $^{79/81}$Br SSNMR line shapes (Figure 3.5c,f), and considering the relationships

between observed SSNMR parameters and the known bromine crystallographic site symmetries, it is clear that the two sites which possess η_Q near 0 and $\kappa = -1$ (indicative of axial $\ddot{V}$ and $\ddot{\sigma}$ tensors) must be due to the bromide ions at $\overline{4}$ sites.[119]
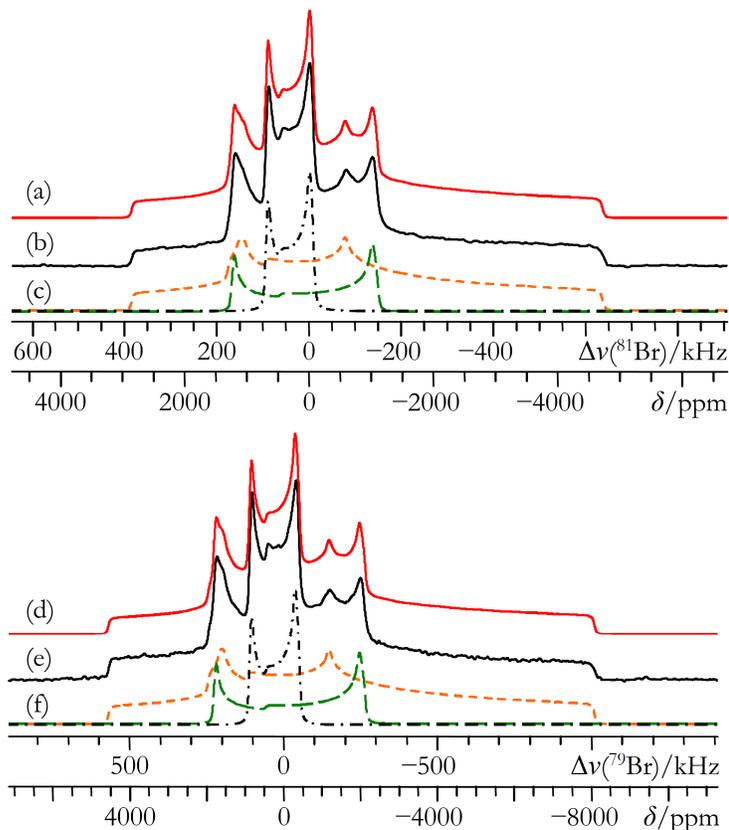
Figure 3.5 Best-fit analytical simulations (a, d), and experimental static VOCS Solomon echo [79/81]Br SSNMR spectra of three of the four unique bromine sites in powdered SrBr$_2$ acquired at $B_0 = 11.75$ T (b, e). In (c) and (f), a deconvolution of the three sites is provided.

With respect to one another, the Br ions at $\overline{4}$ sites possess very similar δ_{iso} values (410(8) ppm and 422(5) ppm), although they are quite distinct from the third site ($\delta_{iso} = 320(10)$ ppm). As a result of GIPAW DFT computations (*vide infra*), the sites with $C_Q(^{81}Br) = 10.3(3)$ and 18.10(20) MHz are assigned to Br(1) and Br(2), respectively. The remaining signal (Br(3)) is assigned to a bromide ion at a 1 site in the lattice. The $\nu_Q(^{79}Br)$ values for SrBr$_2$ observed using

NQR are too large to be assigned to either Br(1) or Br(2). For Br(3), however, using the measured $C_Q(^{79}Br) = 30.6(2)$ MHz and $\eta_Q = 0.695(15)$ values in **(3.1)** leads to an NMR-derived $\nu_Q(^{79}Br)$ value of 16.5 MHz, which is in excellent agreement with the smaller of the two previously reported $\nu_Q(^{79}Br)$ values for SrBr$_2$ (Table 3.1).
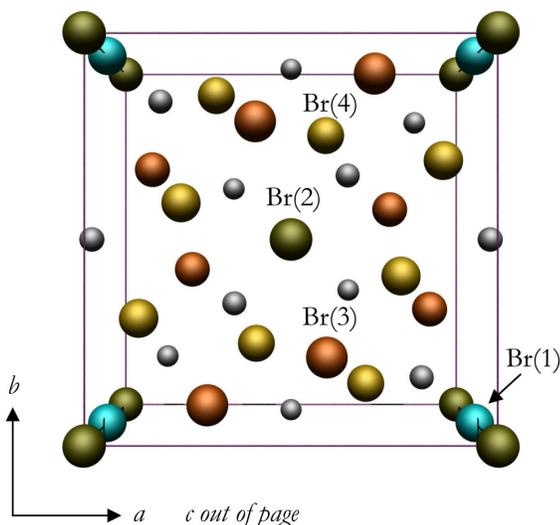
Figure 3.6 POV-ray rendering of the SrBr$_2$ unit cell. The strontium ions are denoted in grey. The following colour and labeling scheme is used to distinguish the four magnetically inequivalent bromides: Br(1) = turquoise; Br(2) = green; Br(3) = orange; and Br(4) = gold.

The three resolved sites have appreciable bromine CSA, although each is more modest than in CaBr$_2$. For Br(1) and Br(2), the rather small spans ($\Omega(Br(1)) = 50(20)$ ppm; $\Omega(Br(2)) = 85(25)$ ppm) are reflective of the small distortions from tetrahedral symmetry about these ions. This is consistent with observations of small chlorine CSA for nearly tetrahedral chlorine environments, e.g., for LiAl$_2$(OH)$_6$ClO$_4 \cdot n$H$_2$O, $\Omega = 32$ ppm.[120] As Br(3) is at a 1 position, it is therefore expected that the measured Ω value would be larger relative to Br(1) and Br(2). Indeed, this is in agreement with the observations ($\Omega(Br(3)) = 110(30)$ ppm). As with CaBr$_2$, line shape fits for SrBr$_2$ indicate noncoincident $\ddot{V}$ and $\ddot{\sigma}$ PASs (see Appendix A, Figure A.4 for some of the models considered when fitting the $^{79/81}$Br SSNMR line shapes of SrBr$_2$). Variation

of β again produces significant changes in simulated $^{79/81}$Br SSNMR line shapes, while variation in α or γ leads to more subtle changes.

The ratio of the integrated intensities between the Br(1), Br(2), and Br(3) NMR signals is $0.25 \pm 0.01 : 0.25 \pm 0.02 : 1$, in agreement with the accepted crystal structure; however, a fourth site is expected based upon the accepted structure. Due to the broad $^{79/81}$Br SSNMR line shapes of SrBr$_2$, the additional signal may simply not be resolved, although if this was the case, then quantitative agreement between the experimental integrated intensities and those predicted from the crystal structure would not be expected. As well, an additional signal, associated with a large ν_Q, was observed using ^{79}Br NQR. Hence, $^{79/81}$Br SSNMR experiments were performed at $B_0 =$ 21.1 T, this time scanning a greater frequency range. An additional site (Br(4)) possessing a large $(C_Q(^{79}\text{Br}) = 64.2(6)$ MHz), nonaxial ($\eta_Q = 0.33(2)$)) QI, is observed (Figure 3.7). The observed $\ddot{V}$ tensor symmetry is consistent with a Br at a 1 lattice position. Using **(3.1)** and the above values of C_Q and η_Q, $\nu_Q(^{79}\text{Br})$ is calculated to be 32.7 MHz for Br(4), in very good agreement with one of the $\nu_Q(^{79}\text{Br})$ values measured previously using NQR. Due to interference from the other three bromine sites in the $^{79/81}$Br SSNMR spectra of Br(4), a reliable experimental estimate of the bromine CS tensor magnitude could not be obtained for this site.

Although four sites have been observed, and while they have been grouped into Br belonging to $\overline{4}$ sites and those at 1 sites, it is difficult to assign them conclusively to individual crystallographic sites without considering additional information. Further discussion is postponed until Section 3.3.2, when the GIPAW DFT computational results are considered.
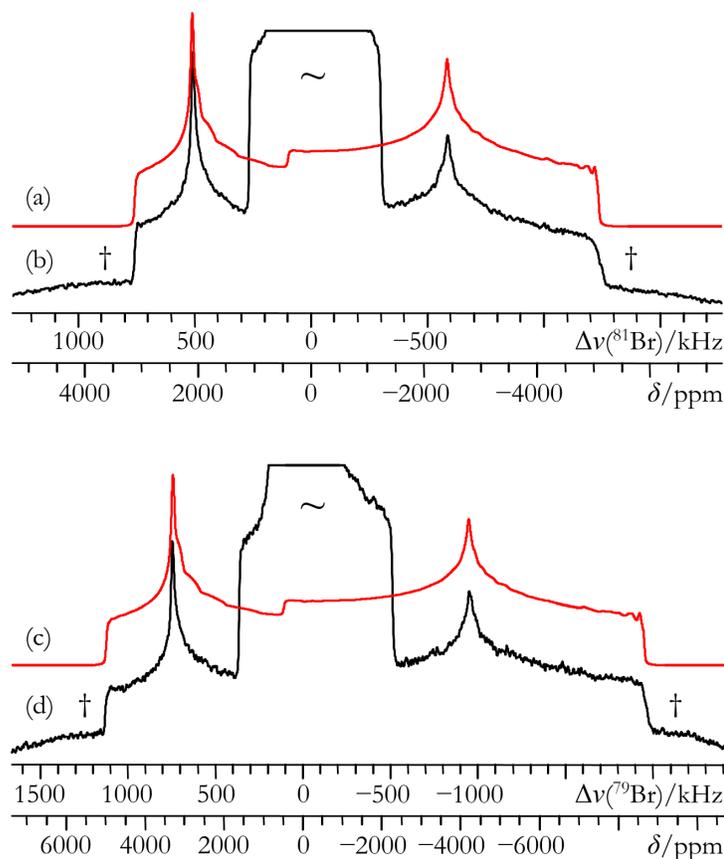
Figure 3.7 Best-fit analytical simulations (a, c), and experimental static VOCS Solomon echo $^{79/81}$Br SSNMR spectra of the broadest of the four unique bromine sites in SrBr$_2$ acquired at $B_0 = 21.1$ T (b, d). Partially excited ST are denoted using '†'. The spectral region corresponding to the three other SrBr$_2$ sites (partially cut off vertically) is denoted using '~'.

3.3.1.1.3   *BaBr$_2$: Deficiencies in ^{79}Br NQR Data*

Static $^{79/81}$Br SSNMR experiments on BaBr$_2$ at $B_0 = 11.75$ T and $B_0 = 21.1$ T yield well-defined spectra which exhibit many discontinuities (Figures 3.8 and 3.9). After line shape analysis was performed using all four datasets, the two expected crystallographic sites are resolved (Figure 3.9b,d) and the $^{79/81}$Br SSNMR parameters are precisely determined (Tables 3.1 and 3.2).
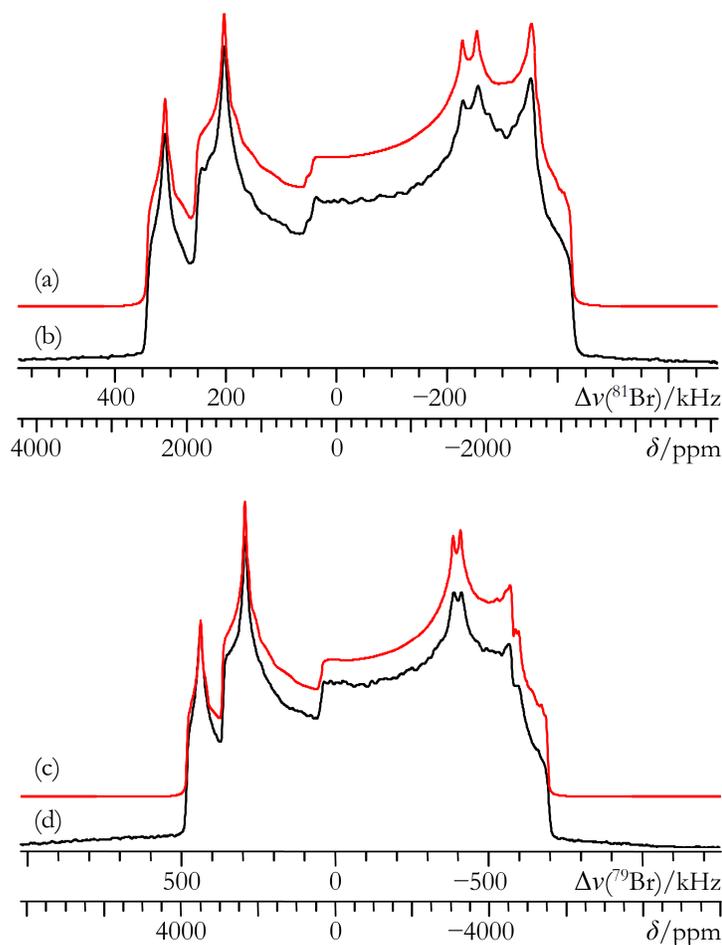
Figure 3.8 Best-fit analytical simulations (a, c), and experimental static VOCS Solomon echo $^{79/81}$Br SSNMR spectra of powdered BaBr$_2$ acquired at $B_0 = 11.75$ T (b, d).

Refined pXRD data have established that the stable orthorhombic form of BaBr$_2$ is isomorphic to BaCl$_2$ and crystallizes in the *Pnma* space group.[106,121] One unique Br site is surrounded by Ba^{2+} ions in a highly distorted tetrahedral arrangement (Figure 3.10), while the second unique Br site has five Ba^{2+} ions within the sum of the Br and Ba vdW radii (i.e., $r_{\text{Br-Ba}} <$ 4.51 Å).[109] Both crystallographic bromines are at *m* sites, which requires one principal axis (i.e., eigenvector) of $\ddot{V}$ to be collinear with one principal axis of $\ddot{\sigma}$. A ^{79}Br NQR study measured two ν_Q values (in agreement with the proposed crystal structure) and highlighted the temperature

dependence of $v_Q(^{79}Br)$.[122]   Bromine-79/81 SSNMR experiments have been carried out previously on this system,[123] but the second-order QI-broadened line shapes were not resolved, the crystallographic sites were not distinguished, and discussion pertaining to the $\ddot{\sigma}$ and $\ddot{V}$ tensors was not provided.
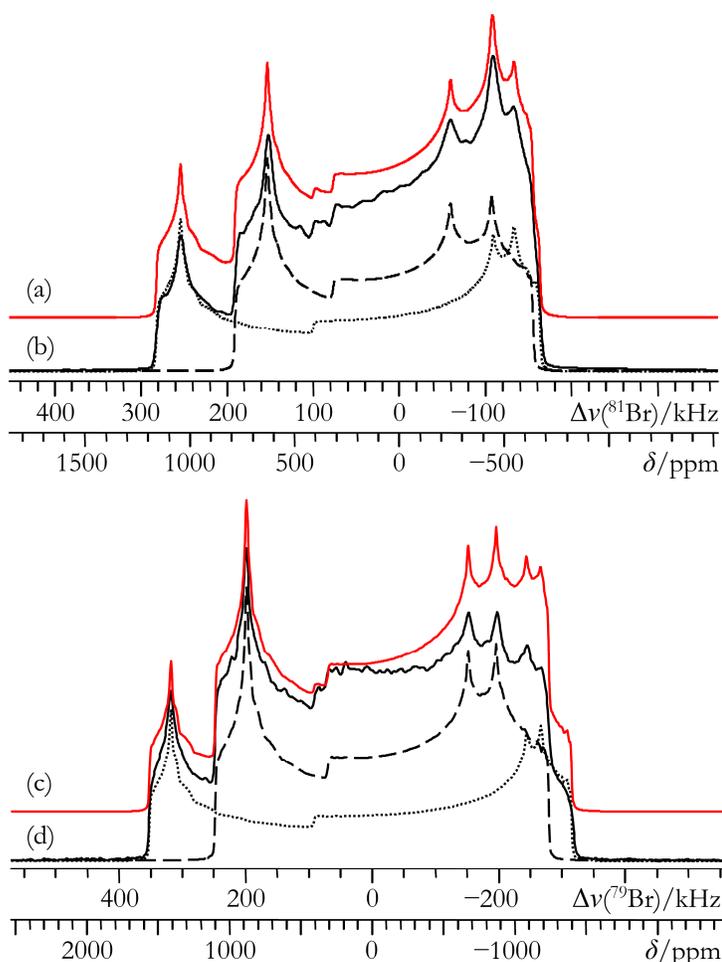
Figure 3.9 Best-fit analytical simulations (a, c), experimental static Solomon echo [81]Br SSNMR spectrum (b), and experimental static VOCS Solomon echo [79]Br SSNMR spectrum (d) of powdered BaBr$_2$ acquired at B_0 = 21.1 T. In each of (b) and (d), a deconvolution of the two sites is provided.

As with CaBr$_2$ and SrBr$_2$, although the dominant features of the [79/81]Br SSNMR line shapes for BaBr$_2$ are due to second-order quadrupolar broadening, additional fine structure is clearly present in all spectra. This additional structure cannot be reproduced by analytical

simulations that consider only the QI. Spectral fits yield bromine CS tensor parameters and are also indicative of noncoincident $\ddot{\sigma}$ and $\ddot{V}$ PASs (Table 3.2). The measured $C_Q(^{79/81}Br)$ values for the two bromine sites in $BaBr_2$ are quite similar.
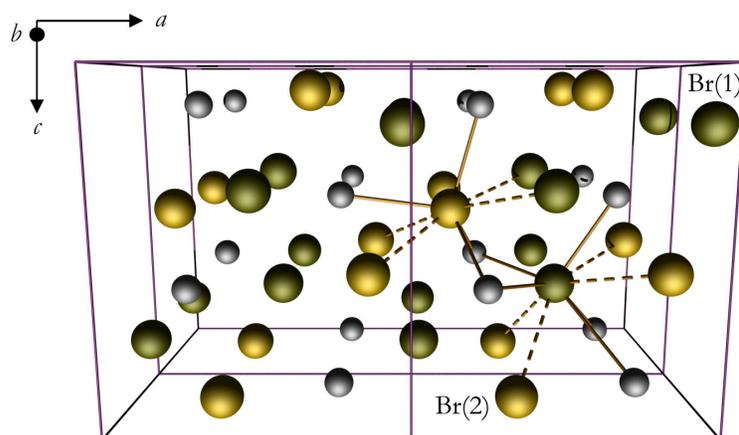
Figure 3.10 POV-ray rendering of the $BaBr_2$ quadruple unit cell, viewed nearly along b (rotated 10° counterclockwise about the positive a axis). The barium ions are denoted in grey. The following colour and labeling scheme is used to distinguish the two inequivalent bromides: Br(1) = green; Br(2) = gold. Solid lines denote ions within the sum of the Ba and Br vdW radii (i.e., $r_{Ba-Br} < 4.51$ Å), while dotted lines denote homoatomic contacts slightly beyond twice the Br vdW radius (i.e., slightly > 3.66 Å).

While the SSNMR observation of two sites agrees with all prior data, the ratio between the ^{79}Br C_Qs determined using NMR, and the ^{79}Br C_Qs (calculated using **(3.1)**) from NQR are in disagreement (Table 3.1). For example, for the Br(1) site in $BaBr_2$ (site label as a result of GIPAW DFT computations, *vide infra*), $C_Q(^{79}Br) = 28.1(4)$ MHz and $\eta_Q = 0.17(2)$; hence $v_Q(^{79}Br,$ Br(1)) = 14.1 MHz, in good agreement with one of the ^{79}Br NQR signals. Using the same procedure for Br(2), $v_Q(^{79}Br) = 16.3$ MHz, in poor agreement with the NQR data. While the temperature variation in $v_Q(^{79}Br)$ for Br(2), measured with NQR experiments, is significant (−20 kHz/K over the range $T = 77$ to 209 K), this alone cannot account for the discrepancies between the ^{79}Br SSNMR and NQR data. It is believed that the NQR datum is in error, as GIPAW DFT calculations do not support substantially different $^{79/81}Br$ C_Qs at the two Br sites in

BaBr$_2$, in agreement with the current SSNMR experimental results. After extensive searching for an additional broad [81]Br SSNMR signal at both 11.75 and 21.1 T, it was concluded that only two magnetically unique Br sites were present. According to the authors of the NQR study in ref. 122, the "signal-to-noise ratio with maximum sensitivity of the instrument did not exceed 1.5 – 2". Hence, it is entirely possible that the two sites were not resolved via [79]Br NQR, and that the larger ν_Q signal was due to an impurity. As well, a [35]Cl SSNMR study on the isomorphic BaCl$_2$ system resolved two sites with similar $C_Q(^{35}\text{Cl})$ values.[124] If one considers the $|C_Q(^{81}\text{Br})/C_Q(^{35}\text{Cl})|$ value for both sites using the approach outlined earlier for CaBr$_2$, it is calculated (see Appendix A, Table A.4, for the parameters used) as 7.09 for both sites. Experimentally, $|C_Q(^{81}\text{Br})/C_Q(^{35}\text{Cl})|$ = 6.71 and 6.89 for sites 1 and 2, respectively, which is in good agreement, especially when noting that chlorine CSA was not considered in the [35]Cl SSNMR fits.[124] In addition, for both BaCl$_2$ and BaBr$_2$, the site with the larger halogen C_Q value is associated with a much greater δ_{iso}. Likewise, when comparing measured halogen η_Q values, it is observed that within experimental error, the value for Br(1) agrees with that for 'Cl(1)' and the value for Br(2) agrees with that for 'Cl(2)', as expected by symmetry.

3.3.1.2 Stable Hydrates of the Alkaline Earth Metal Bromides

Using a series of alkaline earth metal chloride hydrates, it has been shown that [35/37]Cl SSNMR spectroscopy is sensitive to the degree of sample hydration.[57] Presently, the results of [79/81]Br SSNMR experiments at multiple applied fields on BaBr$_2\cdot$2H$_2$O, MgBr$_2\cdot$6H$_2$O, and SrBr$_2\cdot$6H$_2$O, are discussed. The data are summarized in Tables 3.3 and 3.4.

Table 3.3 Experimental $^{79/81}$Br EFG tensor parameters: alkaline earth metal bromide hydrates[a]

compound	site label	$\lvert C_Q(^{81}Br)\rvert$ / MHz	$\lvert C_Q(^{79}Br)\rvert$ / MHz	η_Q	$v_Q(^{79}Br)$[b] / MHz
MgBr$_2$·6H$_2$O	—	19.0(2)	22.7(2)	0.23(3)	—
SrBr$_2$·6H$_2$O	—	27.7(3)	33.2(3)	< 0.01	—
BaBr$_2$·2H$_2$O	—	7.32(3)	8.74(4)	0.76(2)	4.58(5)
CaBr$_2$·xH$_2$O	Br(1)	—	—	—	—
	Br(2)	12.8(4)	15.4(5)	0.32(4)	—
	Br(3)	23.0(4)	27.6(5)	0.25(3)	—

[a] Error bounds are in parentheses. Parameter definitions are in Section 2.3.3.2.
[b] From literature.[122] The measurement occurred at T = 209 K.

Table 3.4 Experimental bromine CS tensor parameters: alkaline earth metal bromide hydrates[a]

compound	site label	δ_{iso}[b] / ppm	Ω / ppm	κ	α, β, γ / °
MgBr$_2$·6H$_2$O	—	57(7)	50(20)	0.7(3)	170(10), 57(10), 180[c]
SrBr$_2$·6H$_2$O	—	95(15)	70(30)	-1[d]	210[c], 90(20), 180(10)
BaBr$_2$·2H$_2$O	—	218.2(1.0)	86(5)	$-0.20(15)$	70(5), 95(8), 253(5)
CaBr$_2$·xH$_2$O	Br(1)	$-55(4)$	—	—	—
	Br(2)	205(15)	—	—	—
	Br(3)	170(15)	—	—	—

[a] Includes Euler angle values. Error bounds are in parentheses. Parameter definitions are in Sections 2.3.2.4, 2.3.3.1, and 2.3.3.3.
[b] With respect to solid KBr (δ_{iso} = 0.00 ppm).
[c] Simulated NMR line shape is insensitive to parameter variation; the value is assigned based on computational results.
[d] Assumed based on crystallographic site symmetry.

3.3.1.2.1 *BaBr$_2$·2H$_2$O: An Example of ^{79}Br MAS NMR*

Static $^{79/81}$Br{^{1}H} SSNMR experiments at B_0 = 11.75 and 21.1 T reveal relatively narrow (~100 kHz) bromine line shapes (Figures 3.11 and 3.12). The relatively small QI ($C_Q(^{81}Br)$ = 7.32(3) MHz) allowed for $^{79/81}$Br MAS NMR experiments to be performed at B_0 = 21.1 T (Figure 3.13), which represents the first report of ^{79}Br MAS SSNMR of a spectrum broadened by a second-order QI. As the CT centreband under MAS conditions depends only upon δ_{iso},

C_Q, and η_Q, the measurement errors associated with the $^{79/81}$Br SSNMR parameters are greatly reduced relative to the anhydrous samples.
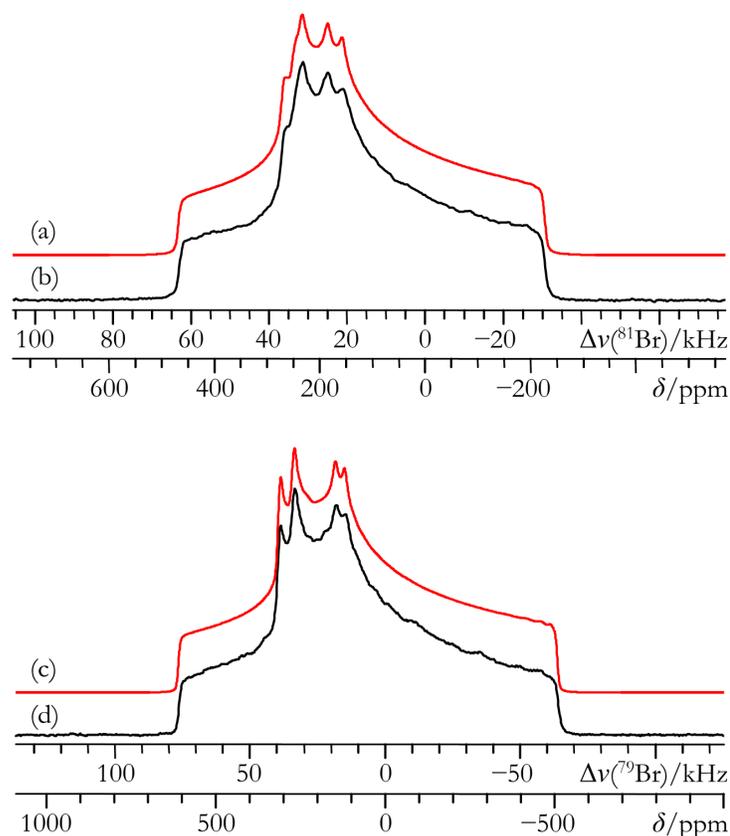
Figure 3.11 Best-fit analytical simulations (a, c), and experimental static Solomon echo $^{79/81}$Br$\{^1$H$\}$ SSNMR spectra of powdered BaBr$_2\cdot$2H$_2$O acquired at $B_0 = 11.75$ T (b, d).

Single-crystal XRD[125,126] and neutron diffraction[127] studies confirm that BaBr$_2\cdot$2H$_2$O belongs to the monoclinic $C2/c$ space group. The bromide ions are at 1 lattice positions, which place no symmetry restrictions on the $\ddot{V}$ and $\ddot{\sigma}$ tensor parameters. The closest three contacts to each bromide ion are hydrogen atoms, two of which are located at a distance of ca. 2.44 Å, and one at ca. 2.96 Å. Single-crystal ^{1}H NMR studies on this system have focused on the location and dynamics of the H atoms,[128-131] and IR spectroscopy has been used to establish the presence of H$_2$O librational motions at room temperature.[132]
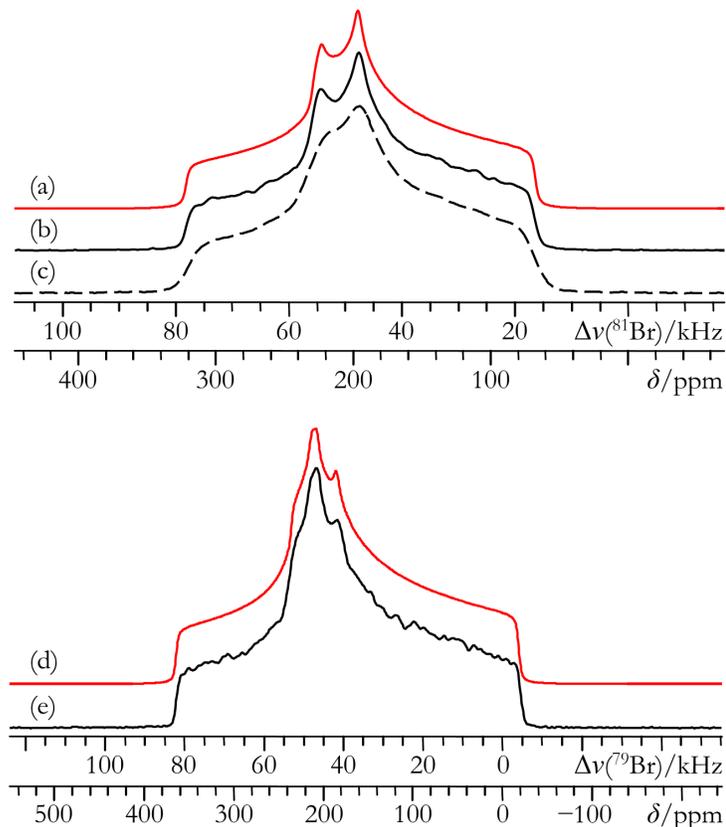
Figure 3.12 Best-fit analytical simulations (a, d), and experimental static Solomon echo $^{79/81}$Br{^{1}H} SSNMR spectra of powdered BaBr$_2$·2H$_2$O acquired at B_0 = 21.1 T (b, e). The spectrum in (c) was acquired under identical conditions as (b), except that ^{1}H decoupling was not applied.

The difference in $C_Q(^{79/81}$Br) values between the hydrated and anhydrous forms of BaBr$_2$ shows that $^{79/81}$Br SSNMR spectroscopy is a very sensitive method to determine the hydration state of this system. As well, these spectra may be acquired in a reasonable amount of time: a high quality static ^{81}Br{^{1}H} SSNMR spectrum of the hydrate can be obtained in under 15 minutes at 11.75 T. The bromine $\ddot{\sigma}$ and $\ddot{V}$ tensors in the dihydrate are nonaxial (η_Q = 0.76(2); κ = −0.20(0.15)) and their PASs are noncoincident. As shown in Figure 3.12c, due to (i) the proximity of the ^{1}H and $^{79/81}$Br nuclei and (ii) the relatively narrow signal, ^{1}H decoupling is essential to observe the fine structure in these $^{79/81}$Br SSNMR line shapes. A ^{79}Br NQR study at

$T = 209$ K measured $v_Q(^{79}Br) = 4.58(0.05)$ MHz.[122] Using the NMR-based $C_Q(^{79}Br)$ and η_Q values and applying **(3.1)**, it is found that $v_Q(^{79}Br) = 4.77$ MHz, which is in fair agreement with the NQR finding, especially when noting that the librational motions of the water molecules are not equivalent at 209 K and room temperature.
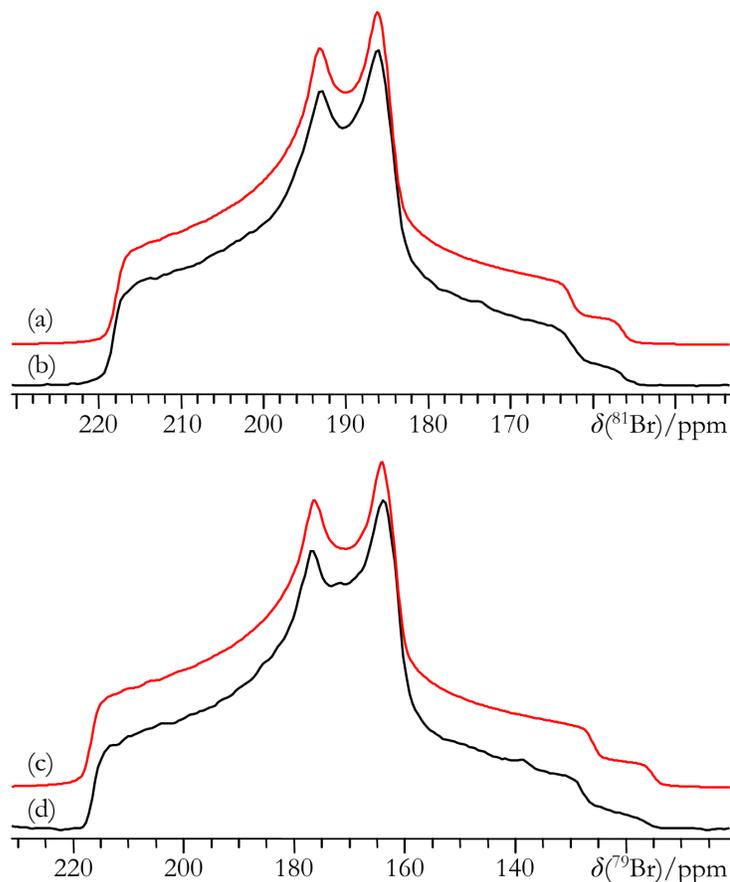

Figure 3.13 Best-fit analytical simulations (a, c), and experimental MAS Solomon echo $^{79/81}Br\{^1H\}$ SSNMR spectra of powdered $BaBr_2 \cdot 2H_2O$ acquired at $B_0 = 21.1$ T with (b) $v_{MAS} = 20.000$ kHz; (d) $v_{MAS} = 26.318$ kHz.

In addition to the significant change in the QI at the Br nuclei, the bromine chemical shift of $BaBr_2 \cdot 2H_2O$ is reduced relative to either Br site in $BaBr_2$. In fact, it is more shielded than any anhydrous bromide site by at least 60 ppm. This decrease in chemical shift upon hydration is consistent with the trend observed in the $^{35/37}Cl$ SSNMR spectra of the analogous

alkaline earth metal chloride systems.[55,57,124] The decreased shift upon hydration is also corroborated by GIPAW DFT computations (*vide infra*). Hence, it appears that the bromine δ_{iso} is also a reliable indicator of the presence of hydration for alkaline earth metal bromide systems.

3.3.1.2.2 *MgBr$_2$·6H$_2$O and SrBr$_2$·6H$_2$O: On the Relationship between Bromine NMR Parameters and Hydration State*

Static $^{79/81}$Br SSNMR spectra for both these compounds were collected at B_0 = 11.75 and 21.1 T. The spectra exhibit similar line shape features as the systems discussed above (Figures 3.14, 3.15, and Appendix A, Figure A.5) and were precisely fit (Tables 3.3 and 3.4). The space group ($C2/m$), unit cell parameters, and atomic positions of MgBr$_2$·6H$_2$O were initially reported in 1934,[97,133] and a precise determination of the unit cell was later carried out.[98] There is one unique bromine crystallographic site, which possesses m symmetry. Neutron diffraction data do not exist for this compound; hence, the H positions are unknown. However, they should be very similar to the H positions in the isomorphic MgCl$_2$·6H$_2$O compound, the structure of which was determined using neutron diffraction.[134] There are no prior $^{79/81}$Br NQR data for MgBr$_2$·6H$_2$O, but ^{25}Mg NQR[135] and ^{1}H SSNMR[136] measurements have been reported.

As with BaBr$_2$·2H$_2$O, MgBr$_2$·6H$_2$O is observed to have a relatively small, nonaxial $\ddot{V}$ tensor ($C_Q(^{81}\text{Br})$ = 19.0(2) MHz; η_Q = 0.23(3)) and is significantly more shielded (δ_{iso} = 57(7) ppm) than its anhydrous form (see Chapter 6).[137] The observed bromine NMR line shapes, especially the ^{81}Br SSNMR signal acquired at 21.1 T, clearly exhibit noncoincident $\ddot{\sigma}$ and $\ddot{V}$ tensors (Figure 3.14). The feature in the low frequency portion of Figures 3.14b, 3.14c, and 3.14e indicates that β is not equal to 0° or 90° (β = 57(10)°), while variation of α or γ does not significantly alter the simulated line shapes. All findings are consistent with the known Br crystal site symmetry and are in fair agreement with GIPAW DFT calculations (*vide infra*).

Finally, the calculated ratio $|C_Q(^{81}Br)/C_Q(^{35}Cl)|$ for the $MgBr_2 \cdot 6H_2O$ and $MgCl_2 \cdot 6H_2O$ isomorphs is found to be 6.73 (see Appendix A, Table A.4, for the parameters used), in reasonable agreement with the experimentally observed ratio of 6.29.[57]
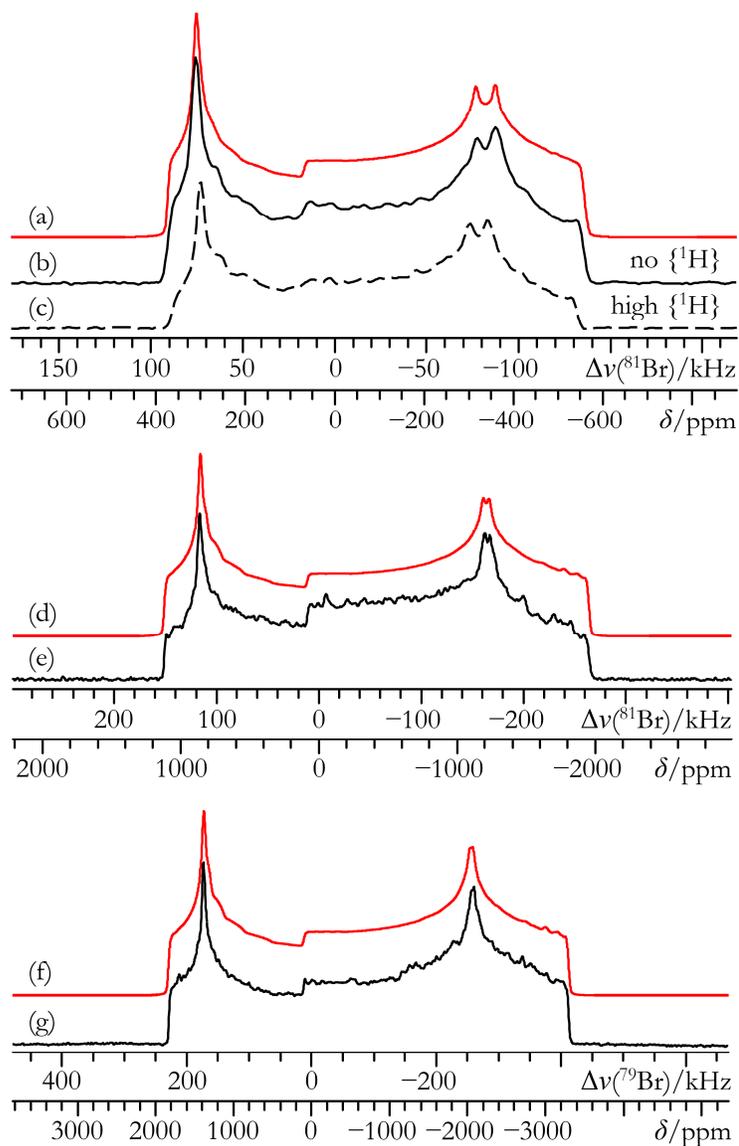
Figure 3.14 Best-fit analytical simulations (a, d, f), experimental static Solomon echo (b, c, e), and experimental static VOCS Solomon echo (g) $^{79/81}Br\{^1H\}$ SSNMR spectra of powdered $MgBr_2 \cdot 6H_2O$ acquired at $B_0 = 21.1$ T (b, c), and 11.75 T (e, g). Low power ^1H decoupling ($\nu_1(^1H) \approx 40$ kHz) is applied to acquire (e) and (g) and does not lead to significant line shape augmentations, while high power ^1H decoupling ($\nu_1(^1H) \approx 100$ kHz) causes sample heating, which alters the QI at the Br nuclei in (c).
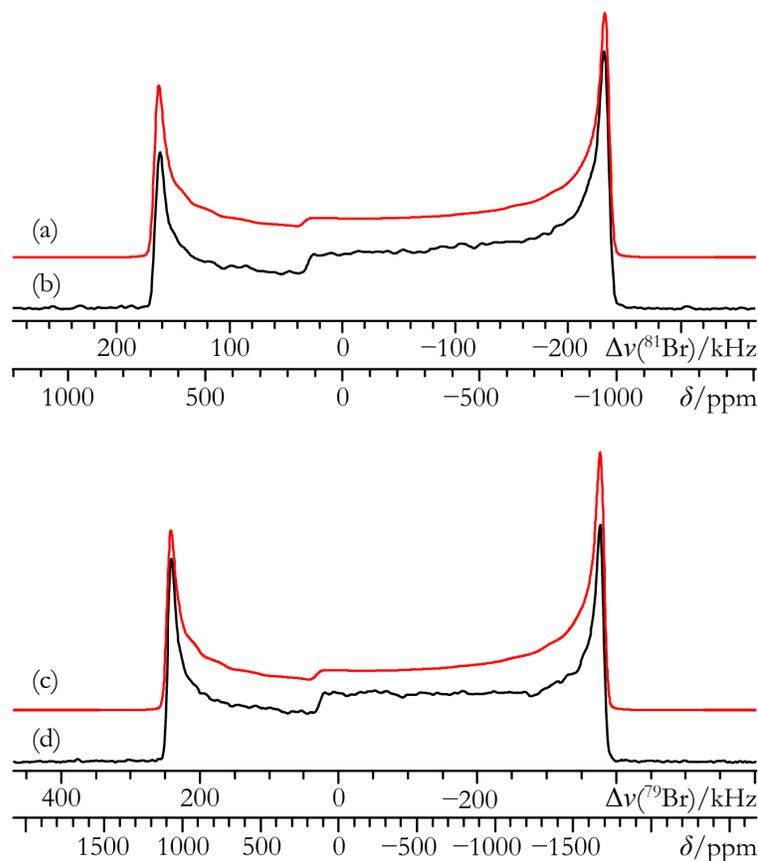
Figure 3.15 Best-fit analytical simulations (a, c), experimental static Solomon echo (b), and experimental static VOCS Solomon echo (d) $^{79/81}$Br SSNMR spectra of powdered SrBr$_2$·6H$_2$O acquired at B_0 = 21.1 T. High power ^{1}H decoupling (v_1(^{1}H) ≈ 100 kHz) does not alter the $^{79/81}$Br SSNMR signals significantly (i.e., within experimental error).

The crystal structure of SrBr$_2$·6H$_2$O has been solved using XRD data,[99,138] and belongs to the same space group (P321) as SrCl$_2$·6H$_2$O, CaCl$_2$·6H$_2$O, and CaBr$_2$·6H$_2$O.[100,101] In all these systems, the metal environment is a distorted octahedron of the form [M(H$_2$O)$_6$]$^{2+}$, while there is one magnetically unique halide located on a C_3 axis. Bromine-79/81 NQR data are not available for SrBr$_2$·6H$_2$O. According to ^{1}H SSNMR, the H$_2$O molecules in SrBr$_2$·6H$_2$O are thought to be stationary at room temperature.[139] Presently, the static Solomon echo $^{79/81}$Br SSNMR spectra at 11.75 and 21.1 T were fit using axially symmetric (i.e., η_Q < 0.01; κ = −1.0) EFG and CS tensor

parameters (Figure 3.15 and Appendix A, Figure A.5). The observation of axially symmetric tensors is fully consistent with the accepted crystal structure. Relative to the magnesium bromide hydrate, the bromine QI for $SrBr_2 \cdot 6H_2O$ is larger ($C_Q(^{81}Br)$ = 27.7(3) MHz), but once again for a hydrate, δ_{iso} is much lower than for the corresponding anhydrous compound (δ_{iso} = 95(15) ppm). The bromine CSA in this compound is relatively small (Ω = 70(30) ppm), and the simulated line shape is particularly sensitive to the β value. The ratio $|C_Q(^{81}Br)/C_Q(^{35}Cl)|$ for the $SrCl_2 \cdot 6H_2O$ and $SrBr_2 \cdot 6H_2O$ isomorphs was calculated to be 6.55 (using the parameters in Appendix A, Table A.4), in fair agreement with the experimentally observed ratio of 7.08.[57]

3.3.1.3 CaBr₂·xH₂O: Characterization of a Mixture of Unknown Composition

Calcium bromide is hygroscopic and hence it is commercially available as a 'hydrated' mixture of unknown composition, $CaBr_2 \cdot xH_2O$, where $x \approx 1$. A VOCS Solomon echo ^{81}Br SSNMR spectrum of the mixture, acquired at B_0 = 21.1 T, (Figure 3.16) resolves four components. The broadest signal is fit to ^{81}Br SSNMR parameters characteristic of $CaBr_2$ (i.e., $C_Q(^{81}Br)$ = 62.7(5) MHz). A VOCS QCPMG ^{81}Br SSNMR experiment performed on this mixture at B_0 = 11.75 T also resolves this broad signal (see Appendix A, Figure A.6). The remaining three sites are observed in Solomon echo ^{81}Br SSNMR spectra acquired at 21.1 T and 11.75 T (Figure 3.16b,e), as well as the ^{79}Br SSNMR spectra acquired at both fields (see Appendix A, Figure A.7). The three narrow signals were deconvoluted and fit using the parameters in Tables 3.3 and 3.4.

Due to its bromine chemical shift, and lack of significant QI and CSA, site 1 is assigned to NaBr.[4] This assignment is further supported by the observation of a narrow ^{23}Na SSNMR signal, which was serendipitously measured while acquiring the QCPMG ^{81}Br SSNMR spectrum of the mixture at 11.75 T (Appendix A, Figure A.6), since the Larmor frequencies of ^{23}Na and

[81]Br are similar to one another (% difference = 2.1 %). The remaining two sites are due to CaBr$_2$ hydrates. By observing the δ_{iso} values, it is suspected that the hexahydrate form[101] is not present. This is due to the observations made earlier in this Chapter, where the values of δ_{iso} for the hexahydrates are all below 100 ppm. Likewise, GIPAW DFT computations using the known CaBr$_2$·6H$_2$O crystal structure[101] predict an axial QI and low chemical shift (Tables 3.7 and 3.8), which does not agree with any of the experimentally observed NMR parameters. Hence, the presence of CaBr$_2$·6H$_2$O in this mixture is very unlikely.
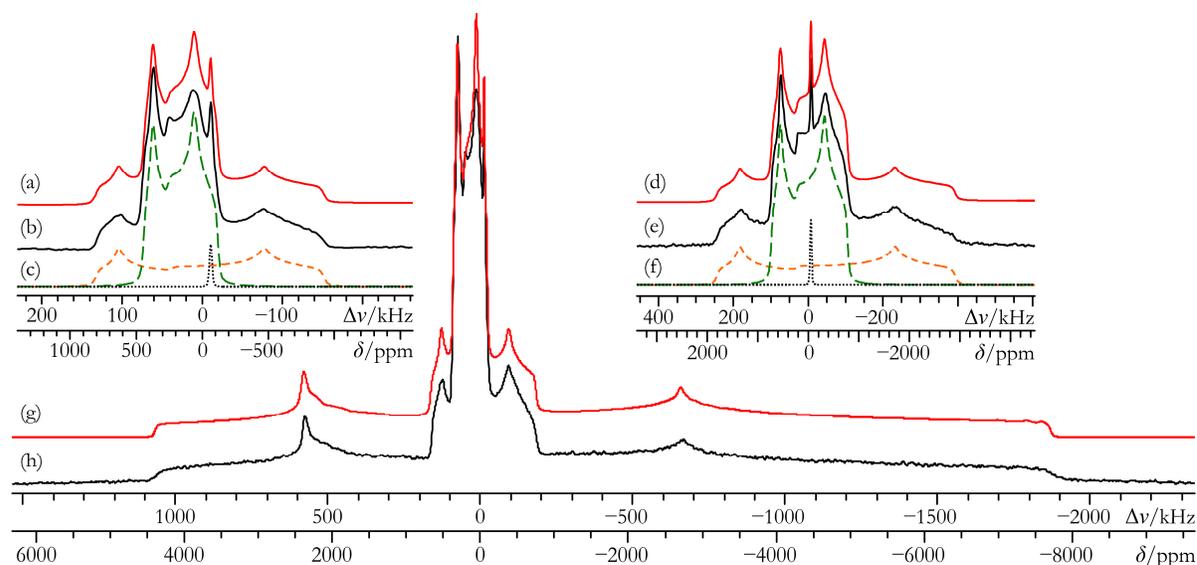
Figure 3.16 Best-fit analytical simulations (a, g), and experimental static VOCS Solomon echo [81]Br SSNMR spectra of powdered CaBr$_2$·xH$_2$O acquired at B_0 = 21.1 T (b, h). Best-fit analytical simulation (d) and experimental static VOCS Solomon echo [81]Br SSNMR spectrum of the three central signals acquired at B_0 = 11.75 T (e). In (c) and (f), a deconvolution of the central three sites is provided.

In addition to the hexahydrate, a detailed study by Paulik *et al.* established the existence of mono-, di-, and tetrahydrates of CaBr$_2$.[140] According to the current literature, the crystal structures for these hydrates are not known. Using [79]Br NQR, Smirnov and Volkov reported that ν_Q([79]Br) = 19.09 MHz at T = 300 K for CaBr$_2$·H$_2$O.[103] Using the current [79]Br SSNMR

parameters and **(3.1)**, $v_Q(^{79}Br)$ = 7.88 and 14.1 MHz for sites 2 and 3, respectively. Both these values are in significant disagreement with the accepted value for $CaBr_2 \cdot H_2O$, and hence the presence of the monohydrate is unlikely. The remaining known hydrates of $CaBr_2$, namely $CaBr_2 \cdot 2H_2O$ and $CaBr_2 \cdot 4H_2O$, are therefore the likely additional components in the mixture.

Integrated intensity measurements of the $^{79/81}Br$ SSNMR signals at two fields establish that 61(2) % of the bromine signal intensity is due to $CaBr_2$, 24(2) % is due to site 2, and 15(2) % is due to site 3. Incidentally, the integrated intensity of the NaBr signal is < 1 %, hinting that $^{79/81}Br$ SSNMR experiments are a sensitive method for the detection of cubic bromide impurities. If site 2 is assigned to the dihydrate and site 3 to the tetrahydrate, then $x \approx 1.08$, which is in fair agreement with the value listed by the manufacturer (i.e., $x \approx 1$). If the opposite assignment is made, then $x \approx 1.26$, which is in relatively poor agreement. Similarly, it has been established in the above sections, and for the corresponding chlorides,[57] that a negative correlation exists between $\delta_{iso}(X, X = Cl, Br)$ and the degree of hydration (i.e., a decreased $\delta_{iso}(X)$ is observed with increased hydration). Thus, the assignment of $CaBr_2 \cdot 2H_2O$ to the site with a greater δ_{iso} value is consistent with this correlation.

3.3.2 GIPAW DFT Quantum Chemical Computations

To complement the experimental $^{79/81}Br$ SSNMR observations, all pure systems were subjected to GIPAW DFT quantum chemical calculations, the results of which are presented in Tables 3.5 to 3.8. Norm-conserving[141] and 'ultrasoft' pseudopotential (usp)[88,142] GIPAW DFT methods[85] have been used to calculate $\ddot{\sigma}$ tensors in a variety of systems for several NMR-active nuclei.[86,143-146] For the calculation of $\ddot{V}$, modified PAW DFT methods[147,148] have been applied to oxygen-containing systems such as SiO_2 polymorphs,[86] sodium silicates,[149] metal oxides, and

aluminosilicates.[150] Recent studies employing the GIPAW DFT method include aluminum-containing oxides,[151] inorganic calcium materials,[152,153] alkaline earth metal chlorides,[57] and amino acids.[51] The first reported GIPAW DFT calculations of $^{79/81}$Br NMR parameters were used as part of the structural refinement of $MgBr_2$ (see Chapter 6).[137] This prior account demonstrated that the $\ddot{V}$ tensor at the bromide could be accurately calculated in $MgBr_2$, and that the bromine EFG was extremely sensitive to structure.

Table 3.5 GIPAW DFT $^{79/81}$Br EFG tensor parameters: alkaline earth metal bromides[a]

compound	functional	site label	$C_Q(^{81}Br)$[b] / MHz	$C_Q(^{79}Br)$ / MHz	η_Q	$\nu_Q(^{79}Br)$ / MHz
$CaBr_2$	PBE	—	−69.15	−82.60	0.496	42.96
	PW91	—	−69.53	−83.07	0.498	43.21
$SrBr_2$	PBE	Br(1)	−9.80	−11.71	0.000	5.85
		Br(2)	−17.72	−21.17	0.000	10.58
		Br(3)	−27.16	−32.45	0.827	17.98
		Br(4)	−60.43	−72.20	0.297	36.62
	PW91	Br(1)	−9.83	−11.74	0.000	5.87
		Br(2)	−17.82	−21.29	0.000	10.64
		Br(3)	−27.22	−32.52	0.837	18.06
		Br(4)	−60.86	−72.71	0.298	36.89
$BaBr_2$	PBE	Br(1)	−20.49	−24.48	0.093	12.26
		Br(2)	31.52	37.65	0.082	18.85
	PW91	Br(1)	−20.60	−24.61	0.098	12.32
		Br(2)	31.71	37.88	0.082	18.96

[a] Parameter definitions are in Section 2.3.3.2. $CaBr_2$ calculations used E_{cut} = 800 eV and a 5 × 5 × 8 k-point grid; $SrBr_2$ calculations used E_{cut} = 500 eV and a 3 × 3 × 5 k-point grid; $BaBr_2$ calculations used E_{cut} = 600 eV and a 3 × 5 × 3 k-point grid. For further details, see Appendix A, Table A.5.
[b] To convert $V_{33}(^{81}Br)$ and $V_{33}(^{79}Br)$ into frequency units, conversion factors of 61.56077 MHz/a.u. and 73.54397 MHz/a.u. were used, and the unit EFG is 9.71736166 × 10²¹ J C⁻¹ m⁻².

Table 3.6 GIPAW DFT bromine CS tensor parameters: alkaline earth metal bromides[a]

compound	functional	site label	δ_{iso} / ppm	Ω / ppm	κ	α, β, γ / °
CaBr$_2$	PBE	—	390.4	351.1	0.06	270.0, 89.5, 180.0
	PW91	—	398.4	354.1	0.07	270.0, 89.5, 180.0
SrBr$_2$	PBE	Br(1)	487.3	58.0	−1.00	90.0, 90.0, 180.0
		Br(2)	462.7	110.2	−1.00	90.0, 90.0, 180.0
		Br(3)	366.4	132.6	0.11	43.3, 88.4, 231.9
		Br(4)	352.4	182.5	−0.19	242.4, 72.5, 214.5
	PW91	Br(1)	486.0	56.7	−1.00	90.0, 90.0, 180.0
		Br(2)	460.7	107.5	−1.00	90.0, 90.0, 180.0
		Br(3)	364.2	128.8	0.13	44.3, 88.3, 233.3
		Br(4)	349.1	181.0	−0.18	242.4, 72.5, 213.8
BaBr$_2$	PBE	Br(1)	333.3	252.3	−0.48	0.0, 49.6, 180.0
		Br(2)	532.8	208.3	0.18	180.0, 19.2, 180.0
	PW91	Br(1)	336.3	253.0	−0.47	0.0, 49.6, 180.0
		Br(2)	537.4	209.3	0.19	180.0, 19.4, 180.0

[a] Includes Euler angle values. Parameter definitions are in Sections 2.3.2.4, 2.3.3.1, and 2.3.3.3. Selected calculation details are given in Table 3.5. For further details, see Appendix A, Table A.6.

Table 3.7 GIPAW DFT $^{79/81}$Br EFG tensor parameters: alkaline earth metal bromide hydrates[a]

compound	functional	model label	C_Q(^{81}Br) / MHz	C_Q(^{79}Br) / MHz	η_Q	ν_Q(^{79}Br) / MHz
MgBr$_2$·6H$_2$O	PBE	A	26.37	31.50	0.014	15.75
	PW91	A	26.02	31.09	0.018	15.54
	PBE	B	25.68	30.68	0.137	15.54
	PW91	B	25.34	30.27	0.133	15.18
CaBr$_2$·6H$_2$O	PBE	—	−34.44	−41.14	0.000	20.57
	PW91	—	−34.38	−41.07	0.000	20.53
SrBr$_2$·6H$_2$O	PBE	A	−18.42	−22.00	0.000	11.00
	PW91	A	−18.39	−21.97	0.000	10.99
	PBE	B	−40.97	−48.94	0.000	24.47
	PW91	B	−41.01	−48.99	0.000	24.50
BaBr$_2$·2H$_2$O	PBE	—	−8.73	−10.43	0.395	5.35
	PW91	—	−9.09	−10.86	0.411	5.58

[a] MgBr$_2$·6H$_2$O calculations used E_{cut} = 750 eV and a 2 × 3 × 4 k-point grid; CaBr$_2$·6H$_2$O calculations used E_{cut} = 610 eV and a 4 × 4 × 6 k-point grid; SrBr$_2$·6H$_2$O calculations used E_{cut} = 800 eV and a 4 × 4 × 6 k-point grid; BaBr$_2$·2H$_2$O calculations used E_{cut} = 800 eV and a 3 × 3 × 3 k-point grid. See also footnote b of Table 3.5. For further details, see Appendix A, Table A.7.

Table 3.8 GIPAW DFT bromine CS tensor parameters: alkaline earth metal bromide hydrates[a]

compound	functional	model label	δ_{iso} / ppm	Ω / ppm	κ	α, β, γ / °
MgBr$_2$·6H$_2$O	PBE	A	3.0	59.4	0.46	0.0, 58.1, 0.0
	PW91	A	3.7	60.2	0.44	0.0, 57.9, 0.0
	PBE	B	8.6	64.0	0.31	270.0, 55.2, 180.0
	PW91	B	9.4	64.8	0.29	270.0, 55.1, 180.0
CaBr$_2$·6H$_2$O	PBE	—	62.1	41.0	−1.00	247.2, 89.8, 180.2
	PW91	—	62.0	40.8	−1.00	223.1, 89.9, 180.3
SrBr$_2$·6H$_2$O	PBE	A	68.2	31.5	−1.00	224.3, 89.9, 180.4
	PW91	A	67.2	31.2	−1.00	226.6, 89.9, 180.4
	PBE	B	41.1	80.7	−1.00	210.9, 90.0, 180.2
	PW91	B	40.3	80.6	−1.00	212.2, 90.0, 180.2
BaBr$_2$·2H$_2$O	PBE	—	199.5	94.1	−0.24	61.0, 84.1, 240.7
	PW91	—	202.5	94.4	−0.23	64.0, 84.5, 240.6

[a] Includes Euler angle values. Parameter definitions are in Sections 2.3.2.4, 2.3.3.1, and 2.3.3.3. Selected calculation details are given in Table 3.7. For further details, see Appendix A, Table A.8.

3.3.2.1 Calculation of Bromine $\vec{V}$ and $\ddot{\sigma}$ Tensor Magnitudes and Symmetries

The agreement between experimental and GIPAW DFT computed [79/81]Br NMR parameters is very good for several parameters (Figure 3.17). Relative to the experimental values, computed C_Q([81]Br) values are slightly higher in most cases, while the computed Ω values are higher in all cases. Only the computed and experimental Ω values for BaBr$_2$ are in disagreement with one another, after considering the errors associated with the measurement of Ω. The consistent overestimation of computed span values suggests the possibility of nonnegligible relativistic contributions to bromine MS, as is generally observed in diatomic systems.[154] Rather good agreement is also seen between experimental and computed δ_{iso} and η_Q values. With respect to the experimental values of δ_{iso}, all computed data for the anhydrous compounds are overestimated, while all computed values for the hydrates are underestimated.

For all compounds except BaBr$_2$·2H$_2$O, the agreement between the calculated and experimental η_Q values is very good.
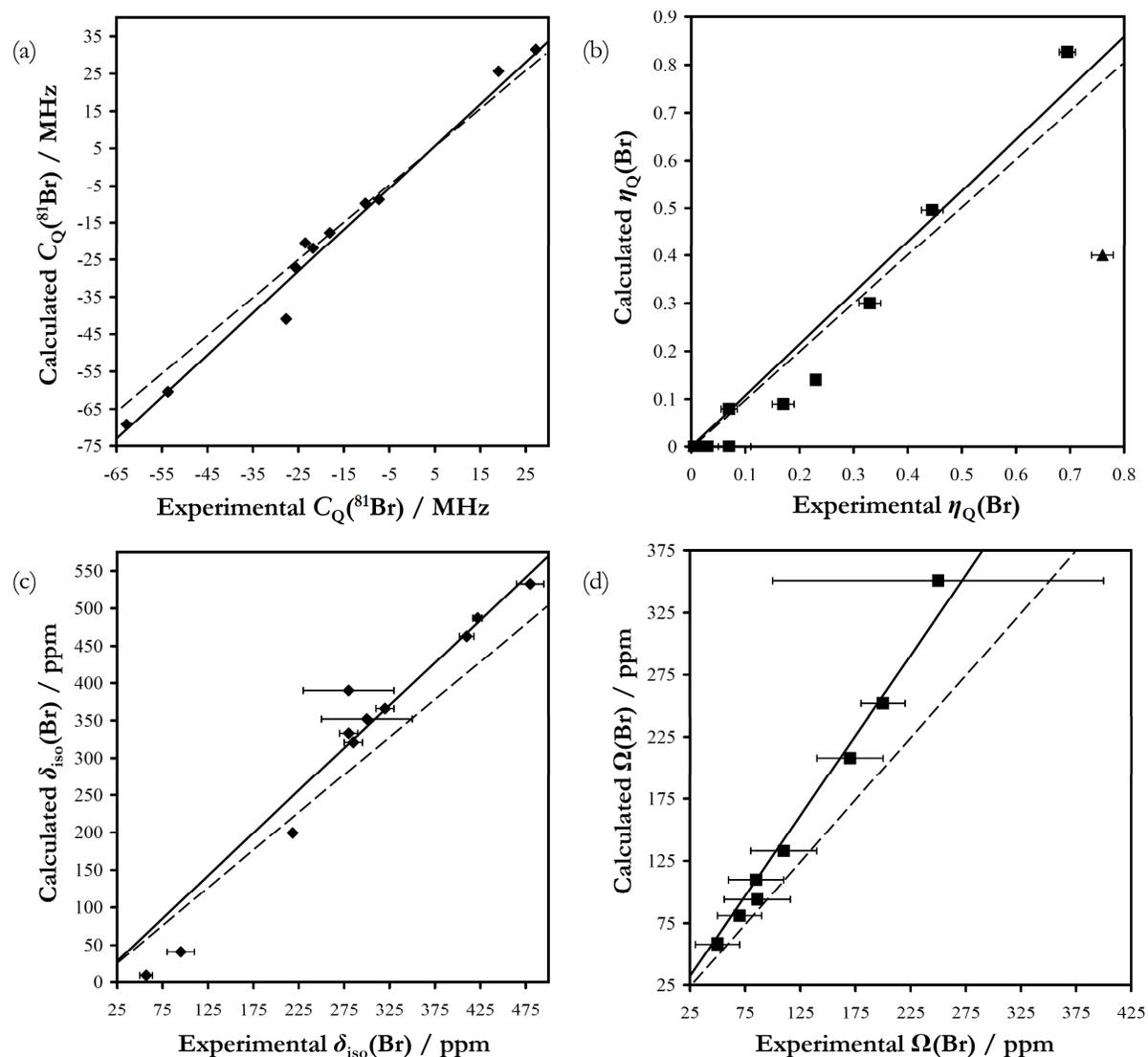
Figure 3.17 Plots of GIPAW DFT computed versus experimental values (a) for C_Q(^{81}Br); (b) for η_Q; (c) for δ_{iso}; (d) for Ω. Experimental data are from Tables 3.1 to 3.4, while the calculated data are from Tables 3.5 to 3.8. All computed values are from PBE XC functional calculations. Values for MgBr$_2$ are included, from Chapter 6. For MgBr$_2$·6H$_2$O and SrBr$_2$·6H$_2$O, the computed values used model B. Solid lines are of best linear fit, while dashed lines denote an ideal fit (i.e., $y = x$): C_Q(^{81}Br,calc) = 1.1235(C_Q(^{81}Br,expt)), R^2 = 0.982, rmsd = 5.55 MHz; η_Q(calc) = 1.0737(η_Q(expt)), R^2 = 0.946, rmsd = 0.0649; δ_{iso}(calc) = 1.1395(δ_{iso}(expt)), R^2 = 0.946, rmsd = 57.7 ppm; Ω(calc) = 1.2921(Ω(expt)), R^2 = 0.981, rmsd = 42.2 ppm. In (b), the line of best fit and rmsd omit the data point for BaBr$_2$·2H$_2$O (▲).

Where experimental Euler angles were measured, agreement between computation and experiment is excellent: for all the anhydrous compounds and $SrBr_2 \cdot 6H_2O$, the differences are within experimental error, while for $BaBr_2 \cdot 2H_2O$, the differences lie just outside the experimental error bounds. The slightly increased discrepancy between experimental and computed NMR parameters for $BaBr_2 \cdot 2H_2O$ could be due to the librational motions of the H_2O molecules.[155] Only the α value computed for $MgBr_2 \cdot 6H_2O$ cannot be reconciled with experiment, but it should be noted that the XRD data used to solve for the structure of this compound carried large measurement errors.[97] An additional structural model can be proposed that remains within the XRD measurement errors, while resulting in somewhat better agreement between the GIPAW DFT computed and experimental bromine SSNMR parameters, most notably the clearly nonzero experimental value for η_Q (Table 3.7).

The reported structure for $SrBr_2 \cdot 6H_2O$[99] should be isomorphic to $SrCl_2 \cdot 6H_2O$; however, the reported structure places Br atoms at $(a, b, -c)$, while (a, b, c) would place them in positions isomorphic to $SrCl_2 \cdot 6H_2O$ (see Section 3.2.3 for details). Hence, computations using both sets of Br atomic values, optimizing the H positions for each prior to NMR parameter computations, were carried out. Although inconclusive, NMR parameter agreement is slightly better for the model which places the bromide ions in positions isomorphic to $SrCl_2 \cdot 6H_2O$ (i.e., model B). This is primarily due to the drastic increase in the computed Ω value, as one goes from model A to model B.

Finally, due to the high level of correlation between calculation and experiment, and as their crystal structures are known, for $BaBr_2$ and $SrBr_2$ full assignments of the measured $^{79/81}Br$ SSNMR signals to specific crystallographic sites can be made (see Figures 3.6 and 3.10, and Table 3.1 for the labeling scheme used).

3.3.2.2 Calculated Bromine $\ddot{V}$ and $\ddot{\sigma}$ Absolute Tensor Orientations

The relative orientation of the $\ddot{V}$ and $\ddot{\sigma}$ tensor PASs may be measured in powdered samples and, under certain conditions, their absolute orientation may also be inferred.[57,156] Computational methods generally offer insight regarding the absolute orientations of these PASs. As noted in Section 3.3.1, it is the local symmetry at the nuclear site which restricts the relative orientation of the $\ddot{V}$ and $\ddot{\sigma}$ tensor frames. In all pure samples studied in this Chapter, evidence of noncoincident tensor frames was observed and quantified (Tables 3.2 and 3.4), and it was observed that $^{79/81}$Br SSNMR spectra are sensitive to the β value (i.e., the angular separation between the $\boldsymbol{\sigma}_{33}$ (or equivalently, $\boldsymbol{\delta}_{33}$) and V_{33} eigenvectors, see also Figure 2.12).

The local symmetry at the Br ions in $CaBr_2$ is m, with the mirror plane lying perpendicular to the c crystal axis. As expected, the computed $\ddot{V}$ and (symmetric) $\ddot{\sigma}$ eigenvectors at the Br are either parallel or perpendicular to this mirror plane (Figure 3.18a). The eigenvector associated with the direction of the smallest EFG (V_{11}) orients along c, directly towards a neighbouring bromide ion. As the EFG magnitude bears a $1/r^3$ dependence, and as the bromide-bromide distance along the c axis is greater (4.34 Å) than the corresponding distance parallel to the mirror plane (3.80 Å), the orientation of V_{11} is perhaps unsurprising. The $\ddot{V}$ tensor eigenvalues are similar for the eigenvectors parallel to the mirror plane (hence, the large computed η_Q value of 0.496). With regards to bromine MS in $CaBr_2$, there is no unique component ($\kappa \sim 0$) and $\boldsymbol{\sigma}_{22}$ orients perpendicular to the mirror plane. Halogen chemical shifts in ionic systems are largely determined by the degree of ion orbital overlap with nearest neighbours (NN) and next-nearest neighbours (NNN).[11] From the perspective of the Br ions in $CaBr_2$, the NN are the three calcium ions, each located at essentially the same distance (2.88 to 2.92 Å) and hence the contributions to magnetic shielding from the NN are likely to be rather

similar. Considering the NNN, several bromide ions are found between 3.80 to 4.34 Å. Due to this spread in distance, the shielding should be slightly greater in the direction of the shortest NNN internuclear distance. Indeed, $\boldsymbol{\sigma}_{33}$ is oriented very nearly along (i.e., < 10° away) the shortest Br-Br internuclear vector. There are no proximate bromide ions near the $\boldsymbol{\sigma}_{11}$ direction, where reduced ion orbital overlap is expected.
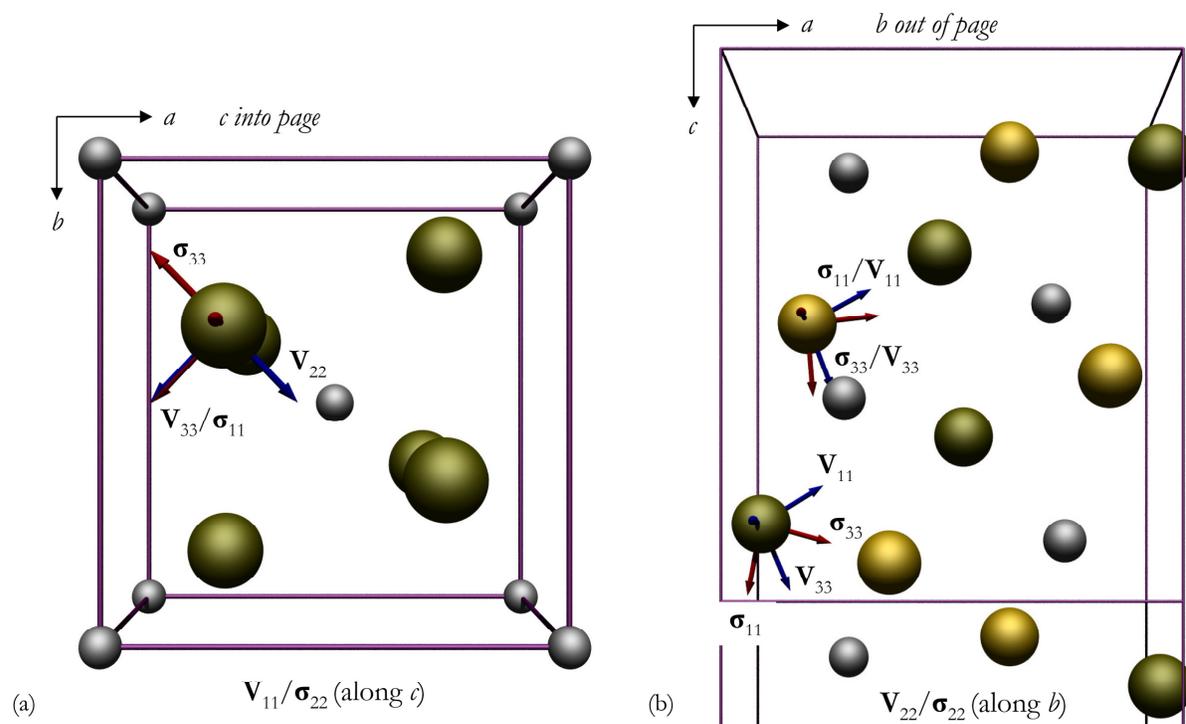
Figure 3.18 POV-Ray renderings of computed bromine $\ddot{V}$ ($\mathbf{V}_{ii}$, i = 1, 2, 3, in blue) and symmetric $\ddot{\sigma}$ ($\boldsymbol{\sigma}_{ii}$, red) tensor eigenvectors in the crystal frames of (a) CaBr$_2$ and (b) BaBr$_2$. For each, the metal cation is in grey, and the orientation is such that the mirror plane lies parallel to the page. CaBr$_2$: E_{cut} = 800 eV, and a 5 × 5 × 8 k-point grid; BaBr$_2$: E_{cut} = 600 eV, and a 3 × 5 × 3 k-point grid. Both employed the PBE XC functional. For (b), the unique bromine sites are Br(1) (green) and Br(2) (gold). Eigenvectors are displayed once per unique Br and were placed using Diamond 3.2.

As stated earlier, there are two magnetically unique Br sites in BaBr$_2$. Each possesses local m symmetry, with the mirror plane orienting perpendicular to the b crystal axis. The calculated eigenvector orientations associated with the $\ddot{V}$ and $\ddot{\sigma}$ tensors at each distinct

bromide lie either perpendicular or parallel to the mirror plane. Considering Br(1), $\mathbf{V}_{11}$ and $\mathbf{V}_{33}$ lie parallel to the mirror plane, with $\mathbf{V}_{22}$ orienting perpendicular to it (Figure 3.18b). The $\mathbf{V}_{33}$ eigenvector orients very nearly towards the nearest Ba^{2+} ion ($\angle(\mathbf{V}_{33}$–Br–Ba) = 5.8°), while $\mathbf{V}_{22}$ points directly at an adjacent Br ion. The $\boldsymbol{\sigma}_{33}$ and $\boldsymbol{\sigma}_{11}$ eigenvectors lie parallel to the mirror plane, with $\boldsymbol{\sigma}_{22}$ orienting parallel to b. As with $CaBr_2$, $\boldsymbol{\sigma}_{33}$ directs not towards a metal cation, but rather roughly towards a somewhat distant ($r = 5.58$ Å) Br(2) ion. Likewise, $\boldsymbol{\sigma}_{22}$ points directly at the most local bromide in the b direction. With regards to the Br(2) sites in $BaBr_2$, the $\ddot{V}$ tensor orients very similarly as that for the Br(1) site. In fact, the directions of the $\mathbf{V}_{22}/\boldsymbol{\sigma}_{22}$ eigenvectors are equivalent. The $\boldsymbol{\sigma}_{33}$ eigenvector for Br(2) nearly bisects the angle that the Br(2) ion makes with the two most proximate Br(1) ions, while $\boldsymbol{\sigma}_{11}$ for Br(2) points roughly toward a fairly remote ($r = 5.43$ Å) Br(2) ion.

Considering the $\ddot{V}$ and $\ddot{\sigma}$ tensor orientations across all samples (Figure 3.18 and Appendix A: Figures A.8 – A.11, and Table A.9), beyond simple symmetry constraints (i.e., that the site symmetry will constrain the tensor eigenvectors to be directed along rotational axes, parallel or perpendicular to mirror planes, etc.) it is not straightforward to rationalize their orientation in a general manner. In a number of cases, $\mathbf{V}_{33}$ orients toward a nearby M^{2+} ion (e.g., both $BaBr_2$ sites; the Br(3) and Br(4) sites in $SrBr_2$), but it is also seen that $\mathbf{V}_{33}$ can orient towards a nearby bromide ion (e.g., $CaBr_2$ and sites Br(1) and Br(2) in $SrBr_2$). The situation is similar when looking at the orientation of $\boldsymbol{\sigma}_{33}$. Among all compounds studied, it appears that the local ions dictate the tensor orientation; hence, the resultant tensors typically possess eigenvectors that are oriented at or near either NN or NNN ions.

3.3.3 Calculation of Bromine $\ddot{V}$ Tensors Using a Point Charge Model

To determine the effect of the ionic lattice upon the resultant $\ddot{V}$ tensor at the Br nuclei, calculations using a point charge model[157] were carried out for the anhydrous compounds, the results of which are shown in Table 3.9. After the inclusion of Sternheimer antishielding factors, small QIs are reproduced rather well (e.g., the Br(1) and Br(2) sites in SrBr$_2$). For moderate C_Q values (e.g., Br(3) in SrBr$_2$), the agreement between observation and calculation becomes worse, with the point charge model overestimating the experimental $C_Q(^{81}Br)$ values. Agreement is very poor in cases of a substantial bromine QI (e.g., CaBr$_2$ or Br(4) in SrBr$_2$).

Table 3.9 Calculated ^{81}Br EFG tensor parameters: point charge model[a]

compound	site label	$C_Q(^{81}Br)$ / MHz	η_Q
CaBr$_2$	—	−143.4	0.70
SrBr$_2$	Br(1)	−10.9	0.00
	Br(2)	−15.0	0.00
	Br(3)	39.3	0.61
	Br(4)	−105.9	0.59
BaBr$_2$	Br(1)	−17.8	0.40
	Br(2)	50.4	0.03

[a] The following equation was used to calculate the ij^{th} (i, j = x, y, z) component of $\ddot{V}$: $V_{ij} = ((Ze)/(4\pi\varepsilon_0 r^3))((3r_i r_j)/(r^2) - \delta^K_{ij})$, where Z is the integer value associated with a point charge (i.e., −1 for Br and +2 for the alkaline earth metal) located a distance r away from the probe nucleus, ε_0 is the electric constant, and δ^K_{ij} is the Kronecker Delta function. See also footnote b of Table 3.5.

It is postulated that this overestimation is due to reduced ionicity, which would decrease the effective ionic charges at all ion sites and hence reduce the bromine C_Q values (see Appendix A, Figure A.12, for a plot demonstrating this relationship within the point charge model). Similarly, there should be increasing point dipole effects,[158] which are neglected in the point charge model used here. It therefore appears that a more sophisticated approach, such as GIPAW DFT, is

essential to obtain an accurate bromine $\ddot{V}$ tensor in simple ionic bromide systems that possess significant QIs.

3.4   Conclusions

Chapter 3 has presented the first systematic $^{79/81}$Br SSNMR study relating $^{79/81}$Br EFG and CS tensor parameters to local structure in noncubic inorganic solids. The large range of values observed for the various parameters (e.g., $C_Q(^{79/81}$Br) values) clearly demonstrates the sensitivity of such experiments to the notable differences in local structure and symmetry for the bromide-containing systems studied.   Advantages over bromine NQR include ease of measurement (e.g., no need for powdered samples in gram scale quantities or large single crystals), the opportunity to observe the full $\ddot{V}$ tensor, and the opportunity to measure CS tensors. Indeed, deficiencies in the ^{79}Br NQR data for BaBr$_2$ and SrBr$_2$ have been explained and corrected. Measurement of bromine $\ddot{V}$ and $\ddot{\delta}$ tensors, as well as their relative orientations, has been found generally useful across the samples studied: by quantifying the contributions that each tensor makes to the observed $^{79/81}$Br SSNMR line shape, local site symmetry can be constrained (e.g., as demonstrated in the case of two of the four Br sites in SrBr$_2$), or, in favourable situations (either very high or very low site symmetry), it can be unambiguously specified (e.g., the $^{79/81}$Br SSNMR data clearly show that the Br ions in BaBr$_2$·2H$_2$O must be located at crystal lattice positions possessing 1 site symmetry).

As a result of the state-of-the-art high magnetic field used in this study (i.e., 21.1 T), bromine CSA has been measured in a series of powdered samples for the first time using both NMR-active bromine isotopes. These measurements establish bromine CSA as a new tool for characterizing bromide sites in diverse materials. The resolving power of $^{79/81}$Br SSNMR

spectroscopy has been established on samples containing up to four magnetically inequivalent sites. Rare examples of $^{79/81}$Br MAS NMR spectra have been presented for a sample possessing a noncubic crystal lattice and hence exhibiting second-order quadrupolar line shape broadening. With the development of commercially-available MAS probes capable of sample rotation frequencies of nearly 70 kHz,[159,160] additional applications of $^{79/81}$Br MAS NMR spectroscopy can be anticipated.

The sensitivity of the isotropic bromine chemical shift and C_Q values to the degree of sample hydration has been demonstrated. This sensitivity has been exploited to characterize the composition of $CaBr_2 \cdot xH_2O$. It is seen that the bulk of this mixture is anhydrous $CaBr_2$, but substantial amounts of the dihydrate and tetrahydrate pseudopolymorphs have also been quantified. Bromine SSNMR thus holds promise for the characterization of unknown solid mixtures containing ionic bromides.

The point charge model, after appropriate Sternheimer antishielding corrections, has been found to qualitatively reproduce trends in $C_Q(^{81}Br)$, but is in poor quantitative agreement with many of the experimental observations. For this reason, first-principles calculations (e.g., GIPAW DFT) are preferable. Agreement between experimentally measured and GIPAW DFT computed $^{79/81}$Br SSNMR parameters has been found to be very good to excellent in most cases. This has allowed for the unambiguous assignment of experimentally observed $^{79/81}$Br SSNMR signals to unique sites in the crystal lattices for $SrBr_2$ and $BaBr_2$.

On the basis of the range of observed tensor parameters, it appears that $^{79/81}$Br SSNMR may be applied as a general spectroscopic tool for the study of bromide-containing systems. The development of larger applied magnetic fields (e.g., Bruker's 1 GHz)[161] and advanced pulse sequences (e.g., 'wideband uniform-rate and smooth truncation'-QCPMG (WURST-QCPMG) and 'direct enhancement of integer spin magnetization' (DEISM))[162,163] will facilitate future

studies on more challenging materials. As correctly noted recently by Alonso *et al.*, bromine SSNMR should be applicable to the study of complex interfaces, such as mesoporous materials.[31,32] Additional opportunities for $^{79/81}$Br SSNMR can also be envisioned: molecular systems, such as those containing anion-π interactions;[164] biological systems, such as the bromide mimic of photosystem II (recently shown to have oxygen-evolving capacity);[165] chemical catalysts;[166] and layered photocatalysts, such as BiOBr.[167] Bromine SSNMR could also provide key data in an effort to quantify the role of halogen bonding in supramolecular chemistry.[168]

3.5   References

1   F. A. Cotton and G. Wilkinson, The Group VII Elements: F, Cl, Br, I, At In *Advanced Inorganic Chemistry: A Comprehensive Text*, 4th edn., Wiley-Interscience: Toronto, **1980**, 542-576.

2   C. E. Housecroft and A. G. Sharpe, The group 17 elements In *Inorganic Chemistry*, 1st edn., Pearson Education Limited: Harlow, England, **2001**, 386.

3   R. W. Murray, *Anal. Chem.*, **2009**, *81*, 2415.

4   C. M. Widdifield, R. P. Chapman and D. L. Bryce, Chlorine, Bromine, and Iodine Solid-State NMR Spectroscopy In *Annu. Rep. Nucl. Magn. Reson. Spectrosc.*, G. A. Webb, Ed., Elsevier: New York, *66*, **2009**, 195-326.

5   R. P. Chapman, C. M. Widdifield and D. L. Bryce, *Prog. Nucl. Magn. Reson. Spectrosc.*, **2009**, *55*, 215-237.

6   P. Pyykkö, *Mol. Phys.*, **2008**, *106*, 1965-1974.

7   R. Sternheimer, *Phys. Rev.*, **1954**, *95*, 736-750.

8   E. A. C. Lucken, Sternheimer Shielding In *Nuclear Quadrupole Coupling Constants*, Academic Press: London, **1969**, 79-96.

9   T. Kanda, *J. Phys. Soc. Jpn.*, **1955**, *10*, 85-88.

10   E. G. Wikner, W. E. Blumberg and E. L. Hahn, *Phys. Rev.*, **1960**, *118*, 631-639.

11   Y. Yamagata, *J. Phys. Soc. Jpn.*, **1964**, *19*, 10-23.

12   B. D. Günther and R. A. Hultsch, *J. Magn. Reson.*, **1969**, *1*, 609-617.

13   S. Hayashi and K. Hayamizu, *J. Chem. Phys.*, **1990**, *92*, 2818-2827.

14   S. Hayashi and K. Hayamizu, *Bull. Chem. Soc. Jpn.*, **1990**, *63*, 913-919.

15   S. Hayashi and K. Hayamizu, *J. Phys. Chem. Solids*, **1992**, *53*, 239-248.

16   V. P. Tarasov, S. A. Petrushin and Y. K. Gusev, *Dokl. Akad. Nauk SSSR*, **1987**, *293*, 1423-1426.

17   V. P. Tarasov, S. A. Petrushin and Y. K. Gusev, *Russ. J. Inorg. Chem.*, **1988**, *33*, 452-454.

18   V. P. Tarasov, V. I. Privalov, K. S. Gavrichev, V. E. Gorbunov, Y. K. Gusev and Y. A. Buslaev, *Russ. J. Coord. Chem.*, **1990**, *16*, 854-861.

19   V. P. Tarasov, V. I. Privalov, Y. A. Buslaev and U. Eichhoff, *Z. Naturforsch. B*, **1990**, *45*, 1005-1009.

20   T. J. Bastow, S. N. Stuart, W. G. McDugle, R. S. Eachus and J. M. Spaeth, *J. Phys.: Condens. Matter*, **1994**, *6*, 8633-8644.

21   R. Jelinek, B. F. Chmelka, A. Stein and G. A. Ozin, Multinuclear Solid-State NMR Study of a Sodalite Semiconductor Supralattice In *Materials Research Society Symposium Proceedings*, San Francisco, California, USA, **1992**, *272*, 235.

22   R. Jelinek, A. Stein and G. A. Ozin, *J. Am. Chem. Soc.*, **1993**, *115*, 2390-2396.

23   H. Trill, H. Eckert and V. I. Srdanov, *J. Am. Chem. Soc.*, **2002**, *124*, 8361-8370.

24   H. Trill, H. Eckert and V. I. Srdanov, *J. Phys. Chem. B*, **2003**, *107*, 8779-8788.

25   D. Brinkmann, H. Huber, M. Mali, J. Roos and H. Arend, *Helv. Phys. Acta*, **1982**, *55*, 568.

26   P. Brenni, D. Brinkmann, H. Huber, M. Mali, J. Roos and H. Arend, *Solid State Commun.*, **1983**, *47*, 415-418.

27   T. Erge, D. Michel, J. Petersson and F. Engelke, *Phys. Status Solidi A*, **1991**, *123*, 325-331.

28   D. Michel, U. Häcker, T. Erge and J. Petersson, *Phys. Status Solidi B*, **1994**, *185*, 257-264.

29   A. Kehrer, N. Weiden and A. Weiss, *Z. Phys. Chem.*, **1992**, *178*, 1-24.

30   J. Persons and G. S. Harbison, *J. Magn. Reson.*, **2007**, *186*, 347-351.

31   B. Alonso, D. Massiot, P. Florian, H. H. Paradies, P. Gaveau and T. Mineva, *J. Phys. Chem. B*, **2009**, *113*, 11906-11920.

32 B. Alonso, T. Mineva, P. Innocenzi, G. Trimmel, K. Stubenrauch, I. Melnyk, Y. Zub, F. Fayon, P. Florian and D. Massiot, *C. R. Chim.*, **2010**, *13*, 431-442.

33 D. L. Bryce and G. D. Sward, *Magn. Reson. Chem.*, **2006**, *44*, 409-450.

34 F. H. Larsen, H. J. Jakobsen, P. D. Ellis and N. C. Nielsen, *J. Phys. Chem. A*, **1997**, *101*, 8597-8606.

35 A. P. M. Kentgens and R. Verhagen, *Chem. Phys. Lett.*, **1999**, *300*, 435-443.

36 Z. Yao, H. T. Kwak, D. Sakellariou, L. Emsley and P. J. Grandinetti, *Chem. Phys. Lett.*, **2000**, *327*, 85-90.

37 R. W. Schurko, I. Hung and C. M. Widdifield, *Chem. Phys. Lett.*, **2003**, *379*, 1-10.

38 R. Siegel, T. T. Nakashima and R. E. Wasylishen, *Chem. Phys. Lett.*, **2004**, *388*, 441-445.

39 R. Siegel, T. T. Nakashima and R. E. Wasylishen, *Concepts Magn. Reson. A*, **2005**, *26A*, 47-61.

40 R. Siegel, T. T. Nakashima and R. E. Wasylishen, *Concepts Magn. Reson. A*, **2005**, *26A*, 62-77.

41 L. A. O'Dell and R. W. Schurko, *Chem. Phys. Lett.*, **2008**, *464*, 97-102.

42 S. Jurga, G. S. Harbison, B. Blümich, H. W. Spiess, F. Fujara and A. Olinger, *Ber. Bunsen-Ges. Phys. Chem.*, **1986**, *90*, 1153-1159.

43 S. L. Segel, S. Maxwell, R. D. Heyding, P. Ingman, E. Ylinen and M. Punkkinen, *Solid State Commun.*, **1988**, *66*, 1039-1041.

44 T. J. Bastow, R. J. C. Brown and S. L. Segel, *J. Chem. Phys.*, **1988**, *89*, 1203-1204.

45 T. J. Bastow and S. N. Stuart, *J. Phys.: Condens. Matter*, **1989**, *1*, 4649-4657.

46 T. L. Weeding and W. S. Veeman, *J. Chem. Soc., Chem. Commun.*, **1989**, , 946-948.

47 V. P. Tarasov, M. A. Meladze, G. A. Kirakosyan, A. E. Shvelashvili and Y. A. Buslaev, *Phys. Status Solidi B*, **1991**, *167*, 271-279.

48 V. P. Tarasov, M. A. Meladze and G. A. Kirakosyan, *Russ. J. Coord. Chem.*, **1992**, *18*, 707-717.

49 Y. Furukawa and R. Ikeda, *Ber. Bunsen-Ges. Phys. Chem.*, **1993**, *97*, 1143-1146.

50 J. Skibsted and H. J. Jakobsen, *Inorg. Chem.*, **1999**, *38*, 1806-1813.

51 C. Gervais, R. Dupree, K. J. Pike, C. Bonhomme, M. Profeta, C. J. Pickard and F. Mauri, *J. Phys. Chem. A*, **2005**, *109*, 6960-6969.

52   D. L. Bryce, G. D. Sward and S. Adiga, *J. Am. Chem. Soc.*, **2006**, *128*, 2121-2134.

53   D. L. Bryce and G. D. Sward, *J. Phys. Chem. B.*, **2006**, *110*, 26461-26470.

54   R. P. Chapman and D. L. Bryce, *Phys. Chem. Chem. Phys.*, **2007**, *9*, 6219-6230.

55   T. O. Sandland, L. S. Du, J. F. Stebbins and J. D. Webster, *Geochim. Cosmochim. Acta*, **2004**, *68*, 5059-5069.

56   M. Vittadello, P. E. Stallworth, F. M. Alamgir, S. Suarez, S. Abbrent, C. M. Drain, V. Di Noto and S. G. Greenbaum, *Inorg. Chim. Acta*, **2006**, *359*, 2513-2518.

57   D. L. Bryce and E. B. Bultz, *Chem. Eur. J.*, **2007**, *13*, 4786-4796.

58   H. Hamaed, J. M. Pawlowski, B. F. T. Cooper, R. Fu, S. H. Eichhorn and R. W. Schurko, *J. Am. Chem. Soc.*, **2008**, *130*, 11056-11065.

59   A. J. Rossini, R. W. Mills, G. A. Briscoe, E. L. Norton, S. J. Geier, I. Hung, S. Zheng, J. Autschbach and R. W. Schurko, *J. Am. Chem. Soc.*, **2009**, *131*, 3317-3330.

60   R. P. Chapman and D. L. Bryce, *Phys. Chem. Chem. Phys.*, **2009**, *11*, 6987-6998.

61   I. Hung, K. Shetty, P. D. Ellis, W. W. Brey and Z. Gan, *Solid State Nucl. Magn. Reson.*, **2009**, *36*, 159-163.

62   P. G. Gordon, D. H. Brouwer and J. A. Ripmeester, *J. Phys. Chem. A*, **2008**, *112*, 12527-12529.

63   P. G. Gordon, D. H. Brouwer and J. A. Ripmeester, *Chem. Phys. Chem.*, **2010**, *11*, 260-268.

64   T. Saito, H. Inoue, J. Tonisi, A. Oosawa, T. Goto, T. Sasaki, N. Kobayasi, S. Awaji and K. Watanabe, *J. Phys: Conf. Ser.*, **2006**, *51*, 203-206.

65   H. Inoue, S. Tani, S. Hosoya, T. Suzuki, T. Goto, H. Tanaka, T. Sasaki and N. Kobayashi, ^{2}D, $^{35/37}$Cl, $^{63/65}$Cu-NMR Study of the Quantum Spin System NH$_4$CuCl$_3$ In *Low Temperature Physics: 24th International Conference on Low Temperature Physics*, **2006**, *850*, 1061-1062.

66   T. Imai, E. A. Nytko, B. M. Bartlett, M. P. Shores and D. G. Nocera, *Phys. Rev. Lett.*, **2008**, *100*, 077203.

67   H. Inoue, S. Tani, S. Hosoya, K. Inokuchi, T. Fujiwara, T. Saito, T. Suzuki, A. Oosawa, T. Goto, M. Fujisawa, H. Tanaka, T. Sasaki, S. Awaji, K. Watanabe and N. Kobayashi, *Phys. Rev. B*, **2009**, *79*, 174418.

68   H. Tou, M. Sera, Y. Maniwa and S. Yamanaka, *Int. J. Mod. Phys. B*, **2007**, *21*, 3340-3342.

69   H. Liang, H. Hanzawa, T. Horikawa and K. Machida, *J. Alloy Compd.*, **2008**, *457*, L6-L8.

70   K. A. Temelkov, N. K. Vuchkov, B. L. Pan, N. V. Sabotinov, B. Ivanov and L. Lyutov, *J. Phys. D: Appl. Phys.*, **2006**, *39*, 3769-3772.

71   N. Iwase, S. Tadaki, S. Hidaka and N. Koshino, *J. Lumin.*, **1994**, *60&61*, 618-619.

72   G. Corradi, M. Secu, S. Schweizer and J. M. Spaeth, *J. Phys.: Condens. Matter*, **2004**, *16*, 1489-1500.

73   J. Selling, S. Schweizer, M. D. Birowosuto and P. Dorenbos, *J. Appl. Phys.*, **2007**, *102*, 074915.

74   J. Selling, M. D. Birowosuto, P. Dorenbos and S. Schweizer, *J. Appl. Phys.*, **2007**, *101*, 034901.

75   H. Tanaka, *Thermochim. Acta*, **1985**, *90*, 101-107.

76   R. K. Harris, E. D. Becker, S. M. Cabral De Menezes, P. Granger, R. E. Hoffman and K. W. Zilm, *Pure Appl. Chem.*, **2008**, *80*, 59-84.

77   I. Solomon, *Phys. Rev.*, **1958**, *110*, 61-65.

78   I. D. Weisman and L. H. Bennett, *Phys. Rev.*, **1969**, *181*, 1341-1350.

79   A. C. Kunwar, G. L. Turner and E. Oldfield, *J. Magn. Reson.*, **1986**, *69*, 124-127.

80   H. Y. Carr and E. M. Purcell, *Phys. Rev.*, **1954**, *94*, 630-638.

81   S. Meiboom and D. Gill, *Rev. Sci. Instrum.*, **1958**, *29*, 688-691.

82   D. Massiot, I. Farnan, N. Gautier, D. Trumeau, A. Trokiner and J. P. Coutures, *Solid State Nucl. Magn. Reson.*, **1995**, *4*, 241-248.

83   A. Medek, V. Frydman and L. Frydman, *J. Phys. Chem. A*, **1999**, *103*, 4830-4835.

84   R. W. Schurko, S. Wi and L. Frydman, *J. Phys. Chem. A*, **2002**, *106*, 51-62.

85   C. J. Pickard and F. Mauri, *Phys. Rev. B*, **2001**, *63*, 245101.

86   M. Profeta, F. Mauri and C. J. Pickard, *J. Am. Chem. Soc.*, **2003**, *125*, 541-548.

87   S. J. Clark, M. D. Segall, C. J. Pickard, P. J. Hasnip, M. I. J. Probert, K. Refson and M. C. Payne, *Z. Kristallogr.*, **2005**, *220*, 567-570.

88   J. R. Yates, C. J. Pickard and F. Mauri, *Phys. Rev. B*, **2007**, *76*, 024401.

89   J. P. Perdew, K. Burke and M. Ernzerhof, *Phys. Rev. Lett.*, **1996**, *77*, 3865-3868.

90   J. P. Perdew, K. Burke and M. Ernzerhof, *Phys. Rev. Lett.*, **1997**, *78*, 1396.

91   J. P. Perdew, Unified Theory of Exchange and Correlation Beyond the Local Density Approximation In *Electronic Structure of Solids '91*, P. Ziesche and H. Eschrig, Eds., Akademie Verlag: Berlin, **1991**, 11-20.

92   J. P. Perdew, J. A. Chevary, S. H. Vosko, K. A. Jackson, M. R. Pederson, D. J. Singh and C. Fiolhais, *Phys. Rev. B*, **1992**, *46*, 6671-6687.

93   J. P. Perdew, J. A. Chevary, S. H. Vosko, K. A. Jackson, M. R. Pederson, D. J. Singh and C. Fiolhais, *Phys. Rev. B*, **1993**, *48*, 4978.

94   J. P. Perdew, K. Burke and Y. Wang, *Phys. Rev. B*, **1996**, *54*, 16533-16539.

95   K. Burke, J. P. Perdew and Y. Wang, Derivation of a Generalized Gradient Approximation: the PW91 Density Functional In *Electronic Density Functional Theory: Recent Progress and New Directions*, J. F. Dobson, G. Vignale and M. P. Das, Eds., Plenum: New York, **1998**, 81-111.

96   H. J. Monkhorst and J. D. Pack, *Phys. Rev. B*, **1976**, *13*, 5188-5192.

97   K. R. Andress and J. Gundermann, *Z. Kristallogr.*, **1934**, *87*, 345-369.

98   C. A. Sorrell and R. R. Ramey, *J. Chem. Eng. Data*, **1974**, *19*, 307-308.

99   I. Abrahams and E. Vordemvenne, *Acta Cryst. C*, **1995**, *C51*, 183-185.

100 P. A. Agron and W. R. Busing, *Acta Cryst. C*, **1986**, *C42*, 141-143.

101 A. LeClaire and M. M. Borel, *Acta Cryst. B*, **1977**, *B33*, 2938-2940.

102 K. J. D. MacKenzie and M. E. Smith, *Multinuclear Solid-State NMR of Inorganic Materials*, Pergamon: Amsterdam, **2002**.

103 N. I. Smirnov and A. F. Volkov, *Teor. Eksp. Khim.*, **1976**, *13*, 88-90.

104 A. Abragam, *The Principles of Nuclear Magnetism*, Oxford University Press: New York, **1961**.

105 A. K. van Bever and W. Nieuwenkamp, *Z. Kristallogr.*, **1935**, *90*, 374-376.

106 V. W. Döll and W. Klemm, *Z. Anorg. Allg. Chem.*, **1939**, *241*, 239-258.

107 E. B. Brackett, T. E. Brackett and R. L. Sass, *J. Inorg. Nucl. Chem.*, **1963**, *25*, 1295-1296.

108 A. Bondi, *J. Phys. Chem.*, **1964**, *68*, 441-451.

109 M. Mantina, A. C. Chamberlin, R. Valero, C. J. Cramer and D. G. Truhlar, *J. Phys. Chem. A*, **2009**, *113*, 5806-5812.

110 Z. Lin, M. E. Smith, F. E. Sowrey and R. J. Newport, *Phys. Rev. B*, **2004**, *69*, 224107.

111 E. A. C. Lucken, *Nuclear Quadrupole Coupling Constants*, Academic Press: London, **1969**.

112 A. D. Bain, *Mol. Phys.*, **2003**, *101*, 3163-3175.

113 A. D. Bain and B. Berno, *Prog. Nucl. Magn. Reson. Spectrosc.*, **2011**, *59*, 223-244.

114 G. Wu and V. Terskikh, *J. Phys. Chem. A*, **2008**, *112*, 10359-10364.

115 R. Fusaro and J. W. Doane, *J. Chem. Phys.*, **1967**, *47*, 5446-5447.

116 M. A. Kamermans, *Z. Kristallogr.*, **1939**, *101*, 406-411.

117 R. L. Sass, T. Brackett and E. Brackett, *J. Phys. Chem.*, **1963**, *67*, 2862-2863.

118 J. G. Smeggil and H. A. Eick, *Inorg. Chem.*, **1971**, *10*, 1458-1460.

119 A. D. Buckingham and S. M. Malm, *Mol. Phys.*, **1971**, *22*, 1127-1130.

120 X. Hou and R. J. Kirkpatrick, *Chem. Mater.*, **2002**, *14*, 1195-1200.

121 E. B. Brackett, T. E. Brackett and R. L. Sass, *J. Phys. Chem.*, **1963**, *67*, 2132-2135.

122 A. F. Volkov and N. I. Smirnov, *Dokl. Akad. Nauk SSSR*, **1973**, *211*, 1377-1379.

123 D. M. Potrepka, J. I. Budnick, D. B. Fenner, W. A. Hines, M. Balasubramanian and A. R. Moodenbaugh, *Phys. Rev. B*, **1999**, *60*, 10489-10499.

124 J. F. Stebbins and L. S. Du, *Am. Mineral.*, **2002**, *87*, 359-363.

125 E. Bang, *Mat. Fys. Medd. Dan. Vid. Selsk.*, **1961**, *33*, 1-23.

126 H. D. Lutz, B. Engelen and C. Freiburg, *Acta Cryst. B*, **1980**, *B36*, 437-438.

127 T. Kellersohn, B. Engelen, H. D. Lutz, H. Bartl, B. P. Schweiss and H. Fuess, *Z. Kristallogr.*, **1991**, *197*, 175-184.

128 J. W. McGrath and A. A. Silvidi, *J. Chem. Phys.*, **1960**, *33*, 644-647.

129 J. W. McGrath and A. A. Silvidi, *J. Chem. Phys.*, **1962**, *37*, 194-195.

130 J. W. McGrath and A. A. Silvidi, *J. Chem. Phys.*, **1962**, *36*, 1082.

131 J. W. McGrath, *J. Chem. Phys.*, **1965**, *43*, 3746-3749.

132 A. A. Silvidi, *J. Chem. Phys.*, **1966**, *45*, 3892-3894.

133 J. D. Hanawalt, H. W. Rinn and L. K. Frevel, *Ind. Eng. Chem., Anal. Ed.*, **1938**, *10*, 457-512.

134 P. A. Agron and W. R. Busing, *Acta Cryst. C*, **1985**, *C41*, 8-10.

135 Y. Hiyama, P. M. Woyciesjes, T. L. Brown and D. A. Torchia, *J. Magn. Reson.*, **1987**, *72*, 1-12.

136 T. Sidei and S. Yano, *J. Chem. Phys.*, **1955**, *23*, 1554-1555.

137 C. M. Widdifield and D. L. Bryce, *Phys. Chem. Chem. Phys.*, **2009**, *11*, 7120-7122.

138 Z. Herrmann, *Z. Anorg. Allg. Chem.*, **1931**, *196*, 79-84.

139 S. Yano, *J. Phys. Soc. Jpn.*, **1959**, *14*, 942-954.

140 J. Paulik, F. Paulik, É. Buzágh-Gere and M. Arnold, *Thermochim. Acta*, **1979**, *31*, 93-100.

141 N. Troullier and J. L. Martins, *Phys. Rev. B*, **1991**, *43*, 1993-2006.

142 D. Vanderbilt, *Phys. Rev. B*, **1990**, *41*, 7892-7895.

143 F. Mauri, N. Vast and C. J. Pickard, *Phys. Rev. Lett.*, **2001**, *87*, 085506.

144 I. Farnan, E. Balan, C. J. Pickard and F. Mauri, *Am. Mineral.*, **2003**, *88*, 1663-1667.

145 C. Gervais, M. Profeta, V. Lafond, C. Bonhomme, T. Azaïs, H. Mutin, C. J. Pickard, F. Mauri and F. Babonneau, *Magn. Reson. Chem.*, **2004**, *42*, 445-452.

146 K. Bouchmella, S. G. Dutremez, B. Alonso, F. Mauri and C. Gervais, *Cryst. Growth Des.*, **2008**, *8*, 3941-3950.

147 P. E. Blöchl, *Phys. Rev. B*, **1994**, *50*, 17953-17979.

148 J. W. Zwanziger and M. Torrent, *Appl. Magn. Reson.*, **2008**, *33*, 447-456.

149 T. Charpentier, S. Ispas, M. Profeta, F. Mauri and C. J. Pickard, *J. Phys. Chem. B*, **2004**, *108*, 4147-4161.

150 M. Profeta, M. Benoit, F. Mauri and C. J. Pickard, *J. Am. Chem. Soc.*, **2004**, *126*, 12628-12635.

151 M. Choi, K. Matsunaga, F. Oba and I. Tanaka, *J. Phys. Chem. C*, **2009**, *113*, 3869-3873.

152 C. Gervais, D. Laurencin, A. Wong, F. Pourpoint, J. Labram, B. Woodward, A. P. Howes, K. J. Pike, R. Dupree, F. Mauri, C. Bonhomme and M. E. Smith, *Chem. Phys. Lett.*, **2008**, *464*, 42-48.

153 D. L. Bryce, E. B. Bultz and D. Aebi, *J. Am. Chem. Soc.*, **2008**, *130*, 9282-9292.

154 C. J. Jameson and A. C. de Dios, Theoretical and physical aspects of nuclear shielding In *Nuclear Magnetic Resonance*, G. A. Webb, Ed., RSC Publishing: Dorchester, **2009**, 68-93.

155 J. van der Elsken and D. W. Robinson, *Spectrochim. Acta*, **1961**, *17*, 1249-1256.

156 M. Edén, *Chem. Phys. Lett.*, **2009**, *470*, 318-324.

157 C. P. Slichter, Electric Quadrupole Effects In *Principles of Magnetic Resonance*, 3rd edn., M. Cardona, P. Fulde, K. von Klitzing, H.-J. Queisser and H. K. V. Lotsch, Eds., Springer: New York, **1990**, 485.

158 O. H. Han and E. Oldfield, *Inorg. Chem.*, **1990**, *29*, 3666-3669.

159 A. Samoson, T. Tuherm and Z. Gan, *Solid State Nucl. Magn. Reson.*, **2001**, *20*, 130-136.

160 A. Samoson, T. Tuherm, J. Past, A. Reinhold, T. Anupõld and I. Heinmaa, *Top. Curr. Chem.*, **2005**, *246*, 15-31.

161 A. Bhattacharya, *Nature*, **2010**, *463*, 605-606.

162 L. A. O'Dell, A. J. Rossini and R. W. Schurko, *Chem. Phys. Lett.*, **2009**, *468*, 330-335.

163 L. A. O'Dell and R. W. Schurko, *J. Am. Chem. Soc.*, **2009**, *131*, 6658-6659.

164 B. P. Hay and R. Custelcean, *Cryst. Growth Des.*, **2009**, *9*, 2539-2545.

165 K. Kawakami, Y. Umena, N. Kamiya and J. R. Shen, *Proc. Natl. Acad. Sci. USA*, **2009**, *106*, 8567-8572.

166 Y. J. Zhao, L. J. S. Tan, B. Li, S. M. Li and T. P. Loh, *Chem. Commun.*, **2009**, 3738-3740.

167 W. L. Huang, *J. Comput. Chem.*, **2009**, *30*, 1882-1891.

168 P. Metrangolo, F. Meyer, T. Pilati, G. Resnati and G. Terraneo, *Angew. Chem. Int. Ed.*, **2008**, *47*, 6114-6127.

Chapter Four

Solid-State ^{127}I NMR and GIPAW DFT Study of Metal Iodides and Their Hydrates: Structure and Symmetry

4.1   Introduction

Iodine, found naturally in seawater, minerals, kelp, and the brines associated with oil and gas wells, finds use in a number of industrial and consumer products (e.g., food stabilizers, animal feed supplements, disinfectants, inks, dyes, and pharmaceuticals).[1] Likewise, numerous important chemical compounds contain the iodide anion (I^-). For example, NaI promotes amine carbonylation reactions,[2] bis(trimethylammonium) alkane diiodides can resolve mixtures of key intermediates which are used in the synthesis of fluorochemicals and fluoropolymers,[3] and SmI_2 has recently been touted as "one of the premier single-electron reducing agents in synthetic chemistry".[4] Substantial effort has been expended with the aim of developing hypervalent I(III) and I(V) reagents. One example of an important I(V) reagent is *ortho*-iodoxybenzoic acid, which finds use in the synthesis of α-aminoaldehydes and carbon-heteroatom oxidations.[5] The 'Togni reagent', used in the mild electrophilic addition of CF_3 moieties to carbon- and sulfur-centered nucleophiles, owes its selectivity to a hypervalent I(III).[6]

While many chemical properties of the halogens are similar, their nuclear properties differ significantly; hence, the development of their corresponding SSNMR methods is rather distinct. Fluorine-19 SSNMR spectroscopy is a highly developed characterization tool with well-established applications.[7-9] While the SSNMR spectroscopy of the remaining halogens is substantially less developed relative to ^{19}F, several recent applications of $^{35/37}$Cl and $^{79/81}$Br SSNMR spectroscopy towards the study of chlorine- and bromine-containing systems have been

published (as outlined in Section 3.1). Unlike $^{35/37}$Cl and $^{79/81}$Br, the development of ^{127}I SSNMR has nearly reached a standstill. Other than a study on the dynamical structure of γ-Ag$_x$Cu$_{1-x}$I,[10] and brief mentions within reports on ionic liquids[11] and pulse sequence advances,[12] there have been no applications of ^{127}I SSNMR since 2001.[13] As no substantial ^{127}I SSNMR account has been published in about a decade, a systematic ^{127}I SSNMR study employing modern techniques and apparatus does not exist. In fact, aside from the trivial cases involving cubic environments, no iodide site has ever been fully characterized (i.e., quantification of both the CS and EFG tensors) using ^{127}I SSNMR.

The ^{127}I nucleus is 100 % naturally abundant, possesses a γ value slightly less than ^{13}C, and is quadrupolar ($I(^{127}$I$) = 5/2$). The primary experimental challenge associated with using the ^{127}I nucleus as a SSNMR probe is its moderately large nuclear electric quadrupole moment ($Q(^{127}$I$) = -6.96 \times 10^{-29}$ m^2).[14] As outlined in earlier sections, this QI serves to broaden the SSNMR signal in powdered samples.[15] In cases where the QI is moderately small, this broadening provides significant information regarding the local electronic structure in molecules and crystalline materials.[16] For cases where the QI is large, the broadening may be such that the SSNMR signal is undetectable. Of the naturally occurring isotopes where the atomic number is less than 61, only the $^{113/115}$In nuclides possess Q values larger than ^{127}I; hence, the acquisition of high-quality ^{127}I SSNMR spectra is a particular challenge. As second-order quadrupolar line shape broadening scales inversely with B_0 (Section 2.4.3), a potential remedy is to conduct the SSNMR experiments within a very large B_0 (i.e., $B_0 > 18.8$ T).

In Chapter 4, an ^{127}I SSNMR study of a variety of MI$_2$ and MI$_2$ hydrates is presented, and the information that can be gained by conducting ^{127}I SSNMR experiments in both standard and high fields is highlighted. Unlike ^{127}I NQR experiments, isotropic chemical shift values, as well as CSA, are potential observables in ^{127}I SSNMR spectra; hence, the SSNMR spectra are

potentially richer in information. Discussion is provided on the ability of ^{127}I SSNMR experiments to probe hydration states in alkaline earth metal hydrates, and several halogen SSNMR parameter trends across the alkaline earth metal halides and corresponding hydrates are detailed. Experimental observations are complemented with GIPAW DFT calculations and the ability of these computations to reproduce the observed NMR parameter values is documented.

4.2 Experimental Details

4.2.1 Sample Preparation

MgI$_2$ (99.998 %), CaI$_2$ (99.95 %), BaI$_2$ (99.995 %), CdI$_2$ (99.999 %), SrI$_2$·6H$_2$O (> 99.99 %), and BaI$_2$·2H$_2$O (98 %) were purchased from Sigma–Aldrich. All anhydrous compounds were received as beads, while all hydrates were received as powders. Sample purity was confirmed for each compound by the manufacturer (see Appendix B, Section B.1.1). As all compounds are hygroscopic and light sensitive, they were stored and prepared for use in minimal light conditions under either dry N$_2$ or Ar, except CdI$_2$, which was stored in a dry, dark cabinet. BaI$_2$·2H$_2$O was found to be air-stable for an extended period under low humidity conditions. Prior to ^{127}I SSNMR experiments, samples were powdered and tightly packed into either 3.2 mm or 4 mm o.d. Bruker MAS ZrO$_2$ rotors.

4.2.2 Solid-state ^{127}I NMR

Data were primarily acquired at the National Ultrahigh-field NMR Facility for Solids in Ottawa using a standard bore (54 mm) Bruker AVANCEII spectrometer operating at $B_0 = 21.1$ T ($v_0(^1$H$) = 900.08$ MHz). Additional ^{127}I SSNMR data were acquired at the University of Ottawa using a wide bore (89 mm) Bruker AVANCE spectrometer operating at $B_0 = 11.75$ T

($\nu_0(^1H)$ = 500.13 MHz). At 21.1 T, experiments used 3.2 mm or 4 mm Bruker HX MAS probes

($\nu_0(^{127}I)$ = 180.08 MHz), while at 11.75 T, experiments used a 4 mm Bruker HXY MAS probe

($\nu_0(^{127}I)$ = 100.06 MHz). All spectra were referenced to 0.1 mol/dm^3 KI in D$_2$O at 0 ppm[17]

using NaI or KI as secondary standards (δ_{iso}(NaI(s)) = 226.71 ppm, δ_{iso}(KI(s)) = 192.62 ppm).[18]

Iodine $\pi/2$ pulse widths were established using the ^{127}I SSNMR signals of powdered KI or NaI

under 10 kHz MAS. NaI and KI are cubic salts; hence, the CT selective (i.e., solid $\pi/2$) pulse

widths used for all samples under study were scaled by $1/(I + 1/2) = 1/3$, relative to the $\pi/2$

pulse width determined using the cubic salts.

Iodine-127 SSNMR signals were primarily acquired using either Solomon echo[19-21] or

Hahn echo[22] pulse sequences. Typical parameters were as follows: $\pi/2$ = 1.0 μs (π = 2.0 μs);

spectral window = 2 MHz; τ_1 = 18.6 to 30 μs; τ_2 = 4.3 to 20 μs; recycle delay = 0.25 s; and 512

or 1 024 complex time-domain data points were collected per transient. For all experiments,

between 4 000 to 18 800 transients were acquired. For BaI$_2$·2H$_2$O, CW ^1H decoupling was

tested ($\nu_1(^1H)$ ∼ 85 kHz). Due to the line width associated with the ^{127}I SSNMR signal of

SrI$_2$·6H$_2$O at 21.1 T (i.e., $\Delta\nu_{NMR}$ > 3 MHz), ^1H decoupling was not required. For full

experimental details, see Appendix B, Section B.1.2, and Table B.1. VOCS data acquisition

methods[23-25] were usually required to acquire the ^{127}I SSNMR signals. Offsets were typically 200

to 300 kHz for Solomon/Hahn echo experiments. Each sub-spectrum was combined in the

frequency-domain by co-addition to produce the total spectrum.

4.2.3 Solid-State ^{127}I NQR

Experiments used either a 4 mm Bruker HXY MAS probe or a 7 mm Bruker HX static

probe, and were performed to confirm the measured ^{127}I EFG tensor parameters for selected

compounds. Spectra were acquired using the Hahn echo pulse sequence. Short ($\tau_{RF} < 2$ μs), high-power pulses were used as the transmitter frequency was varied until the resonances were found. Typical offsets while searching for the NQR signals were 200 kHz. For further details, see Appendix B, Table B.1.

4.2.4 Quantum Chemical Calculations

GIPAW DFT computations used CASTEP-NMR (v. 4.1),[26-29] with input files generated using Materials Studio 3.2, and either usp[27,30] or otfg pseudopotentials. The iodine otfg pseudopotential was obtained from Accelrys Inc. (San Diego, CA). All geometry optimizations and NMR calculations (i.e., $\ddot{V}$ and $\ddot{\sigma}$ tensors) used the GGA, along with either the PBE XC functional,[31,32] or the PW91 XC functional.[33-37] Computed σ_{ij} values are expressed as δ_{ij} values using the following procedure: the iodine σ_{iso} for the reference (NaI) was computed using $E_{cut} =$ 1000 eV, a $6 \times 6 \times 6$ k-point grid and the same XC functional as the sample of interest. Using the calculated σ_{iso} and the known δ_{iso} value of 226.71 ppm for NaI(s),[18] the calculated σ_{ij} values were placed on an experimental δ scale using **(2.12)**. The E_{cut} and k-point grid used for each system are in the footnotes to Tables 4.5 and 4.7. Computed structure energies, structure references, pseudopotentials used, and additional details are in Appendix B, Table B.2. The structural parameters used for NMR computations are in Appendix B, Table B.3.

The SrI$_2$·6H$_2$O crystal structure has not been fully determined, but the unit cell, Sr, (fully determined) and I (a, b coordinates) atomic positions have been reported.[38] It is thought that SrI$_2$·6H$_2$O is isostructural to SrCl$_2$·6H$_2$O, whose structure has been determined using neutron diffraction techniques.[39] For the geometry optimization of SrI$_2$·6H$_2$O, the unit cell and Sr atomic positions were frozen to the reported values. For the I, O, and H atoms, the initial guess

was set to the analogous atomic positions in $SrCl_2 \cdot 6H_2O$. For $BaI_2 \cdot 2H_2O$, no structural data exist, but based upon prior [127]I NQR data,[40,41] it is suspected to be isostructural to $BaBr_2 \cdot 2H_2O$, the structure of which is known.[42] Hence, the $BaBr_2 \cdot 2H_2O$ crystal structure was used as the starting point when optimizing the $BaI_2 \cdot 2H_2O$ crystal structure.

4.3   Results and Discussion

4.3.1   Iodine-127 SSNMR Experiments

4.3.1.1 Anhydrous Alkaline Earth Metal Iodides

The parameters extracted from line shape analysis of the [127]I SSNMR spectra for stationary (i.e., static) samples of MgI_2, CaI_2, SrI_2, BaI_2, and CdI_2 (4H) are summarized in Tables 4.1 and 4.2.

Table 4.1 Experimental [127]I EFG tensor parameters: alkaline earth metal iodides and CdI_2[a]

compound	site label	$\|C_Q(^{127}I)\|$[b] / MHz	η_Q	notes
MgI_2	—	79.8(5)	0.02(2)	—
CaI_2	—	43.5(3)	0.02(2)	—
SrI_2[c]	I(1)	105.2(7)	0.467(12)	—
	I(2)	214.0(1)[d]	0.316(2)[d]	NQR: ν_{Q1} = 35.415(15); ν_{Q2} = 62.980(15)[e]
BaI_2	I(1)	96.2(8)	0.175(15)	—
	I(2)	120.9(2)[d]	0.015(15)[d]	NQR: ν_{Q1} = 18.13(2); ν_{Q2} = 36.26(2)[e]
CdI_2 (4H)	—	95.7(1.0)	0[f]	one-site model
CdI_2 (4H)	I(1)	95.7(1.0)	0[f]	two-site model
	I(2)	97.5(1.0)	0[f]	

[a] Error bounds are in parentheses. Parameter definitions are in Section 2.3.3.2.
[b] While C_Q may take any real value, $|C_Q|$ is measured using conventional SSNMR experiments.
[c] Formal discussion of the observed [127]I SSNMR parameters for SrI_2 is postponed until Chapter 5.
[d] Established with the aid of [127]I NQR experiments.
[e] All [127]I NQR frequencies are in MHz, ν_{Q1} and ν_{Q2} refer to quadrupolar resonance frequencies for $I = 5/2$, and are ordered such that ν_{Q1} ($m = \pm1/2 \leftrightarrow \pm3/2$ transition) < ν_{Q2} ($m = \pm3/2 \leftrightarrow \pm5/2$ transition).
[f] Assumed, based upon crystallographic site symmetry.

Table 4.2 Experimental iodine CS tensor parameters: alkaline earth metal iodides and CdI$_2$[a]

compound	site label	δ_{iso}[b] / ppm	Ω / ppm	κ	α, β, γ / °
MgI$_2$	—	920(50)	120(80)	–1[c]	90[d], 90(20), 0[d]
CaI$_2$	—	755(10)	< 50	—	—
SrI$_2$[e]	I(1)	880(70)	—	—	—
	I(2)	720(150)[f]	—	—	—
BaI$_2$	I(1)	650(70)[f]	300(100)	< –0.5	0[d], 45(20), 180[d]
	I(2)	1 000(80)[f]	—	—	—
CdI$_2$ (4H)	—	1 450(100)	—	—	—
CdI$_2$ (4H)	I(1)	1 420(100)	—	—	—
	I(2)	1 420(100)	—	—	—

[a] Includes Euler angle values. Error bounds are in parentheses. Parameter definitions are in Sections 2.3.2.4, 2.3.3.1, and 2.3.3.3.
[b] With respect to 0.1 mol/dm³ KI in D$_2$O (δ_{iso} = 0.00 ppm).
[c] Assumed based on crystallographic site symmetry.
[d] Simulated NMR line shape is insensitive to parameter variation; the value is assigned based on computational results.
[e] Formal discussion of the observed ^{127}I SSNMR parameters for SrI$_2$ is postponed until Chapter 5.
[f] Established with the aid of exact simulation software.

4.3.1.1.1   CaI$_2$: Iodide Ions at High Symmetry Lattice Positions

Iodine-127 SSNMR experiments were performed on powdered CaI$_2$ at B_0 = 11.75 and 21.1 T (Figures 4.1 and 4.2). The CaI$_2$ crystal structure belongs to the $P\bar{3}m1$ space group and CdI$_2$ (2H polytype) structure class (Figure 4.3a).[43] There is one crystallographically unique iodide ion (3m symmetry), which forms hexagonal close-packed layers with other iodide ions (Figures 4.3b and 4.3c). The local Ca–I coordination is trigonal pyramidal with r_{Ca-I} = 3.12 Å, while the closest iodide-iodide approach is 4.34 Å. The observed ^{127}I CT SSNMR signals possess, within experimental error, axially symmetric second-order quadrupolar-broadened line shapes ($\eta_Q(^{127}$I) = 0.02(0.02)). The observed ^{127}I $\ddot{V}$ tensor symmetry implies a threefold (or greater) rotational axis at the iodide,[44] in agreement with the crystal structure. Due to the strong ^{127}I CT SSNMR signal of CaI$_2$, the $\ddot{V}$ tensor was precisely characterized by collecting most of the ST at 11.75 T. The full m = ±3/2 ↔ ±1/2 ST and the high intensity portion of the m = ±5/2 ↔ ±3/2 ST were

observed (Figure 4.2b). While the VOCS Hahn echo spectrum in Figure 4.2b required the collection of 50 sub-spectra, each experiment lasted ca. 20 minutes; hence, the composite spectrum was acquired in only ~17 hours.
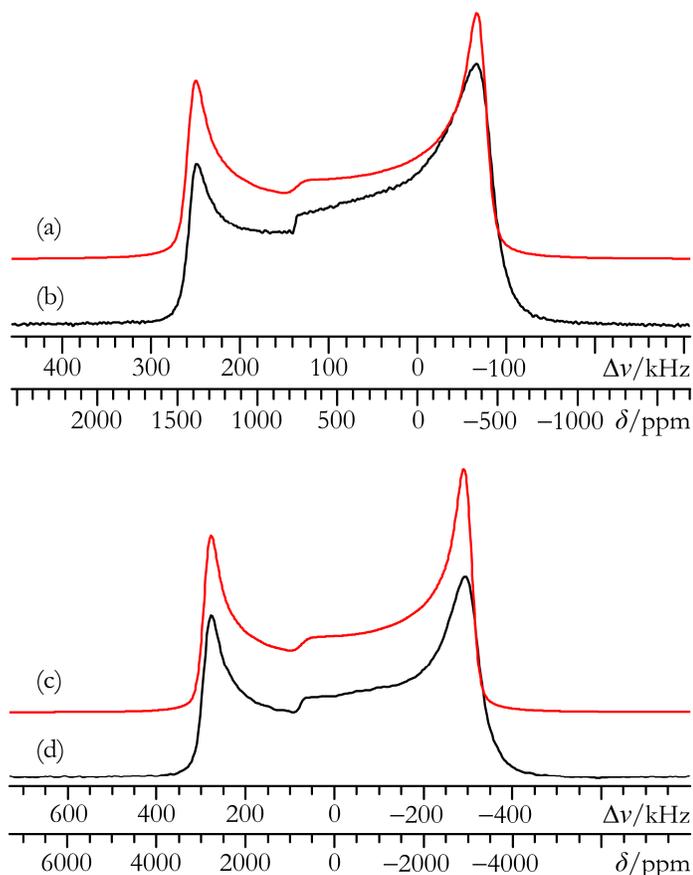
Figure 4.1 Best-fit analytical simulations (a, c), experimental static Solomon echo (b), and experimental static VOCS Hahn echo (d) [127]I CT SSNMR spectra of powdered CaI$_2$ acquired at (b) B_0 = 21.1 T (v_0 = 180.08 MHz) and (d) B_0 = 11.75 T (v_0 = 100.06 MHz).

Analytical fits of all observed spectra establish C_Q([127]I) as 43.5(0.3) MHz and δ_{iso} as 755(10) ppm. Using analytical simulations, it is estimated that Ω < 50 ppm for CaI$_2$, in agreement with quantum chemical calculations (*vide infra*).
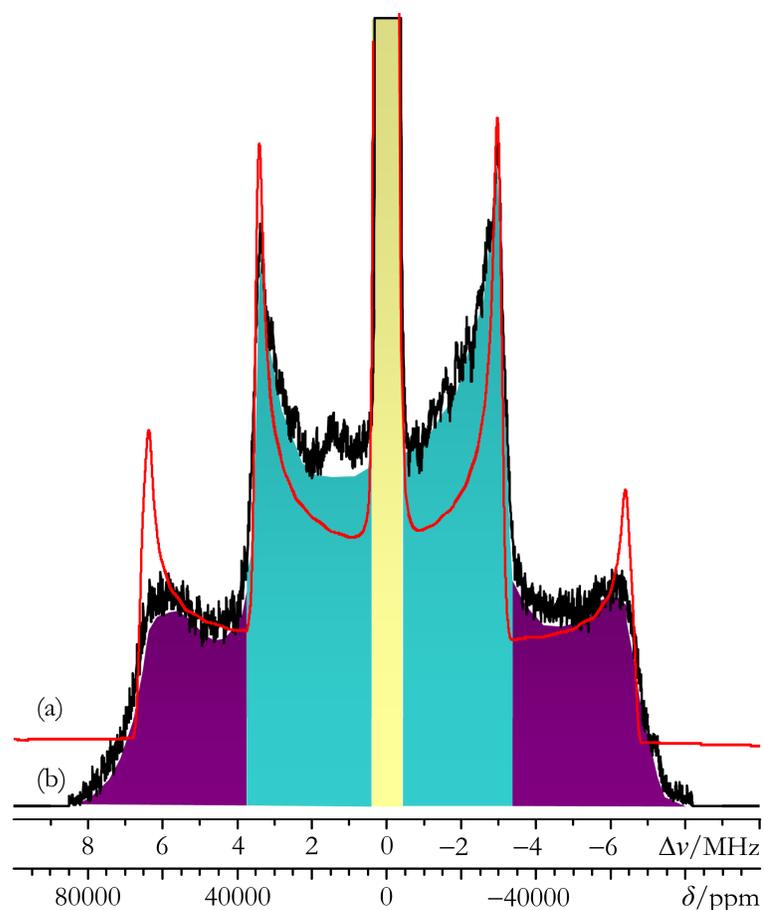
Figure 4.2 Best-fit analytical simulation (a), and experimental static VOCS Hahn echo (b) [127]I SSNMR spectrum of powdered CaI$_2$ acquired at B_0 = 11.75 T. Much of the spectral region shown corresponds to the ST. The CT is located roughly within the region from Δv = +0.3 to −0.4 MHz (gold), the inner ST (m = ±3/2 ↔ ±1/2) contribute most significantly from ca. Δv = +3.7 to +0.3 MHz and from Δv = −0.4 to −3.4 MHz (aqua), and the outer ST (m = ±5/2 ↔ ±3/2) contribute most significantly above Δv = +3.7 MHz and below Δv = −3.4 MHz (purple).

4.3.1.1.2 *MgI₂: Clear Evidence of Iodine Chemical Shift Anisotropy*

Iodine-127 SSNMR experiments were carried out on MgI$_2$ powder at B_0 = 11.75 and 21.1 T (Figure 4.4), and all the observed signals were fit analytically using identical parameters (Tables 4.1 and 4.2). Powder[43] and single-crystal[45] XRD data confirm that MgI$_2$ belongs to the same space group ($P\bar{3}m1$) and structure class as CaI$_2$. In the iodide first coordination sphere,

MgI_2 has three equivalent Mg–I contacts at internuclear distances of 2.9183(5) Å. However, unlike CaI_2, there exist numerous inequivalent I–I distances (Figure 4.5) as the unique I in MgI_2 is located at $z/c = 0.24237$, rather than $z/c = 0.25$ as in CaI_2.
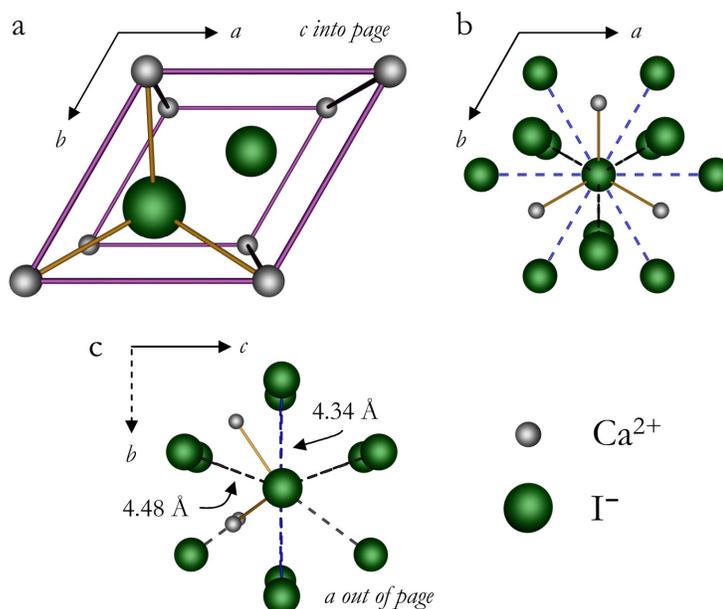
Figure 4.3 POV-ray renderings of the local structure of CaI_2. The unit cell is shown in (a). For the unique I, solid lines connect ions within the sum of the Ca and I vdW radii (i.e., $r_{Ca-I} < 4.29$ Å).[46,47] In (b – c), the local iodide environment (within 4.5 Å) for CaI_2 is shown. Six equivalent contacts (blue dashed lines) arrange hexagonally in the ab plane. A second set of equivalent contacts (black dashed lines) is related by a reflection in the ab plane.

The qualitative features of the ^{127}I SSNMR spectra of MgI_2 (Figure 4.4) are similar to those observed for CaI_2. The axial $\ddot{V}$ tensor ($\eta_Q = 0.02(0.02)$) supports the XRD-determined local site symmetry of the iodide ions ($3m$). It is interesting to note that the measured $C_Q(^{127}I)$ value of 79.8(0.5) MHz is nearly twice that of CaI_2, despite the very similar crystal structures of CaI_2 and MgI_2. This finding demonstrates the pronounced sensitivity of the ^{127}I QI to the iodide environment. To understand the origin of the drastically different $\ddot{V}$ tensor magnitudes in CaI_2 and MgI_2, quantum chemical calculations were carried out (*vide infra*, Section 4.3.2.3).
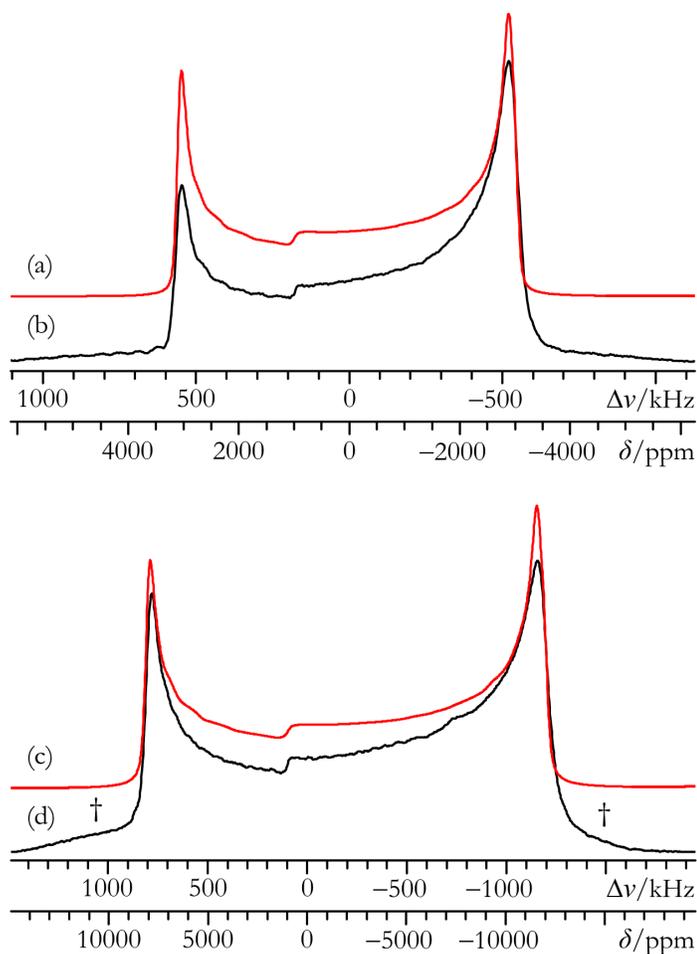
Figure 4.4 Best-fit analytical simulations (a, c), and experimental static VOCS Solomon echo (b, d) [127]I CT SSNMR spectra of powdered MgI$_2$ acquired at (b) B_0 = 21.1 T and (d) B_0 = 11.75 T. Partially excited ST are denoted using †.

The measured iodine δ_{iso} value of 920(50) ppm is significantly greater than that for CaI$_2$. This can be understood by considering the Mg–I distances in the first coordination sphere of MgI$_2$, which are less than the corresponding distances in CaI$_2$. Relative to CaI$_2$, this should lead to enhanced occupied-virtual wave function mixing in MgI$_2$, which in turn results in more significant paramagnetic shielding contributions to the $\ddot{\sigma}$ tensor.[48] Although the QI in MgI$_2$ contributes to most of the observed [127]I SSNMR line width, effects due to iodine CSA in MgI$_2$ were observed (Ω = 120(80) ppm; see also Appendix B, Figure B.1). According to the current

literature, this represents the second reliable measurement of iodine CSA (the first for an iodide). It is roughly an order of magnitude larger than the only other precisely measured iodine Ω value, which is 18(4) ppm for $CsIO_4$.[13] In addition, it has been experimentally observed that β = 90(20)° for MgI_2, which is the first experimental observation of noncoincident iodine $\boldsymbol{\delta}_{33}$ and $\mathbf{V}_{33}$ eigenvectors. Information describing the 'interplay' between the $\ddot{V}$ and $\ddot{\delta}$ tensors has been useful in the determination of crystallographic information, even in cases where conclusive diffraction studies are absent.[49]
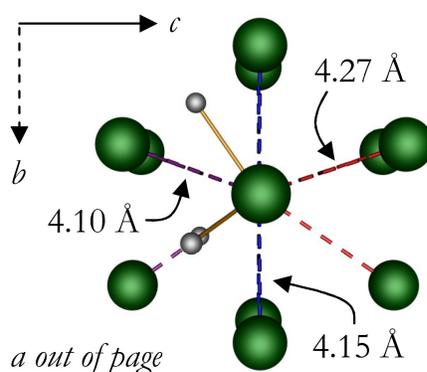
Figure 4.5 POV-ray rendering of the local structure of MgI_2. The local iodide environment (within 4.5 Å) is shown. The iodide environment in MgI_2 is similar to CaI_2 (compare with Figure 4.3c), but possesses inequivalent I–I close contacts both above and below the plane defined by the hexagonally-arranged iodides (red/orange and purple dashed lines, respectively).

4.3.1.1.3 BaI_2: Resolution of Iodide Sites Possessing Similar QIs, and Observation of High-Order Quadrupole-Induced Effects When the High-Field Approximation Is Not Clearly Valid at a Standard Field

Iodine-127 SSNMR experiments were carried out on powdered BaI_2 at B_0 = 11.75 and 21.1 T, and the measured parameters are in Tables 4.1 and 4.2. All observed [127]I SSNMR signals were fit to identical parameters using analytical simulations, except for the chemical shift of site I(2), as analytical simulations at the two applied fields produced two different apparent chemical shift values. Exact simulations (i.e., those which employ full matrix diagonalization, rather than

treating the QI as a perturbation upon the Zeeman states)[50,51] were performed and confirm the

δ_{iso} value for site I(2) measured at $B_0 = 21.1$ T (Appendix B, Figure B.2). BaI$_2$ belongs to the

Pnma space group and possesses two unique I$^-$ within the crystal lattice, which are labeled I(1)

and I(2), as in Figure 4.6.[52] Both I sites possess *m* symmetry, which constrains the potential

Euler angle values. The primary difference between the two I$^-$ sites in BaI$_2$ is that I(1) is

coordinated by 5 Ba^{2+} ions, while I(2) is coordinated by 4 Ba^{2+} ions.
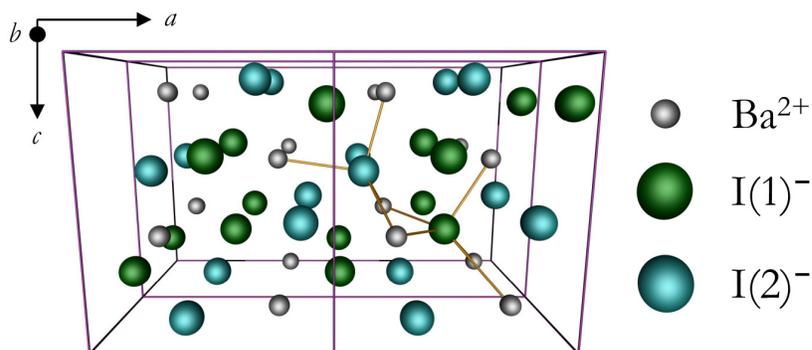
Figure 4.6 POV-ray rendering of the BaI$_2$ quadruple unit cell, as viewed nearly along *b* (10° counterclockwise rotation about the +*a* axis). For the unique I, solid lines connect heteroatoms within the sum of the Ba and I vdW radii (i.e., $r_{Ba-I} < 4.66$ Å). For each I site, numerous additional homoatomic contacts exist within the I first coordination sphere.

Inspection of the ^{127}I SSNMR spectra of BaI$_2$ (Figures 4.7 and 4.8) clearly reveals that

the $\ddot{V}$ tensor magnitudes for both I sites are similar, as the corresponding ^{127}I SSNMR signal

line widths are comparable. Relative to SrI$_2$ (*vide infra*, Chapter 5), BaI$_2$ represents a more

stringent test of the resolving power of ^{127}I SSNMR. The $C_Q(^{127}$I) value for the 5-coordinate I(1)

site is slightly smaller than that for the 4-coordinate I(2) site (i.e., 96.2(0.8) MHz vs. 120.9(0.2)

MHz). While the ^{127}I EFG tensor at the I(1) site is not axially symmetric ($\eta_Q = 0.175(0.015)$),

the $\ddot{V}$ tensor at the I(2) site is observed to be axial ($\eta_Q = 0.015(0.015)$). The $\ddot{V}$ tensor is not

constrained here to be axial by the lattice symmetry. Likewise, quantum chemical calculations

using the accepted crystal structure do not predict an axial EFG tensor (*vide infra*) for either site, in disagreement with the ^{127}I SSNMR data for I(2). For the I(2) site, however, ^{127}I NQR experiments were performed and confirm the $\ddot{V}$ tensor parameters determined using analytical fits to the ^{127}I SSNMR signals (see Appendix B, Figure B.3 for the ^{127}I NQR spectra of site I(2)).
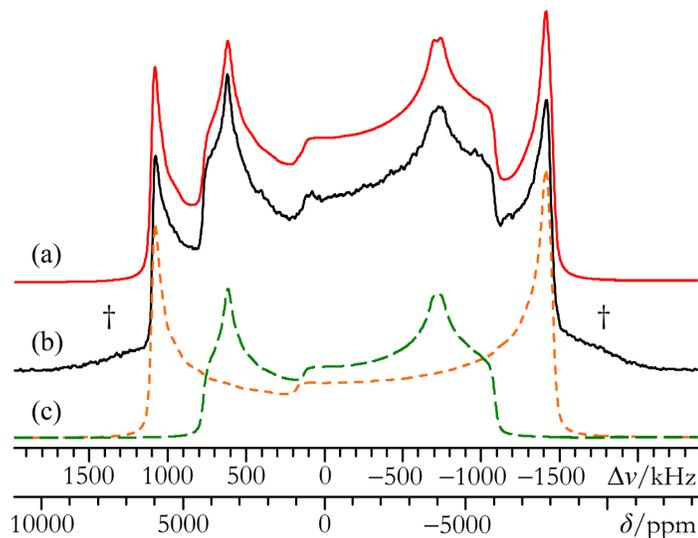
Figure 4.7 Best-fit analytical simulation (a), and experimental static VOCS Solomon echo (b) ^{127}I CT SSNMR spectrum of powdered BaI$_2$ acquired at B_0 = 21.1 T. A de-convolution is shown using the dotted line traces in (c). Partially excited ST are denoted with "†".

Definitive evidence of iodine CSA is present in the ^{127}I SSNMR spectrum of site I(1), due to the characteristic broadening of the low-frequency 'horn' discontinuity, which often results from β deviating from either 0° or 90° (β = 45(20)°; see Appendix B, Figure B.4). The measured iodine Ω value for the I(1) site is the largest reported (Ω = 300(100) ppm). While analytical line shape simulations at both B_0 lead to the same δ_{iso} value for the I(1) site, this is not the case for the I(2) site, which possesses the larger $C_Q(^{127}$I$)$ value. An analytical simulation of the I(2) signal acquired at B_0 = 21.1 T leads to δ_{iso} = 1 000(80) ppm, while the same simulation method using the signal acquired at B_0 = 11.75 T produces an *apparent* chemical shift of 650

ppm. As detailed in Chapter 5, this type of behaviour is clear evidence of high-order quadrupole-induced effects (HOQIE) for the I(2) site at 11.75 T only. It is interesting that the HOQIE are only detectable at the lower applied field, and only for the site with the larger C_Q value. This behaviour should be expected, as HOQIE are anticipated for lower v_0/v_Q ratios. Of course, one may easily rule out iodine CSA effects as the source of the seemingly field-dependent chemical shift for site I(2) in BaI$_2$, as CSA effects scale directly with the applied field, rather than inversely.
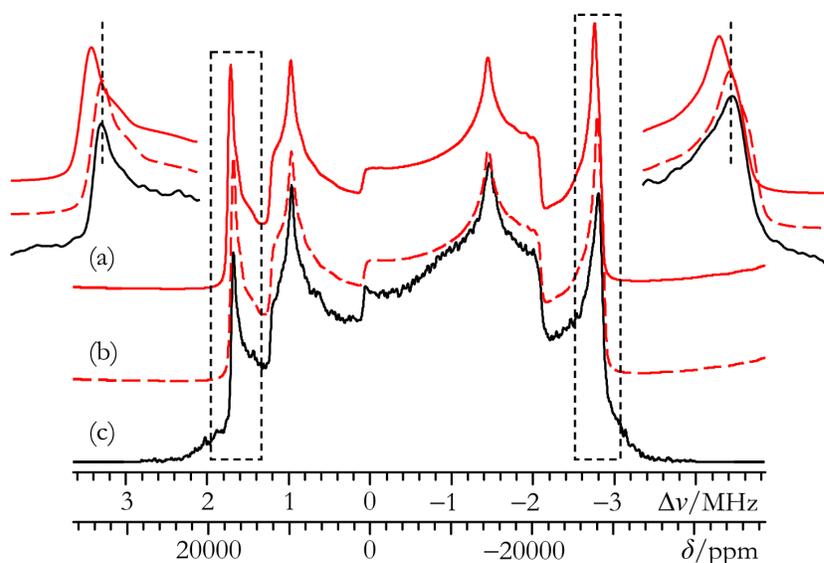
Figure 4.8 Analytical simulation using the known correct parameters (a), best-fit analytical simulation (b), and experimental static VOCS Solomon echo (c) ^{127}I CT SSNMR spectrum of powdered BaI$_2$ acquired at B_0 = 11.75 T. The spectra inset above (a) correspond to the regions in the dotted boxes. They highlight the detectable deviation in the apparent chemical shift when comparing analytical simulations at 11.75 and 21.1 T. This discrepancy is due to orientation-dependent HOQIE (see main text and Appendix B, Figure B.5 for details). The spectra in (a) and (b) employ identical parameters, but for (a), δ_{iso} = 1 000 ppm (i.e., the same value as in Figure 4.7a, and also shown to be correct using exact theory simulations), and for (b), δ_{iso} = 650 ppm.

4.3.1.2 Hydrated Alkaline Earth Metal Iodides: The Effects of Hydration upon Iodine SSNMR Parameters

Iodine-127 SSNMR experiments were carried out on two alkaline earth metal iodide hydrates to observe if there is an effect on the ^{127}I SSNMR parameters as a result of hydration. Previously, $^{35/37}$Cl and $^{79/81}$Br SSNMR experiments on several $MX_2 \cdot nH_2O$ systems (M = alkaline earth metal, X = Cl or Br, n = 2, 4, 6) have established that a decrease in the halogen chemical shift correlates with an increasing degree of hydration (see also Chapter 3).[53,54] It has also been observed in many cases (but not always) that an increase in hydration leads to a decrease in the value of the halogen C_Q. The observed NMR parameters are summarized in Tables 4.3 and 4.4.

Table 4.3 Experimental ^{127}I EFG tensor parameters: alkaline earth metal iodide hydrates[a]

compound	$|C_Q(^{127}I)|$ / MHz	η_Q	notes
BaI$_2$·2H$_2$O	53.8(3)	0.53(1)	T = 295 K
	52.4(3)	0.56(1)	$T \approx 243$ K
	53.7(3)	0.532(0.004)	ref. 41
SrI$_2$·6H$_2$O	133.6(1)[b]	< 0.01	NQR: ν_{Q1} = 20.034(15); ν_{Q2} = 40.068(15)[c]

[a] Error bounds are in parentheses. Parameter definitions are in Section 2.3.3.2.
[b] Established with the aid of ^{127}I NQR experiments.
[c] All ^{127}I NQR frequencies are in MHz.

Table 4.4 Experimental iodine CS tensor parameters: alkaline earth metal iodide hydrates[a]

compound	δ_{iso}[b] / ppm	Ω / ppm	κ	α, β, γ / °	notes
BaI$_2$·2H$_2$O	630(20)	60(15)	> 0.5	45(15), 45(15), —	T = 295 K
	630	60	> 0.5	45, 45, —	$T \approx 243$ K
SrI$_2$·6H$_2$O	440(25)[c]	—	—	—	—

[a] Includes Euler angle values. Error bounds are in parentheses. Parameter definitions are in Sections 2.3.2.4, 2.3.3.1, and 2.3.3.3.
[b] With respect to 0.1 mol/dm³ KI in D$_2$O (δ_{iso} = 0.00 ppm).
[c] Established with the aid of exact simulation software.

4.3.1.2.1   BaI₂·2H₂O

The crystal structure of $BaI_2 \cdot 2H_2O$ has not been determined; however, using [127]I and [135/137]Ba NQR data, it has been suggested that $BaI_2 \cdot 2H_2O$ is isostructural to $BaBr_2 \cdot 2H_2O$.[40,41] Further comments will be provided on their isostructural nature and a proposal for the solid state structure of $BaI_2 \cdot 2H_2O$ will be presented in the quantum chemical calculations section (see Section 4.3.2.1).
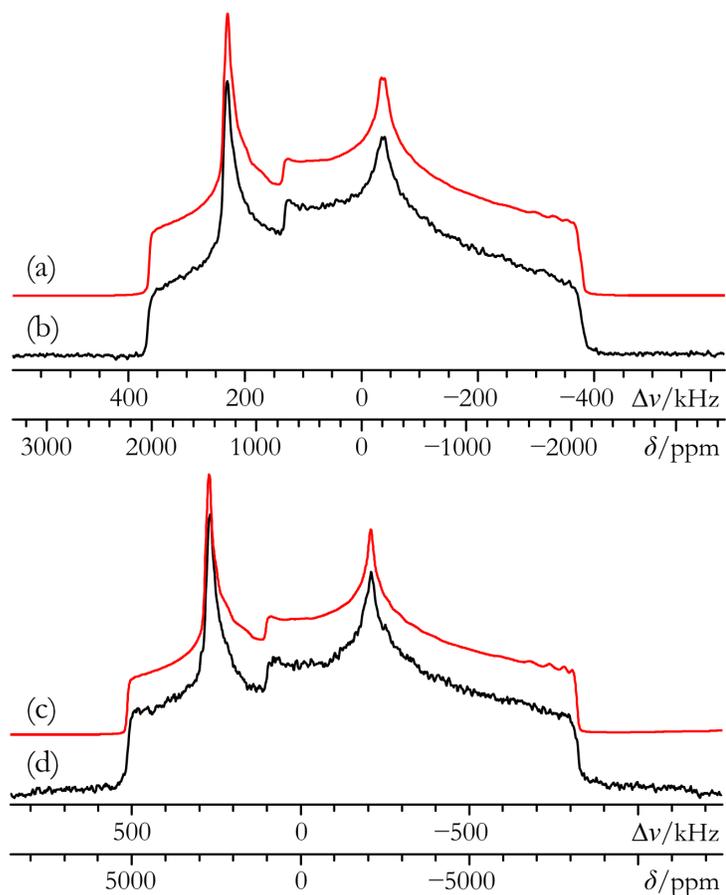
Figure 4.9 Best-fit analytical simulations (a, c), experimental static VOCS [127]I{[1]H} CT Solomon echo (b), and experimental static VOCS [127]I CT Hahn echo (d) SSNMR spectra of powdered $BaI_2 \cdot 2H_2O$ acquired at (b) $B_0 = 21.1$ T and (d) $B_0 = 11.75$ T.

Using powdered $BaI_2 \cdot 2H_2O$, identical ^{127}I EFG and CS tensor parameters were extracted from the ^{127}I SSNMR spectra measured at B_0 = 11.75 and 21.1 T (Figure 4.9). It is interesting to note that grinding the sample, even under an inert atmosphere, creates a second phase (Appendix B, Figures B.6 and B.7). The $\ddot{V}$ tensor parameters measured using the ^{127}I SSNMR line shapes in Figure 4.9 (i.e., $C_Q(^{127}I)$ = 53.8(3) MHz; η_Q = 0.53(1)) match quantitatively with those measured using ^{127}I NQR.[40] Perhaps surprisingly, ^1H decoupling was essential to resolve the fine spectral detail at 21.1 T (Appendix B, Figure B.6), and allows for the quantification of $\ddot{V}$ and $\ddot{\sigma}$ tensor noncoincidence. It has also been confirmed, using variable temperature ^{127}I SSNMR experiments (Appendix B, Figure B.7), that the temperature dependence of the $\ddot{V}$ tensor parameters is identical to that observed using ^{127}I NQR. As expected, the iodine chemical shift (δ_{iso} = 630(20) ppm) is low relative to the anhydrous compounds discussed earlier.

4.3.1.2.2 $SrI_2 \cdot 6H_2O$

While the unit cell and select heavy atom positions of $SrI_2 \cdot 6H_2O$ were determined many years ago,[38] the full crystal structure remains unpublished. It is currently accepted that $SrI_2 \cdot 6H_2O$ is isostructural with $SrCl_2 \cdot 6H_2O$.[39] Iodine-127 SSNMR experiments were carried out using powdered $SrI_2 \cdot 6H_2O$ at B_0 = 21.1 T (Figure 4.10), and the measured parameters may be found in Tables 4.3 and 4.4. The observed ^{127}I SSNMR signal provides evidence for a single I environment, which is within an axial EFG (η_Q = 0). Using analytical simulation software, the measured iodine shift (δ = 390(25) ppm) is shielded relative to all the other compounds studied, consistent with the expected trend for halogen δ_{iso} values upon increasing hydration (Chapter 3).

As the iodine QI in $SrI_2 \cdot 6H_2O$ is rather significant ($C_Q(^{127}I)$ = 133.6(1) MHz, hence, $v_0/v_Q \approx 9$), ^{127}I NQR experiments were also performed for this compound and confirmed the

$\ddot{V}$ tensor parameters extracted from modeling the ^{127}I SSNMR spectrum. In addition, since the ^{127}I SSNMR spectrum possessed very sharply defined 'horn' discontinuities, exact simulations were carried out for this compound in the hopes of finding HOQIE. Using exact theory simulations in tandem with ^{127}I NQR measurements (Appendix B, Figures B.8 and B.9), the above $C_Q(^{127}$I) and η_Q values are confirmed, but it is also found that $\delta_{iso} = 440(25)$ ppm, which is evidence of HOQIE for this compound. Due to the large QI, iodine CSA could not be conclusively measured in SrI$_2\cdot$6H$_2$O.
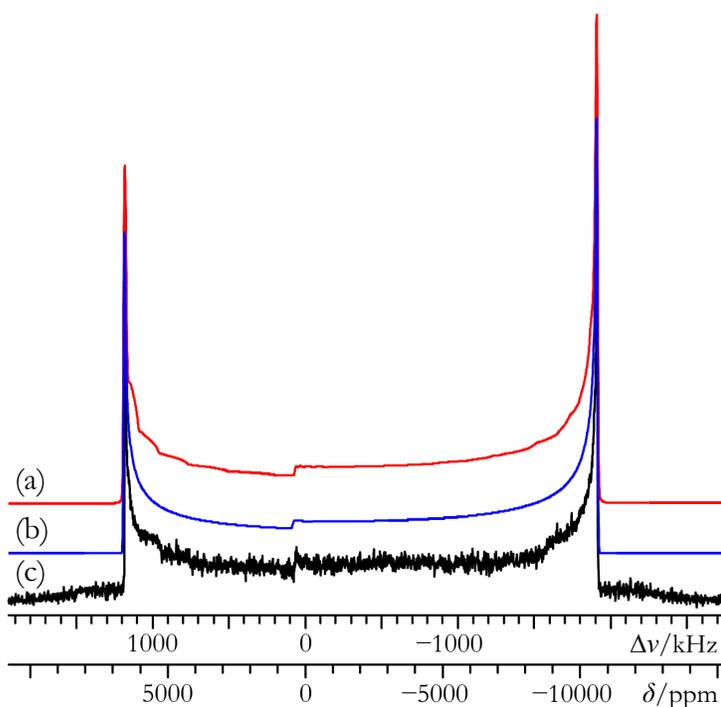
Figure 4.10 Best-fit analytical simulation (a), best-fit exact simulation (b), and experimental static VOCS Solomon echo (c) ^{127}I CT SSNMR spectrum of powdered SrI$_2\cdot$6H$_2$O acquired at $B_0 = 21.1$ T.

4.3.1.3 CdI$_2$ (4H): Application of Iodine-127 SSNMR to a Semiconducting Material

Cadmium iodide is a polytypic semiconducting material.[55] In general, polytypic materials result from one-dimensional disorder due to stacking faults. The common polytype of CdI$_2$, denoted as 4H, belongs to the $P6_3mc$ space group and possesses a stacking fault along the c axis,

which doubles the c value relative to the CdI$_2$ (2H) polytype.[56] There are two unique iodide sites per unit cell (Figure 4.11). Both ^{127}I NQR[57-59] and ^{113}Cd NMR[60-62] data exist for CdI$_2$ (4H).
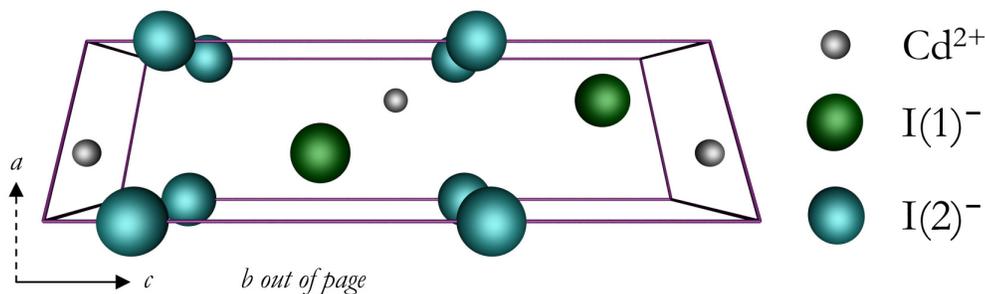
Figure 4.11 POV-ray rendering of the CdI$_2$ (4H) unit cell, as viewed along b.

Iodine-127 SSNMR experiments were performed at 11.75 and 21.1 T on a powdered sample of CdI$_2$ (4H) (see Tables 4.1 and 4.2 for the relevant SSNMR parameters). The observed ^{127}I SSNMR signals at both fields exhibit very broad 'horn' discontinuities (Figure 4.12); hence, it is not possible to resolve the two expected I sites in this material. According to prior ^{127}I NQR data, the v_Q values for the two sites differ by only 2 %;[58] thus, the inability to resolve the sites using ^{127}I SSNMR is not surprising. Using a one-site model (Figures 4.12a and 4.12d), a moderately large ($C_Q(^{127}\text{I}) = 95.7(1.0)$ MHz), axial QI is observed, in very good agreement with prior ^{127}I NQR measurements. The breadth of the horn discontinuities hints at a second iodine site, which has a similar EFG tensor (see Figures 4.12b and 4.12e for fits using a two-site model). Although CSA was neglected in the line shape simulations, the observed δ_{iso} value of 1450(100) ppm (one-site model) is very significantly deshielded relative to the other compounds studied. This effect could be expected, as semiconducting materials have a relatively reduced HOMO–LUMO gap (Δ_{HL}). According to Ramsey's model of magnetic shielding,[63-65] paramagnetic shielding contributions are enhanced by a smaller Δ_{HL}, which generally leads to reduced nuclear shielding (i.e., a more positive chemical shift value).
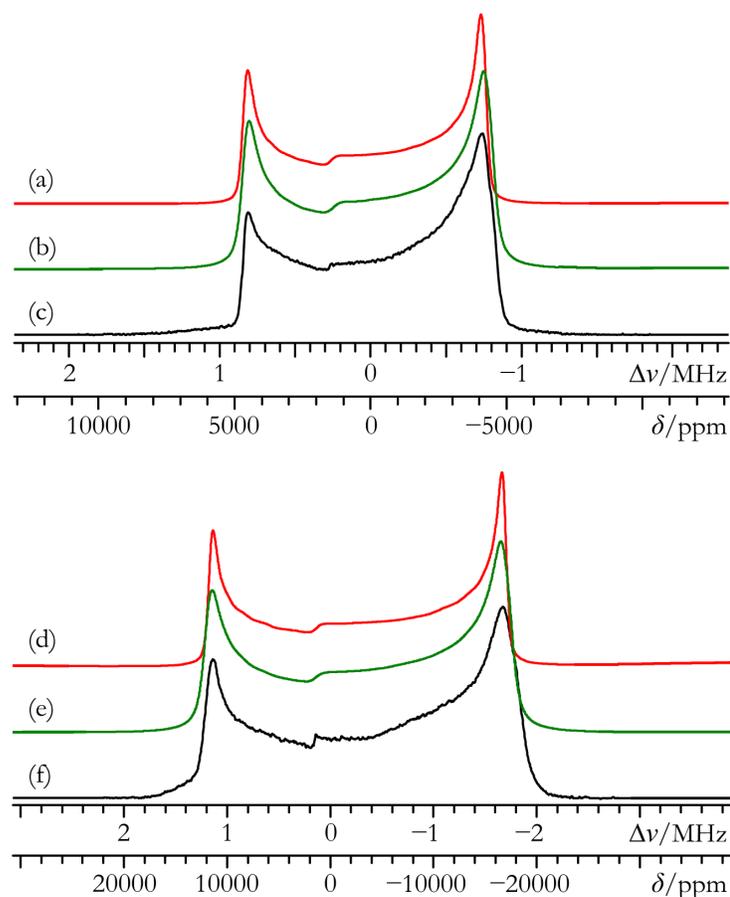
Figure 4.12 One-site analytical simulations (a, d), two-site analytical simulations (b, e), and experimental static VOCS Solomon echo (c, f) ^{127}I CT SSNMR spectra of powdered CdI$_2$ (4H) acquired at B_0 = 21.1 T (c) and B_0 = 11.75 T (f).

4.3.1.4 Discussion of Halogen SSNMR Parameters across the Alkaline Earth Metal Halides

4.3.1.4.1 Nuclear Quadrupole Coupling Constants

Earlier (including in Chapter 3), it was observed that the alkaline earth metal chloride and bromide hydrates nearly always possessed smaller $C_Q(X)$ values when compared to their anhydrous analogs.[53,54] This appears to also hold true for the alkaline earth metal iodides. As each quadrupolar halogen nucleus possesses a unique Q, direct comparisons of interhalogen $C_Q(X)$ values should not be made. Clearly, when one compares similar systems, it is typically observed that $C_Q(^{127}I) \gg C_Q(^{79}Br) > C_Q(^{81}Br) \gg C_Q(^{35}Cl) > C_Q(^{37}Cl)$.

As noted in Chapter 3, it has been demonstrated that a linear relationship exists when C_Q is plotted against $Q(1 - \gamma_\infty)/V$.[66] Within the alkaline earth metal halide compounds that have been studied, many isostructural compounds are known (i.e., $MgBr_2/MgI_2$, $MgCl_2 \cdot 6H_2O/MgBr_2 \cdot 6H_2O$, $CaCl_2/CaBr_2$, $BaCl_2/BaBr_2/BaI_2$, $SrCl_2 \cdot 6H_2O/SrBr_2 \cdot 6H_2O$), while others are suspected (i.e., $BaBr_2 \cdot 2H_2O/BaI_2 \cdot 2H_2O$, $Sr(Cl/Br)_2 \cdot 6H_2O/SrI_2 \cdot 6H_2O$). From the known isostructural series where sufficient data exist, the linear relationship between C_Q and $Q(1 - \gamma_\infty)/V$ is again observed (Figure 4.13).
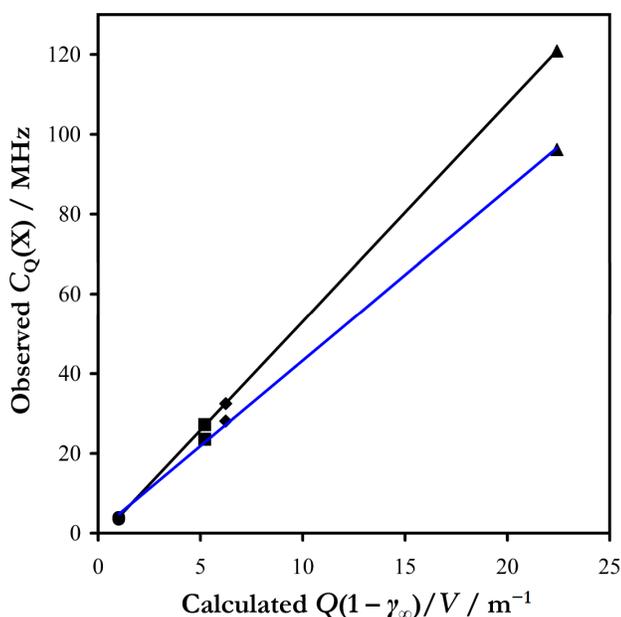
Figure 4.13 A plot of observed halogen C_Q versus calculated $Q(1 - \gamma_\infty)/V$ for the unique halide sites in the known isostructural BaX_2 (X = Cl, Br, I) series. Data for the site possessing generally larger C_Q values across this series, corresponding to a 4-coordinate halide ion, are fit to the following equation (black): $C_Q(X) = 5.4606[Q(1 - \gamma_\infty)/V] - 1.478$ ($R^2 = 1.0$). Data for the site possessing generally smaller C_Q values, corresponding to a 5-coordinate halide ion, are fit to the following (blue): $C_Q(X) = 4.2891[Q(1 - \gamma_\infty)/V] + 0.4246$ ($R^2 = 0.9994$). Observed data points correspond to ^{35}Cl (●), ^{81}Br (■), ^{79}Br (◆), and ^{127}I (▲) SSNMR measurements. Source data for all relevant parameters are in Appendix B, Table B.4.

Where data are sparse, observed C_Q ratios (e.g., $C_Q(^{81}Br)/C_Q(^{35}Cl)$ in $CaBr_2/CaCl_2$) should closely agree with the corresponding calculated $Q(1 - \gamma_\infty)/V$ ratios.[54] Input data for

these computations, as well as the ratios, are summarized in Appendix B, Tables B.4 and B.5. Overall, there is fair agreement between the C_Q and $Q(1 - \gamma_\infty)/V$ ratios (average difference = 20.1 %). On the basis of the above results, it is likely that the relationship between C_Q and $Q(1 - \gamma_\infty)/V$ could help confirm whether two compounds are isostructural. Simple calculations have been carried out, using literature values (see Appendix B, Tables B.4 and B.5) for the relevant parameters (except the unit cell volume for $BaI_2 \cdot 2H_2O$, which was computationally optimized (*vide infra*)) to establish if $Sr(Cl/Br)_2 \cdot 6H_2O$ and $BaBr_2 \cdot 2H_2O$ are isostructural to $SrI_2 \cdot 6H_2O$ and $BaI_2 \cdot 2H_2O$, respectively. By plotting C_Q versus $Q(1 - \gamma_\infty)/V$ for the suspected isostructural series of $SrX_2 \cdot 6H_2O$ (X = Cl, Br, I), a linear relationship is observed (Figure 4.14).
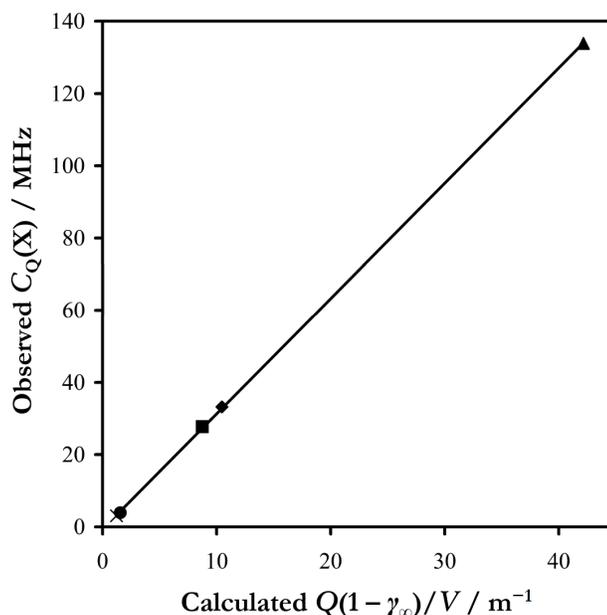
Figure 4.14 A plot of observed halogen C_Q values versus calculated $Q(1 - \gamma_\infty)/V$ for the suspected isostructural $SrX_2 \cdot 6H_2O$ (X = Cl, Br, I) series. The data are fit to the following linear equation: $C_Q(X)$ = 3.1868$[Q(1 - \gamma_\infty)/V]$ − 0.596 (R^2 = 0.9999). Observed data points correspond to [37]Cl (×), [35]Cl (●), [81]Br (■), [79]Br (◆), and [127]I (▲) SSNMR measurements. Relevant source data are in Appendix B, Table B.4.

This finding adds support to the argument that $SrI_2 \cdot 6H_2O$ belongs to this isostructural series. Similarly for $BaBr_2 \cdot 2H_2O$ and $BaI_2 \cdot 2H_2O$, the $C_Q(^{127}I)/C_Q(^{79}Br)$ ratio is 6.16, whereas the

calculated $(Q(^{127}\text{I})[1 - \gamma_\infty(\text{I})]/V_\text{I})/(Q(^{79}\text{Br})[1 - \gamma_\infty(\text{Br})]/V_\text{Br})$ ratio is 3.71 (% difference = 49.6 %). The $C_\text{Q}/[Q(1 - \gamma_\infty)/V]$ relationship therefore cannot confirm the postulated isostructural nature between $\text{BaBr}_2 \cdot 2\text{H}_2\text{O}$ and $\text{BaI}_2 \cdot 2\text{H}_2\text{O}$; rather it hints that they are not exactly isostructural.

4.3.1.4.2 Halogen Chemical Shifts

If the halogen chemical shift values of the alkaline earth metal halides can be understood in a similar fashion as the alkali metal halides, then it is the orbital overlap between the halogen ion and both its NN and NNN which largely determines the observed chemical shifts.[67,68] As with the alkaline earth metal chlorides and bromides, a significant decrease in the observed iodine chemical shift results upon increasing the degree of hydration for the alkaline earth metal iodides. Structurally, it is also generally seen that increasing hydration increases the average internuclear metal-halogen first-coordination sphere distance $(\overline{r(\text{M}-\text{X})})$, and/or decreases the number of M^{2+} species in the halogen first-coordination sphere. Neglecting polarization effects, an increase in $\overline{r(\text{M}-\text{X})}$ must lead to reduced M–X orbital overlap, which in turn decreases paramagnetic shielding contributions to $\ddot{\sigma}$.[48] As paramagnetic shielding normally corresponds to positive chemical shifts, a reduced contribution to this shielding mechanism would lead to reduced chemical shifts, as typically observed.

It has also been observed that there is some overlap in the halogen CS regions corresponding to anhydrous, dihydrate, and hexahydrate compounds for the chlorides,[53] while this overlap is not observed for the heavier halogens (see also Chapter 3). The reason for the decreased overlap for the heavier nuclides may be rationalized using the arguments of Jameson and Gutowsky: they noted that the CS ranges for the main group elements correlates with the value of $\langle 1/r^3 \rangle_{np}$, which is the average value of $1/r^3$ over the valence p electrons for a free

atom.[69] As diamagnetic shielding strongly depends upon the core electrons,[48] its value is largely invariant with respect to the chemical environment. Hence, the observed variation in the δ_{iso} ranges across the main group nuclides is primarily due to differences in paramagnetic shielding. According to a recent review of the quadrupolar halogen nuclei, the total known chlorine, bromine, and iodine δ_{iso} ranges are roughly 1 100, 2 700, and 4 050 ppm, respectively.[18] Corresponding δ_{iso} ranges for the alkaline earth metal chlorides, bromides, and iodides (including hydrates) are ca. 185, 420, and 560 ppm.[53,54,70] When these ranges are plotted as functions of $\langle a_0^3 / r^3 \rangle_{np}$ (a_0 is the atomic Bohr radius), linear relationships with high correlation coefficients (both $R^2 > 0.997$) are observed (Figure 4.15). According to the above relationship, the δ_{iso} ranges for particular groupings of compounds should exhibit less spectral overlap for bromine and iodine, relative to chlorine, as observed.
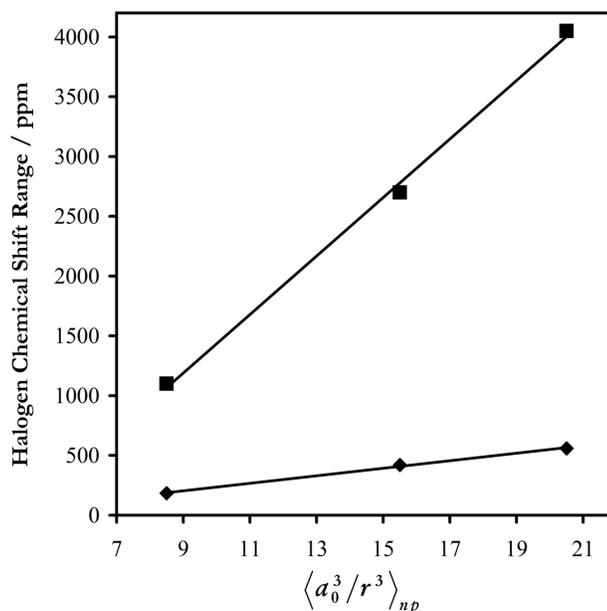
Figure 4.15 Plot of observed halogen CS ranges versus $\langle a_0^3 / r^3 \rangle_{np}$ for all compounds ($\blacksquare$ series), and for the alkaline earth metal halides ($\blacklozenge$ series). The lines of best-fit are as follows: $\blacklozenge$ series, $y = 31.399x - 77.42$, $R^2 = 0.9976$; $\blacksquare$ series: $y = 244.72x - 1013.4$, $R^2 = 0.9978$. All $\langle a_0^3 / r^3 \rangle_{np}$ values are from ref. 71.

4.3.2 GIPAW DFT Quantum Chemical Computations

GIPAW DFT[26] quantum chemical calculations have recently proven to be accurate for the calculation of NMR parameters for a variety of nuclei in inorganic systems.[53,54,72-78] As crystal structures exist for all the anhydrous compounds studied here, the GIPAW DFT method was used to calculate energies and $\ddot{\sigma}/\ddot{V}$ for these compounds. Computed energies and the crystal structures used can be found in Appendix B, Tables B.2 and B.3, while the calculated iodine SSNMR parameters are in Tables 4.5 – 4.8.

Table 4.5 GIPAW DFT ^{127}I EFG tensor parameters: alkaline earth metal iodides and CdI$_2$[a]

compound	functional	site label	$C_Q(^{127}I)$ / MHz	η_Q	$\nu_Q(^{127}I)$ / MHz
MgI$_2$	PBE	—	80.97	0.000	12.14
	PW91	—	81.42	0.000	12.21
CaI$_2$	PBE	—	42.21	0.000	6.33
	PW91	—	43.19	0.000	6.48
SrI$_2$	PBE	I(1)	−107.92	0.326	16.47
		I(2)	231.34	0.321	35.29
	PW91	I(1)	−108.59	0.325	16.57
		I(2)	232.83	0.319	35.51
BaBr$_2$	PBE	I(1)	84.60	0.176	12.76
		I(2)	−151.19	0.078	22.70
	PW91	I(1)	84.73	0.180	12.78
		I(2)	−151.86	0.077	22.80
CdI$_2$ (4H)	PBE	I(1)	90.09	0.000	13.51
		I(2)	93.30	0.000	14.00
	PW91	I(1)	92.05	0.000	13.81
		I(2)	95.37	0.000	14.30

[a] Parameter definitions are in Section 2.3.3.2. MgI$_2$ calculations used E_{cut} = 1000 eV and a 9 × 9 × 6 k-point grid; CaI$_2$ calculations used E_{cut} = 1200 eV and a 9 × 9 × 6 k-point grid; SrI$_2$ calculations used E_{cut} = 550 eV and a 2 × 4 × 4 k-point grid; BaI$_2$ calculations used E_{cut} = 600 eV and a 4 × 6 × 3 k-point grid; CdI$_2$ (4H) calculations used E_{cut} = 1000 eV and a 9 × 9 × 2 k-point grid. For further details, see Appendix B, Table B.6.
[b] To convert $V_{33}(^{127}I)$ into frequency units, a conversion factor of −163.535487 MHz/a.u. was used, and the unit EFG is 9.71736166 × 10^{21} J C^{-1} m^{-2}.

Table 4.6 GIPAW DFT iodine CS tensor parameters: alkaline earth metal iodides and CdI_2[a]

compound	functional	site label	δ_{iso} / ppm	Ω / ppm	κ	α, β, γ / °
MgI_2	PBE	—	1189.8	145.1	−1.00	89.3, 90.0, 0.0
	PW91	—	1192.8	144.0	−1.00	89.3, 90.0, 0.0
CaI_2	PBE	—	1076.8	5.8	1.00	90.0, 0.0, 90.0
	PW91	—	1099.6	6.0	1.00	90.0, 0.0, 90.0
SrI_2	PBE	I(1)	1034.1	221.3	0.39	138.7, 36.3, 259.1
		I(2)	947.6	460.5	0.63	104.6, 89.8, 333.7
	PW91	I(1)	1043.5	217.0	0.40	137.1, 35.5, 257.7
		I(2)	953.9	458.4	0.63	104.2, 89.7, 333.2
BaI_2	PBE	I(1)	889.4	493.8	−0.63	0.0, 47.1, 180.0
		I(2)	1230.6	239.4	0.48	180.0, 36.4, 180.0
	PW91	I(1)	906.0	496.4	−0.63	0.0, 47.2, 180.0
		I(2)	1250.7	242.6	0.49	180.0, 36.5, 180.0
CdI_2 (4H)	PBE	I(1)	2078.2	171.8	−0.99	273.1, 90.0, 180.0
		I(2)	1937.5	428.0	−1.00	273.0, 90.0, 180.0
	PW91	I(1)	2169.6	181.7	−0.99	273.0, 90.0, 180.0
		I(2)	2023.8	449.1	−1.00	273.0, 90.0, 180.0

[a] Includes Euler angle values. Parameter definitions are in Sections 2.3.2.4, 2.3.3.1, and 2.3.3.3. Selected calculation details are as given in Table 4.5. For further details, see Appendix B, Table B.7.

Table 4.7 GIPAW DFT ^{127}I EFG tensor parameters: alkaline earth metal iodide hydrates

compound	functional	$C_Q(^{127}I)$ / MHz	η_Q	$\nu_Q(^{127}I)$ / MHz
$SrI_2 \cdot 6H_2O$[a]	PBE	191.37	0.000	28.70
	PW91	191.17	0.000	28.68
$BaI_2 \cdot 2H_2O$[b]	PBE	65.86	0.408	10.15
	PW91	66.67	0.429	10.30

[a] Geometry optimization used E_{cut} = 700 eV, while NMR parameter calculations used E_{cut} = 800 eV. All calculations used a $5 \times 5 \times 8$ k-point grid.
[b] Geometry optimization used E_{cut} = 450 eV, while NMR parameter calculations used E_{cut} = 650 eV. All calculations used a $2 \times 3 \times 3$ k-point grid. See also footnote b of Table 4.5. For further details, see Appendix B, Table B.8.

Table 4.8 GIPAW DFT iodine CS tensor parameters: alkaline earth metal iodide hydrates[a]

compound	functional	δ_{iso} / ppm	Ω / ppm	κ	α, β, γ / °
$SrI_2 \cdot 6H_2O$	PBE	352.9	14.3	−0.99	357.7, 90.0, 180.1
	PW91	362.9	14.9	−0.99	358.8, 90.0, 180.1
$BaI_2 \cdot 2H_2O$	PBE	663.6	82.5	−0.38	250.4, 86.4, 325.0
	PW91	681.0	84.1	−0.36	251.7, 86.4, 324.7

[a] Includes Euler angle values. Parameter definitions are in Sections 2.3.2.4, 2.3.3.1, and 2.3.3.3. Selected calculation details are as given in Table 4.7. For further details, see Appendix B, Table B.9.

4.3.2.1 *Structure Proposals for BaI₂·2H₂O and SrI₂·6H₂O*

As noted earlier, fully refined structural data are not available for $SrI_2 \cdot 6H_2O$ and structural data do not exist for $BaI_2 \cdot 2H_2O$. Earlier studies have assumed that $SrI_2 \cdot 6H_2O$ and $BaI_2 \cdot 2H_2O$ are isostructural to their analogous metal bromide hydrates.[38,40,41] GIPAW DFT was successfully used to generate optimized structures for both, the coordinates of which can be found in Appendix B, Table B.3. These optimized structures were used for subsequent SSNMR parameter calculations.

4.3.2.2 *Calculated Iodine $\ddot{\sigma}$ and $\ddot{V}$ Tensor Magnitudes, Symmetries, and Orientations*

As with the alkaline earth metal chlorides and bromides studied earlier (see also Chapter 3),[53,54] the GIPAW DFT method reproduces the experimental halogen SSNMR parameters rather well in several cases (Figure 4.16), as quantified by R^2 values of near unity. Calculated and experimental $C_Q(^{127}I)$ values are in very good to excellent agreement (rmsd = 13.8 MHz, excluding the $SrI_2 \cdot 6H_2O$ datum) in most cases (Figure 4.16a), although the computed magnitudes are typically slightly greater than those observed (this is rather notably so for the optimized hydrate structures). Quantitative agreement between calculated and experimental η_Q values (Figure 4.16b) is observed in all cases where the local site symmetry constrains the EFG tensor to be axial (i.e., MgI_2, CaI_2, CdI_2 (4H), $SrI_2 \cdot 6H_2O$) and in select cases when the EFG is

not constrained to be axial (i.e., SrI_2, site I(2), BaI_2, site I(1)). On the basis of the very good agreement between the experimental and computed values for C_Q and η_Q, it can be stated that relativistic effects on the $\ddot{V}$ tensor appear to be minimal in these systems. Calculated δ_{iso} values are typically overestimated relative to experiment (Figure 4.16c), but reproduce the observed trend in δ_{iso} (i.e., $\delta_{iso}(CdI_2 (4H)) >> \delta_{iso}(MI_2) > \delta_{iso}(BaI_2·2H_2O) > \delta_{iso}(SrI_2·6H_2O)$).
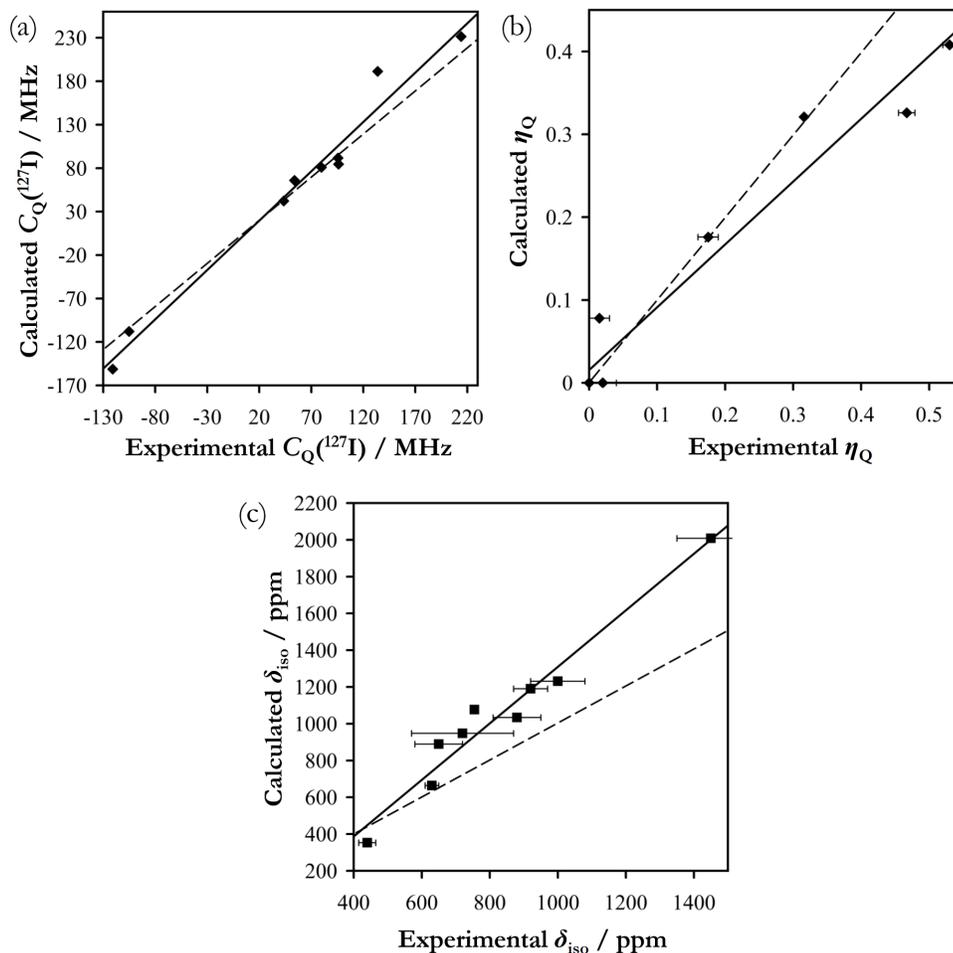
Figure 4.16 Plots of GIPAW DFT computed versus experimental values for (a) $C_Q(^{127}I)$; (b) for η_Q; (c) for δ_{iso}. Experimental data are from Tables 4.1 to 4.4, while calculated data are from Tables 4.5 to 4.8. All computed values are from PBE XC functional calculations. Solid lines are of best linear fit, while dashed lines denote an ideal fit (i.e., $y = x$). The lines of best fit are as follows: (a) $C_Q(^{127}I,calc) = 1.135(C_Q(^{127}I,exp)) - 3.127$, $R^2 = 0.9755$; (b) $\eta_Q(calc) = 0.758(\eta_Q(exp)) + 0.016$, $R^2 = 0.9457$; (c) $\delta_{iso}(calc) = 1.537(\delta_{iso}(exp)) - 227.48$, $R^2 = 0.9581$.

For the remaining parameters, experimental data exist for only three compounds; hence, definitive conclusions cannot be made. The $\ddot{V}$ and $\ddot{\sigma}$ eigenvectors have been calculated and are presented in their respective crystal frames in Figures B.10 to B.16 of Appendix B, while normalized eigenvector components are in Table B.10 of Appendix B. As with the alkaline earth metal bromides,[54] the tensor eigenvectors often (but not in general) point towards a nearby ion.

4.3.2.3 Understanding the Dramatically Different $C_Q(^{127}I)$ Values for MgI₂ and CaI₂

Here, the substantial difference in the observed $C_Q(^{127}I)$ values for MgI_2 and CaI_2, two compounds which were long considered to be isostructural, is rationalized. In 2003, it was revealed that while both belong to the $P\bar{3}m1$ space group and place the halide anions at 2d Wyckoff sites (i.e., $x/a = 0, y/b = 0, z/c = u$, where u is variable), they possess slightly different u values ($u = 0.25$ and 0.24237 for CaI_2 and MgI_2, respectively).[45] As demonstrated above for several isostructural compounds, if MgI_2 and CaI_2 were isostructural, they should possess similar $C_Q(^{127}I)$ values, likely scaled by the ratio of their unit cell volumes. As the halogen u value is the only clear difference between these two structures, a quantum chemical study was undertaken where the u value for each of MgI_2 and CaI_2 was incremented. A summary of the $C_Q(^{127}I)$ and system energy variation as a result of small displacements (i.e., ±0.07 Å) from the crystallographic positions parallel to the c crystal axis (i.e., Δc) is provided in Figure 4.17. It is immediately clear that very subtle alterations in u result in a substantial augmentation of the calculated $C_Q(^{127}I)$ value for both compounds. For MgI_2, the total variation in the calculated $C_Q(^{127}I)$ values is from 140 to 19.6 MHz (Figure 4.17a). Similar behaviour is seen for CaI_2 (Figure 4.17b). In light of the sensitivity of $C_Q(^{127}I)$ to structure, it is remarkable that the values calculated for CaI_2 and MgI_2 using the known crystal structures agree nearly quantitatively with

experiment. It is clear that ^{127}I SSNMR observations, when coupled with GIPAW DFT calculations, may be applied to further *refine* crystal structures of inorganic iodide-containing materials, which echoes earlier findings for other nuclides.[49,70] This may also explain why the computed $C_Q(^{127}I)$ values for the GIPAW DFT optimized BaI$_2$·2H$_2$O and SrI$_2$·6H$_2$O crystal structures differ more from the observed values, relative to the cases where XRD or neutron diffraction structures were available.
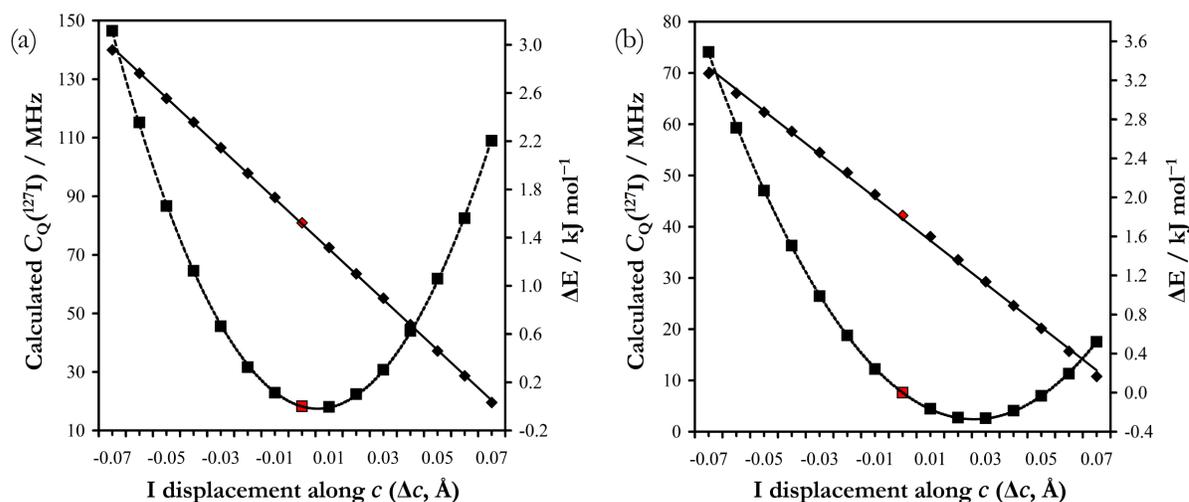
Figure 4.17 Plots of GIPAW DFT computed $C_Q(^{127}I)$ (left vertical axis, ◆) and relative system energies (right vertical axis, ■) as functions of the iodide *c*-axis displacement in (a) MgI$_2$ and (b) CaI$_2$. Relative energies are such that the energy associated with the accepted crystal structure (E_{xtal}) = 0 kJ mol^{-1}. The *c*-axis displacements are such that the accepted crystal structure *c* displacement (Δc_{xtal}) = 0.0 Å. All calculations used E_{cut} = 800 eV, 9 × 9 × 6 *k*-points, and the PBE XC functional. The lines of best fit are as follows: (a) $C_Q(^{127}I)$ = −861.0(Δc) + 80.58, R^2 = 0.9999; ΔE = 543.6(Δc)^2 − 6.358(Δc) − 0.0005, R^2 = 0.9998; (b) $C_Q(^{127}I)$ = −421.9(Δc) + 41.51, R^2 = 0.9988; ΔE = 407.7(Δc)^2 − 21.08(Δc) − 0.0004, R^2 = 0.9999. For each series, the data point corresponding to (Δc_{xtal}, E_{xtal}) is in red.

4.4   Conclusions

Iodine-127 SSNMR has been established as a useful tool for probing the environment of iodide ions in inorganic solids. The pronounced sensitivity of the ^{127}I NMR interaction tensors

to local symmetry elements and structure has been demonstrated and holds a potential application in crystallographic structure refinement. As ultrahigh magnetic fields become increasingly accessible, it is clear that SSNMR experiments on 'exotic' quadrupolar nuclei like [127]I will be able to provide useful information regarding the structure and electronic environment about iodide ions. It has been found that multiple field data acquisition can be used to aid in the extraction of iodine CSA data; however, due to the extreme CT signal breadths in several of these systems, one is not always able to perform the experiments at a lower field due to sensitivity issues.

High-order quadrupole-induced effects have been observed using NMR spectroscopy in tandem with exact QI simulation software. While for the systems considered in this Chapter, these effects produced only minor changes in the observed SSNMR line shapes, the proper consideration of these effects will be essential for the correct interpretation of SSNMR spectra for a variety of quadrupolar nuclei which experience a large quadrupolar interaction (as will be demonstrated in Chapter 5).

A number of pertinent trends have been observed. Using C_Q values, halogen SSNMR spectroscopy is shown to be useful in confirming isostructural series, and its predictive power in this regard is illustrated using the $SrX_2 \cdot 6H_2O$ (X = Cl, Br, I) series. There is a clear trend in decreasing halogen δ_{iso} values as the hydration level of the alkaline earth metal halide structure is increased, which is primarily due to the increase in the $\overline{r(M-X)}$ value upon hydration. Finally, quantum chemical computations which employ the GIPAW DFT method reproduce the iodine $\ddot{V}$ tensor parameters in these systems with a high degree of accuracy. These calculations also provided reasonable estimates of iodine δ_{iso} values, although the computed values are generally greater than those observed.

While the prohibitively large EFGs associated with covalent halides are likely to preclude their routine observation using SSNMR experiments, it is nevertheless exciting to ponder the array of systems that halogen SSNMR experiments may be applied to when a halogen anion is present. For example, halogen anions may be intercalated into mesoporous materials, and the utility of ^{81}Br SSNMR experiments at probing these environments has very recently appeared in the literature.[79] Perhaps the most interesting area of application for halogen NMR involves anion receptors[80] (whether biological,[81] biomimetic,[82] organic,[83] etc.), where a number of weak interactions, such as $X^{-}\cdots H$ (hydrogen bonding), $X^{-}\cdots X$ (halogen bonding) and $X^{-}\cdots\pi$ work either individually or in tandem to stabilize the host anion(s). It will be interesting to see if halogen SSNMR experiments can serve as useful probes of the weak interactions experienced in these systems.

4.5   References

1   C. E. Housecroft and A. G. Sharpe, *Inorganic Chemistry*, Pearson Education Limited: Harlow, England, **2001**.

2   P. A. Shelton, Y. Zhang, T. H. H. Nguyen and L. McElwee-White, *Chem. Commun.*, **2009**, 947-949.

3   P. Metrangolo, Y. Carcenac, M. Lahtinen, T. Pilati, K. Rissanen, A. Vij and G. Resnati, *Science*, **2009**, *323*, 1461-1464.

4   K. C. Nicolaou, S. P. Ellery and J. S. Chen, *Angew. Chem. Int. Ed.*, **2009**, *48*, 7140-7165.

5   T. Wirth, *Angew. Chem. Int. Ed.*, **2005**, *44*, 3656-3665.

6   I. Kieltsch, P. Eisenberger and A. Togni, *Angew. Chem. Int. Ed.*, **2007**, *46*, 754-757.

7   R. K. Harris and P. Jackson, *Chem. Rev.*, **1991**, *91*, 1427-1440.

8   J. M. Miller, *Prog. Nucl. Magn. Reson. Spectrosc.*, **1996**, *28*, 255-281.

9   A. S. Ulrich, *Prog. Nucl. Magn. Reson. Spectrosc.*, **2005**, *46*, 1-21.

10 M. Mizuno, T. Iijima, J. Kimura, K. Endo and M. Suhara, *J. Mol. Struct.*, **2002**, *602-603*, 239-244.

11 P. G. Gordon, D. H. Brouwer and J. A. Ripmeester, *Chem. Phys. Chem.*, **2010**, *11*, 260-268.

12 R. Siegel, T. T. Nakashima and R. E. Wasylishen, *Concepts Magn. Reson. A*, **2005**, *26A*, 62-77.

13 G. Wu and S. Dong, *Solid State Nucl. Magn. Reson.*, **2001**, *20*, 100-107.

14 P. Pyykkö, *Mol. Phys.*, **2008**, *106*, 1965-1974.

15 M. H. Cohen and F. Reif, *Solid State Phys.*, **1957**, *5*, 321-438.

16 S. E. Ashbrook, *Phys. Chem. Chem. Phys.*, **2009**, *11*, 6892-6905.

17 R. K. Harris, E. D. Becker, S. M. Cabral De Menezes, P. Granger, R. E. Hoffman and K. W. Zilm, *Pure Appl. Chem.*, **2008**, *80*, 59-84.

18 R. P. Chapman, C. M. Widdifield and D. L. Bryce, *Prog. Nucl. Magn. Reson. Spectrosc.*, **2009**, *55*, 215-237.

19 I. Solomon, *Phys. Rev.*, **1958**, *110*, 61-65.

20 I. D. Weisman and L. H. Bennett, *Phys. Rev.*, **1969**, *181*, 1341-1350.

21 A. C. Kunwar, G. L. Turner and E. Oldfield, *J. Magn. Reson.*, **1986**, *69*, 124-127.

22 E. L. Hahn, *Phys. Rev.*, **1950**, *80*, 580-594.

23 D. Massiot, I. Farnan, N. Gautier, D. Trumeau, A. Trokiner and J. P. Coutures, *Solid State Nucl. Magn. Reson.*, **1995**, *4*, 241-248.

24 A. Medek, V. Frydman and L. Frydman, *J. Phys. Chem. A*, **1999**, *103*, 4830-4835.

25 R. W. Schurko, S. Wi and L. Frydman, *J. Phys. Chem. A*, **2002**, *106*, 51-62.

26 C. J. Pickard and F. Mauri, *Phys. Rev. B*, **2001**, *63*, 245101.

27 J. R. Yates, C. J. Pickard and F. Mauri, *Phys. Rev. B*, **2007**, *76*, 024401.

28 M. Profeta, F. Mauri and C. J. Pickard, *J. Am. Chem. Soc.*, **2003**, *125*, 541-548.

29 S. J. Clark, M. D. Segall, C. J. Pickard, P. J. Hasnip, M. I. J. Probert, K. Refson and M. C. Payne, *Z. Kristallogr.*, **2005**, *220*, 567-570.

30 D. Vanderbilt, *Phys. Rev. B*, **1990**, *41*, 7892-7895.

31 J. P. Perdew, K. Burke and M. Ernzerhof, *Phys. Rev. Lett.*, **1996**, *77*, 3865-3868.

32 J. P. Perdew, K. Burke and M. Ernzerhof, *Phys. Rev. Lett.*, **1997**, *78*, 1396.

33 K. Burke, J. P. Perdew and Y. Wang, Derivation of a Generalized Gradient Approximation: the PW91 Density Functional In *Electronic Density Functional Theory: Recent Progress and New Directions*, J. F. Dobson, G. Vignale and M. P. Das, Eds., Plenum: New York, **1998**, 81-111.

34 J. P. Perdew, Unified Theory of Exchange and Correlation Beyond the Local Density Approximation In *Electronic Structure of Solids '91*, P. Ziesche and H. Eschrig, Eds., Akademie Verlag: Berlin, **1991**, 11-20.

35 J. P. Perdew, J. A. Chevary, S. H. Vosko, K. A. Jackson, M. R. Pederson, D. J. Singh and C. Fiolhais, *Phys. Rev. B*, **1992**, *46*, 6671-6687.

36 J. P. Perdew, J. A. Chevary, S. H. Vosko, K. A. Jackson, M. R. Pederson, D. J. Singh and C. Fiolhais, *Phys. Rev. B*, **1993**, *48*, 4978.

37 J. P. Perdew, K. Burke and Y. Wang, *Phys. Rev. B*, **1996**, *54*, 16533-16539.

38 Z. Herrmann, *Z. Anorg. Allg. Chem.*, **1931**, *197*, 212-218.

39 P. A. Agron and W. R. Busing, *Acta Cryst. C*, **1986**, *C42*, 141-143.

40 A. F. Volkov, *Phys. Stat. Sol. B*, **1972**, *50*, K43-K44.

41 A. F. Volkov, *J. Magn. Reson.*, **1973**, *11*, 73-76.

42 T. Kellersohn, B. Engelen, H. D. Lutz, H. Bartl, B. P. Schweiss and H. Fuess, *Z. Kristallogr.*, **1991**, *197*, 175-184.

43 H. Blum, *Z. Physik. Chem. B*, **1933**, *B22*, 298-304.

44 O. H. Han and E. Oldfield, *Inorg. Chem.*, **1990**, *29*, 3666-3669.

45 M. A. Brogan, A. J. Blake, C. Wilson and D. H. Gregory, *Acta Cryst. C*, **2003**, *C59*, i136-i138.

46 A. Bondi, *J. Phys. Chem.*, **1964**, *68*, 441-451.

47 M. Mantina, A. C. Chamberlin, R. Valero, C. J. Cramer and D. G. Truhlar, *J. Phys. Chem. A*, **2009**, *113*, 5806-5812.

48 C. M. Widdifield and R. W. Schurko, *Concept. Magn. Reson. A*, **2009**, *34A*, 91-123.

49 D. L. Bryce, Tensor Interplay In *NMR Crystallography*, R. K. Harris, R. E. Wasylishen and M. J. Duer, Eds., John Wiley & Sons: West Sussex, United Kingdom, **2009**, 289-301.

50   A. D. Bain, *Mol. Phys.*, **2003**, *101*, 3163-3175.

51   A. D. Bain and B. Berno, *Prog. Nucl. Magn. Reson. Spectrosc.*, **2011**, *59*, 223-244.

52   E. B. Brackett, T. E. Brackett and R. L. Sass, *J. Phys. Chem.*, **1963**, *67*, 2132-2135.

53   D. L. Bryce and E. B. Bultz, *Chem. Eur. J.*, **2007**, *13*, 4786-4796.

54   C. M. Widdifield and D. L. Bryce, *J. Phys. Chem. A*, **2010**, *114*, 2102-2116.

55   G. C. Trigunayat and G. K. Chadha, *Phys. Stat. Sol. A*, **1971**, *4*, 9-42.

56   R. S. Mitchell, *Z. Kristallogr.*, **1956**, *108*, 296-315.

57   S. L. Segel, R. G. Barnes and W. H. Jones, Jr., *Bull. Am. Phys. Soc.*, **1960**, *5*, 412.

58   R. G. Barnes, S. L. Segel and W. H. Jones, Jr., *J. Appl. Phys.*, **1962**, *33*, 296-302.

59   D. L. Lyfar, V. E. Goncharuk and S. M. Ryabchenko, *Phys. Stat. Sol. B*, **1976**, *76*, 183-189.

60   A. Nolle, *Z. Naturforsch. A*, **1978**, *33*, 666-671.

61   P. D. Ellis, *Science*, **1983**, *221*, 1141-1146.

62   S. Sakida and Y. Kawamoto, *J. Phys. Chem. Solids*, **2002**, *63*, 151-161.

63   N. F. Ramsey, *Phys. Rev.*, **1950**, *78*, 699-703.

64   N. F. Ramsey, *Phys. Rev.*, **1951**, *83*, 540-541.

65   N. F. Ramsey, *Physica (The Hague)*, **1951**, *17*, 303-307.

66   G. Wu and V. Terskikh, *J. Phys. Chem. A*, **2008**, *112*, 10359-10364.

67   Y. Yamagata, *J. Phys. Soc. Jpn.*, **1964**, *19*, 10-23.

68   S. Hayashi and K. Hayamizu, *Bull. Chem. Soc. Jpn.*, **1990**, *63*, 913-919.

69   C. J. Jameson and H. S. Gutowsky, *J. Chem. Phys.*, **1964**, *40*, 1714-1724.

70   C. M. Widdifield and D. L. Bryce, *Phys. Chem. Chem. Phys.*, **2009**, *11*, 7120-7122.

71   C. J. Jameson and J. Mason, The Chemical Shift In *Multinuclear NMR*, J. Mason, Ed., Plenum Press: New York, **1987**, 59-65.

72   S. E. Ashbrook, A. J. Berry, D. J. Frost, A. Gregorovic, C. J. Pickard, J. E. Readman and S. Wimperis, *J. Am. Chem. Soc.*, **2007**, *129*, 13213-13224.

73   D. L. Bryce, E. B. Bultz and D. Aebi, *J. Am. Chem. Soc.*, **2008**, *130*, 9282-9292.

74   H. Hamaed, M. W. Laschuk, V. V. Terskikh and R. W. Schurko, *J. Am. Chem. Soc.*, **2009**, *131*, 8271-8279.

75   L. S. Cahill, J. V. Hanna, A. Wong, J. C. C. Freitas, J. R. Yates, R. K. Harris and M. E. Smith, *Chem. Eur. J.*, **2009**, *15*, 9785-9798.

76   A. Sutrisno, C. Lu, R. H. Lipson and Y. Huang, *J. Phys. Chem. C*, **2009**, *113*, 21196-21201.

77   I. Moudrakovski, S. Lang, S. Patchkovskii and J. Ripmeester, *J. Phys. Chem. A*, **2010**, *114*, 309-316.

78   J. V. Hanna, K. J. Pike, T. Charpentier, T. F. Kemp, M. E. Smith, B. E. G. Lucier, R. W. Schurko and L. S. Cahill, *Chem. Eur. J.*, **2010**, *16*, 3222-3239.

79   B. Alonso, T. Mineva, P. Innocenzi, G. Trimmel, K. Stubenrauch, I. Melnyk, Y. Zub, F. Fayon, P. Florian and D. Massiot, *C. R. Chim.*, **2010**, *13*, 431-442.

80   C. Caltagirone and P. A. Gale, *Chem. Soc. Rev.*, **2009**, *38*, 520-563.

81   K. Kawakami, Y. Umena, N. Kamiya and J. R. Shen, *Proc. Natl. Acad. Sci. USA*, **2009**, *106*, 8567-8572.

82   F. Sansone, L. Baldini, A. Casnati, M. Lazzarotto, F. Ugozzoli and R. Ungaro, *Proc. Natl. Acad. Sci. USA*, **2002**, *99*, 4842-4847.

83   M. A. Saeed, F. R. Fronczek and M. A. Hossain, *Chem. Commun.*, **2009**, 6409-6411.

Chapter Five

Definitive Solid-State ^{127}I and $^{185/187}Re$ NMR Spectral Evidence for and Analysis of the Origin of High-Order Quadrupole-Induced Effects for I = 5/2

5.1 Introduction

As noted earlier in this dissertation, the Q of a quadrupolar nucleus can couple with the local EFG at the nucleus.[1] The resulting QI provides information that can be used to complement other SSNMR observables, such as δ_{iso}. Unfortunately, this QI may also drastically broaden the SSNMR signal in powdered samples, sometimes to the extent that the experiment becomes impractical. Despite this potential drawback, SSNMR experiments using quadrupolar nuclei are valuable, as these nuclei can be found in many important areas of chemical research, including biochemistry (e.g., ^2H, ^{14}N, ^{17}O, ^{23}Na, ^{25}Mg, ^{43}Ca, ^{67}Zn), and materials science (e.g., $^{6/7}Li$, ^{11}B, ^{17}O, ^{27}Al).[2] A method for the precise determination of the QI is of critical importance to correctly characterize a wide variety of systems using SSNMR spectroscopy. Until now, it was most common to use second-order perturbation theory to model SSNMR line shapes. The fashion in which first-order perturbation theory modifies the Zeeman eigenstates may be found in Figure 2.10, while the resulting anisotropic CT line shape broadening associated with the second-order QI is depicted in Figure 2.11. Although second-order perturbation theory modeling has been very successful to date, as the sensitivity of SSNMR experiments continues to increase, experiments probing previously 'inaccessible' nuclei are becoming more common and additional care needs to be taken when analyzing the SSNMR spectra of quadrupolar nuclei that experience a very large QI.

A brief overview of the importance of iodine and iodine-containing materials in chemistry, as well as prior [127]I SSNMR literature accounts, can be found in Chapter 4. Likewise, several recent literature reviews on iodine SSNMR have been published.[3-5] Rhenium, a group 7 transition metal, was first detected in 1925, occurs naturally within molybdenum sulfide ores in the earth's crust ($\sim 10^{-7}$ % abundance), and may exist in at least nine oxidation states (ranging from -1 to $+7$).[6,7] Compounds containing rhenium in a relatively reduced oxidation state, such as Re(III), exhibit metal-metal bonding interactions: for example, $K_2Re_2Cl_8$ is recognized as containing the first example of a metal-metal quadruple bond.[8] Rhenium metal possesses very high thermal stability, and is present within the high-temperature alloys used to make jet engine parts.[7] In addition, rhenium-containing compounds have been used as catalysts in many types of organic reactions.[9-11] The nuclei of the two stable isotopes of rhenium ([185]Re/[187]Re) are NMR-active, are present in high natural abundance (37.398(16) % and 62.602(16) % for [185]Re and [187]Re, respectively),[12] and are quadrupolar (I([185/187]Re) $= 5/2$). In addition, they possess relatively high magnetogyric ratios (γ([185]Re) $= 6.1057 \times 10^7$ rad s^{-1} T^{-1}; γ([187]Re) $= 6.1682 \times 10^7$ rad s^{-1} T^{-1}).[13] Despite the potential wealth of diagnostic information that could be extracted using [185/187]Re SSNMR experiments, very few literature reports exist, and they are nearly exclusively restricted to compounds that exhibit very high symmetry,[14-16] or are from measurements carried out at liquid helium temperatures.[17-19] The paucity of [185/187]Re SSNMR studies may be attributed to the very large Q for both NMR-active nuclides (Q([185]Re) $= 2180(20)$ mb; Q([187]Re) $= 2070(20)$ mb).[20] In fact, the line width factor for [185]Re is the highest of the stable elements (1.5×10^4 relative to ^{1}H).[13] As such, even a very small EFG can result in a rhenium QI that broadens the SSNMR powder pattern to the point that it is undetectable. As demonstrated earlier in this dissertation, by performing the SSNMR experiments within as high a B_0 as possible, a partial remedy to this problem is found.

Thankfully, as high magnetic fields (i.e., $B_0 > 18.8$ T) are becoming increasingly available, SSNMR experiments on previously inaccessible nuclei are now potentially feasible, but remain technically challenging as they often require sensitivity-enhancing pulse sequences[21,22] and/or VOCS data acquisition.[23-25] In Chapter 4, it was shown that rather subtle HOQIE are present in the SSNMR spectra for [127]I at $B_0 = 11.75$ T and 21.1 T for some alkaline earth metal iodides.[26] In those cases, the observed HOQIE manifested as very slight non-uniform frequency-dependent shifts in the [127]I SSNMR spectrum, and appeared to influence ones ability to determine the value for δ_{iso}. While high-order (i.e., greater than second-order) perturbation theory would have been useful for modeling these [127]I SSNMR line shapes, a simulation code that included Zeeman and QI effects exactly,[27,28] as well as [127]I NQR experiments, were used to precisely measure the EFG tensor magnitude, as well as the isotropic iodine chemical shift.

In order to more generally and completely understand the origin and ramifications of HOQIE on SSNMR spectra for $I = 5/2$ nuclides, reported in this Chapter are [127]I SSNMR/NQR spectra for SrI_2, and [185/187]Re SSNMR/NQR spectra for NH_4ReO_4 and $NaReO_4$. The motivation behind the choice of these systems is rather simple. According to quantum chemical calculations presented earlier (see Table 4.5), the iodine QI for one of the two sites in SrI_2 should be the largest of the alkaline earth metal iodides. Hence, one must anticipate more substantial HOQIE in the [127]I SSNMR spectrum of SrI_2 when compared to the compounds studied earlier. Likewise, prior [185/187]Re SSNMR measurements on NH_4ReO_4 and $NaReO_4$ highlighted some of the largest QIs ever measured using NMR, although quantitative EFG tensor information could not be extracted for $NaReO_4$.[25] Indeed, while repeating the prior [185/187]Re SSNMR measurements on $NaReO_4$ at 11.75 T, unexpected and previously unobserved fine structure was detected. Using both second-order perturbation theory and exact QI simulations, discussion is provided upon the origin of this fine structure, and some general

guidelines are outlined that are applicable when modeling the SSNMR spectra for any $I = 5/2$ nucleus which experiences a large and axially symmetric QI.

5.2 Experimental Details

5.2.1 Sample Preparation

SrI$_2$ ($\geq$ 99.99 %), NaReO$_4$ (99.99 %), and NH$_4$ReO$_4$ (99.999 %) were purchased from Sigma-Aldrich and received as powders. Sample purity was confirmed by the manufacturer (See Appendix C, Section C.1.1). As SrI$_2$ is hygroscopic and light sensitive, a sample of this material was stored and prepared for use in minimal light conditions under dry Ar. Both Re-containing compounds are stable under normal conditions, and hence did not require any special storage or preparation considerations. Prior to experiments, all samples were gently powdered and tightly packed into 3.2 or 4 mm o.d. Bruker MAS ZrO$_2$ rotors.

5.2.2 Solid-State ^{127}I and $^{185/187}Re$ NMR

Experimental data were primarily acquired at the National Ultrahigh-field NMR Facility for Solids in Ottawa using a standard bore (54 mm) Bruker AVANCEII spectrometer operating at $B_0 = 21.1$ T ($\nu_0(^1H) = 900.08$ MHz). Additional $^{185/187}$Re SSNMR data were acquired at the University of Ottawa using a wide bore (89 mm) Bruker AVANCE spectrometer operating at $B_0 = 11.75$ T ($\nu_0(^1H) = 500.13$ MHz). At 21.1 T, ^{127}I SSNMR experiments used either a 3.2 mm Bruker HX MAS probe ($\nu_0(^{127}I) = 180.08$ MHz) or a 4 mm Bruker HX MAS probe, while all $^{185/187}$Re SSNMR experiments ($\nu_0(^{185}Re) = 202.738$ MHz, and $\nu_0(^{187}Re) = 204.781$ MHz) used a 4 mm Bruker HX MAS probe. At 11.75 T, $^{185/187}$Re SSNMR experiments used a 4 mm Bruker HXY MAS probe ($\nu_0(^{185}Re) = 112.652$ MHz, and $\nu_0(^{187}Re) = 113.787$ MHz).

The ^{127}I SSNMR spectra were referenced to 0.1 mol/dm^3 KI in D$_2$O at 0 ppm[29] using solid NaI or KI as secondary standards (δ_{iso}(NaI(s)) = 226.71 ppm, δ_{iso}(KI(s)) = 192.62 ppm).[5] Iodine $\pi/2$ pulse widths were established using the ^{127}I SSNMR signals of powdered KI or NaI under 10 kHz MAS. The $^{185/187}$Re SSNMR signals were referenced to a 0.1 mol/dm^3 solution of NaReO$_4$ in D$_2$O at 0.0 ppm. The $^{185/187}$Re pulse lengths used for experiments on NH$_4$ReO$_4$ were established using the solution reference. All calibrated pulses include a scaling of the optimized cubic solid/solution pulse by $1/[I + 1/2] = 1/3$ to selectively excite the CT of the solid under study. Due to the excessive width of the $^{185/187}$Re SSNMR signals of NaReO$_4$ (*vide infra*), the high- and low-frequency pulse lengths were calibrated using the high- and low-frequency CT and ST discontinuities of the actual sample. For further details on the frequency-dependence of the pulse lengths used to acquire the $^{185/187}$Re SSNMR signals of NaReO$_4$, see Appendix C, Table C.1.

SSNMR signals were primarily acquired using either Solomon echo[30-32] or Hahn echo[33] pulse sequences. Typical parameters were as follows: $\pi/2$ = 1.0 to 1.7 μs (π = 2.0 to 3.4 μs); spectral window = 2 MHz; τ_1 = 13.2 to 30 μs; and 512 or 1 024 complex time-domain data points were collected. For all experiments, between 4 000 and 17 500 transients were acquired with a recycle delay of typically 90 to 100 ms (for $^{185/187}$Re) and 0.25 s (for ^{127}I). For full experimental details, see Appendix C, Table C.1. VOCS data acquisition methods[23-25] were always required to acquire the SSNMR signals presented in this Chapter. Offsets were typically 200 to 300 kHz for Solomon/Hahn echo experiments. Each processed sub-spectrum was combined in the frequency-domain by co-addition to produce the total VOCS spectrum. In order to rapidly acquire the ^{127}I SSNMR spectrum for site I(2) in SrI$_2$, WURST echo experiments[34] were employed. The WURST echo used a 1 MHz sweep bandwidth via a 50 μs WURST pulse shape,[35,36] and the VOCS method offset was optimized to 848 kHz (limited by

the probe bandwidth). Due to the temperature dependence of the $^{185/187}$Re QI for the Re-containing compounds, all $^{185/187}$Re SSNMR experiments were performed at $T = 291.8(0.2)$ K, as monitored via a Bruker 'type-T' thermocouple and regulated using a standard Bruker variable temperature unit.

5.2.3   Solid-State ^{127}I and $^{185/187}$Re NQR

All NQR experiments were carried out at the University of Ottawa using the AVANCE spectrometer outlined above. All NQR experiments used either a 4 mm Bruker HX or a 4 mm HXY MAS probe, and all $^{185/187}$Re spectra were acquired using the Hahn echo pulse sequence at $T = 291.8(0.2)$ K. Non-optimized, short (≤ 2 μs), high-powered pulses were used as the RF was varied until a particular resonance was detected. The offset used while searching for NQR signals was 200 kHz. For further details, see Appendix C, Table C.1.

5.2.4   Details Pertaining to the Generation of Figure 5.11

To generate Figure 5.11, additional line shape broadening effects, such as rhenium CSA, dipole-dipole, J, etc., were not included. In addition, only the case where $I = 5/2$ and $\eta_Q = 0$ is considered. Under these assumptions, a model which includes the QI exactly will give the correct results for the parameters δ_{iso} and C_Q, while second-order perturbation theory will produce values that are somewhat in error. It is noted that only the relative value between ν_0 and ν_Q are important, and only the CT frequencies are considered. For an axial EFG, the high-frequency CT discontinuity corresponds to a crystallite orientation such that $\mathbf{V}_{33}$ is perpendicular to B_0, and the low-frequency CT discontinuity corresponds to a crystallite such that $\mathbf{V}_{33}$ makes an angle of ca. 41.81° (i.e., the solution to $\cos(\theta) = 5^{1/2}/3$) with respect to B_0.[37] The central (i.e., 'step') discontinuity corresponds to a crystallite where $\mathbf{V}_{33}$ is parallel to B_0 and hence its position

is unaffected by the QI. Under the current conditions, one needs only to calculate the transition frequencies at these three 'critical' orientations. These critical orientation CT frequencies may be simply calculated under second-order perturbation theory for $I = 5/2$ and $\eta_Q = 0$:[38]

$$\nu_{CT,\,high} \quad = \quad \nu_0 \quad + \quad \frac{\left(\nu_Q\right)^2}{2\nu_0}, \tag{5.1}$$

$$\nu_{CT,\,low} \quad = \quad \nu_0 \quad - \quad \left(8/9\right)\frac{\left(\nu_Q\right)^2}{\nu_0}, \tag{5.2}$$

where **(5.1)** specifies the position of the high-frequency CT discontinuity ($\nu_{CT,\,high}$) and **(5.2)** specifies the position of the low-frequency CT discontinuity ($\nu_{CT,\,low}$). Recall that the step discontinuity position is unaffected by the QI.

For the exact QI simulations, while it remains true that the high-frequency CT discontinuity corresponds to the case where $\mathbf{V}_{33}$ is perpendicular to B_0, and that the step discontinuity corresponds to the crystallite where $\mathbf{V}_{33}$ is parallel to B_0, the crystallite orientation corresponding to the low-frequency CT discontinuity will vary as a function of ν_0/ν_Q. For large ν_0/ν_Q values (i.e., strong Zeeman interaction), it is such that the angle roughly corresponds to 41.81°, but as the ν_0/ν_Q value decreases, the $\mathbf{V}_{33}/B_0$ angle will change such that its value is reduced. A plot of this dependence is shown in Appendix C, Figure C.1. In any event, three critical points also exist for the exact QI simulations of the CT. The CT frequencies were calculated at these critical orientations using both the exact and second-order perturbation theory models assuming a variety of ν_0/ν_Q values.

Once the transition frequencies at these critical points are known, the C_Q and δ_{iso} values may be determined from second-order perturbation theory line shape models in a relatively straightforward fashion: ν_Q is related to the spread in frequency between the high- and low-

frequency CT discontinuities (Δv_{CT}) using the following equation (i.e., by taking the difference between **(5.1)** and **(5.2)**):

$$\Delta v_{CT} \quad = \quad v_{CT,\,high} \quad - \quad v_{CT,\,low} \quad = \quad (25/18)\frac{\left(v_Q\right)^2}{v_0}. \tag{5.3}$$

After the application of **(5.3)**, C_Q can be determined as $C_Q = 20v_Q/3$ under the conditions considered here.

In general, it is observed that for a given C_Q value, second-order perturbation theory will give a line width that exceeds the true value. Hence, to fit the data using second-order perturbation theory would require the apparent C_Q value to underestimate the real value. The amount by which an apparent C_Q value deviated from the true C_Q value (i.e., from exact QI theory) was used to calculate the percentage errors in Figure 5.11a. After adjusting the width of the line shape due to the error in C_Q, the line shape generated using second-order perturbation theory will still be shifted in the positive frequency direction. The correction required to match the frequencies of the high- and low-frequency CT discontinuities is related to the error in the extracted δ_{iso} value (Figure 5.11b). To determine the apparent δ_{iso} value using second-order perturbation theory, a simple frequency shift is applied (always in the negative direction). Hence, the chemical shift arrived at using second-order perturbation theory will always be negative relative to the true value. After these two corrections are implemented, the second-order perturbation theory and exact theory simulations will have high- and low-frequency CT discontinuities that match. As a result of this procedure, it must be noted that the step discontinuity will not match between the second-order and exact theory models. Indeed, there exists no meaningful case where all three discontinuities would exactly match between the second-order perturbation theory and exact theory simulations. Selected data from these calculations can also be found in Appendix C, Table C.2.

5.3 Results and Discussion

5.3.1 Iodine-127 and Rhenium-185/187 SSNMR Experiments

5.3.1.1 SrI₂: Moderate HOQIE Manifest as Non-Uniform, Frequency-Dependent Shifts

Due to the very large ^{127}I QIs observed in SrI$_2$ (Figures 5.1 and 5.2), ^{127}I SSNMR experiments were performed at $B_0 = 21.1$ T only. The extracted ^{127}I SSNMR parameters were presented in Tables 4.1 and 4.2. The SrI$_2$ crystal structure belongs to the *Pbca* space group.[39] There are two inequivalent I sites, labeled as I(1) and I(2) (Figure 5.3), which are present in equal proportions in the lattice. The primary differences between the two I sites are the number and geometric arrangement of the Sr^{2+} about each unique iodide: I(1) is coordinated by four Sr^{2+}, forming a distorted tetrahedron, while I(2) is coordinated by three Sr^{2+} in a distorted trigonal planar fashion. Symmetry elements do not pass through either I site; hence, both possess 1 symmetry and the $\ddot{\sigma}/\ddot{V}$ parameters are not restricted to particular values based upon the lattice.
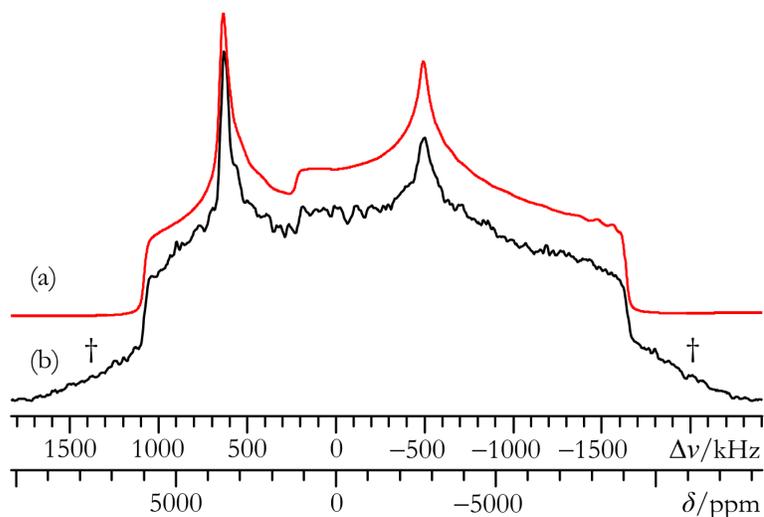
Figure 5.1 Best-fit analytical simulation (a), and experimental static VOCS Solomon echo (b) ^{127}I CT SSNMR spectrum of site I(1) in powdered SrI$_2$ acquired at $B_0 = 21.1$ T. † = Signal due primarily to the partially excited CT of site I(2).
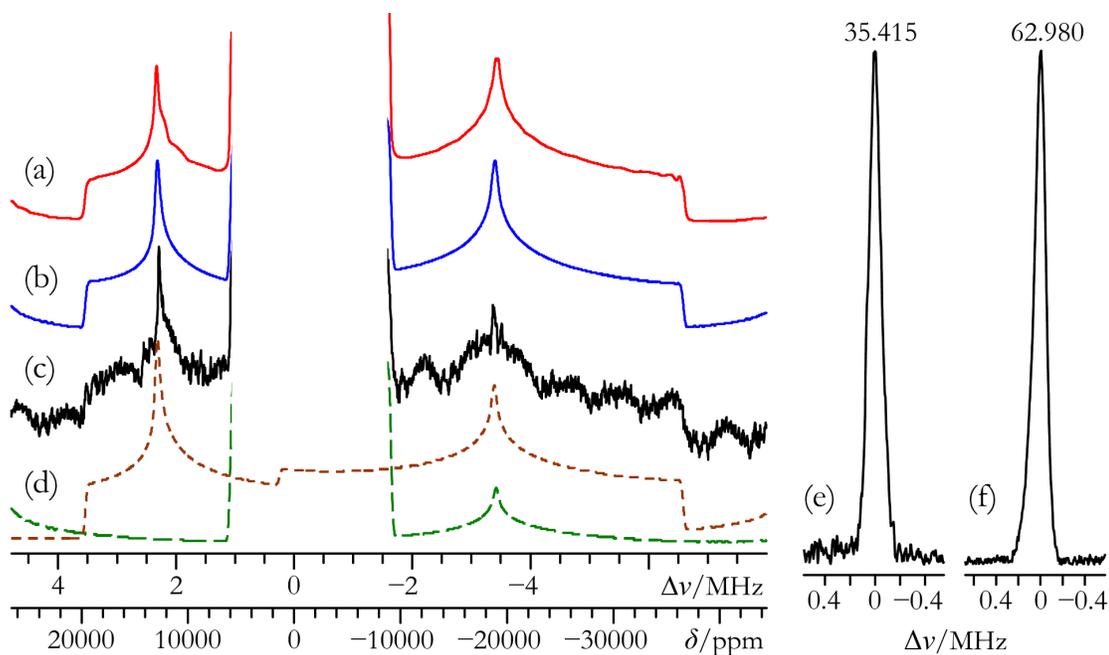
Figure 5.2 Analytical simulation (a), best-fit exact simulation (b), and experimental static VOCS WURST echo (c) ^{127}I SSNMR spectrum of powdered SrI_2 acquired at $B_0 = 21.1$ T. In (d), the two I sites are deconvoluted (I(1) = long dash; I(2) = short dash). ST inclusion from I(1) is essential to reproduce the total spectrum. Experimental ^{127}I NQR spectra of site I(2) in SrI_2 are in (e) ($m = \pm 1/2 \leftrightarrow \pm 3/2$) and (f) ($m = \pm 3/2 \leftrightarrow \pm 5/2$), and the ^{127}I NQR transition frequencies (in MHz) are listed above (e) and (f).
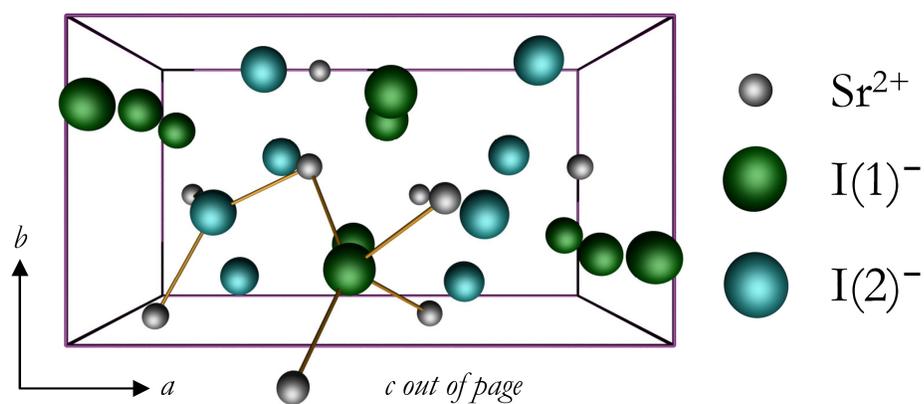
Figure 5.3 POV-ray rendering of the SrI_2 unit cell. For the unique I, solid lines connect heteroatoms within the sum of the Sr and I vdW radii (i.e., $r_{Sr-I} < 4.47$ Å). For each I site, numerous additional homoatomic contacts exist within the iodide first coordination sphere.

Data acquisition and analysis were carried out using conventional methods for the I(1) site; however, data collection and line shape analysis for the I(2) site required more care. For I(1), VOCS Solomon echo experiments and analytical line shape simulations (Figure 5.1) of the ^{127}I SSNMR signal establish a substantial ($C_Q(^{127}$I$)$ = 105.2(0.7) MHz), non-axial (η_Q = 0.467(0.012)) QI. The measured δ_{iso} value of 880(70) ppm lies between CaI$_2$ and MgI$_2$; hence, the measured iodine δ_{iso} values should not be used as direct probes of the number of heteroatomic contacts in the I first coordination sphere. For I(2), although WURST pulses were used to uniformly excite broad regions of each sub-spectrum, moderate line shape distortions (Figure 5.2c) were still observed, and are attributed to the finite bandwidth of the NMR probe. According to a recent survey of the literature, this appears to be the first time that the WURST echo pulse sequence has been used in tandem with VOCS data acquisition, although VOCS WURST-QCPMG experiments have been reported.[40] The total spectrum depicted in Figure 5.2c was acquired in 5 h; hence, the choice of acquisition parameters reflects a balance between uniform line shape excitation and efficient data acquisition.

For the I(2) site in SrI$_2$, it was also realized that the available analytical line shape fitting software[41] may not be able to accurately extract $\ddot{V}$ and $\ddot{\delta}$ tensor parameters. This analytical simulation software assumes the data are collected under high-field conditions (typically taken to be satisfied if $v_0 > 10v_Q$) and includes the QI as perturbations to the Zeeman states to second-order. Using simulation software that exactly combines the Zeeman and QI states (provided by Prof. A. D. Bain, McMaster University), it is suggested that as a rule of thumb for $I = 5/2$, the high-field approximation is valid for the extraction of $\ddot{V}$ parameters if $v_0/v_Q > 5$ (Figure 5.4).[4]

Analytical line shape fits to the observed ^{127}I SSNMR signal for the I(2) site produce the following parameters: $C_Q(^{127}$I$)$ = 213(1) MHz; η_Q = 0.32(1); δ = 300(150) ppm. As might be expected, the origin of this 'shift' is not specified, but it is not a pure chemical shift (*vide infra*).

To determine if the high-field approximation is valid for the I(2) site in SrI$_2$ at $B_0 = 21.1$ T, v_0/v_Q must be determined. As [127]I NQR experiments can be used to independently and precisely measure v_Q, they were performed on powdered SrI$_2$. The expected two signals for site I(2) were observed at 35.415 ($m = \pm 1/2 \leftrightarrow 3/2$) and 62.980 ($m = \pm 3/2 \leftrightarrow \pm 5/2$) MHz (Figures 5.2e and 5.2f). These [127]I NQR transition frequencies establish that $C_Q(^{127}I) = 214.0(0.1)$ MHz and $\eta_Q = 0.316(0.002)$.[42] It is important to note that these values are in quantitative agreement (i.e., within experimental error) with the $\ddot{V}$ tensor parameters extracted from the [127]I SSNMR data by way of analytical simulations, despite the low v_0/v_Q ratio (i.e., $v_0 < 10v_Q$).
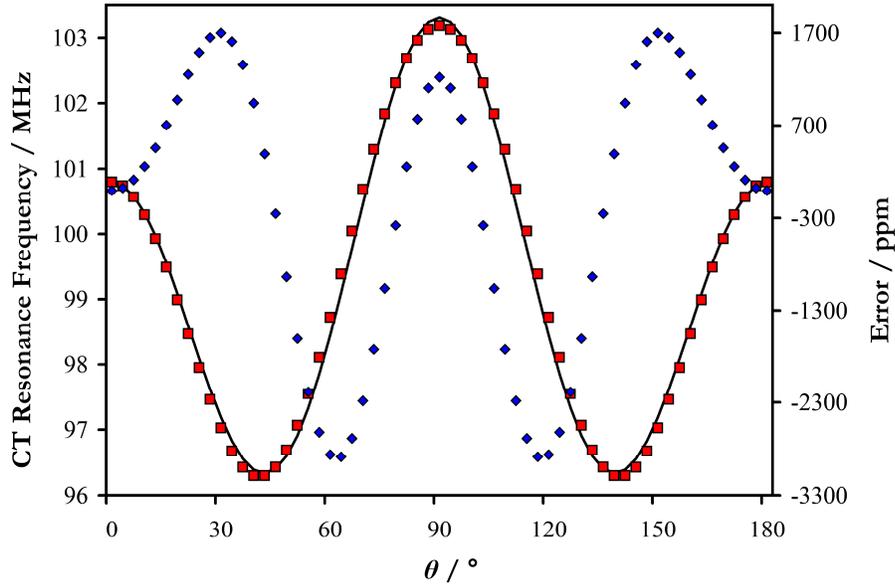
Figure 5.4 Comparison between analytical second-order perturbation theory (solid black line) and exact theory (red squares) approaches for the calculation of the CT resonance frequency (left vertical axis) corresponding to a fictitious single crystal sample, as **V**$_{33}$ is rotated about an axis perpendicular to B_0. The angle between **V**$_{33}$ and B_0 is represented by θ. The blue diamonds correspond to the difference (right vertical axis) between the perturbation theory and exact theory values for a particular crystal orientation. The case considered here is as follows: $I = 5/2$, $C_Q = 150$ MHz, $v_0 = 100.8$ MHz, and is intended to model somewhat typical QI parameters for ionic [127]I. As well, $\eta_Q = 0$ and CS effects are neglected. In this regime, it is believed that the error between the two models is similar to the associated measurement errors; hence, any stronger QI at this applied field should lead to detectable HOQIE.

Using the above $\ddot{V}$ tensor parameters determined from NQR experiments and **(3.1)**, it is rather easily determined that $v_Q = 32.6$ MHz and hence $v_0/v_Q \approx 5.5$. This is near the estimate of where the high-field approximation should no longer be valid, as outlined in Figure 5.4. Using the $\ddot{V}$ tensor parameters determined from [127]I NQR experiments, a simulation using the exact QI software was generated. After adding a chemical shift ($\delta_{iso} = 720(150)$ ppm) to this simulated spectrum (Figure 5.2b), the agreement between it and the experimental spectrum is excellent. The [127]I SSNMR signal associated with the I(2) site in SrI$_2$ has thus provided a strict test of the earlier assertion that v_0/v_Q needs only to be greater than 5 for the high-field approximation to be valid, at least for the determination of C_Q and η_Q for $I = 5/2$ nuclei.

However, considering the large difference in the 'shifts' obtained for the I(2) site in SrI$_2$ (i.e., second-order perturbation theory gives an apparent shift of 300(150) ppm, while exact theory gives 720(150) ppm), it is clear that the extraction of a chemical shift in this regime is *not* possible using second-order perturbation theory. Using the [127]I $\ddot{V}$ tensor parameters which were determined from [127]I NQR experiments and neglecting chemical shift effects, the line shape generated using second-order perturbation theory is compared with one from an exact calculation (solid red and blue traces, respectively, in Figure 5.5). While the pattern widths and shapes are approximately identical, it is particularly interesting to note that they are offset slightly in the frequency domain (Figure 5.6). Importantly, all of the horn and edge discontinuities of the exact QI simulation lie to lower frequency, relative to these same points generated using second-order perturbation theory. Only the central step discontinuity lacks this effect (Figure 5.6iii, red and blue traces) as it corresponds to crystallites where $\mathbf{V}_{33}$ and B_0 are collinear (i.e., $\theta = 0°$) and thus it is necessarily not affected by angular QI terms (see also Figure 5.4):[43]

$$v_{CT,\,axial}^2 \quad = \quad -\frac{1}{2v_0}\left(\frac{3C_Q}{20}\right)^2\left(1-\cos^2\theta\right)\left(9\cos^2\theta-1\right), \tag{5.4}$$

where $v^2_{CT, axial}$ is the frequency shift of the CT Zeeman eigenstates under second-order perturbation theory. Note that in **(5.4)** it has been assumed that $I = 5/2$ and $\eta_Q = 0$.
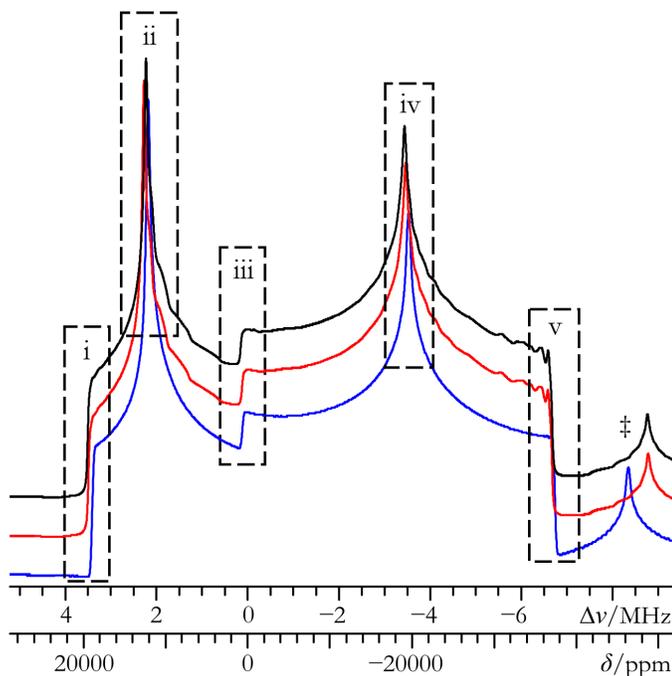
Figure 5.5 Comparison of [127]I SSNMR powder patterns generated using second-order perturbation theory (red and black traces) with one calculated using exact theory (blue trace). All were generated using the $\ddot{V}$ parameters obtained independently from [127]I NQR experiments (i.e., C_Q = 214 MHz; η_Q = 0.316); however, CS effects are ignored in the red/blue traces. Iodine CSA is included in the black trace simulation using the GIPAW DFT computed parameters in Table 4.6 (PBE method). Relative to the second-order perturbation theory simulation, the exact simulation is nonuniformly shifted to lower frequency. The origin of this difference is attributed to frequency-dependent HOQIE, as outlined in the main text. Low-frequency discontinuities (‡) are from the ST, and highlight the drastic difference in the computed position of one of the ST discontinuities, which are affected by third-order QIE.

To explain further, note that for quadrupolar nuclei with an appreciable C_Q, there is a well-known measurable shift in the SSNMR signal to lower frequency, which is known as the second-order quadrupole-induced shift (QIS). The second-order QIS for the CT of a spin-5/2 nucleus (δ^2_{QIS}, in ppm) is quantified using the following equation:[44]

$$\delta_{\text{QIS}}^2 \quad = \quad -\frac{3}{500}\left(\frac{C_{\text{Q}}}{v_0}\right)^2\left(1 + \frac{\eta_{\text{Q}}^2}{3}\right)\times 10^6.$$ (5.5)

For modest C_{Q} values, the chemical shift of the CT is adequately represented as: $\delta_{\text{iso}} = \delta_{\text{cg}} - \delta_{\text{QIS}}^2$, where δ_{cg} is the measured position of the CT centre of gravity. While third-order effects on the CT spectra for half-integer quadrupolar nuclei are zero,[45] they are nonzero for the ST and contribute to the observed line shapes in 2D experiments which involve the ST.[46] Fourth-order (and greater even-ordered) effects on the CT have not been quantified (they are thought to be nonzero); however, methods which incorporate the QI exactly are known.[27,47-49]
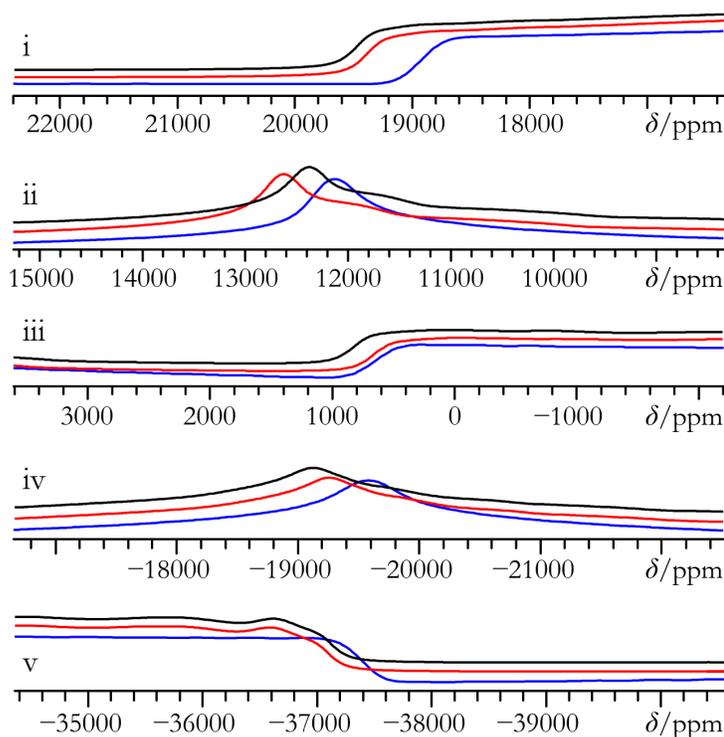
Figure 5.6 Horizontal expansions of the regions in Figure 5.5, as denoted by the dashed boxes. These illustrate that the incorporation of a large iodine CSA (i.e., Ω = 460 ppm) generally influences the positions of the critical discontinuities to a lesser extent than the HOQIE in this case. The notable exception is the discontinuity in (ii), where the CSA effects are comparable to HOQIE. In (iii), the discontinuity is minimally affected by QIE, as described by **(5.4)** and in the main text.

Returning to Figures 5.5 and 5.6, the differences in the positions of the discontinuities between the two simulated spectra can be attributed to HOQIE. Due to the dependence of these effects upon the crystallite orientation in a powder (i.e., the angle between $\mathbf{V}_{33}$ and B_0 for each crystallite), one is not able to assign a single value to describe this effect for the total line shape. What is clear, however, is that in this regime there are differences between the calculated positions of the discontinuities in the frequency domain (Figure 5.6) and that second-order perturbation theory consistently predicts the frequencies of these discontinuities to be too high, relative to the exact theory simulations. Hence, one cannot use second-order perturbation theory to obtain an accurate measure of the chemical shift in this v_0/v_Q regime due to these frequency-dependent shifts. It is also expected that as the v_0/v_Q ratio decreases (i.e., $v_0/v_Q < 5$ for $I = 5/2$), the ability to reliably extract $\ddot{V}$ tensor parameters using second-order perturbation theory will also diminish (this scenario will be addressed as part of the discussion provided in Section 5.3.1.2). It is precisely because this is a borderline case that there exists the ability to properly extract C_Q and η_Q using the second-order simulation (within experimental error).

In addition, an example is provided of what impact typical CSA effects would have on the line shape (black traces in Figures 5.5 and 5.6). Although it was not possible to experimentally measure iodine CSA in SrI_2, in the black simulated spectrum the $\ddot{\sigma}$ values were set equal to the computed values which were presented in Table 4.6 (PBE method). Clearly, for the edge discontinuities, inclusion of even $\Omega = 460$ ppm leads to minimal differences as compared to simulations which do not include CSA (i.e., contrast the black and red traces in Figure 5.6). Only the high-frequency horn discontinuity (Figure 5.6ii) appears to be appreciably influenced by including iodine CSA, but this lies within the measurement errors for the ca. 56 000 ppm (Δv_{NMR} ~10 MHz) broad line width for the I(2) site in SrI_2. It has been additionally verified that HOQIE for the ^{127}I SSNMR signal of I(1) in SrI_2 are below the measurement errors

(Appendix C, Figure C.2). This is expected, as the fourth-order term (i.e., the leading nonzero term not included in second-order perturbation theory) that would influence the CT should possess roughly a (C_Q^4 / v_0^3) dependence.

5.3.1.2 NaReO₄: Never-Before Observed NMR Spectral Fine Structure

Under ambient conditions, this material crystallizes in the scheelite-type tetragonal structure class (space group, $I4_1/a$).[50] The oxygen atoms in the ReO_4^- cluster arrange themselves in a distorted tetrahedral fashion about the central Re: there are four equivalent Re-O bond distances (r_{Re-O} = 1.728 Å); however, the O-Re-O bond angles range from 108.5° to 111.4°.[51] As the structure is not perfectly tetrahedral, the expected EFG at the Re nucleus is nonzero. Indeed, prior [185/187]Re NQR measurements on this system highlight a substantial, axially symmetric (i.e., η_Q = 0) and temperature-dependent rhenium QI.[52,53] Previous [185/187]Re SSNMR measurements are consistent with a large rhenium QI, but were not used to precisely determine the rhenium EFG/CS tensor magnitudes (estimated values: C_Q([185]Re) ~ 278 MHz and C_Q([187]Re) ~ 268 MHz).[25] Prior rhenium NQR data collected at T = 296 K found that v_Q([185]Re) = 44.997(0.005) (C_Q([185]Re) = 299.98(0.04) MHz) and v_Q([187]Re) = 42.606(0.005) MHz (C_Q([187]Re) = 284.04(0.04) MHz) for $NaReO_4$ (see the footnotes to Table 5.1 for the definition of v_Q used here).[54] It is clear that there exists a large discrepancy between the previously reported NQR and SSNMR results for the rhenium QI of $NaReO_4$. This compound was chosen for study in order to investigate the possible impact of HOQIE in the [185/187]Re SSNMR spectra and to potentially observe rhenium CS effects.

Rhenium-185/187 NQR experiments were performed (Appendix C, Figure C.3) and the resulting transition frequencies (Table 5.1) clearly confirm that η_Q([185/187]Re) = 0. As the ratio between the $m = \pm3/2 \leftrightarrow \pm5/2$ and $m = \pm1/2 \leftrightarrow \pm3/2$ transition frequencies ($|\Delta m|$ = 1) is

exactly 2 within experimental error, it is concluded that there is no evidence of a nuclear electric hexadecapole interaction (HDI).[55] Briefly, the HDI is the electric 16th-pole interaction that is supposed to exist between the nuclear electric hexadecapole moment for a given nucleus and the second derivative of the EFG at the nucleus. The HDI is theoretically nonzero for any $I > 3/2$, although according to current literature accounts, its effect has been too subtle to be convincingly measured using NMR methods, even after careful experimental design.[56,57] There does however appear to be evidence of the HDI in the high inertia rotational bands of certain molecules, as observed via high-resolution gas-phase spectroscopy.[58,59] As a general rule of thumb, the strength of a given HDI is about six orders of magnitude less than the analogous QI.[55] Using the newly-measured NQR data, it is therefore established that $C_Q(^{185}Re) = 300.68(0.02)$ MHz and $C_Q(^{187}Re) = 284.54(0.02)$ MHz at 291.8 K. The slight discrepancy between the current $C_Q(^{185/187}Re)$ values and those measured earlier can be fully attributed to the difference in the respective measurement temperatures.[60]

Table 5.1 Experimental $^{185/187}$Re EFG tensor parameters and δ_{iso} values for rhenium-containing systems[a]

compound	$v_{Q1}/v_{Q2}(^{185}Re)$ / MHz	$v_{Q1}/v_{Q2}(^{187}Re)$ / MHz	$\|C_Q(^{185}Re)\|$ / MHz	$\|C_Q(^{187}Re)\|$ / MHz	η_Q	δ_{iso} / ppm
NaReO$_4$	45.102(6)/90.204(9)	42.681(5)/85.362(8)	300.68(2)	284.54(2)	<0.003	70(40)
NH$_4$ReO$_4$	—/35.068(10)	—/33.186(8)	116.90(4)	110.62(3)	<0.003	0(40)

[a] All values are extracted via the exact modeling of the QI. Error bounds are in parentheses. When $I = 5/2$ *and* $\eta_Q = 0$, $v_{Q1} = v_Q = 3C_Q/20$ and $v_{Q2} = 2v_Q = 3C_Q/10$. All measurements were carried out at $T = 291.8(2)$ K. EFG tensor parameters established using NQR data were determined using the procedure outlined by Semin.[42] While C_Q may take any real value, $|C_Q|$ is measured using conventional NQR/SSNMR experiments. On the basis of the data presented, it is found that the maximum possible value for the ^{185}Re nuclear electric HDI in NaReO$_4$ is ca. 750 Hz.[55] Rhenium chemical shifts are reported relative to 0.1 mol/dm^3 NaReO$_4$ in D$_2$O ($\delta_{iso}(^{185/187}Re) = 0$ ppm).

To measure the rhenium EFG and CS tensors for this sample using SSNMR, $^{185/187}$Re SSNMR experiments were carried out on powdered NaReO$_4$ at $B_0 = 11.75$ and 21.1 T (Figures 5.7 and 5.8). In the present study, the $^{185/187}$Re SSNMR signals from each NMR-active nuclide

typically overlap one another due to their similar Larmor frequencies. After careful line shape analysis using exact QI simulation software[27] (it is noted again that other exact QI models exist[47-49,61]), quantitative agreement between the rhenium EFG tensor parameters determined using $^{185/187}$Re NQR and SSNMR measurements was established. In addition, it was possible to measure for the first time an isotropic rhenium CS in a solid sample (δ_{iso} = 70(40) ppm relative to 0.1 mol/dm^3 NaReO$_4$ in D$_2$O). This opens up the possibility that $^{185/187}$Re SSNMR experiments could be used to report on the local rhenium bonding environment or the oxidation state (under favourable conditions) in solid samples. Selected aspects of the current progress on assessing rhenium oxidation states via rhenium SSNMR chemical shifts will be briefly outlined as part of the topics covered in Chapter 9. Indeed, the sparse solution $^{185/187}$Re NMR literature data highlight a chemical shift range of ~6 800 ppm.[62,63] Unfortunately, it was not possible to measure rhenium CSA for this sample.
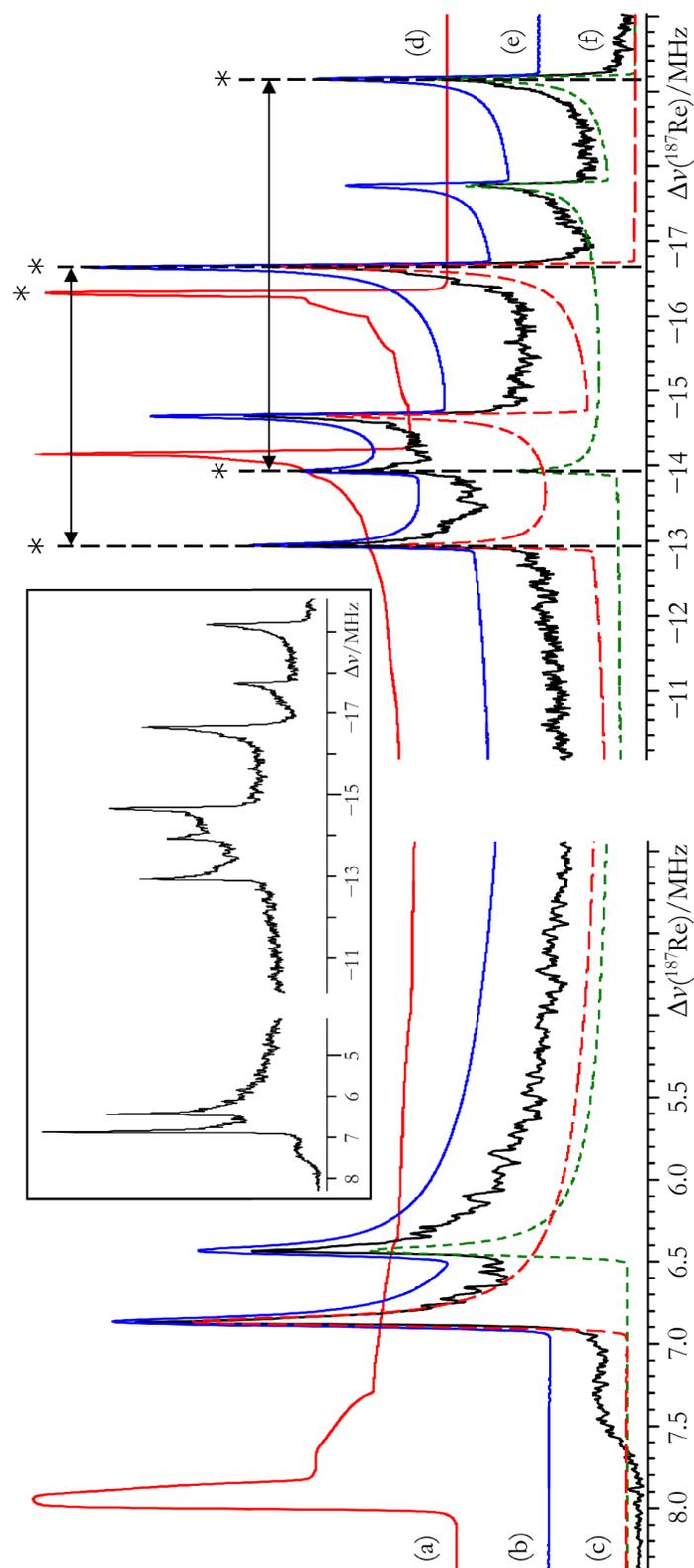
Figure 5.7 Analytical simulations (a, d), best-fit exact simulations (b, e), and experimental static VOCS Hahn echo (c, f) $^{185/187}$Re SSNMR spectrum of powdered NaReO$_4$ acquired at B_0 = 11.75 T ($v_0(^{187}$Re) = 113.787 MHz; $v_0(^{185}$Re) = 112.652 MHz) and T = 291.8 K. The analytical simulation includes only the ^{187}Re SSNMR signal, to enhance clarity. The high-frequency region is depicted in (a, b, c), and the low-frequency region is in (d, e, f). Please note that the horizontal scale is not equivalent between (a, b, c) and (d, e, f); in the inset, the experimental spectrum is displayed using equivalent horizontal scaling for both regions. Below (c) and (f), the exact simulation line shapes associated with each of ^{185}Re and ^{187}Re are deconvoluted: the long dashed red trace is ^{187}Re, while the short dashed green trace is ^{185}Re. Low-frequency splittings (denoted by double-headed arrows and guide lines) are not predicted by second-order perturbation theory. The discontinuities due to the $m = 1/2 \leftrightarrow 3/2$ ST are marked by '*', while the remainder of the discontinuities are due to the CT. All simulations used identical EFG tensor parameters, which were also measured independently via $^{185/187}$Re NQR experiments. Minor discontinuities in the slopes of traces (a) and (d) are artifacts due to the POWDER algorithm[64] used for powder averaging.
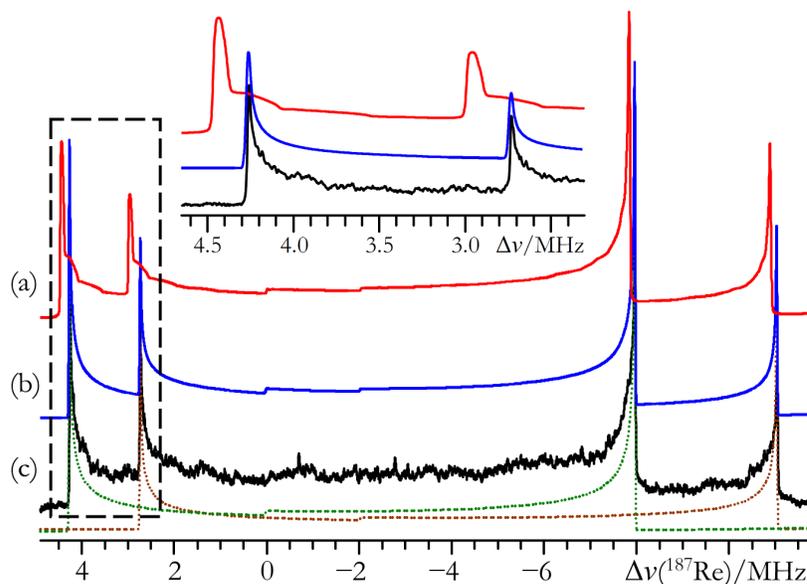
Figure 5.8 Analytical simulation (a), best-fit exact simulation (b), and experimental static VOCS Solomon echo (c) [185/187]Re SSNMR spectrum of powdered NaReO$_4$ acquired at $B_0 = 21.1$ T (v_0([187]Re) = 204.781 MHz; v_0([185]Re) = 202.738 MHz) and $T = 291.8$ K. Below (c), the exact simulation signals associated with each of [185]Re and [187]Re are deconvoluted: the dotted green trace is [187]Re, while the dotted brown trace is [185]Re. Low-frequency splittings are not observed (as were seen in Figure 5.7); however, the expected positions of the discontinuities in the analytical simulation are subject to a nonuniform, frequency-dependent shift, which is evidence of HOQIE. All simulations used identical EFG tensor parameters, which were also measured independently via [185/187]Re NQR experiments. The inset (top, middle) corresponds to the region within the dashed box, and is meant to highlight the significant difference between the exact and second-order perturbation theory models. For the inset, the deconvolution traces have been omitted to enhance clarity.

After inspection of Figures 5.7 and 5.8, it is immediately clear that the predominantly CT line shapes at both applied fields are very broad (~16 and 25 MHz for the spectra acquired at B_0 = 21.1 and 11.75 T, respectively). The most striking aspect of the spectrum at 11.75 T is the presence of unexpected high-intensity discontinuities (i.e., not predicted using second-order perturbation theory, see Figure 5.7f). It is intriguing that these extra discontinuities do not appear in the [185/187]Re SSNMR spectrum acquired at 21.1 T. This B_0-dependent system response is consistent with the expected behaviour of a second-order (or greater) QIE, and can be fully

attributed to HOQIE (*vide infra*). While it is perhaps clear that up to two additional low-frequency discontinuities could be due to the inner ($m = 1/2 \leftrightarrow 3/2$, assuming $C_Q(^{185/187}Re) > 0$) ST (one from each of ^{185}Re and ^{187}Re), second-order perturbation theory still fails rather spectacularly when one applies the correct ^{187}Re EFG tensor parameters (as from NQR and exact line shape simulations) and includes the ST within the model (Figure 5.7a and 5.7d). The high-frequency ^{187}Re CT discontinuity position is overestimated by ~1 MHz, as are both the position of the corresponding low-frequency CT discontinuity and that of the $m = 1/2 \leftrightarrow 3/2$ ST. Line shape modeling using exact QI software leads to both the correct number and frequency positions for all eight observed discontinuities for $NaReO_4$ using the parameters in Table 5.1. Most importantly, the exact QI model predicts the experimentally observed fine structure in the low-frequency spectral region for both ^{185}Re and ^{187}Re (Figure 5.7e). These additional features are field-dependent, are attributed to the $m = 1/2 \leftrightarrow 3/2$ ST (*vide infra*), and do not interfere with the $^{185/187}Re$ CT SSNMR spectra at 21.1 T (Figure 5.8).

Although second-order perturbation theory does not predict the correct placement of the $^{185/187}Re$ CT discontinuities for $NaReO_4$, even at 21.1 T (Figure 5.8a), this model predicts the correct *number* of discontinuities at the higher applied field. At 21.1 T, the additional fine structure observed at 11.75 T is not present and it appears that HOQIE manifest as a non-uniform frequency-dependent shift in the positions of the discontinuities (with a notable bias towards a negative-frequency shift; the effective parameters determined using second-order perturbation theory are summarized in Appendix C, Table C.3). It is therefore clear that the unusual B_0-dependent behavior is due to HOQIE, and that the fine structure observed at 11.75 T must be due to a third-order QIE on the ST and/or a fourth-order QIE on the CT and ST (as third-order effects on the CT are known to be zero).[45] Beyond fourth-order effects are also potentially significant, but are expected to be much smaller than the leading-order contributions.

It is possible that fourth-order perturbation theory would be able to produce accurate line shape models in the regime where the value of ν_Q becomes somewhat comparable to ν_0. Overall, it is seen that second-order perturbation theory cannot lead to the correct values for either δ_{iso} or $C_Q(^{185/187}\text{Re})$ under these conditions, and in fact both quantities will be underestimated relative to their true values (*vide infra*).

5.3.1.3 *NH₄ReO₄: Large QI, But Still Within the High-Field Approximation*

As with NaReO$_4$, NH$_4$ReO$_4$ has the tetragonal scheelite-type structure (space group, $I4_1/a$).[65] Due to the anomalous dependence of its $^{185/187}$Re NQR transition frequencies with respect to temperature and pressure, NH$_4$ReO$_4$ has been featured in numerous rhenium NQR studies[52,66-71] and one rhenium SSNMR[25] account. All prior reports suggest a large and axially symmetric rhenium QI. Relative to NaReO$_4$, the [ReO$_4$]$^-$ cluster in NH$_4$ReO$_4$ is significantly less distorted from tetrahedral: there are four equivalent Re–O bond distances ($r_{\text{Re-O}}$ = 1.734 Å) and the unique O-Re-O bond angles are 108.8 and 110.8°. Based upon this information, one would expect the rhenium QI in NH$_4$ReO$_4$ to be reduced relative to that of NaReO$_4$ and indeed this is the case (*vide infra*). This compound has been chosen for study to establish potential HOQIE in the SSNMR spectra for the case of a very significant, yet relatively more modest rhenium QI, and to observe chemical shift effects.

To provide a second independent measure of the $^{185/187}$Re EFG tensor parameters in NH$_4$ReO$_4$, rhenium NQR experiments were performed (see Appendix C, Figure C.4) and the measured NQR transition frequencies are summarized in Table 5.1. Using the rhenium NQR data in tandem with multiple field $^{185/187}$Re SSNMR measurements (Figure 5.9) (SSNMR data analyzed using exact QI line shape modeling), it is observed that $C_Q(^{185}\text{Re})$ = 116.90(4) MHz, $C_Q(^{187}\text{Re})$ = 110.62(3) MHz, and $\eta_Q(^{185/187}\text{Re})$ = 0 at T = 291.8 K for this sample. After adjusting

for the well-known temperature dependence of the rhenium QI in NH_4ReO_4, these measurements are fully consistent with prior NQR findings. Unlike the [185/187]Re SSNMR spectra of $NaReO_4$ recorded at 11.75 T, there is no evidence of unexpected additional fine structure in the [185/187]Re CT SSNMR spectrum of NH_4ReO_4.
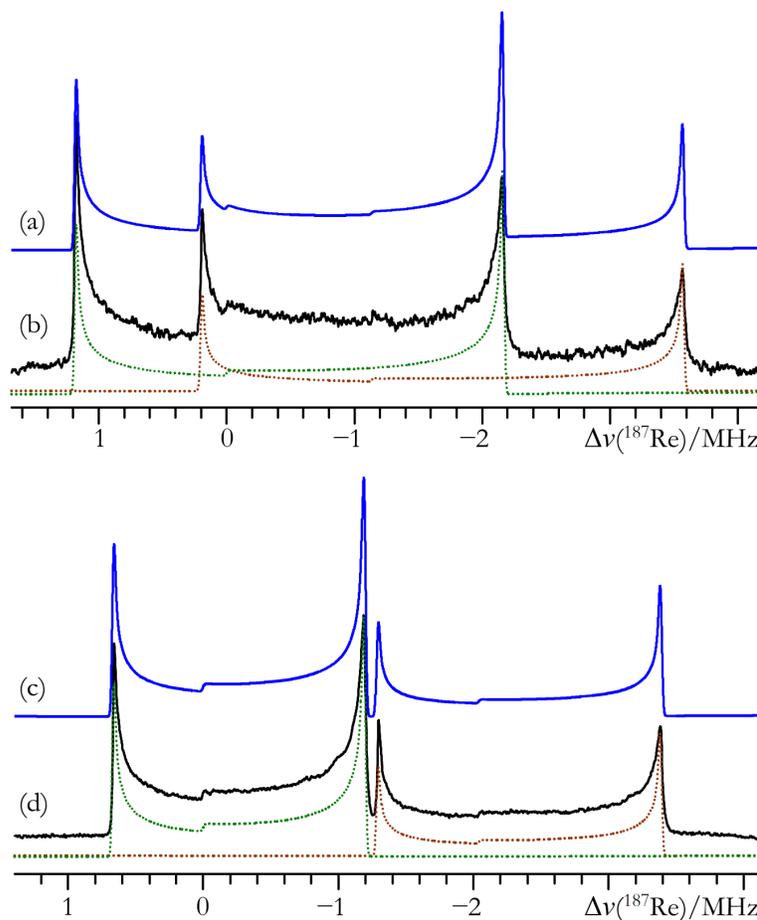
Figure 5.9 Best-fit exact simulations (a, c), experimental static VOCS Hahn echo (b), and static VOCS Solomon echo (d) [185/187]Re SSNMR spectra of powdered NH_4ReO_4 acquired at (b) B_0 = 11.75 T and (d) B_0 = 21.1 T. Below (b) and (d), the exact simulation signals associated with each of [185]Re (dotted brown traces) and [187]Re (dotted green traces) are deconvoluted. All experiments were performed at T = 291.8 K.

Using exact QI simulation software, it was possible to measure the isotropic rhenium chemical shift for this sample as 0(40) ppm. At the lower applied field, the extracted isotropic

chemical shifts using second-order perturbation theory and exact theory do not agree with one another. As was the case with the ^{127}I SSNMR data presented in Section 5.3.1.1, and with the $^{185/187}$Re SSNMR spectral simulations of NaReO$_4$ at 21.1 T, the second-order simulation produces a chemical shift that is smaller than the true value (for the values extracted using second-order perturbation theory, see Appendix C, Table C.3). Unlike the rhenium SSNMR line shape simulations for NaReO$_4$, however, the rhenium EFG tensor parameters extracted for NH$_4$ReO$_4$ using both second-order perturbation theory and exact theory match, within experimental error, when modeling the spectrum acquired at 11.75 T. At 21.1 T, quantitative agreement is found between second-order and exact theory for *all* the reported parameters in Table 5.1. Hence, there is no evidence of HOQIE in the spectra for NH$_4$ReO$_4$ at 21.1 T and second-order perturbation theory is sufficient to model this SSNMR line shape. The quantitative agreement for this final case is sensible, as at 21.1 T, the ratio between v_0 and v_Q for NH$_4$ReO$_4$ exceeds 10 to 1, which is a regime where HOQIE are not expected to be significant (i.e., the high-field approximation is valid).

As the two CT $^{185/187}$Re SSNMR signals for NH$_4$ReO$_4$ are separated at 21.1 T (Figure 5.9d), and as the central step discontinuity is clearly defined for both isotopes, attempts were made to include rhenium CSA in the line shape models for this sample. Unfortunately, the rhenium CS tensor span was too small to be measured and it is noted that the span must be less than ca. 80 ppm for this to be the case. A small tensor span is consistent with the nearly tetrahedral local symmetry about the rhenium atoms.

5.3.2 Fine Structure Origins in the $^{185/187}$Re SSNMR Spectrum of NaReO$_4$ at 11.75 T

At this point, it is clear that the fashion in which HOQIE will manifest in an SSNMR spectrum will depend upon the v_0/v_Q ratio. While it appears as though the onset of these effects

leads to a non-uniform frequency-dependent shift in the resulting SSNMR powder pattern, the $^{185/187}$Re SSNMR spectrum of $NaReO_4$ acquired at 11.75 T presents previously unobserved fine structure. This fine structure was attributed to HOQIE and at this point its origin is briefly outlined. Discussions are also presently provided upon the v_0/v_Q regime where HOQIE may manifest in an SSNMR spectrum where $I = 5/2$ and $\eta_Q = 0$.

In Figure 5.10, line shape simulations are presented which were generated using an exact treatment of the QI. The regime examined included all of the v_0/v_Q ratio values from 4.0 to 2.0 in steps of -0.2. As comments upon the origin of the fine structure will be provided for this particular case, the value for v_0 has been set to 113.787 MHz (i.e., the value of the NMR resonance condition for the ^{187}Re solution standard at 11.75 T). At $v_0/v_Q = 4$, it is noted that the inner ST discontinuity (i.e., $m = 1/2 \leftrightarrow 3/2$) is expected to have a relatively high intensity, and there is no additional fine structure. However, as the v_0/v_Q value is further decreased, this inner low-frequency ST splits into two discontinuities. Eventually, the discontinuities shift to such an extent that they will both occur within the spectral region which is normally (using second-order perturbation theory) attributed to the CT. For the experimental case of $^{185/187}$Re SSNMR of $NaReO_4$ at 11.75 T, the v_0/v_Q value is roughly 2.6:1, which closely resembles the ratio used to generate the trace indicated using a dagger in Figure 5.10. Hence, it is concluded that the experimentally observed fine structure is due to a high-order splitting in the $m = 1/2 \leftrightarrow 3/2$ ST for each of the ^{185}Re and ^{187}Re nuclides. One can expect this type of fine structure to exist (although it will not likely interfere with the CT signal until $v_0/v_Q < 3$) once v_0/v_Q becomes less than 4. This effect on the ST appears to be similar in nature to the splittings observed in certain STMAS experiments, which were attributed to a third-order QI effect.[72] Fine structure due to third-order QI effects is also predicted to arise in ^{14}N ($I = 1$) MAS spectra when the value of C_Q becomes large, although it appears that this has not been experimentally validated.[73]
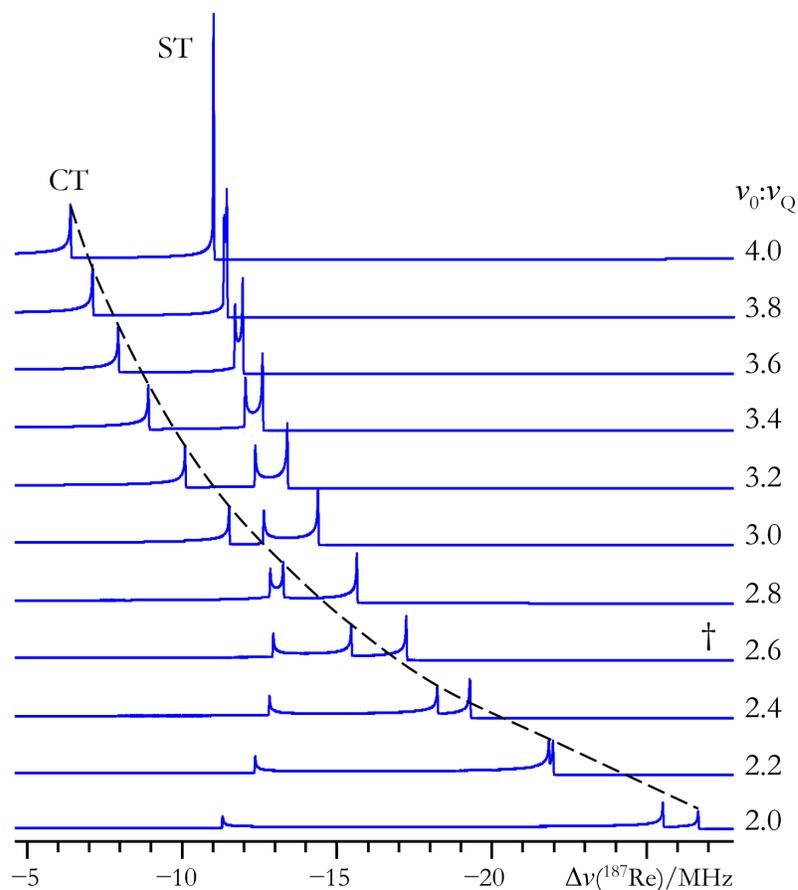
Figure 5.10 Exact simulations of the low-frequency spectral region (part of the CT and $m = 1/2 \leftrightarrow 3/2$ satellite transition discontinuities only), which highlight the onset and origin of the HOQIE fine structure for NaReO₄. For this figure, the ^{187}Re nucleus at 11.75 T has been assumed; hence $\nu_0 = 113.787$ MHz. By adjusting ν_Q, the ν_0/ν_Q ratio is varied from 4.0 (top trace) to 2.0 (bottom trace) in steps of -0.2. The dashed line trace clarifies the evolution of the low-frequency CT discontinuity as a function of ν_0/ν_Q. The spectrum corresponding closely to the best-fit spectrum in Figure 5.7 is demarked with a dagger above it.

5.3.3 General Guidelines for NMR Spectral Analysis When An I = 5/2 Nucleus Experiences a Very Large, Axial, QI

It is well known that second-order perturbation theory is a valid method to model many SSNMR line shapes associated with half-integer quadrupolar nuclei; however, care must be taken to ensure that the high-field condition is satisfied (often taken as $\nu_0 > 10\nu_Q$). For a large

enough QI (i.e., $\nu_0 < 4\nu_Q$), it was established above, using experiment and theory, that additional fine structure is present in the SSNMR spectrum. Under these conditions, second-order perturbation theory does not even predict the correct number of discontinuities, and it is not meaningful to quantify the differences in the extracted NMR parameters between perturbation theory and exact theory. Between these two cases, however, there exists a region where the high-field approximation is not clearly valid, but the additional fine structure is not observable. Here, comments are provided upon the errors in the SSNMR parameters extracted (namely C_Q and δ_{iso}) in this intermediate regime when using second-order perturbation theory as compared to exact theory. Methodology details for this section can be found in Section 5.2.4.
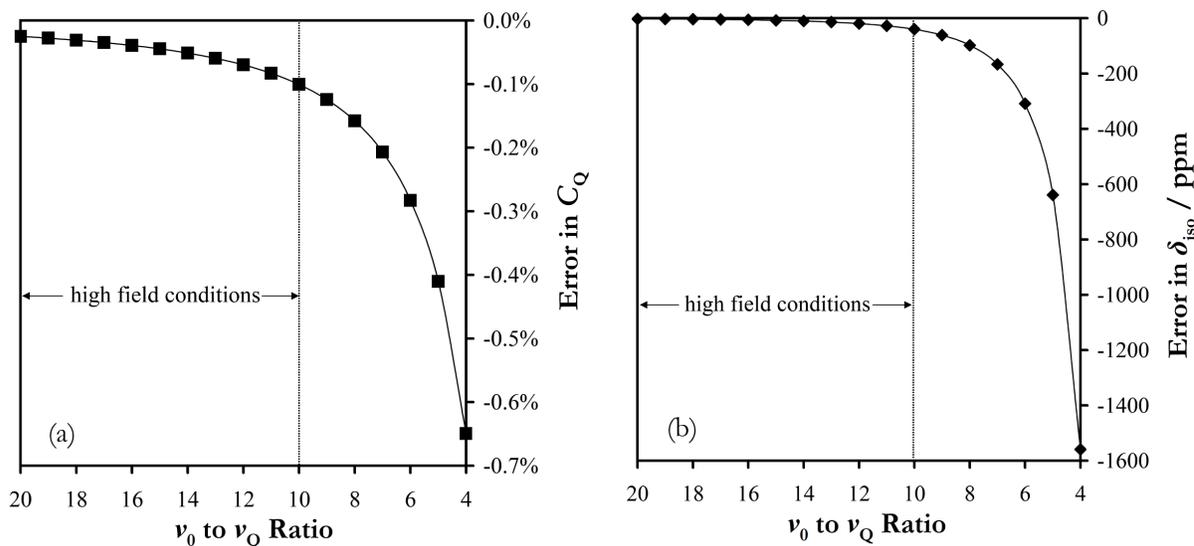
Figure 5.11 Illustrations of the errors associated with using second-order perturbation theory to model SSNMR line shapes for the case where $I = 5/2$ and $\eta_Q = 0$, relative to an exact simulation. (a) Error in the C_Q value as a function of the ν_0/ν_Q ratio, and (b) error in the δ_{iso} value as a function of the ν_0/ν_Q ratio. High-field conditions are traditionally assumed to be satisfied if $\nu_0/\nu_Q > 10$. The lines connecting the data points are meant as guides for the eyes only.

Considered here is the case where a nuclear spin having $I = 5/2$ is subjected to an axial EFG and B_0. The inclusion of additional effects, such as $\eta_Q \neq 0$, CSA, dipole-dipole, etc., is

beyond the scope of the current study. For cases where the high-field approximation is traditionally viewed as being valid, it is found that the error in the extracted C_Q value is at most ca. 0.1 % (Figure 5.11a). However, the error in the isotropic chemical shift value, even within the high-field condition, can be as large as 40 ppm (Figure 5.11b). For a fictitious example where $v_0 = 100$ MHz and $v_Q = 10.0$ MHz (i.e., $C_Q = 66.7$ MHz), this would mean an error in the C_Q value of ~67 kHz, while the error in the shift frequency would be 4.0 kHz. As the value of the ratio between v_0 and v_Q is decreased (i.e., increasing C_Q or decreasing v_0), a point is reached where the error in the extracted C_Q and δ_{iso} values would exceed typical experimental measurement errors. The point at which this would occur is of course highly dependent upon the measurement conditions and the sample. As an additional example, for the case where $v_0 = 4v_Q$, the error in the chemical shift extracted using second-order perturbation theory exceeds 1500 ppm (Figure 5.11b). At the onset of the additional fine structure ($v_0 \approx 4v_Q$), the error in the C_Q value determined using second-order perturbation theory will be slightly in excess of 0.6 % (Figure 5.11a). These findings echo the observations noted previously for spin-5/2 nuclei (although not restricted to $\eta_Q = 0$): when using second-order perturbation theory to model SSNMR line shapes, the error in the chemical shift value becomes detectable at a relatively greater v_0/v_Q value, as compared to the error in C_Q.[4,26] Importantly, it is observed and calculated that the errors in both parameters will always be such that second-order perturbation theory underestimates the true value of the parameter.

5.4 Conclusions

In this Chapter, unambiguous evidence of HOQIE in SSNMR spectra is presented and it is shown that they can manifest in unexpected ways (i.e., not always as simple shifts in the

frequencies of the spectral discontinuities). For example, the $^{185/187}$Re SSNMR spectrum of NaReO$_4$ at $B_0 = 11.75$ T displays additional fine structure in the low-frequency region, which is not predicted by second-order perturbation theory, but which is predicted using an exact QI model. At 21.1 T, this fine structure is not observed experimentally, and is not predicted to be present using exact QI line shape simulations. This is in accord with the expected behaviour of a quadrupole-induced effect on a SSNMR line shape (i.e., higher B_0 leads to smaller QI spectral effects). All of the observed $\ddot{V}$ tensor parameters have been confirmed with corresponding NQR measurements. While the QIs within all systems studied in this Chapter are very significant, it was not possible (within experimental error) to quantify HDI effects. Exact QI simulations have been used to establish that the fine structure will potentially become observable when the v_0/v_Q value drops below 4, and that the fine structure originates from the $m = 1/2 \leftrightarrow 3/2$ satellite transition, which also happens to overlap with the CT. For v_0/v_Q values greater than 4, it has been both observed and calculated that the true values of δ_{iso} and C_Q will be underestimated when the spectra are modeled using second-order perturbation theory. Knowledge of HOQIE are of critical importance for the accurate line shape analysis of SSNMR spectra of many quadrupolar nuclei that may experience large QIs, including $^{63/65}$Cu, ^{67}Zn, ^{75}As, $^{79/81}$Br, ^{91}Zr, ^{93}Nb, ^{105}Pd, ^{115}In, ^{127}I, ^{209}Bi, and others.

5.5   References

1   C. P. Slichter, *Principles of Magnetic Resonance*, 3rd edn., M. Cardona, P. Fulde, K. von Klitzing, H. J. Queisser and H. K. V. Lotsch, Eds., Springer-Verlag: New York, **1990**, 485-502.

2   S. E. Ashbrook, *Phys. Chem. Chem. Phys.*, **2009**, *11*, 6892-6905.

3   D. L. Bryce and G. D. Sward, *Magn. Reson. Chem.*, **2006**, *44*, 409-450.

4   C. M. Widdifield, R. P. Chapman and D. L. Bryce, Chlorine, Bromine, and Iodine Solid-State NMR Spectroscopy In *Annu. Rep. Nucl. Magn. Reson. Spectrosc.*, G. A. Webb, Ed., Elsevier: New York, *66*, **2009**, 195-326.

5   R. P. Chapman, C. M. Widdifield and D. L. Bryce, *Prog. Nucl. Magn. Reson. Spectrosc.*, **2009**, *55*, 215-237.

6   F. A. Cotton and G. Wilkinson, Technetium and Rhenium In *Advanced Inorganic Chemistry: A Comprehensive Text*, 4th edn., Wiley-Interscience: Toronto, **1980**, 883-901.

7   A. V. Naumov, *Russ. J. Non-Ferrous Metals*, **2007**, *48*, 418-423.

8   F. A. Cotton, *Acc. Chem. Res.*, **1969**, *2*, 240-247.

9   Y. Kuninobu and K. Takai, *Chem. Rev.*, **2011**, *111*, 1938-1953.

10   R. Hua and J. L. Jiang, *Curr. Org. Synth.*, **2007**, *4*, 151-174.

11   A. T. Herrmann, T. Saito, C. E. Stivala, J. Tom and A. Zakarian, *J. Am. Chem. Soc.*, **2010**, *132*, 5962-5963.

12   I. L. Barnes, T. L. Chang, P. De Bièvre, J. W. Gramlich, R. J. C. Hageman, N. E. Holden, T. J. Murphy, K. J. R. Rosman and M. Shima, *Pure Appl. Chem.*, **1991**, *63*, 991-1002.

13   R. K. Harris, E. D. Becker, S. M. Cabral De Menezes, R. Goodfellow and P. Granger, *Pure Appl. Chem.*, **2001**, *73*, 1795-1818.

14   M. Bernasson, P. Descouts and G. A. Styles, *Helv. Phys. Acta*, **1970**, *43*, 393-401.

15   J. E. Schirber, L. J. Azevedo and A. Narath, *Phys. Rev. B*, **1979**, *20*, 4746-4747.

16   D. G. Klobasa and P. K. Burkert, *Magn. Reson. Chem.*, **1987**, *25*, 154-157.

17   A. Narath and D. C. Barham, *Phys. Rev.*, **1968**, *176*, 479-483.

18   S. Wada and K. Asayama, *J. Phys. Soc. Jpn.*, **1973**, *34*, 1163-1167.

19   Y. Nishihara, Y. Yamaguchi, S. Waki and T. Kohara, *J. Phys. Soc. Jpn.*, **1983**, *52*, 2301-2303.

20   P. Pyykkö, *Mol. Phys.*, **2008**, *106*, 1965-1974.

21   R. Siegel, T. T. Nakashima and R. E. Wasylishen, *Concepts Magn. Reson. A*, **2005**, *26A*, 62-77.

22   R. Siegel, T. T. Nakashima and R. E. Wasylishen, *Concepts Magn. Reson. A*, **2005**, *26A*, 47-61.

23   D. Massiot, I. Farnan, N. Gautier, D. Trumeau, A. Trokiner and J. P. Coutures, *Solid State Nucl. Magn. Reson.*, **1995**, *4*, 241-248.

24   A. Medek, V. Frydman and L. Frydman, *J. Phys. Chem. A*, **1999**, *103*, 4830-4835.

25   R. W. Schurko, S. Wi and L. Frydman, *J. Phys. Chem. A*, **2002**, *106*, 51-62.

26   C. M. Widdifield and D. L. Bryce, *J. Phys. Chem. A*, **2010**, *114*, 10810-10823.

27   A. D. Bain, *Mol. Phys.*, **2003**, *101*, 3163-3175.

28   A. D. Bain and B. Berno, *Prog. Nucl. Magn. Reson. Spectrosc.*, **2011**, *59*, 223-244.

29   R. K. Harris, E. D. Becker, S. M. Cabral De Menezes, P. Granger, R. E. Hoffman and K. W. Zilm, *Pure Appl. Chem.*, **2008**, *80*, 59-84.

30   I. Solomon, *Phys. Rev.*, **1958**, *110*, 61-65.

31   I. D. Weisman and L. H. Bennett, *Phys. Rev.*, **1969**, *181*, 1341-1350.

32   A. C. Kunwar, G. L. Turner and E. Oldfield, *J. Magn. Reson.*, **1986**, *69*, 124-127.

33   E. L. Hahn, *Phys. Rev.*, **1950**, *80*, 580-594.

34   R. Bhattacharyya and L. Frydman, *J. Chem. Phys.*, **2007**, *127*, 194503.

35   L. A. O'Dell and R. W. Schurko, *Chem. Phys. Lett.*, **2008**, *464*, 97-102.

36   E. Kupče and R. Freeman, *J. Magn. Reson., Ser. A*, **1995**, *115*, 273-276.

37   K. J. Ooms, K. W. Feindel, V. V. Terskikh and R. E. Wasylishen, *Inorg. Chem.*, **2006**, *45*, 8492-8499.

38   M. E. Smith and E. R. H. van Eck, *Prog. Nucl. Magn. Reson. Spectrosc.*, **1999**, *34*, 159-201.

39   E. T. Rietschel and H. Bärnighausen, *Z. Anorg. Allg. Chem.*, **1969**, *368*, 62-72.

40   L. A. O'Dell, A. J. Rossini and R. W. Schurko, *Chem. Phys. Lett.*, **2009**, *468*, 330-335.

41   K. Eichele and R. E. Wasylishen, *WSolids1: Solid-State NMR Spectrum Simulation Package*, v. 1.19.11, Universität Tübingen: Tübingen, **2009**.

42   G. K. Semin, *Russ. J. Phys. Chem. A*, **2007**, *81*, 38-46.

43   A. Abragam, *The Principles of Nuclear Magnetism*, Oxford University Press: New York, **1961**.

44   K. J. D. MacKenzie and M. E. Smith, *Multinuclear Solid-State NMR of Inorganic Materials*, Pergamon: Amsterdam, **2002**.

45   A. D. Bain, *J. Magn. Reson.*, **2006**, *179*, 308-310.

46   Z. Gan, P. Srinivasan, J. R. Quine, S. Steuernagel and B. Knott, *Chem. Phys. Lett.*, **2003**, *367*, 163-169.

47   R. B. Creel and D. A. Drabold, *J. Mol. Struct.*, **1983**, *111*, 85-90.

48   R. B. Creel, *J. Magn. Reson.*, **1983**, *52*, 515-517.

49   G. M. Muha, *J. Magn. Reson.*, **1983**, *53*, 85-102.

50   A. Atzesdorfer and K. J. Range, *Z. Naturforsch. B*, **1995**, *50*, 1417-1418.

51   J. Spitaler, C. Ambrosch-Draxl, E. Nachbaur, F. Belaj, H. Gomm and F. Netzer, *Phys. Rev. B*, **2003**, *67*, 115127.

52   A. A. Boguslavskii, R. S. Lotfullin, R. V. Magera and V. V. Pechenov, *Fiz. Tverd. Tela*, **1974**, *16*, 2453-2454.

53   R. A. Johnson and M. T. Rogers, Temperature Dependence of the Nuclear Quadrupole Resonance Spectra of Perrhenates and Periodates In *Advances in Nuclear Quadrupole Resonance: Papers Presented at the International Symposium on Nuclear Quadrupole Resonance, Sept. 28-29, 1972, Queen Elizabeth College, University of London, England*, J. A. S. Smith, Ed., Heyden: London, **1974**, 297-313.

54   M. T. Rogers and K. V. S. R. Rao, *J. Chem. Phys.*, **1973**, *58*, 3233-3235.

55   S. L. Segel, *J. Chem. Phys.*, **1978**, *69*, 2434-2438.

56   E. B. Doering and J. S. Waugh, *J. Chem. Phys.*, **1986**, *85*, 1753-1756.

57   A. S. Tracey and K. Radley, *Liq. Cryst.*, **1989**, *6*, 319-323.

58   K. Burzyński, P. Magierski, J. Dobaczewski and W. Nazarewicz, *Phys. Scr. T*, **1995**, *T56*, 228-230.

59   J. Cederberg, D. Olson, A. Nelson, D. Laine, P. Zimmer, M. Welge, M. Feig, T. Höft and N. London, *J. Chem. Phys.*, **1999**, *110*, 2431-2436.

60   S. Günther, O. Lutz, A. Nolle and P. G. Schrade, *Z. Naturforsch. A*, **1978**, *33*, 1018-1020.

61   B. C. Sanctuary, T. K. Halstead and P. A. Osment, *Mol. Phys.*, **1983**, *49*, 753-784.

62   A. Müller, E. Krickemeyer, H. Bögge, M. Penk and D. Rehder, *Chimia*, **1986**, *40*, 50-52.

63   Y. Do, E. D. Simhon and R. H. Holm, *Inorg. Chem.*, **1985**, *24*, 4635-4642.

64   D. W. Alderman, M. S. Solum and D. M. Grant, *J. Chem. Phys.*, **1986**, *84*, 3717-3725.

65   I. P. Swainson and R. J. C. Brown, *Acta Cryst.*, **1997**, *B53*, 76-81.

66   K. V. S. R. Rao and M. T. Rogers, *J. Magn. Reson.*, **1972**, *8*, 392-397.

67   P. K. Burkert and M. F. Eckel, *Z. Naturforsch. B*, **1973**, *28*, 379-382.

68   R. A. Johnson and M. T. Rogers, *J. Magn. Reson.*, **1974**, *15*, 584-589.

69   R. J. C. Brown, *J. Magn. Reson.*, **1975**, *18*, 558-559.

70   R. J. C. Brown, J. G. Smeltzer and R. D. Heyding, *J. Magn. Reson.*, **1976**, *24*, 269-274.

71   R. J. C. Brown and S. L. Segel, *J. Chem. Phys.*, **1977**, *67*, 3163-3169.

72   S. E. Ashbrook and S. Wimperis, *Prog. Nucl. Magn. Reson. Spectrosc.*, **2004**, *45*, 53-108.

73   S. Cavadini, *Prog. Nucl. Magn. Reson. Spectrosc.*, **2010**, *56*, 46-77.

Chapter Six

Aspects of 'NMR Crystallography' Using Quadrupolar Halogen Nuclei

6.1   Introduction

As demonstrated in Chapters 3 – 5, SSNMR spectroscopy is an important tool which may be used to probe structure and dynamics within a range of chemical systems. To obtain a more complete picture of a given solid state system, however, it is often desirable to complement the SSNMR data with information acquired using other methods. In the earlier Chapters, GIPAW DFT methods[1] were used to calculate a number of relevant NMR observables at the nuclei in solid materials. This approach is not limited to the class of compounds studied here, and a number of recent accounts have illustrated that NMR tensor parameter calculations using GIPAW DFT can provide additional insights in the study of a variety of chemical systems.[2-12]

Similarly, XRD measurements are also routinely paired with SSNMR data when discussing solid state structures. It is well-known that single crystal XRD experiments may be performed in order to determine the crystal structures of various materials, but when suitable crystals are not available or other complicating effects are present, so-called 'NMR crystallography' methods may be potentially superior for crystal structure determination.[13] Indeed, there is an increasing interest in NMR crystallography, which in a general sense pertains to obtaining molecular-level and crystal structure information for solid materials using SSNMR data.[13]   Although there have been a number of exciting recent advances in this area of research,[14-21] one cannot currently convert SSNMR data into a unique solid state structure in a

completely generalized manner. However, these earlier accounts, which typically rely upon spin-1/2 probe nuclei observations under MAS conditions, have demonstrated the ability to gain information such as asymmetric units, molecular symmetry, and space groups.[22,23] Likewise, with even a small amount of *a priori* knowledge, NMR crystallography methods have been applied to solve and refine the structures related to certain classes of materials, such as zeolites,[24-26] which are sometimes subject to crystal twinning and typically do not possess enough long range order to produce crystals that would be considered suitable for XRD studies. As well, SSNMR data acquired for spin-1/2 nuclei have been used to solve or refine structures (with the aid of computational modeling) for organic molecules such as β-L-aspartyl-L-alanine[21] and thymol.[17] Similar approaches have also been used to propose structures for host-guest complexes,[27] biomolecules,[28,29] and ^{14}N-containing ($I = 1$) compounds.[30] Thus, while there appears to be a broad range of applications for NMR crystallography methods when $I = 1/2$, there is substantially less literature evidence of using quadrupolar nuclei. As demonstrated in a variety of cases in Chapters 3 – 5, the parameters associated with the $\ddot{V}$ tensor are highly sensitive local probes of molecular structure and are not potential observables for $I = 1/2$ nuclei.

As noted in Chapters 3 and 4, a recent focus of our SSNMR research group has been SSNMR spectroscopy of the quadrupolar halogen nuclides (i.e., $^{35/37}$Cl, $^{79/81}$Br, and ^{127}I).[7,9,31-38] It is clear that the $^{79/81}$Br and ^{127}I SSNMR spectra associated with these nuclei are useful reporters of the EFG produced by the ions and molecules of the surrounding environment. At this point, attention is placed on the remaining stable quadrupolar halogen nuclides: ^{35}Cl and ^{37}Cl. Both NMR-active chlorine nuclides ($I(^{35/37}$Cl$) = 3/2$) are of moderately high abundance (75.779(46) % for ^{35}Cl, 24.221(46) % for ^{37}Cl).[39] The Q associated with these nuclei are moderate ($Q(^{35}$Cl$) = -81.65(80)$ mb; $Q(^{37}$Cl$) = -64.35(64)$ mb;[40] however, their corresponding γ values are rather low (i.e., below ^{15}N). Complications such as probe ringing and second-order QI line shape

broadening may be reduced by performing the SSNMR experiments in a high B_0. A variety of chlorine environments have been probed using $^{35/37}$Cl SSNMR spectroscopy, as outlined in Section 3.1. As a result of these recent studies, a number of trends in the halogen SSNMR parameters have been observed and rationalized. For example, for the alkaline earth metal halides studied to date, it has been observed that sample hydration will: (i) generally result in a decrease in the halogen δ_{iso} value; and (ii) nearly always lead to a decrease in the halogen C_Q value.[7,9,41] It was noted in Section 3.3.1.1.1, however, that the currently available ^{35}Cl SSNMR data for $CaCl_2$, collected by Sandland et al.,[42] seem to indicate that this system does not follow the latter trend: the data suggest rather that upon hydration the C_Q value *increases* substantially. Additional SSNMR studies on $CaCl_2$ should therefore be performed to confirm or refute the prior ^{35}Cl SSNMR data.

In the first portion of this Chapter, an example of a combined SSNMR and GIPAW DFT crystallographic structure refinement is provided, which relies primarily on the EFG tensor data that are unavailable for spin-1/2 nuclei. Compared to $I = 1/2$ nuclei, quadrupolar nuclei have the potential to provide additional long range crystallographic information, due to the fact that contributions to the EFG from the lattice decrease relatively slowly as a function of the distance from the probe nucleus (i.e., $1/r^3$). $MgBr_2$ is an excellent test case, due to the small number of degrees of structural freedom and the resulting lack of ambiguity in the interpretation of the NMR data. From a technical standpoint, there are particular challenges associated with ^{25}Mg and $^{79/81}$Br SSNMR experiments and computations; hence, $MgBr_2$ represents a rigorous test case in these respects.

In the second portion of this Chapter, results of ^{35}Cl SSNMR measurements for $CaCl_2$ and $CaCl_2 \cdot 6H_2O$ are outlined. The ^{37}Cl and ^{43}Ca SSNMR spectra of anhydrous $CaCl_2$ are also discussed. The results of GIPAW DFT computations on $CaCl_2$ and all of its known stable

crystalline hydrates (i.e., $CaCl_2 \cdot 2H_2O$, $(\alpha/\beta/\gamma)-CaCl_2 \cdot 4H_2O$, and $CaCl_2 \cdot 6H_2O$) are presented in an attempt to understand the prior ^{35}Cl SSNMR measurements for $CaCl_2$, to refine the hydrogen positions for $CaCl_2 \cdot 2H_2O$, and to complement the experimental SSNMR data.

6.2   Experimental Details

6.2.1 Sample Preparation

$MgBr_2$ (98 %), $CaCl_2$ (99.99 %), and $CaCl_2 \cdot 6H_2O$ (98 %) were purchased from Sigma-Aldrich and received as powders. Sample purity for all compounds was confirmed by the manufacturer or by using pXRD (See Appendix D, Section D.1.1). As $MgBr_2$ and $CaCl_2$ are hygroscopic, samples of these materials were stored and prepared for use under dry N_2 or Ar. $CaCl_2 \cdot 6H_2O$ was handled for short periods of time in a low humidity atmosphere to avoid further hydration. Prior to SSNMR experiments, all samples were powdered and tightly packed into either 4 mm or 7 mm o.d. Bruker MAS ZrO_2 rotors. For pXRD experiments upon $MgBr_2$, the sample was packed into a 1.0 mm o.d. thin wall (10 micron) borosilicate glass capillary, which was then sealed with epoxy and sent for external analysis at Université de Montréal.

6.2.2 Solid-State ^{25}Mg and $^{79/81}Br$ NMR

Experimental data were acquired at the National Ultrahigh-field NMR Facility for Solids in Ottawa using a standard bore (54 mm) Bruker AVANCEII spectrometer operating at $B_0 = 21.1$ T ($\nu_0(^1H) = 900.21$ MHz) and at the University of Ottawa using a wide bore (89 mm) Bruker AVANCE spectrometer operating at $B_0 = 11.75$ T ($\nu_0(^1H) = 500.13$ MHz). At 21.1 T, SSNMR experiments used a 4 mm Bruker HX MAS probe ($\nu_0(^{25}Mg) = 55.098$ MHz; $\nu_0(^{79}Br) = 225.519$ MHz; $\nu_0(^{81}Br) = 243.093$ MHz). At 11.75 T, SSNMR experiments used a 4 mm Bruker

HXY MAS probe ($v_0(^{25}\text{Mg})$ = 30.615 MHz; $v_0(^{79}\text{Br})$ = 125.309 MHz; $v_0(^{81}\text{Br})$ = 135.075 MHz). The bromine $\pi/2$ pulse widths were established, and the $^{79/81}$Br SSNMR spectra were referenced, using solid KBr ($\delta_{\text{iso}}(\text{KBr(s)})$ = 0.0 ppm). Magnesium chemical shifts and $\pi/2$ pulse widths were determined using the ^{25}Mg NMR signal of 1.0 mol/dm^3 aqueous MgCl$_2$ ($\delta_{\text{iso}}(\text{MgCl}_2(\text{aq}))$ = 0.0 ppm). For the non-cubic solid samples under study, CT selective (i.e., solid $\pi/2$) pulse widths included a scaling of the optimized cubic solid/solution pulses by $1/[I + 1/2]$ (i.e., 1/2 for $^{79/81}$Br and 1/3 for ^{25}Mg).

Bromine-79/81 SSNMR signals were primarily acquired using the Solomon echo[43-45] pulse sequence; however, the QCPMG pulse sequence[46-48] was also used at B_0 = 11.75 T to enhance the bromine NMR signal and thus reduce experiment times. The QCPMG sequence was also used at both applied fields to estimate T_2 values. The estimated T_2 values were such that whole echo data acquisition could be carried out, thereby increasing the S/N of the Solomon echo experiment by $\sqrt{2}$ per scan. Typical $^{79/81}$Br Solomon echo parameters (for full details, see Appendix D, Table D.1) were the following: $\pi/2$ = 1.0 to 1.2 μs; spectral window = 1 000 to 2 000 kHz; τ_1 = 250 to 300 μs; recycle delay = 0.4 to 0.6 s; collection of 2 048 to 4 096 data points per transient and 2 048 to 12 000 transients were collected per experiment. Magnesium-25 SSNMR signals were acquired using a Bloch decay (i.e., 'pulse-acquire') sequence under MAS conditions. Full experimental details, including those used for ^{25}Mg SSNMR and $^{79/81}$Br QCPMG SSNMR experiments, can be found in Appendix D, Table D.1. VOCS data acquisition methods[49-51] were required to acquire the $^{79/81}$Br SSNMR signals at B_0 = 11.75 T. Offsets were 300 kHz for Solomon echo experiments, while QCPMG experiments used offsets ranging from 87.8 to 95.9 kHz. Each sub-spectrum was combined in the frequency-domain by co-addition to produce the total VOCS spectrum.

6.2.3 Solid-State $^{35/37}Cl$ and ^{43}Ca NMR

All data were acquired using the two spectrometers denoted in Section 6.2.2. For $^{35/37}Cl$ SSNMR experiments at 21.1 T ($v_0(^{35}Cl)$ = 88.189 MHz; $v_0(^{37}Cl)$ = 73.408 MHz), home-built static probes (single-channel 7 mm or 4 mm HX) were used. Calcium-43 SSNMR experiments at the same field ($v_0(^{43}Ca)$ = 60.575 MHz) employed a single-channel 7 mm Bruker MAS probe. All ^{35}Cl SSNMR experiments at 11.75 T ($v_0(^{35}Cl)$ = 49.002 MHz) used a 4 mm Bruker HX MAS probe. The $^{35/37}Cl$ SSNMR spectra were referenced to 0.1 mol/dm^3 NaCl in D$_2$O at 0.0 ppm[52] using solid KCl as a secondary reference ($\delta_{iso}(KCl(s))$ = 8.54 ppm).[32] Calcium-43 SSNMR spectra were referenced to a 2 mol/dm^3 aqueous solution of CaCl$_2$ (δ_{iso} = 0.0 ppm).[53] Chlorine and calcium pulse widths were established using the $^{35/37}Cl$ and ^{43}Ca SSNMR signals of solid KCl and saturated CaCl$_2$(aq), respectively. As above, CT selective pulse widths included a scaling of the optimized cubic solid/solution pulses by $1/[I + 1/2]$ (i.e., 1/2 for $^{35/37}Cl$ and 1/4 for ^{43}Ca).

All $^{35/37}Cl$ SSNMR signals were acquired using the Solomon echo[43-45] pulse sequence. Typical $^{35/37}Cl$ SSNMR experimental parameters were as follows: CT selective $\pi/2$ pulse width = 2.4 to 3.2 μs; spectral window = 200 to 1 000 kHz; τ_1 = 27.5 to 78.8 μs; and 1 024 to 2 048 complex time-domain data points. All ^{43}Ca SSNMR signals were acquired using the Bloch decay experiment (typical parameters: $\pi/2 \sim$ 1.0 μs; spectral window = 20 kHz; 512 to 1 024 complex time-domain data points). The recycle delays used, as well as the number of scans required for the collection of the spectra, may be found in Appendix D, Table D.1. For ^{35}Cl SSNMR experiments on CaCl$_2$ at 11.75 T, VOCS[49,50] data acquisition was used (offset = 110 kHz). After VOCS data acquisition, each sub-spectrum was combined in the frequency-domain by co-addition to produce the total VOCS spectrum. For CaCl$_2$·6H$_2$O, CW ^{1}H decoupling was tested

at both applied fields ($\nu_1(^1\mathrm{H}) \sim 50$ kHz at 11.75 T and ~ 85 kHz at 21.1 T). For additional experimental details, see Appendix D, Table D.1.

6.2.4   Powder X-Ray Diffraction

Experiments were carried out with an APEX-II single-crystal diffractometer using a MoKα radiation source ($\lambda = 0.7093$ Å) equipped with a charge-coupled device (CCD) area detector. Data were collected over the range $4.96° < 2\theta < 46.78°$ and clearly demonstrate that the MgBr$_2$ sample had not formed the hexahydrate (see Figure 6.5 for the pXRD pattern).

6.2.5   Quantum Chemical Computations: General

GIPAW DFT calculations employed the CASTEP-NMR (v. 4.1) software,[1,54-56] while the input files were generated using Materials Studio (v. 3.2.0.0). Computations used either usp[57] or otfg pseudopotentials and GGA XC functionals. The magnesium, bromine, chlorine, and calcium otfg pseudopotentials were obtained directly from Accelrys Inc. (San Diego, CA). Further details pertaining to the relevant otfg pseudopotentials may be found in Appendix D, Table D.2. Geometry optimizations, as well as $\ddot{\sigma}$ and $\ddot{V}$ tensor calculations were performed using the PBE XC functional.[58,59] Selected additional $\ddot{\sigma}/\ddot{V}$ tensor parameters were calculated using the PW91 XC functional[60-64] and yielded similar values.

6.2.5.1 Specific Computational Details: MgBr$_2$

NMR parameter convergence was established by varying both the Monkhorst-Pack[65] k-point sampling of the Brillouin zone, as well as E_{cut} (Appendix D, Figures D.1 to D.3). All calculations used the 'precise' setting, as defined by Materials Studio, for the FFT grid. It was

found that both the system energy and relevant SSNMR parameters were satisfactorily converged at E_{cut} = 400 eV, using a $10 \times 10 \times 6$ k-point grid (i.e., $E_{1200} - E_{400}$ = –0.35 kJ mol^{-1}; $C_Q(^{81}Br_{1200}) - C_Q(^{81}Br_{400})$ = 0.02 MHz; $\delta_{iso}(^{81}Br_{1200}) - \delta_{iso}(^{81}Br_{400})$ = 0.20 ppm, where the subscripts specify the E_{cut} value used). Usage of a $15 \times 15 \times 8$ k-point grid, relative to a $10 \times 10 \times 6$ k-point grid (using E_{cut} = 610 eV) resulted in no change in the bromine EFG tensor parameters and a ~0.1 ppm change in the calculated isotropic MS values. The 'fully optimized' geometry, E_{cut} = 400 eV, and a $10 \times 10 \times 6$ k-point grid were used for computations that simulated the movement of the bromide ions parallel to the c unit cell direction (Figure 6.4 and Appendix D, Figure D.4). To convert calculated $\ddot{\sigma}$ tensor elements into corresponding $\ddot{\delta}$ tensor elements, the following procedure was used: the bromine σ_{iso} value for the reference compound, KBr (i.e., $\sigma_{iso,\ ref}$), was determined using E_{cut} = 800 eV, a $6 \times 6 \times 6$ k-point grid, and the same XC functional (i.e., either PBE or PW91) as MgBr$_2$. Then, **(2.12)** was used, where σ_{iso} is the isotropic bromine MS value for MgBr$_2$ and δ_{iso} is the isotropic bromine CS value for MgBr$_2$.

6.2.5.2 Specific Computational Details: Chlorine-Containing Systems

Computed chlorine MS tensor elements were transformed into CS tensor elements using the following procedure: the chlorine σ_{iso} for NaCl was determined using E_{cut} = 1200 eV, a $4 \times 4 \times 4$ k-point grid, and the same XC functional as the sample of interest. Using the above calculated σ_{iso} value and the known chlorine CS of solid NaCl relative to 0.1 mol/dm^3 NaCl in D$_2$O (i.e., $\delta_{iso}(NaCl(s))$ = −41.11 ppm),[32] the σ_{iso} value for 0.1 mol/dm^3 NaCl in D$_2$O could be calculated using **(2.12)**; hence, all computed σ_{ij} values could be placed on an experimental δ scale. The E_{cut} value and k-point grid used for the GIPAW DFT calculations on each system are in the footnotes to Tables 6.3 and 6.4. For computed structure energies, structure references,

optimized structure parameters, the pseudopotentials used, and selected additional computational details, see Appendix D, Tables D.2 and D.3.

6.3　Results and Discussion

6.3.1　Structure Refinement of MgBr₂ Using SSNMR Data

6.3.1.1　Bromine-79/81 SSNMR Experiments

For over 100 years, MgBr$_2$ has been of great importance in synthetic chemistry as part of various Grignard reagents.[66] In addition, it has been used to treat nervous system disorders,[67] as a catalyst in esterification reactions,[68] and exhibits luminescence when doped with Ti(II).[69] Using pXRD data, its crystal structure under ambient conditions was proposed in 1929;[70] As a result of this pXRD account, the space group was found to be $P\overline{3}m1$ (№. 164) with the Mg and Br ions being located at 1a and 2d Wyckoff sites, respectively. Additional structural details can be found in Appendix D, Table D.3. While it is believed that the space group and Wyckoff sites are correct, it is anticipated that the atomic positions in the crystalline lattice can be further refined using NMR crystallography methods.

The $^{79/81}$Br SSNMR spectra of a stationary powdered sample of MgBr$_2$ exhibit characteristic second-order QI-broadened powder patterns whose line widths exceed the uniform excitation bandwidth of the probe (Figures 6.1 and 6.2). At the lower applied field, the spectra were thus acquired in a piecewise fashion using VOCS methods. Without recourse to simulations or calculations, the spectra indicate that the $\ddot{V}$ tensor magnitude at the bromine nuclei is nonzero. Bromine-81 SSNMR spectra acquired at $B_0 = 21.1$ T (Figure 6.1b) and $B_0 = 11.75$ T (Figures 6.2b and 6.2c) are complementary, and analytical line shape simulations produce the following EFG tensor parameters: $|C_Q(^{81}\text{Br})| = 21.93(20)$ MHz; $\eta_Q = 0.02(2)$. As

noted in Chapter 3, the ^{79}Br and ^{81}Br nuclei possess similar γ, but different Q values. Hence, a ^{79}Br SSNMR spectrum should be similar to its corresponding ^{81}Br SSNMR spectrum, except for a scaling factor in the measured line width.[34]
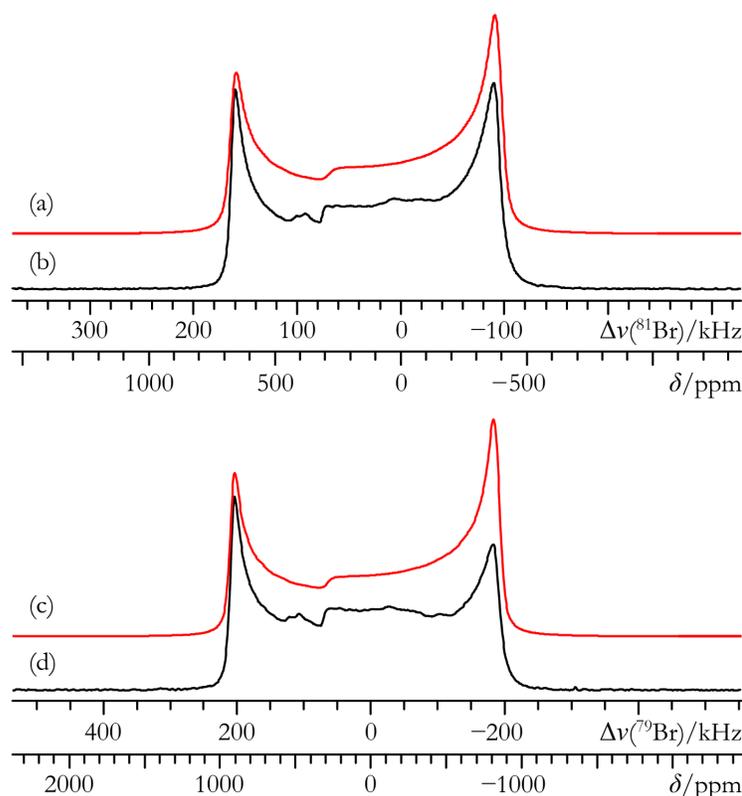
Figure 6.1 Best-fit analytical simulations (a, c), and experimental static Solomon echo $^{79/81}$Br SSNMR spectra of powdered MgBr$_2$ acquired at B_0 = 21.1 T (b, d).

The experimentally measured value for C_Q(^{79}Br) matches, within experimental error, the *a priori* estimated value (Figures 6.1d, 6.2e, and 6.2f). While bromine CSA is expected in MgBr$_2$, it is beneath detection limits (i.e., Ω < 50 ppm), even at 21.1 T. As the extracted $^{79/81}$Br SSNMR parameters are consistent amongst all six experimental bromine NMR spectra, it is clear that the EFG at the Br nucleus is nearly axially-symmetric and conclusively nonzero. While the axial symmetry is fully expected as the bromide anions are on 3*m* lattice positions, the distinctly nonzero C_Q($^{79/81}$Br) values are in marked disagreement with prior calculations based on the

currently accepted crystal structure,[70] and indicate rather that the EFG at the bromine nuclei should be very close to zero.[71]
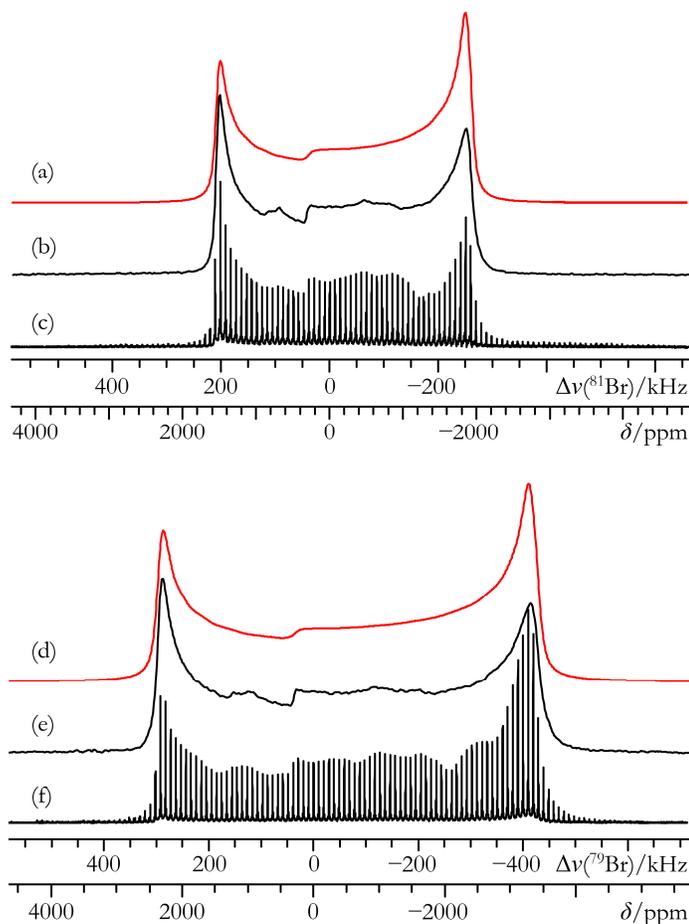
Figure 6.2 Best-fit analytical simulations (a, d), experimental static VOCS Solomon echo (b, e), and experimental static VOCS QCPMG (c, f) [79/81]Br SSNMR spectra of powdered $MgBr_2$ acquired at B_0 = 11.75 T.

6.3.1.2 Magnesium-25 SSNMR Experiments

[25]Mg SSNMR experiments were performed to provide further structural information. Magnesium-25 possesses a smaller Q value (i.e., 199.4(20) mb),[40] but has a low γ, and is only 10.03 % abundant; hence, conducting meaningful [25]Mg SSNMR experiments at natural abundance is often challenging. Recent accounts (many involving expensive isotopic

enrichment) have used [25]Mg SSNMR to study inorganic alloys,[72] organometallic materials,[73] magnesium-containing organic compounds,[74] and bio-inorganic systems.[75] The observed [25]Mg MAS SSNMR spectra of MgBr$_2$ (Figure 6.3) possess several key features which allow for the discussion of the local electronic environment about the [25]Mg nuclei. First, line shape simulations which assume an axially symmetric [25]Mg EFG tensor (i.e., η_Q([25]Mg) = 0) are in excellent agreement with the observed spectra. This finding is consistent with the accepted site symmetry. The derived $\ddot{V}$ tensor magnitude, C_Q([25]Mg) = 850 kHz, highlights a rather small QI at the magnesium (nearly three orders of magnitude smaller than that of [185]Re in NaReO$_4$!). The magnesium isotropic chemical shift is highly shielded (δ_{iso} = −16.25(15) ppm), which hints that contributions to the paramagnetic shielding mechanism are minor.[76,77] This is consistent with the highly ionic bonding character in MgBr$_2$.
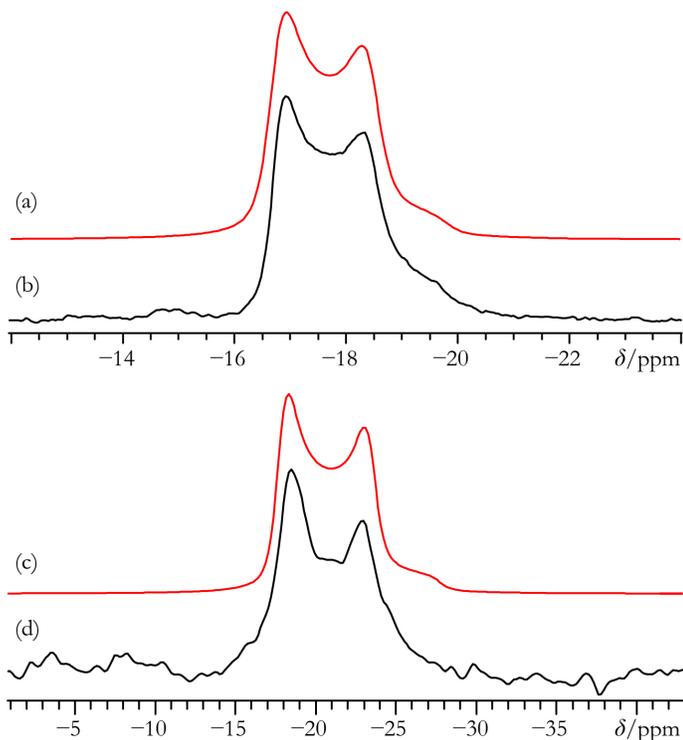
Figure 6.3 Best-fit analytical simulations (a, c), and experimental MAS [25]Mg SSNMR spectra of powdered MgBr$_2$ acquired at B_0 = 21.1 T (b) and B_0 = 11.75 T (d). In (b) and (d), ν_{MAS} = 5.000 kHz.

6.3.1.3 GIPAW DFT Quantum Chemical Computations

GIPAW DFT calculations[1,54-56] of the $\ddot{\sigma}$ and $\ddot{V}$ tensors, carried out using the accepted crystal structure, are in clear disagreement with the experimental $^{79/81}$Br and ^{25}Mg SSNMR data (Table 6.1). Most striking are the calculated $C_Q(^{79/81}$Br) values, which are almost an order of magnitude smaller than observed, while the calculated $C_Q(^{25}$Mg) overestimates experiment by a factor of four. When this research was initially performed and presented in 2009, GIPAW DFT calculations of NMR parameters had not been published for either ^{25}Mg or $^{79/81}$Br, although examples now exist for ^{25}Mg.[78] Recall that as part of the comprehensive study of the alkaline earth metal bromides presented in Chapter 3, $^{79/81}$Br SSNMR experiments and GIPAW DFT calculations were performed on a variety of compounds. As a result, excellent correlation between experimental and GIPAW DFT computed $^{79/81}$Br $\ddot{V}$ tensors has been demonstrated. At the same time, it is noted that universal agreement between experimental and computed ^{25}Mg EFG tensors has not been established. As GIPAW DFT computed bromine $\ddot{V}$ tensor parameters generally display excellent agreement with experimental observations for the alkaline earth metal bromides, the bromine SSNMR parameters can be reasonably used as tools for the *further* refinement of the accepted crystal structure of MgBr$_2$.

As noted earlier, according to the accepted crystal structure, MgBr$_2$ belongs to the trigonal space group $P\bar{3}m1$, with the Br$^-$ and Mg^{2+} ions at $3m$ and $\bar{3}m$ sites, respectively. As all observed SSNMR line shapes were precisely fit using an axially-symmetric EFG tensor, the point symmetry at all NMR-active nuclei must be at least C_3. If one remains within the space group that was assigned previously (i.e., CdI$_2$ (2H) packing), then mirror site symmetry must be present at all ion sites. Hence, it can be reasonably concluded that the Wyckoff positions, as originally assigned using pXRD data, are correct. Under these assumptions, it is realized that

there is one freely adjustable structural parameter: the position (as expressed in fractional unit cell coordinates) of the Br ions parallel to the c unit cell axis (c(Br)).

Table 6.1 Experimental and GIPAW DFT ^{25}Mg/$^{79/81}$Br NMR tensor parameters for MgBr$_2{}^a$

^AX	$|C_Q(^AX)|$ / MHz	η_Q	σ_{iso} / ppm	δ_{iso} / ppm
experimental from SSNMR spectra				
^{81}Br	21.93(20)	0.02(2)	—	285(10)
^{79}Br	26.25(20)	0.02(2)	—	285(15)
^{25}Mg	0.85(20)	0	—	−16.25(15)
computed using fully optimized structure ('full opt.')				
^{81}Br	21.81^b	0.00	2306.8	320.9
^{25}Mg	2.74	0.00	553.9	—
computed using previously accepted pXRD structure ('XRD')				
^{81}Br	3.90	0.00	2274.7	353.1
^{25}Mg	3.47	0.00	552.9	—

^{a} Error bounds (where applicable) are in parentheses. Parameter definitions are in Chapter 2. GIPAW DFT computations of the SSNMR parameters shown here used the PBE XC functional, E_{cut} = 1200 eV and a 10 × 10 × 6 k-point grid, while geometry optimizations used the same XC functional and k-point grid, but E_{cut} = 800 eV. For further details, see Appendix D, Tables D.4 and D.5.
^{b} Calculated $|C_Q(^{79}$Br$)|$ = 26.06 MHz.

In the prior pXRD study, it was assumed that c(Br) = 0.25. By computationally optimizing only c(Br) and holding the unit cell constant, greatly improved agreement between the computed and observed bromine C_Q values is achieved (i.e., $|C_Q(^{81}$Br$)|$ increases from 3.90 to 14.89 MHz), and the computed system energy decreases (Figure 6.4 and Appendix D, Table D.2). When the MgBr$_2$ structure is subjected to a full geometry optimization (i.e., both the unit cell and c(Br) were optimized), an energy minimum is found near c(Br) = 0.21, with an accompanying increase in the c value for the unit cell. For this 'fully optimized' structure, the measured and calculated $C_Q(^{79/81}$Br$)$ values agree within experimental error (Table 6.1) and the calculated δ_{iso}(Br) and $C_Q(^{25}$Mg$)$ values are also in better agreement with the experimental

SSNMR values. By performing GIPAW DFT calculations where the c(Br) value is incremented in a stepwise fashion, a linear correlation between the calculated $C_Q(^{79/81}Br)$ and c(Br) values is established ($R^2 = 0.9998$) (Figure 6.4).
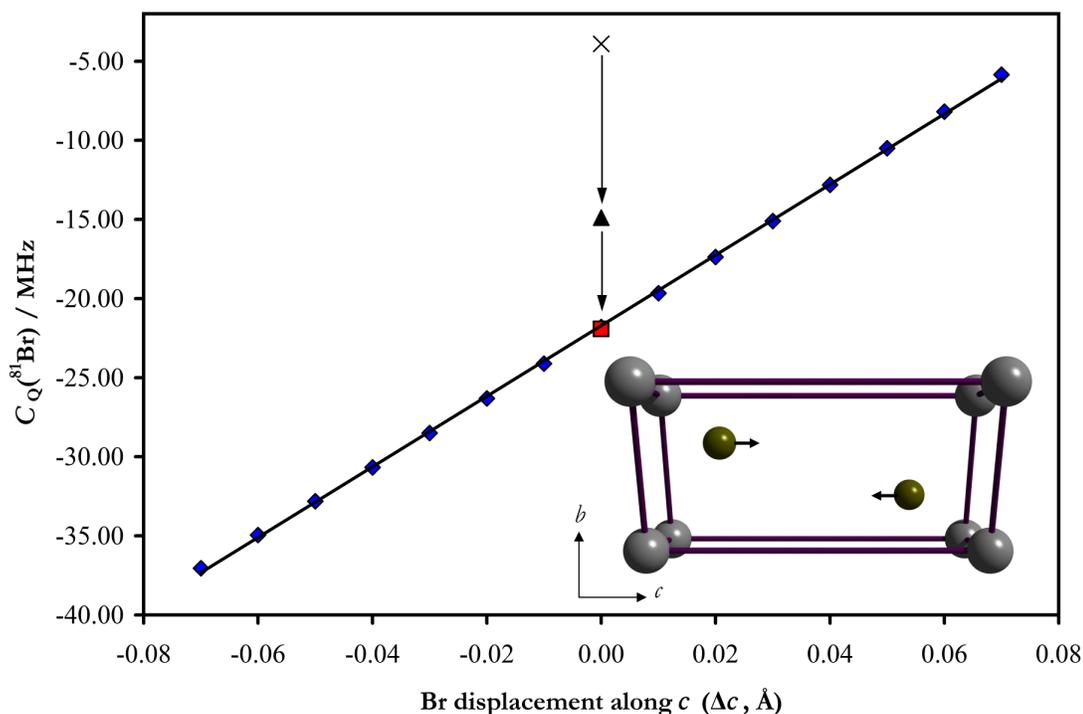
Figure 6.4 GIPAW DFT calculated $C_Q(^{81}Br)$ vs. Δc(Br) for MgBr$_2$. For comparison, $C_Q(^{81}Br)$ calculated using: ($\times$) the accepted pXRD structure, ($\blacktriangle$) partially optimized geometry (i.e., unit cell is held fixed, but c(Br) is allowed to vary). The $C_Q(^{81}Br)$ value calculated from the fully optimized geometry (i.e., Δc(Br) = 0.00 Å) and the experimental value are indistinguishable from one another ($\blacksquare$). ($\blacklozenge$ series, best fit: C_Q(MHz) = 223.01(Δc) − 21.71). Inset: schematic of the fully optimized MgBr$_2$ unit cell, as viewed along a. Vectors originating at the Br$^-$ represent the displacement direction when moving (as shown) along the positive c axis.

This extreme sensitivity of the EFG at the Br nuclei to the structure (notably, for a fixed cell, that a change in the Br position of ca. 0.04 Å can increase $|C_Q(^{81}Br)|$ by ~11 MHz), and the experimental observation that $C_Q(^{79/81}Br)$ is nonzero, clearly shows that c(Br) is not at the previously assumed value of 0.25, but is rather very likely to be near 0.21. It is also clear that the

c unit cell length should be larger than previously determined. Both these findings are consistent

with new pXRD data that were collected with modern equipment (Figure 6.5).
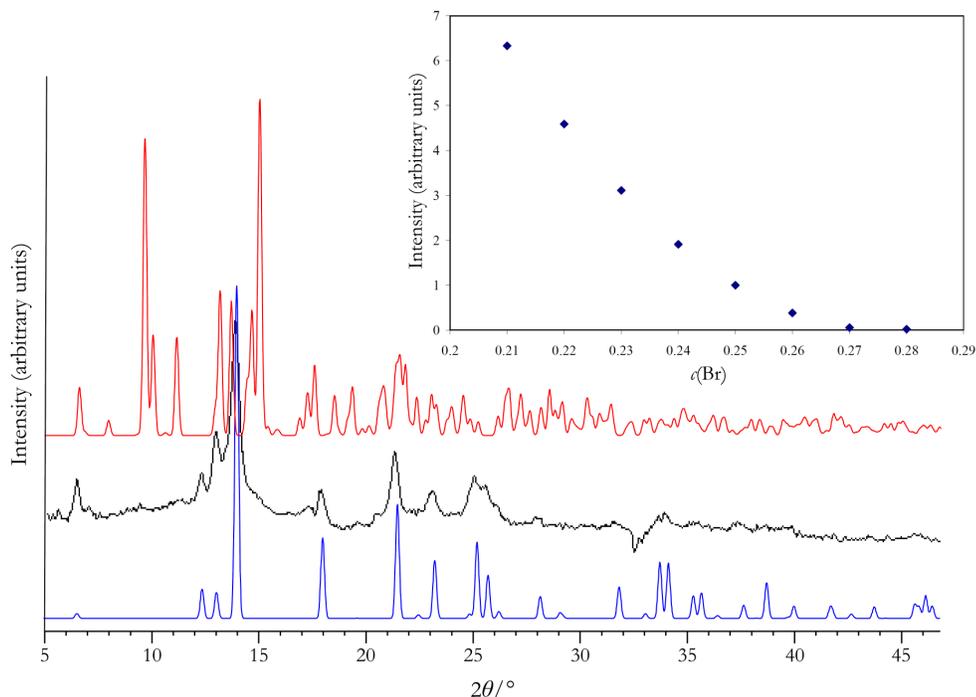
Figure 6.5 The experimental pXRD pattern of the sample used for [25]Mg/[79/81]Br SSNMR experiments (middle) agrees qualitatively with the database entry for $MgBr_2$ (bottom). Agreement is poor; however, between the experimental pXRD pattern and the database entry for $MgBr_2 \cdot 6H_2O$ (top). It is concluded that SSNMR experiments have been performed upon anhydrous $MgBr_2$. The dip around $2\theta = 32°$ is due to a detector defect. As noted in Section 6.3.1, the pXRD data acquired here agree with the main conclusions regarding the modified structure of $MgBr_2$, as explained below. The peaks at $2\theta = 6.32°$ and $12.84°$ belong to the (001) and (002) lattice planes. By a simple application of Bragg's Law, $c = 6.43$ Å and 6.34 Å, both of which are greater than the currently accepted value (6.26 Å), in agreement with the findings above. Also, it is noted that the (001) peak intensity is highly dependent on the $c(Br)$ value (see inset for a plot of the (001) peak intensity vs. $c(Br)$ for a constant unit cell; note that the intensity of the point where $c(Br) = 0.25$ has been arbitrarily normalized to one). Working within the space group of the accepted structure, as $c(Br)$ increases, the (001) peak intensity decreases, becoming vanishingly small for $c(Br) > 0.26$. Thus, based upon only the pXRD data, if $c(Br) = 0.25$, the (001) peak intensity would be very weak (perhaps below detection). If one changes $c(Br)$ to be progressively less than 0.25 (see inset), the (001) peak intensity increases steadily. The observed pXRD data are thus in support of the SSNMR/GIPAW DFT conclusions of a $c(Br)$ value less than the accepted value of 0.25.

6.3.2 SSNMR Study of $CaCl_2$ and Selected Hydrates

6.3.2.1 Chlorine-35/37 and Calcium-43 SSNMR Experiments on $CaCl_2$

The ^{35}Cl $\ddot{V}$ tensor parameters reported previously[42] for $CaCl_2$ appeared to be inconsistent with the trends observed for other alkaline earth metal halides (as detailed in Chapter 4),[7,41] which prompted a reinvestigation of this system using SSNMR spectroscopy. Chlorine-35 SSNMR spectra were obtained for $CaCl_2$ at two applied fields (B_0 = 11.75 and 21.1 T), and analytical modeling of all observed line shapes (Figures 6.6 and 6.7) resulted in identical $\ddot{V}$ and $\ddot{\sigma}$ tensor parameters. Additional ^{37}Cl SSNMR experiments were performed at 21.1 T, and the spectra were modeled using the same parameters as the ^{35}Cl SSNMR line shapes, after appropriate scaling of C_Q by the $Q(^{37}Cl)/Q(^{35}Cl)$ ratio of 0.788 (Figure 6.8). Extracted parameters are summarized in Table 6.2. It is immediately clear that the observed $^{35/37}Cl$ SSNMR line shapes and corresponding EFG tensor parameters are inconsistent with the prior literature account for $CaCl_2$.[42]

The presently measured $C_Q(^{35}Cl)$ value of 8.82(8) MHz is more than twice as large as the values observed for other anhydrous and hydrated alkaline earth metal chlorides.[41,42,79] This is primarily attributed to the arrangement of the Ca^{2+} ions within the first coordination sphere of each chloride, which forms a distorted trigonal plane.[80] The measured $\eta_Q(^{35/37}Cl)$ value of 0.383(15) confirms the absence of any high-symmetry rotational axes (i.e., C_n where n > 2), in support of the local symmetry for this site determined using XRD data, which is m.[80] The observed chlorine chemical shift value (δ_{iso} = 105(8) ppm; or 146 ppm with respect to solid NaCl) is deshielded by 36 ppm relative to $CaCl_2 \cdot 2H_2O$, which is consistent with the general trend observed for halogen chemical shift values upon hydration in the alkaline earth metal halides (see also Chapter 4).[7]
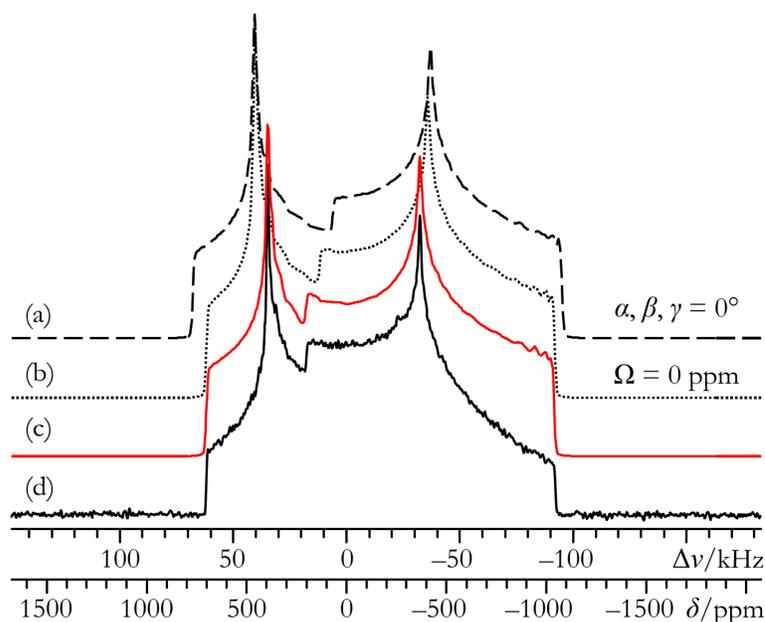
Figure 6.6 Analytical simulations (a, b, c), and experimental static Solomon echo (d) ^{35}Cl SSNMR spectrum of powdered $CaCl_2$ acquired at $B_0 = 21.1$ T ($\nu_0 = 88.189$ MHz). In (a), the PAS orientations of the $\ddot{V}$ and $\ddot{\sigma}$ tensor frames are assumed to be equivalent (i.e., $\alpha = \beta = \gamma = 0°$), while in (b), CSA effects are ignored completely (i.e., $\Omega = 0$ ppm). The best-fit spectrum presented in (c) is simulated with the parameters in Table 6.2.

Experiments at 21.1 T were essential to characterize chlorine CSA and the noncoincident $\ddot{V} / \ddot{\sigma}$ tensor PASs in this sample. The prior ^{35}Cl SSNMR study on $CaCl_2$ was carried out under MAS conditions only and CSA information was therefore not reported.[42] The presently measured chemical shift tensor span of 135 ± 15 ppm is by far the largest measured for an alkaline earth metal chloride system (72 ppm for $CaCl_2 \cdot 2H_2O$ being the second largest value reported).[41] The span value measured by modeling the ^{35}Cl SSNMR spectrum is identical to the one extracted from the ^{37}Cl SSNMR signal at 21.1 T (Figure 6.8). As expected, the ^{35}Cl SSNMR line shape of $CaCl_2$ acquired at 11.75 T was not particularly sensitive to CSA effects, and nearly all of the broadening could be attributed to the QI.[81] The measured Euler angle

values for CaCl$_2$ (i.e., $\alpha = 90(20)°$, $\beta = 90(5)°$, $\gamma = 0(5)°$) are consistent with the presence of mirror plane symmetry at the chloride anion, in agreement with the accepted crystal structure.[80]
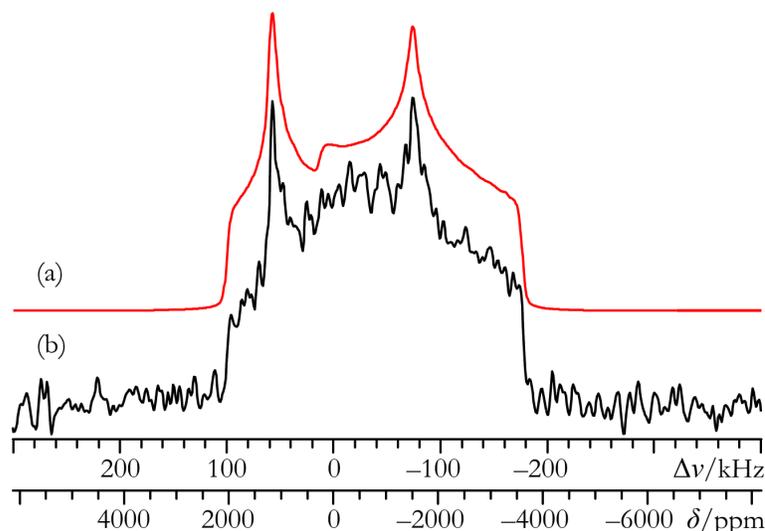
Figure 6.7 Best-fit analytical simulation (a), and experimental static VOCS Solomon echo (b) ^{35}Cl SSNMR spectrum of powdered CaCl$_2$ acquired at $B_0 = 11.75$ T ($\nu_0 = 49.002$ MHz).

Natural abundance ^{43}Ca SSNMR experiments were also performed at $B_0 = 21.1$ T to more completely characterize the sample. The resonance observed in the ^{43}Ca MAS SSNMR spectrum (Figure 6.9e) of CaCl$_2$ (i.e., $\delta_{cg} = 54.1(0.2)$ ppm relative to 2 mol/dm^3 CaCl$_2$(aq)) can not, unfortunately, be rigorously compared with that reported previously by Lin *et al.* ($\delta_{cg} = 53.1(2.0)$ ppm relative to saturated CaCl$_2$(aq)).[82] This is because the reference solution used in the earlier account (i.e., 'saturated' CaCl$_2$(aq)) shows a highly variable resonance position which depends on the preparation method (ca. ± 10 ppm).[53,83] Analytical modeling of the ^{43}Ca MAS SSNMR line shape is used to establish approximate ^{43}Ca $\ddot{V}$ tensor parameters, as well as the isotropic calcium CS for CaCl$_2$: $C_Q(^{43}$Ca$) = -0.95(0.20)$ MHz; $\eta_Q = 0.7(0.2)$; $\delta_{iso} = 54.8(0.5)$ ppm, where the sign of C_Q is assigned based upon the results of GIPAW DFT computations (*vide infra*).
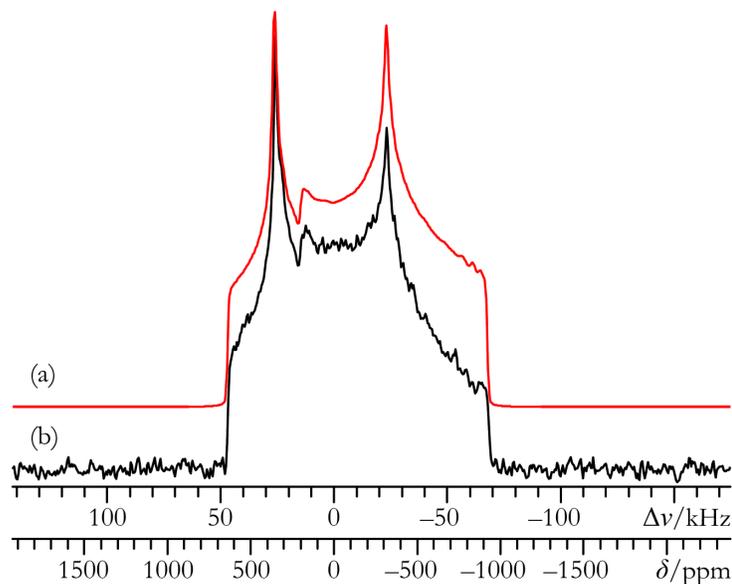
Figure 6.8 Best-fit analytical simulation (a), and experimental static Solomon echo ^{37}Cl SSNMR spectrum (b) of powdered $CaCl_2$ acquired at $B_0 = 21.1$ T ($v_0 = 73.408$ MHz).

Calcium-43 SSNMR experiments were also carried out under stationary conditions (Figure 6.9b) and the parameters measured from the ^{43}Ca MAS NMR spectrum were used to estimate the static line shape broadening that could be attributed to the ^{43}Ca QI (Figure 6.9c). It is clear that the QI does not dominate the line shape for this sample under static conditions at 21.1 T and that additional line broadening due to calcium CSA is present. Analytical line shape modeling of the static ^{43}Ca SSNMR spectrum allows for the measurement of a calcium CS tensor span of 31(5) ppm (Figure 6.9a), which represents the fifth measurement of calcium CSA in the literature[84] and the first where oxygen atoms are not coordinated to calcium. The calcium CS tensor span for $CaCl_2$ is moderate, as calcium CS tensor spans range from 8(2) ppm in the calcite polymorph of $CaCO_3$ to 70(20) ppm in the vaterite polymorph of $CaCO_3$.[83] The remaining calcium SSNMR parameters for $CaCl_2$ are summarized in Table 6.3.

Table 6.2 Experimental $^{35/37}$Cl EFG and CS tensor parameters: CaCl$_2$ and selected hydrates[a]

compound	$\mid C_Q(^{37}Cl)\mid$ / MHz	$\mid C_Q(^{35}Cl)\mid$ / MHz	η_Q	δ_{iso}[b] / ppm	Ω / ppm	κ	α, β, γ / °	notes
CaCl$_2$	—	2.1(1)	0.7(1)	122(5)	—	—	—, —, —	ref. 42
	6.96(7)	8.82(8)	0.383(15)	105(8)	135(15)	0.0(3)	90(20), 90(5), 0(5)	this study
CaCl$_2$·2H$_2$O	—	4.26(3)	0.75(3)	69(2)	72(15)	0.6(2)	90(10), 82(5), 0(20)	ref. 41
CaCl$_2$·6H$_2$O	—	4.33(3)	< 0.01	57(3)	40(8)	−1	N/A, 90(7), 0(8)	this study

[a] Error bounds are in parentheses. Parameter definitions are in Chapter 2. N/A = not applicable.
[b] With respect to 0.1 mol/dm^3 NaCl in D$_2$O ($\delta_{iso}(^{35/37}Cl) = 0.0$ ppm).
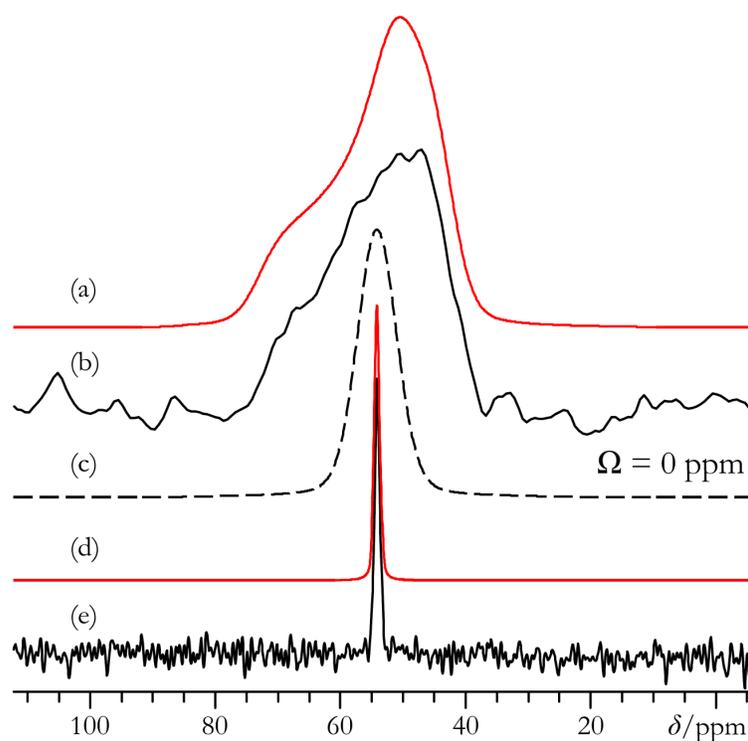
Figure 6.9 Analytical simulations (a, c, d) and experimental Bloch decay (b, e) ^{43}Ca SSNMR spectra of powdered CaCl$_2$ acquired at $B_0 = 21.1$ T ($\nu_0 = 60.575$ MHz) under static (a, b, c) and MAS (d, e) conditions. In (c), the effects due to calcium CSA are ignored (i.e., $\Omega = 0$ ppm), while the best-fit simulation in (a) includes calcium CSA. The spectrum in (e) was acquired using $\nu_{MAS} = 4.000$ kHz.

Table 6.3 Experimental and GIPAW DFT ^{43}Ca EFG and CS tensor parameters for CaCl$_2$[a]

experimental/ computed	|C_Q(^{43}Ca)| / MHz	η_Q	δ_{iso}[b] / ppm	Ω / ppm	κ	α, β, γ / °	notes
experimental	0.95(20)	0.7(2)	54.8(5)	31(5)	−0.5(3)	90[c], 90[c], 0[c]	—
computed[d]	0.98	0.541	67.7[e]	52.7	−0.24	90.0, 89.4, 0.0	X-ray structure, ref. 80

[a] Error bounds are in parentheses. Parameter definitions are in Chapter 2. The calculated results in this table used the PBE XC functional. Additional computational results and details can be found in Appendix D, Tables D.8 and D.9.
[b] With respect to dilute CaCl$_2$(aq) (δ_{iso}(^{43}Ca) = 0.0 ppm), as established using 2 mol/dm^3 CaCl$_2$(aq), which possesses an identical calcium CS as the primary standard.
[c] Value assigned as a result of crystal symmetry and GIPAW DFT results.
[d] Calculation used E_{cut} = 800 eV and a 4 × 4 × 6 k-point grid.
[e] The calculated isotropic calcium MS value (i.e., σ_{iso}) was used as input into the empirical formula developed by Moudrakovski *et al.*: δ_{iso} = (1129.1 − σ_{iso})/1.1857. This method was shown to be reliable for generating GIPAW DFT computed calcium chemical shifts for calcium-containing inorganic systems.[3]

6.3.2.2 Chlorine-35 SSNMR Experiments on CaCl$_2$·6H$_2$O and Other Hydrates

It is well known that CaCl$_2$ is a strongly hygroscopic material, and as such it finds wide use as a desiccant. In this section, the known experimental data for CaCl$_2$ and selected hydrates are discussed in order to ensure that the spectral data above have been correctly interpreted. CaCl$_2$·6H$_2$O has been characterized using ^{35}Cl SSNMR experiments at 11.75 and 21.1 T (Figures 6.10 and 6.11), and analytical line shape modeling of both spectra yields identical parameters, as summarized in Table 6.2.

Discussion of the $^{35/37}$Cl SSNMR data for the CaCl$_2$ hydrates begins by noting that $^{35/37}$Cl SSNMR data were recently reported for CaCl$_2$·2H$_2$O,[41] and that this dihydrate possesses distinctly different $\ddot{V}$ and $\ddot{\sigma}$ tensor parameters compared with anhydrous CaCl$_2$ (Table 6.2). According to the current literature, two other hydrated forms of CaCl$_2$ are stable under typical laboratory conditions: α–CaCl$_2$·4H$_2$O[85] and CaCl$_2$·6H$_2$O.[86] Additional polymorphic forms of the tetrahydrate (β–CaCl$_2$·4H$_2$O[87] and γ–CaCl$_2$·4H$_2$O[88]) may be prepared under normal conditions, but appear to slowly convert to the α-form.[89] As the hexahydrate is commercially available in a high purity form, ^{35}Cl SSNMR experiments were carried out on this material.
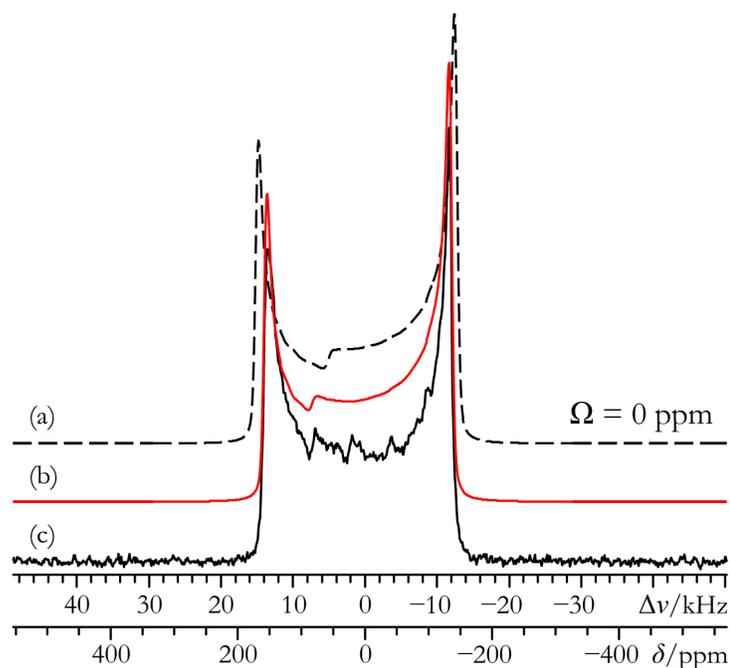
Figure 6.10 Analytical simulations (a, b), and experimental static Solomon echo $^{35}Cl\{^1H\}$ SSNMR spectrum of powdered $CaCl_2 \cdot 6H_2O$ acquired at $B_0 = 21.1$ T (c). The spectrum in (b) is the best-fit to the experimental spectrum, while the spectrum in (a) does not include chlorine CSA (i.e., $\Omega = 0$ ppm).

By observing the ^{35}Cl SSNMR line shapes associated with $CaCl_2 \cdot 6H_2O$ (Figures 6.10 and 6.11), it is clear that it possesses a distinct line shape with respect to both anhydrous $CaCl_2$ and $CaCl_2 \cdot 2H_2O$. The measured ^{35}Cl EFG tensor parameters ($C_Q(^{35}Cl) = 4.33(3)$ MHz; $\eta_Q < 0.01$) strongly suggest that each chloride anion in $CaCl_2 \cdot 6H_2O$ is located on a C_3 (or higher) rotational axis. Relative to $CaCl_2$, the smaller value of $C_Q(^{35}Cl)$ for this sample is consistent with earlier observations for the alkaline earth metal halides, which nearly always exhibit smaller halogen C_Q values upon hydration (see Chapters 3 and 4). It is also important to note that $CaCl_2 \cdot 2H_2O$, as well as all the polymorphs of $CaCl_2 \cdot 4H_2O$, place the chloride anions at positions lacking any local symmetry elements and hence the axial ^{35}Cl EFG observed is unique to the hexahydrate. It is also observed that there is a clear broadening of the discontinuities (Figure 6.11b) when ^1H decoupling is not applied, which indicates that the sample is hydrated.
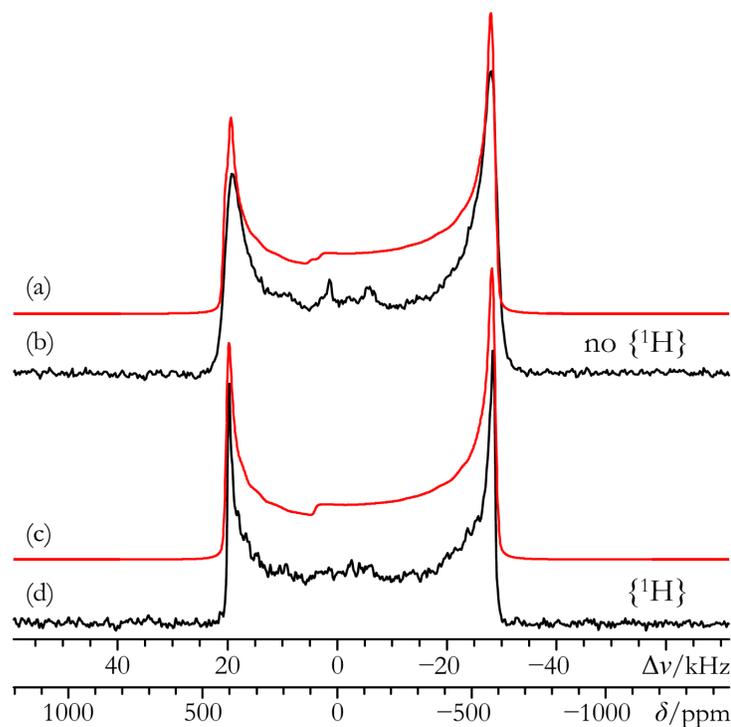
Figure 6.11 Best-fit analytical simulations (a, c), and experimental static Solomon echo [35]Cl SSNMR spectra of powdered $CaCl_2 \cdot 6H_2O$ acquired at $B_0 = 11.75$ T (b, d). The spectrum in (b) did not employ proton decoupling during signal acquisition, while the spectrum in (d) was acquired using proton decoupling. The simulation parameters used in (a) and (c) are identical, except for the addition of 1 000 Hz of dipolar line broadening in (a) ($\alpha_D = \beta_D = 0°$), due to the expected [1]H-[35]Cl distances of ~2.27 Å.

The observed chlorine chemical shift for $CaCl_2 \cdot 6H_2O$ ($\delta_{iso} = 57(3)$ ppm) is smaller than that of both $CaCl_2$ and $CaCl_2 \cdot 2H_2O$, which is in agreement with earlier observations that the halogen shift value decreases (i.e., shielding increases) upon increasing hydration (see Chapters 3 and 4). The observed [35]Cl SSNMR line shape of $CaCl_2 \cdot 6H_2O$ was best modeled when including CSA effects ($\Omega = 40(8)$ ppm; $\kappa = -1$; also see Figure 6.10). The observed chlorine Ω value is quite similar to that measured for other alkaline earth metal chloride hydrates.[41] Based on the above discussion, it is clear that the anhydrous $CaCl_2$ sample presented in this study cannot be $CaCl_2 \cdot 2H_2O$ nor $CaCl_2 \cdot 6H_2O$, and is very unlikely to be a $CaCl_2 \cdot 4H_2O$ polymorph, due to the

observed large positive chlorine chemical shift value, the large $C_Q(^{35}Cl)$ value, and the mirror site symmetry implied by the EFG/CS tensor interplay observed in the $^{35/37}Cl$ SSNMR spectra of $CaCl_2$.

6.3.2.3 GIPAW DFT Quantum Chemical Computations

GIPAW DFT quantum chemical calculations were carried out using the accepted crystal structures of $CaCl_2$,[80] $CaCl_2·2H_2O$,[90] α–$CaCl_2·4H_2O$,[85] β–$CaCl_2·4H_2O$,[87] γ–$CaCl_2·4H_2O$,[88] and $CaCl_2·6H_2O$,[86] although for the hydrates (excepting $CaCl_2·6H_2O$, whose structure was solved using neutron diffraction data), the H positions were optimized computationally (*vide infra*). The computed $^{35/37}Cl$ $\ddot{V}$ and $\ddot{\sigma}$ tensor parameters are presented in Table 6.4, while more detailed computational results can be found in Appendix D, Tables D.6 and D.7.

6.3.2.3.1 Agreement Between Experimental and GIPAW DFT Computed Chlorine $\ddot{V}$ and $\ddot{\sigma}$ Tensor Parameters

For nearly all of the relevant $^{35/37}Cl$ SSNMR tensor parameters, excellent agreement between the present experimental observations and GIPAW DFT computations is seen for $CaCl_2$ and $CaCl_2·6H_2O$. The calculated $C_Q(^{35}Cl)$ values for these compounds are slightly overestimated relative to experiment (~1 MHz), which appears to be a general feature for chloride anions when using this computational method and pseudopotential.[91] In addition, while there is a lack of quantitative agreement between the quantum chemical and experimental δ_{iso} values, the pertinent experimental trend is reproduced computationally (i.e., as hydration increases, δ_{iso} decreases). The quantitative disagreement in δ_{iso} extends to the computational reference standard used in this study (i.e., NaCl(s)). According to the absolute shielding scale established previously,[92] the experimental absolute shielding at the chlorine nuclei in solid NaCl

is 1015(4) ppm, while the present GIPAW DFT calculations furnish a value of 975.06 ppm. These data therefore suggest the presence of a systematic error in the calculation of chlorine σ_{iso} values using the GIPAW DFT method and the current pseudopotential. It is noted that all quantum chemical shift values reported in Table 6.4 used the computational shielding standard (i.e., σ_{iso}(NaCl(s)) = 975.06 ppm).

Table 6.4 GIPAW DFT $^{35/37}$Cl EFG and CS tensor parameters: CaCl$_2$ and hydrates[a]

compound	site label	$\|C_Q(^{35}Cl)\|$ / MHz	η_Q	δ_{iso}[b] / ppm	Ω / ppm	κ	α, β, γ / °	notes
CaCl$_2$	—	9.66	0.419	179.0	200.9	0.12	90.0, 89.7, 0.0	X-ray structure from ref. 80
CaCl$_2$·2H$_2$O	—	6.69	0.04	114.0	141.4	0.36	—, —, —	from ref. 41, non-optimized H
	—	4.43	0.520	109.3	140.7	0.49	118.3, 80.8, 2.7	this study, optimized H
α–CaCl$_2$·4H$_2$O	Cl(1)	3.70	0.405	76.1	73.6	0.39	15.4, 1.4, 18.8	optimized H
	Cl(2)	5.97	0.944	78.7	77.9	−0.47	118.1, 77.3, 178.1	
β–CaCl$_2$·4H$_2$O	Cl(1)	3.75	0.947	92.9	123.5	0.70	183.1, 3.2, 269.3	
	Cl(2)	2.16	0.828	78.9	83.6	0.59	135.5, 73.6, 199.5	optimized H
	Cl(3)	3.97	0.776	104.6	125.6	0.45	65.3, 82.6, 357.7	
γ–CaCl$_2$·4H$_2$O	—	3.59	0.149	48.5	77.1	0.12	111.1, 47.7, 190.6	optimized H
CaCl$_2$·6H$_2$O	—	5.48	0.000	43.3	46.4	−1	N/A, 90.0, 0.3	neutron structure from ref. 86

[a] Parameter definitions are in Chapter 2. CaCl$_2$ and CaCl$_2$·6H$_2$O calculations used E_{cut} = 800 eV and a 4 × 4 × 6 k-point grid; CaCl$_2$·2H$_2$O calculations used a 4 × 3 × 2 k-point grid, but a different E_{cut} depending on the type of calculation: for hydrogen optimization, E_{cut} = 500 eV, while for EFG and MS tensor parameter calculations, E_{cut} = 600 eV; α–CaCl$_2$·4H$_2$O calculations used E_{cut} = 650 eV and a 4 × 4 × 3 k-point grid; β–CaCl$_2$·4H$_2$O calculations used E_{cut} = 500 eV and a 3 × 3 × 2 k-point grid; γ–CaCl$_2$·4H$_2$O calculations used E_{cut} = 650 eV and a 4 × 3 × 3 k-point grid. All calculated results in this table used the PBE XE functional. Additional computational results and details can be found in Appendix D, Tables D.6 and D.7. N/A = not applicable.
[b] For the computational reference, NaCl(s), σ_{iso}($^{35/37}$Cl) was calculated to be 975.06 ppm (E_{cut} = 1200 eV and a 4 × 4 × 4 k-point grid). Additional details can be found in Section 6.2.5.2 and footnote b to Table D.7.

There is also clear disagreement between the chlorine quantum chemical results for CaCl$_2$ and the earlier ^{35}Cl MAS NMR experimental observation:[42] for example, the computed

$C_Q(^{35}Cl)$ is too large by roughly a factor of 4. Therefore, the quantum chemical result for $CaCl_2$ provides independent evidence that the earlier ^{35}Cl MAS NMR experimental measurements were either not correctly interpreted, or were inadvertently carried out on a material other than $CaCl_2$. The GIPAW DFT result for $CaCl_2 \cdot 6H_2O$ confirms the local symmetry (i.e., C_3) for the chloride anions, as $\eta_Q = 0.0$ and $\kappa = -1.0$. It is also rather interesting to note the quantitative agreement between the calculated and experimental Euler angle values for each of $CaCl_2$ and $CaCl_2 \cdot 6H_2O$.

While there typically exists very good agreement between experimental and computed values for the $^{35/37}Cl$ $\ddot{V}$ and $\ddot{\sigma}$ tensors in $CaCl_2$ and $CaCl_2 \cdot 6H_2O$, relatively poor agreement was observed for $CaCl_2 \cdot 2H_2O$ in a previous study.[41] Inspection of the source data for the accepted crystal structure of $CaCl_2 \cdot 2H_2O$ revealed that it was generated using XRD data, rather than neutron diffraction data and hence the hydrogen positions are not precisely known. Out of all the alkaline earth metal chloride hydrates where ^{35}Cl or ^{37}Cl SSNMR data are available, $CaCl_2 \cdot 2H_2O$ represents the only structure for which neutron diffraction data are unavailable. The H positions in $CaCl_2 \cdot 2H_2O$ were therefore optimized using the GIPAW DFT method. Subsequent GIPAW DFT calculation of the EFG and magnetic shielding tensor parameters using this optimized structure produces markedly different tensor parameters as compared to the prior study (Table 6.4). Relative to the earlier computational results, there is a decrease in the computed $C_Q(^{35}Cl)$ value by about 34 % (6.69 MHz to 4.43 MHz), and a substantial increase in the η_Q value (0.04 to 0.520). Both of these significant changes result in better agreement between the experimental and computed $\ddot{V}$ tensor parameter values. This present result echoes earlier findings for chloride-containing materials,[91] therefore, it can be reasonably stated that the optimization of hydrogen atomic positions should be performed if sufficient computational resources are available.

6.3.2.3.2 GIPAW DFT Computations of EFG and MS Tensors for the CaCl₂·4H₂O Polymorphs

Good agreement between the observed and computed $^{35/37}$Cl NMR tensor data was seen for the compounds above; hence, it was explored whether GIPAW DFT computations would predict that chlorine SSNMR experiments could be used to differentiate between the α, β, and γ polymorphs of $CaCl_2 \cdot 4H_2O$. The differentiation of polymorphs using chlorine SSNMR has been demonstrated previously for chlorine-containing pharmaceuticals,[93] and as seen in Table 6.4, ^{35}Cl SSNMR experiments should also be able to distinguish the polymorphs of $CaCl_2 \cdot 4H_2O$. Each polymorph will present a different number of magnetically unique chloride sites (ranging from 1 to 3). In addition, there exists significant disparity in the other relevant SSNMR parameters (notably η_Q, which ranges from 0.149 in γ–$CaCl_2 \cdot 4H_2O$ to above 0.776 for all three sites in β–$CaCl_2 \cdot 4H_2O$). It is noted that a similar ability (i.e., polymorph distinction) is also predicted to exist if one prefers to use ^{43}Ca SSNMR (see Appendix D, Tables D.8 and D.9), but these experiments are very challenging relative to ^{35}Cl SSNMR experiments.

6.3.2.4 Are CaCl₂ and CaBr₂ Isostructural?

Based on prior XRD data, the ambient condition structures of both $CaCl_2$ and $CaBr_2$ belong to the same space group, and place the halogen anions at the same Wyckoff positions.[80,94] As reported in Chapter 3, the $|C_Q(^{81}Br)|$ value for $CaBr_2$ is the largest amongst the alkaline earth metal bromides ($C_Q(^{81}Br)$ = 62.8(4) MHz). At the same time, the previously measured $C_Q(^{35}Cl)$ value for $CaCl_2$ was among the smallest measured relative to the other alkaline earth metal chlorides (i.e., $C_Q(^{35}Cl)$ = 2.1 MHz).[42] The above sections in this Chapter have provided ample evidence that the earlier report was in error, likely caused by the formation of a $CaCl_2$ hydrate, or the neglect to acquire spectral data using VOCS (or equivalent) methods. In addition, reliable $C_Q(^{35/37}Cl)$ measurements for $CaCl_2$ have been provided.

As noted in earlier Chapters, Wu and Terskikh[95] demonstrated that for a series of isostructural compounds, a linear relationship exists between the measured C_Q values and the quantity $Q(1 - \gamma_\infty)/V$.[96-99] This finding has been extended by observations made for the chlorine-35/37,[41,42,79] bromine-79/81,[9,33] and iodine-127[7] nuclides within several isostructural series of the alkaline earth metal halides and selected hydrates thereof. This linear relationship between C_Q and $Q(1 - \gamma_\infty)/V$ is therefore useful for both confirming and predicting isostructural series within classes of analogous compounds. Although enough data do not exist in this case to construct a meaningful plot of $C_Q(X)$ vs. $Q(1 - \gamma_\infty)/V$, it is possible to compare the respective $C_Q(^{81}\text{Br})/C_Q(^{35}\text{Cl})$ and $[Q_{81\text{Br}}(1 - \gamma_{\infty(\text{Br})})/V]/[Q_{35\text{Cl}}(1 - \gamma_{\infty(\text{Cl})})/V]$ ratios, which should be equivalent according to the above model if these two compounds are isostructural. Using the experimental SSNMR data for $CaCl_2$ and $CaBr_2$, the $C_Q(^{81}\text{Br})/C_Q(^{35}\text{Cl})$ ratio is ~7.12. Using additional known information, and the volumes of the unit cells established with X-ray diffraction[80,94] the $[Q_{81\text{Br}}(1 - \gamma_{\infty(\text{Br})})/V]/[Q_{35\text{Cl}}(1 - \gamma_{\infty(\text{Cl})})/V]$ ratio is found to be 5.19 (a 31.4 % difference). This percentage difference is comparable to what has been calculated previously for pairs of alkaline earth metal halide compounds which are understood to be isostructural. In fact, for the isostructural alkaline earth metal chlorides and bromides studied to date, it is observed that $C_Q(^{81}\text{Br})/C_Q(^{35}\text{Cl})$ ratios range between 6.30 and 7.08, while the calculated $[Q_{81\text{Br}}(1 - \gamma_{\infty(\text{Br})})/V]/[Q_{35\text{Cl}}(1 - \gamma_{\infty(\text{Cl})})/V]$ ratios for these same systems vary between 5.48 and 5.64.[7] A likely contributor to the disagreement between the calculated $[Q_{81\text{Br}}(1 - \gamma_{\infty(\text{Br})})/V]/[Q_{35\text{Cl}}(1 - \gamma_{\infty(\text{Cl})})/V]$ ratios and the experimental $C_Q(^{81}\text{Br})/C_Q(^{35}\text{Cl})$ ratios lies in the uncertainty associated with the γ_∞ values. These values for the quadrupolar halogens are not known to high precision, unlike the alkali metal atom γ_∞ values used in the study by Wu and Terskikh. At this time it is noted that, using the accepted structures for $CaCl_2$ and $CaBr_2$, the GIPAW DFT calculated $C_Q(^{81}\text{Br})/C_Q(^{35}\text{Cl})$ ratio is ~7.16, which is in excellent agreement with experimental observations (a difference of 0.56 %).

Likewise, upon consideration of the fine details associated with the $CaCl_2$ and $CaBr_2$ crystal structures, two points are clear: (i) the structure of $CaCl_2$ is rather old (published in 1935), and (ii) the placement of the halide anions is, in fact, not equivalent for the two structures (in $CaBr_2$ the bromide is at $x/a = 0.2636(29)$; $y/b = 0.3417(26)$; $z/c = 0$; whereas in $CaCl_2$ the chloride is at $x/a = 0.275(8)$; $y/b = 0.325(8)$; $z/c = 0$).[80,94] It is therefore probable that this discrepancy in the halide positions within their respective crystalline lattices would contribute to the difference between the $[Q_{81Br}(1 - \gamma_{\infty(Br)})/V]/[Q_{35Cl}(1 - \gamma_{\infty(Cl)})/V]$ ratio and the $C_Q(^{81}Br)/C_Q(^{35}Cl)$ ratio. Indeed, as was demonstrated earlier (including in this Chapter), even very small displacements of the halide anion (typically < 0.05 Å) can dramatically alter the calculated halogen C_Q value for several similar systems.[7,33] Therefore, while it is clear that the $C_Q/[Q(1 - \gamma_{\infty})/V]$ relationship appears to be of general use for the alkaline earth metal halides, the precision of the halogen γ_{∞} values is very likely a limiting factor, and the compounds must be rigorously isostructural to obtain exactly equal ratios.

6.4   Conclusions

This Chapter presented an example of an experimental and computational structural refinement approach for a simple inorganic material composed solely of quadrupolar nuclei, namely $MgBr_2$. Qualitative information was first obtained by briefly considering the experimental data, and a quantitative change in structure was substantiated using experimental SSNMR data to cross-validate the GIPAW DFT results. Incidentally, the $^{79/81}$Br SSNMR spectra in Section 6.3.1.1 were the first literature examples for bromine in a non-cubic environment acquired using modern variable-offset techniques. The sensitivity of the method to crystal lattice EFGs is advantageous, as this represents additional parameters that are not available for spin-1/2 nuclei (e.g., C_Q and η_Q), and because the EFG is generally more sensitive

to long-range crystallographic features (e.g., intermolecular contacts) than are chemical shifts. Indeed, the CS tensor parameters in the present study appear to be less sensitive to structural changes than were the EFG tensor parameters. The general approach is expected to be important in other purely inorganic systems, as the more extensively developed methods for ^{1}H NMR crystallography often cannot be used. For more complex structures with multiple crystallographic sites, one could envision the use of iterative refinement algorithms, such as those developed for CS tensors in zeolites.[100]

In addition, $^{35/37}$Cl SSNMR experiments are clearly sensitive probes of the local structure of inorganic materials and have allowed for the differentiation between selected hydrates of CaCl$_2$. By performing chlorine SSNMR experiments in two applied magnetic fields, both the $\ddot{V}$ and $\ddot{\delta}$ tensor parameters could be accurately measured in CaCl$_2$ and CaCl$_2$·6H$_2$O. The measurement of these tensor parameters allowed for the correction of the ^{35}Cl SSNMR literature data for CaCl$_2$ and illustrate that this species conforms to the established quadrupolar halogen NMR trends for the alkaline earth metal halide systems (i.e., that both the halogen C_Q value and the halogen δ_{iso} value will decrease upon hydration). GIPAW DFT quantum chemical calculations have provided complementary data for the CaCl$_2$ hydrates where experimental SSNMR data exist and predict that $^{35/37}$Cl SSNMR experiments should be able to distinguish the three known polymorphs of CaCl$_2$·4H$_2$O. It is seen that optimization of the H positions for CaCl$_2$·2H$_2$O, whose structure has been determined using XRD data, is necessary to obtain good agreement between the quantum chemical and experimental EFG tensor parameter values. By carrying out ^{43}Ca SSNMR experiments at B_0 = 21.1 T, the fifth calcium CS tensor anisotropy has been measured, which is expected to prove useful in future SSNMR studies that correlate calcium CS tensor information to local structure and symmetry in other calcium-containing materials. Lastly, although it has been demonstrated that comparing $C_Q/[Q(1 - \gamma_\infty)/V]$ ratios

can provide evidence that a series of compounds are isostructural when using alkali metal nuclei as probes, additional problems (i.e., uncertainly in halogen γ_∞ values and a requirement that the compounds be rigorously isostructural) present themselves when the quadrupolar halogen nuclei are used.

6.5   References

1   C. J. Pickard and F. Mauri, *Phys. Rev. B*, **2001**, *63*, 245101.

2   K. E. Johnston, C. C. Tang, J. E. Parker, K. S. Knight, P. Lightfoot and S. E. Ashbrook, *J. Am. Chem. Soc.*, **2010**, *132*, 8732-8746.

3   I. L. Moudrakovski, R. Alizadeh and J. J. Beaudoin, *Phys. Chem. Chem. Phys.*, **2010**, *12*, 6961-6969.

4   H. Hamaed, E. Ye, K. Udachin and R. W. Schurko, *J. Phys. Chem. B*, **2010**, *114*, 6014-6022.

5   D. S. Middlemiss, F. Blanc, C. J. Pickard and C. P. Grey, *J. Magn. Reson.*, **2010**, *204*, 1-10.

6   A. Sutrisno, M. A. Hanson, P. A. Rupar, V. V. Terskikh, K. M. Baines and Y. Huang, *Chem. Commun.*, **2010**, *46*, 2817-2819.

7   C. M. Widdifield and D. L. Bryce, *J. Phys. Chem. A*, **2010**, *114*, 10810-10823.

8   J. V. Hanna, K. J. Pike, T. Charpentier, T. F. Kemp, M. E. Smith, B. E. G. Lucier, R. W. Schurko and L. S. Cahill, *Chem. Eur. J.*, **2010**, *16*, 3222-3239.

9   C. M. Widdifield and D. L. Bryce, *J. Phys. Chem. A*, **2010**, *114*, 2102-2116.

10   I. Moudrakovski, S. Lang, S. Patchkovskii and J. Ripmeester, *J. Phys. Chem. A*, **2010**, *114*, 309-316.

11   M. Kibalchenko, J. R. Yates, C. Massobrio and A. Pasquarello, *Phys. Rev. B*, **2010**, *82*, 020202(R).

12   L. A. Truflandier, F. Boucher, C. Payen, R. Hajjar, Y. Millot, C. Bonhomme and N. Steunou, *J. Am. Chem. Soc.*, **2010**, *132*, 4653-4668.

13   R. K. Harris, Crystallography & NMR: an Overview In *NMR Crystallography*, R. K. Harris, R. E. Wasylishen and M. J. Duer, Eds., John Wiley & Sons: Chichester, United Kingdom, **2009**, 3-18.

14	A. L. Webber, L. Emsley, R. M. Claramunt and S. P. Brown, *J. Phys. Chem. A*, **2010**, *114*, 10435-10442.

15	A. L. Webber, B. Elena, J. M. Griffin, J. R. Yates, T. N. Pham, F. Mauri, C. J. Pickard, A. M. Gil, R. Stein, A. Lesage, L. Emsley and S. P. Brown, *Phys. Chem. Chem. Phys.*, **2010**, *12*, 6970-6983.

16	S. Ganapathy, S. Sengupta, P. K. Wawrzyniak, V. Huber, F. Buda, U. Baumeister, F. Wurthner and H. J. M. de Groot, *Proc. Nat. Acac. Sci. USA*, **2009**, *106*, 11472-1147.

17	E. Salager, R. S. Stein, C. J. Pickard, B. Elena and L. Emsley, *Phys. Chem. Chem. Phys.*, **2009**, *11*, 2610-2621.

18	L. Seyfarth and J. Senker, *Phys. Chem. Chem. Phys.*, **2009**, *11*, 3522-3531.

19	S. E. Ashbrook, M. Cutajar, C. J. Pickard, R. I. Walton and S. Wimperis, *Phys. Chem. Chem. Phys.*, **2008**, *10*, 5754-5764.

20	R. K. Harris, P. Hodgkinson, C. J. Pickard, J. R. Yates and V. Zorin, *Magn. Reson. Chem.*, **2007**, *45*, S174-S186.

21	C. J. Pickard, E. Salager, G. Pintacuda, B. Elena and L. Emsley, *J. Am. Chem. Soc.*, **2007**, *129*, 8932-8933.

22	R. K. Harris, *Solid State Sci.*, **2004**, *6*, 1025-1037.

23	J. Senker, L. Seyfarth and J. Voll, *Solid State Sci.*, **2004**, *6*, 1039-1052.

24	D. H. Brouwer, *J. Mag. Reson.*, **2008**, *194*, 136-146.

25	D. H. Brouwer, *J. Am. Chem. Soc.*, **2008**, *130*, 6306-6307.

26	D. H. Brouwer, P. E. Kristiansen, C. A. Fyfe and M. H. Levitt, *J. Am. Chem. Soc.*, **2005**, *127*, 542-543.

27	D. H. Brouwer, S. Alavi and J. A. Ripmeester, *Phys. Chem. Chem. Phys.*, **2008**, *10*, 3857-3860.

28	F. Castellani, B. van Rossum, A. Diehl, M. Schubert, K. Rehbein and H. Oschkinat, *Nature*, **2002**, *420*, 98-102.

29	C. M. Rienstra, L. Tucker-Kellogg, C. P. Jaroniec, M. Hohwy, B. Reif, M. T. McMahon, B. Tidor, T. Lozano-Pérez and R. G. Griffin, *Proc. Natl. Acad. Sci.*, **2002**, *99*, 10260-10265.

30	B. Zhou, T. Giavani, H. Bildsøe, J. Skibsted and H. J. Jakobsen, *Chem. Phys. Lett.*, **2005**, *402*, 133-137.

31	R. P. Chapman and D. L. Bryce, *Phys. Chem. Chem. Phys.*, **2009**, *11*, 6987-6998.

32 R. P. Chapman, C. M. Widdifield and D. L. Bryce, *Prog. Nucl. Magn. Reson. Spectrosc.*, **2009**, *55*, 215-237.

33 C. M. Widdifield and D. L. Bryce, *Phys. Chem. Chem. Phys.*, **2009**, *11*, 7120-7122.

34 C. M. Widdifield, R. P. Chapman and D. L. Bryce, Chlorine, Bromine, and Iodine Solid-State NMR Spectroscopy In *Annu. Rep. Nucl. Magn. Reson. Spectrosc.*, G. A. Webb, Ed., Elsevier: New York, *66*, **2009**, 195-326.

35 R. P. Chapman and D. L. Bryce, *Phys. Chem. Chem. Phys.*, **2007**, *9*, 6219-6230.

36 D. L. Bryce and G. D. Sward, *J. Phys. Chem. B.*, **2006**, *110*, 26461-26470.

37 D. L. Bryce, G. D. Sward and S. Adiga, *J. Am. Chem. Soc.*, **2006**, *128*, 2121-2134.

38 D. L. Bryce and G. D. Sward, *Magn. Reson. Chem.*, **2006**, *44*, 409-450.

39 T. B. Coplen, J. K. Böhlke, P. De Bièvre, T. Ding, N. E. Holden, J. A. Hopple, H. R. Krouse, A. Lamberty, H. S. Peiser, K. Révész, S. E. Rieder, K. J. R. Rosman, E. Roth, P. D. P. Taylor, R. D. Vocke Jr. and Y. K. Xiao, *Pure Appl. Chem.*, **2002**, *74*, 1987-2017.

40 P. Pyykkö, *Mol. Phys.*, **2008**, *106*, 1965-1974.

41 D. L. Bryce and E. B. Bultz, *Chem. Eur. J.*, **2007**, *13*, 4786-4796.

42 T. O. Sandland, L. S. Du, J. F. Stebbins and J. D. Webster, *Geochim. Cosmochim. Acta*, **2004**, *68*, 5059-5069.

43 I. Solomon, *Phys. Rev.*, **1958**, *110*, 61-65.

44 I. D. Weisman and L. H. Bennett, *Phys. Rev.*, **1969**, *181*, 1341-1350.

45 A. C. Kunwar, G. L. Turner and E. Oldfield, *J. Magn. Reson.*, **1986**, *69*, 124-127.

46 H. Y. Carr and E. M. Purcell, *Phys. Rev.*, **1954**, *94*, 630-638.

47 S. Meiboom and D. Gill, *Rev. Sci. Instrum.*, **1958**, *29*, 688-691.

48 F. H. Larsen, H. J. Jakobsen, P. D. Ellis and N. C. Nielsen, *J. Phys. Chem. A*, **1997**, *101*, 8597-8606.

49 D. Massiot, I. Farnan, N. Gautier, D. Trumeau, A. Trokiner and J. P. Coutures, *Solid State Nucl. Magn. Reson.*, **1995**, *4*, 241-248.

50 A. Medek, V. Frydman and L. Frydman, *J. Phys. Chem. A*, **1999**, *103*, 4830-4835.

51 R. W. Schurko, S. Wi and L. Frydman, *J. Phys. Chem. A*, **2002**, *106*, 51-62.

52 R. K. Harris, E. D. Becker, S. M. Cabral De Menezes, P. Granger, R. E. Hoffman and K. W. Zilm, *Pure Appl. Chem.*, **2008**, *80*, 59-84.

53 C. Gervais, D. Laurencin, A. Wong, F. Pourpoint, J. Labram, B. Woodward, A. P. Howes, K. J. Pike, R. Dupree, F. Mauri, C. Bonhomme and M. E. Smith, *Chem. Phys. Lett.*, **2008**, *464*, 42-48.

54 M. Profeta, F. Mauri and C. J. Pickard, *J. Am. Chem. Soc.*, **2003**, *125*, 541-548.

55 S. J. Clark, M. D. Segall, C. J. Pickard, P. J. Hasnip, M. I. J. Probert, K. Refson and M. C. Payne, *Z. Kristallogr.*, **2005**, *220*, 567-570.

56 J. R. Yates, C. J. Pickard and F. Mauri, *Phys. Rev. B*, **2007**, *76*, 024401.

57 D. Vanderbilt, *Phys. Rev. B*, **1990**, *41*, 7892-7895.

58 J. P. Perdew, K. Burke and M. Ernzerhof, *Phys. Rev. Lett.*, **1996**, *77*, 3865-3868.

59 J. P. Perdew, K. Burke and M. Ernzerhof, *Phys. Rev. Lett.*, **1997**, *78*, 1396.

60 K. Burke, J. P. Perdew and Y. Wang, Derivation of a Generalized Gradient Approximation: the PW91 Density Functional In *Electronic Density Functional Theory: Recent Progress and New Directions*, J. F. Dobson, G. Vignale and M. P. Das, Eds., Plenum: New York, **1998**, 81-111.

61 J. P. Perdew, Unified Theory of Exchange and Correlation Beyond the Local Density Approximation In *Electronic Structure of Solids '91*, P. Ziesche and H. Eschrig, Eds., Akademie Verlag: Berlin, **1991**, 11-20.

62 J. P. Perdew, J. A. Chevary, S. H. Vosko, K. A. Jackson, M. R. Pederson, D. J. Singh and C. Fiolhais, *Phys. Rev. B*, **1992**, *46*, 6671-6687.

63 J. P. Perdew, J. A. Chevary, S. H. Vosko, K. A. Jackson, M. R. Pederson, D. J. Singh and C. Fiolhais, *Phys. Rev. B*, **1993**, *48*, 4978.

64 J. P. Perdew, K. Burke and Y. Wang, *Phys. Rev. B*, **1996**, *54*, 16533-16539.

65 H. J. Monkhorst and J. D. Pack, *Phys. Rev. B*, **1976**, *13*, 5188-5192.

66 V. Grignard, *C. R. Hebd. Seances Acad. Sci.*, **1900**, *130*, 1322.

67 P. Patnaik, *Handbook of Inorganic Chemicals*, McGraw-Hill Professional: New York, **2003**.

68 C. E. Housecroft and A. G. Sharpe, *Inorganic Chemistry*, Pearson Education Limited: Harlow, England, **2001**.

69 S. M. Jacobsen, H. U. Güdel and C. A. Daul, *J. Am. Chem. Soc.*, **1988**, *110*, 7610-7616.

70   A. Ferrari and F. Giorgi, *Atti della Accademia Nazionale dei Lincei, Classe di Scienze Fisiche, Matematiche e Naturali, Rendiconti*, **1929**, *9*, 1134-1140.

71   F. W. de Wette, *Phys. Rev.*, **1961**, *123*, 103-112.

72   Y.-I. Kim, S. Cadars, R. Shayib, T. Proffen, C. S. Feigerle, B. F. Chmelka and R. Seshadri, *Phys. Rev. B*, **2008**, *78*, 195205.

73   I. Hung and R. W. Schurko, *Solid State Nucl. Magn. Reson.*, **2003**, *24*, 78-93.

74   A. Wong, R. Ida, X. Mo, Z. Gan, J. Poh and G. Wu, *J. Phys. Chem. A*, **2006**, *110*, 10084-10090.

75   A. S. Lipton, R. W. Heck, S. Primak, D. R. McNeill, D. M. Wilson III and P. D. Ellis, *J. Am. Chem. Soc.*, **2008**, *130*, 9332-9341.

76   N. F. Ramsey, *Phys. Rev.*, **1950**, *78*, 699-703.

77   N. F. Ramsey, *Phys. Rev.*, **1951**, *83*, 540-541.

78   P. J. Pallister, I. L. Moudrakovski and J. A. Ripmeester, *Phys. Chem. Chem. Phys.*, **2009**, *11*, 11487-11500.

79   J. F. Stebbins and L. S. Du, *Am. Mineral.*, **2002**, *87*, 359-363.

80   A. K. van Bever and W. Nieuwenkamp, *Z. Kristallogr.*, **1935**, *90*, 374-376.

81   K. J. D. MacKenzie and M. E. Smith, *Multinuclear Solid-State NMR of Inorganic Materials*, Pergamon: Amsterdam, **2002**.

82   Z. Lin, M. E. Smith, F. E. Sowrey and R. J. Newport, *Phys. Rev. B*, **2004**, *69*, 224107.

83   D. L. Bryce, E. B. Bultz and D. Aebi, *J. Am. Chem. Soc.*, **2008**, *130*, 9282-9292.

84   D. L. Bryce, *Dalton Trans.*, **2010**, *39*, 8593-8602.

85   A. LeClaire and M. M. Borel, *Acta. Cryst. B*, **1979**, *B35*, 585-588.

86   P. A. Agron and W. R. Busing, *Acta Cryst. C*, **1986**, *C42*, 141-143.

87   A. LeClaire and M. M. Borel, *Acta. Cryst. B*, **1978**, *B34*, 900-902.

88   A. LeClaire, M. M. Borel and J. C. Monier, *Acta. Cryst. B*, **1980**, *B36*, 2757-2759.

89   A. I. Shepelev, M. N. Lyashenko and I. G. Druzhinin, *Dokl. Akad. Nauk SSSR*, **1950**, *75*, 379-381.

90   A. LeClaire and M. M. Borel, *Acta. Cryst. B*, **1977**, *B33*, 1608-1610.

91   R. P. Chapman, J. R. Hiscock, P. A. Gale and D. L. Bryce, *Can. J. Chem.*, **2011**, *89*, 822-834.

92   M. Gee, R. E. Wasylishen and A. Laaksonen, *J. Phys. Chem. A*, **1999**, *103*, 10805-10812.

93   H. Hamaed, J. M. Pawlowski, B. F. T. Cooper, R. Fu, S. H. Eichhorn and R. W. Schurko, *J. Am. Chem. Soc.*, **2008**, *130*, 11056-11065.

94   E. B. Brackett, T. E. Brackett and R. L. Sass, *J. Inorg. Nucl. Chem.*, **1963**, *25*, 1295-1296.

95   G. Wu and V. Terskikh, *J. Phys. Chem. A*, **2008**, *112*, 10359-10364.

96   R. Sternheimer, *Phys. Rev.*, **1950**, *80*, 102.

97   R. Sternheimer, *Phys. Rev.*, **1951**, *84*, 244.

98   R. Sternheimer, *Phys. Rev.*, **1954**, *95*, 736-750.

99   E. A. C. Lucken, Sternheimer Shielding In *Nuclear Quadrupole Coupling Constants*, Academic Press: London, **1969**, 79-96.

100 D. H. Brouwer and G. D. Enright, *J. Am. Chem. Soc.*, **2008**, *130*, 3095-3105.

Chapter Seven

Application of $^{69/71}$Ga SSNMR and ^{127}I NQR Experiments to Elucidate the Composition of 'GaI'

7.1   Introduction

In the preceding Chapters, many examples have been provided which serve to demonstrate the utility of SSNMR experiments that probe quadrupolar halogen nuclei. In essentially all of the cases considered in Chapters 3 – 6, rather simple systems with known structures and compositions were considered (one important exception being CaBr$_2$·xH$_2$O). Studies on such well-established systems are critical, since very little prior SSNMR literature exists where chlorine, bromine, or iodine serve as the probe nuclei. At the same time, while these initial studies on systems of known composition and structure are useful, SSNMR methods are by no means restricted to the study of such materials. It would therefore be interesting to attempt to probe chemically- and industrially-relevant systems of unknown structure or composition.

Over the past decade or so, there has been a significant amount of interest in low-valent group 13 element-containing complexes.[1-5] The synthesis of these materials may be achieved by the careful selection of the supporting ligand, and relies on a subsequent reduction, or preferentially the use of a low-valent element-halide precursor. Most of the chemistry for the group 13 elements occurs primarily in the +3 oxidation state, although due to relativistic effects, the chemistry of the heavier group 13 elements, such as indium and thallium, presents many examples where the metal is in the +1 oxidation state. For the lighter members of group 13, the synthesis of stable +2 or +1 oxidation state materials is both synthetically challenging, as well of

fundamental interest. To date, the only crystallographically authenticated solid gallium(I)-halides have been reported by the group of Schnöckel.[6] Unfortunately, in order to prepare these materials, a complex high temperature reactor is required, which is not available to the average research group.[6] Alternatively, 'GaI', as reported by Green in 1990,[7] has become a popular low-valent gallium precursor due to its ease of synthesis and broad applicability in organic synthesis, coordination chemistry, and cluster fabrication. Both the synthetic applications and the history of 'GaI' have been thoroughly discussed in the literature.[8-10]

As noted above, although many synthetic applications of 'GaI' have been discovered, its structure and full composition have not been elucidated. Based on a Raman spectroscopic analysis of 'GaI' (as prepared by the method of Green), the composition is currently postulated to be a mixture of gallium-subiodides, consisting predominantly of Ga_2I_3 (i.e., $[Ga]_2[Ga_2I_6]$).[8,10] Unfortunately, the Ga_2I_6 compound appears to have many Raman (as well as IR) signatures that are consistent with $[Ga]^+[GaI_4]^-$ (i.e., GaI_2),[11] which makes the attribution to Ga_2I_3, rather than GaI_2, somewhat ambiguous. In this Chapter, a $^{69/71}Ga$ SSNMR and ^{127}I NQR study of 'GaI' powder obtained using Green's ultrasonic synthesis approach is presented. After the analysis of the observed SSNMR/NQR line shapes, new insights into the components of the bulk complex are provided.

7.2   Experimental Details

7.2.1   Sample Preparation

A sample of 'GaI' was provided for this study by the group of Prof. D. Richeson (University of Ottawa). The sample was synthesized according to standard literature methods,[7] and its purity was confirmed using reactivity studies, as well as pXRD experiments.[12] As 'GaI' is both air and moisture sensitive, samples were stored and prepared for use under either dry N_2 or

Ar. Prior to SSNMR and NQR experiments, all samples were gently powdered and tightly packed into 4 mm o.d. Bruker MAS ZrO_2 rotors.

7.2.2 Solid-State $^{69/71}$Ga NMR

Experimental data were acquired at the National Ultrahigh-field NMR Facility for Solids in Ottawa using a standard bore (54 mm) Bruker AVANCEII spectrometer operating at $B_0 = $ 21.1 T ($v_0(^1H) = 900.08$ MHz; $v_0(^{69}Ga) = 216.03$ MHz; $v_0(^{71}Ga) = 274.49$ MHz). Complementary $^{69/71}$Ga SSNMR data were acquired at the University of Ottawa using a wide bore (89 mm) Bruker AVANCE spectrometer operating at $B_0 = 11.75$ T ($v_0(^1H) = 500.13$ MHz; $v_0(^{69}Ga) = 120.04$ MHz; $v_0(^{71}Ga) = 152.52$ MHz). At 21.1 T, SSNMR experiments used a 4 mm Bruker HX MAS probe, while SSNMR experiments at 11.75 T used a 4 mm Bruker HXY MAS probe. MAS experiments were attempted at 21.1 T, but due to the metallic content of the sample (*vide infra*), they were unsuccessful.

Based upon recent IUPAC recommendations,[13] $^{69/71}$Ga $\pi/2$ pulse lengths were determined, and chemical shifts were referenced, using a 1.1 mol/kg $Ga(NO_3)_3$ solution in D_2O ($\delta_{iso}(^{69/71}Ga) = 0.0$ ppm). For SSNMR experiments where the QI at the Ga site was nonzero, CT selective pulse lengths were used, and were determined by scaling the nonselective solution $\pi/2$ pulse length by the factor $1/(I + 1/2) = 1/2$. Gallium-69/71 SSNMR signals were typically acquired using the Solomon echo pulse sequence,[14-16] but the Hahn echo[17] pulse sequence was also used (data not shown). Typical acquisition parameters were as follows: for the shielded (i.e., upfield) Ga site exhibiting a significant QI, $\pi/2 = 1.6$ to 2.4 μs, $\tau_1 = 17.6$ to 50 μs, $\tau_2 = 4.8$ to 30 μs, spectral window = 250 to 1000 kHz, 512 to 2 048 data points, recycle delay = 1.0 s, and the collection of 1 024 to 7 000 transients; for the deshielded (i.e., downfield) Ga site, $\pi/2 = 11.0$ μs, spectral window = 50 kHz, 1 024 data points, recycle delay = 0.35 s, and the collection of 1 024

transients. For complete experimental details, see Appendix E, Table E.1. Subsequent to data collection and processing, SSNMR line shape analysis was carried out using WSolids1.[18]

7.2.3 Solid-State ^{127}I NQR

All NQR experiments were carried out at the University of Ottawa using a Bruker AVANCEIII spectrometer, a 4 mm Bruker HXY MAS probe, and were performed using the Hahn echo pulse sequence. Non-optimized, short (~ 1 μs), high-powered pulses were used as the transmitter frequency was varied until the suspected resonances were detected. Typically, the offset used while searching for NQR signals was 150 kHz. For further details, see Appendix E, Table E.1.

7.3   Results and Discussion

7.3.1 Gallium-69/71 SSNMR Experiments

As the ^{69}Ga and ^{71}Ga nuclei are quadrupolar ($I(^{69/71}$Ga) = 3/2), each possesses a nonzero Q value, and may serve as probes of the local EFG. As noted in prior Chapters, in addition to the usual δ_{iso} value, SSNMR experiments using quadrupolar nuclei may, in favourable situations, provide information on CSA and the QI. Solid-state $^{69/71}$Ga NMR experiments were performed in two applied magnetic fields (i.e., B_0 = 11.75 and 21.1 T) to confirm the observed SSNMR tensor parameters, as the contributions to the total observed line shape from CSA and the QI differ individually as a function of B_0 (see Section 2.4.3). The observed spectra may be found in Figures 7.1 and 7.2, and the extracted gallium SSNMR tensor parameters are summarized in Table 7.1.

Table 7.1 Experimental $^{69/71}$Ga EFG/CS tensor parameters and Euler Angles for 'GaI'[a]

assigned chemical species	$\|C_Q(^{69}Ga)\|$ / MHz	$\|C_Q(^{71}Ga)\|$ / MHz	η_Q	δ_{iso}[b] / ppm	Ω / ppm	κ	α, β, γ / °
Ga(0)	—	—	—	4488.1(3)	—	—	—, —, —
[Ga(III)I$_4$]$^-$	4.95(9)	3.11(8)	1	−424(5)	137(7)	−0.07(7)	42(5), 133(5), 23(5)

[a] Error bounds are in parentheses. Parameter definitions are in Chapter 2.
[b] With respect to 1.1 mol/kg Ga(NO$_3$)$_3$ in D$_2$O ($\delta_{iso}(^{69/71}Ga) = 0.0$ ppm).
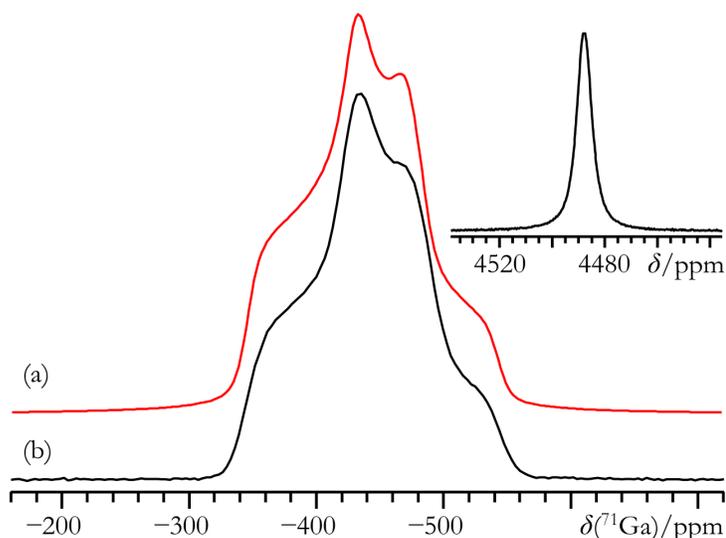
Figure 7.1 Best-fit analytical simulation (a), and experimental static Solomon echo (b) ^{71}Ga SSNMR spectrum for the most shielded (i.e., upfield) site observed in 'GaI', as acquired at $B_0 = 11.75$ T. Inset: downfield site.

Two $^{69/71}$Ga SSNMR signals were consistently observed in each spectrum. One signal possesses a very high shift ($\delta_{iso} = 4488.1(0.3)$ ppm), and does not possess an appreciable gallium QI, as the $^{69/71}$Ga SSNMR line shapes for this site are relatively narrow (the line width of the ^{71}Ga NMR resonance at half-maximum is ca. 1 kHz at 11.75 T). The value of this shift is independent of the gallium isotope and B_0. Based upon its exceptionally deshielded (i.e., 'downfield') chemical shift, this signal is easily attributed to gallium metal. The EFG at the gallium nuclei in solid gallium metal is known to be nonzero, and to possesses a chemical shift

of ca. 1300 ppm;[19] hence, the observed signal cannot be due to solid Ga(0). Interestingly, both the observed gallium chemical shift value, and very small QI for this site indicate that the gallium metal is present in a 'liquid-like' state: the measured shift value is within 2 ppm of the value measured by Knight in his seminal paper.[20] MAS experiments were attempted at B_0 = 21.1 T, but failed, as stable spinning speeds could not be maintained and sample degradation occurred. This fortuitous observation lends additional support to the prior statements that the 'GaI' sample contains Ga metal, as a rapidly rotating metallic species within a magnetic field is expected to generate inductive (Joule) heating. This heating also likely provided the mechanism by which the sample degraded, as 'GaI' is thermally unstable above room temperature.
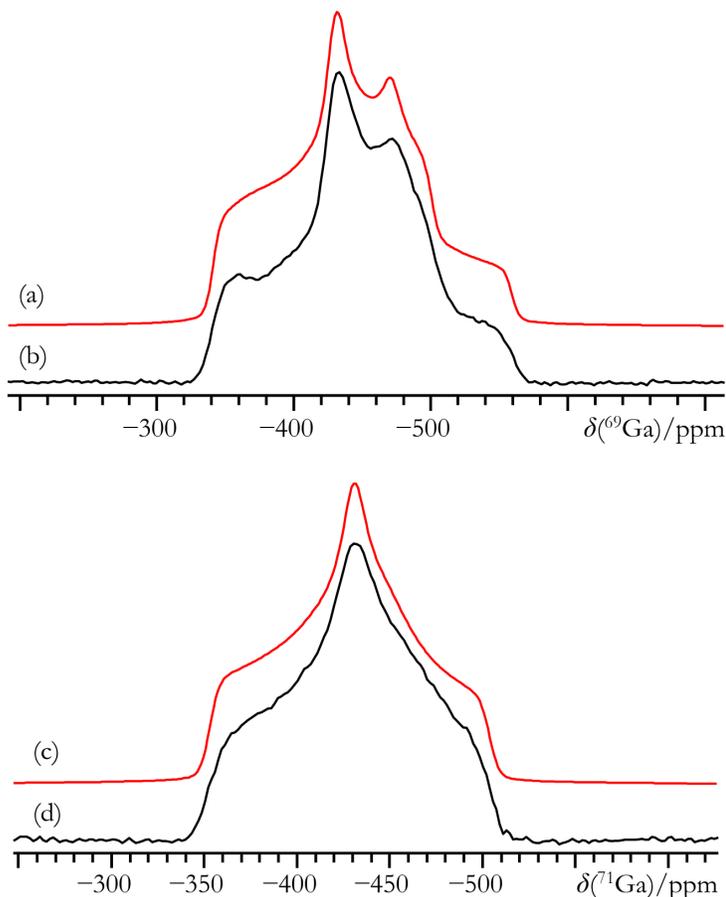
Figure 7.2 Best-fit analytical simulations (a, c), and experimental static Solomon echo (b, d) [69/71]Ga SSNMR spectra for the most shielded site in 'GaI', as acquired at B_0 = 21.1 T.

The second signal possesses a line shape which is broadened by both a QI and CSA. The observed δ_{iso} for this site (−424(5) ppm) lies in a region of the Ga shift range that belongs to tetraiodogallate (i.e., $[GaI_4]^-$).[21,22] If the $[GaI_4]^-$ units were perfect tetrahedrons, one would expect to measure no QI for this site, in contradiction with the SSNMR data, where a nonzero ($C_Q(^{71}Ga)$ = 3.11(8) MHz; $C_Q(^{69}Ga)$ = 4.95(9) MHz) QI is observed. If one considers the structurally similar $[GaCl_4]^-$, a nonzero gallium QI was also recently experimentally observed.[23] As well, in structures where this unit is present as a counter ion (i.e., $(NH_4)[GaCl_4]$), it has been shown via XRD that these units are not perfectly tetrahedral;[24] hence, the presence of a distorted $[GaI_4]^-$ unit is not terribly surprising. Over the course of the present study, it was established that there existed some variability in the QI and CS tensor parameters for this site as a function of the sample preparation conditions used; however, both the Ga(0) and $[GaI_4]^-$ species are consistently observed. In addition, a pronounced gallium chemical shift anisotropy in the signal associated with the $[GaI_4]^-$ units (Ω = 137(7) ppm) has been quantified, and it has been possible to clearly establish noncoincidence between the EFG and CS tensor PASs, as evidenced by Euler angle values distinct from zero. As there is no signal in the −600 to −900 ppm region, there do not appear to be any $^{69/71}Ga$ SSNMR signals associated with the high symmetry Ga^+ species.[23] The lack of the Ga^+ cation is surprising, as Ga_2I_4 is known to exist as $Ga^+[GaI_4]^-$.[25] From the $^{69/71}Ga$ SSNMR data alone, however, one cannot rule out other gallium iodide species, such as GaI_3, which experience a very large QI and would therefore be difficult to detect using SSNMR experiments.[26] In fact, even at 21.1 T, any species of this nature could not be detected.

7.3.2   Iodine-127 NQR Experiments

From the $^{69/71}Ga$ SSNMR data, there is clear evidence that metallic gallium is present, due primarily to the diagnostic Knight-shifted signal that is consistently measured at +4488.1

ppm. While there is strong evidence for the $[GaI_4]^-$ unit, any additional conclusions based upon the NMR data alone cannot be made. As ^{127}I NQR experiments are very sensitive probes of local electronic structure,[27] and as prior ^{127}I NQR measurements have been performed on both solid GaI_2 and GaI_3 at room temperature,[28,29] iodine-127 NQR experiments were performed to establish the presence of either GaI_2 or GaI_3 in 'GaI'. After searching exhaustively for the ^{127}I NQR signal in GaI_3 (and corresponding negative results for the ^{69}Ga NQR signal), it can be reasonably stated that there does not appear to be a significant amount of GaI_3 in 'GaI'. As GaI_3 is one of the main constituents in Ga_2I_3 (i.e., $Ga_2I_3 = [Ga]_2[Ga_2I_6]$) this casts doubt on earlier interpretations of Raman spectra, which hinted at its presence.[8] It is again noted that many of the Raman peaks from Ga_2I_3 can also be attributed to GaI_2. Indeed, ^{127}I NQR measurements on 'GaI' were able to very rapidly (experiment times < 5 minutes) confirm the presence of three of the four expected ^{127}I NQR signals in GaI_2 (see Table 7.2 and Figure 7.3).

Table 7.2 Experimental ^{127}I NQR parameters for 'GaI'[a]

compound	site label	$\nu_{Q1}{}^{b}$ / MHz	notes
'GaI'	A	113.69(1)	assigned to site I(1) of GaI_2
	B	132.03(1)	assigned to site I(2) of GaI_2
	C	134.375(15)	assigned to site I(3) of GaI_2
GaI_3	I(1)	133.687	
	I(2)	173.650	ref. 28
	I(3)	174.589	
	Ga	21.45	ref. 26, ^{69}Ga isotope
GaI_2	I(1)	113.65	
	I(2)	131.94	ref. 29
	I(3)	134.27	
	I(4)	163.71	

[a] Error bounds are in parentheses. Parameter definition is in the footnotes to Table 4.1. It is noted here that there were negative results when attempting to detect both the ^{69}Ga and ^{127}I NQR signals of GaI_3.
[b] All listed ^{127}I NQR transitions correspond to the $m = \pm 1/2 \leftrightarrow \pm 3/2$ transition. For ^{69}Ga, $\nu_{Q1} = \nu_Q$. Higher frequency transitions could not be observed due to probe tuning limitations.
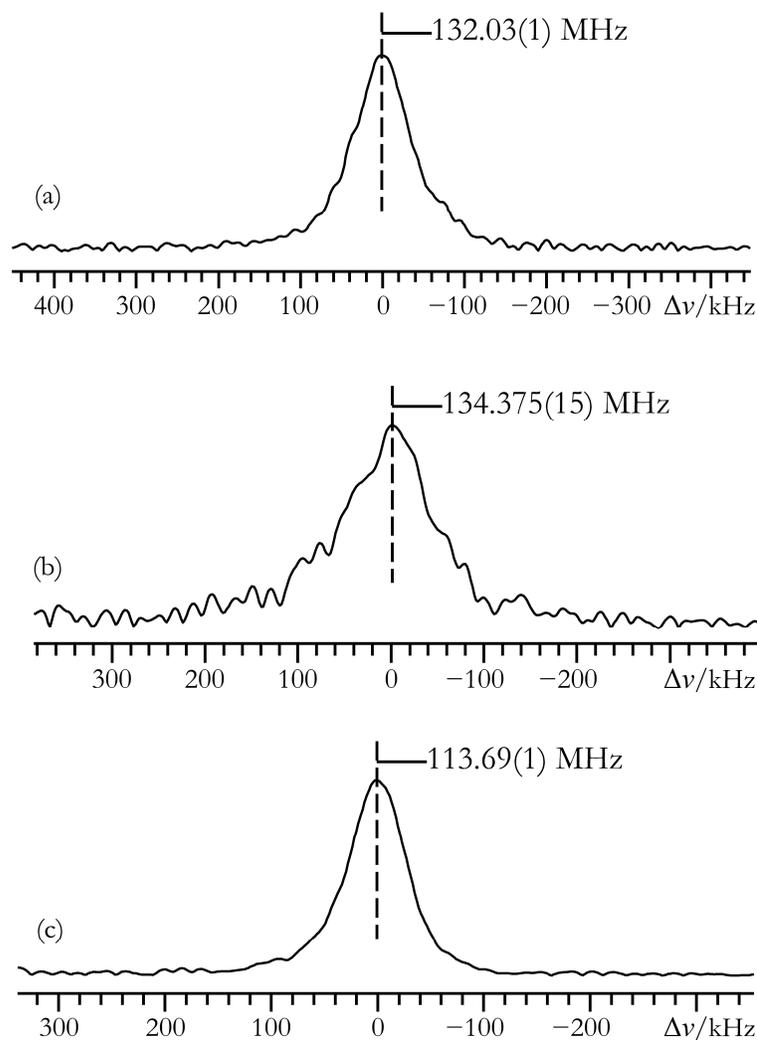
Figure 7.3 Experimental Hahn echo ^{127}I NQR spectra of 'GaI'. (a) ν_{RF} = 132.0 MHz; (b) ν_{RF} = 134.37 MHz; (c) ν_{RF} = 113.75 MHz. For additional experimental details, see Appendix E, Table E.1.

Due to probe tuning limitations, it was not possible to detect the fourth expected iodine site in GaI_2, which is suspected to be located at ~163.7 MHz.[29] Hence, the ^{127}I NQR data conclusively demonstrate the presence of GaI_2, and cast significant doubt on the presence of Ga_2I_3.

7.4   Conclusions

Using multiple-field $^{69/71}$Ga SSNMR experiments and ^{127}I NQR measurements, further discussion as to the full nature of 'GaI' has been provided. This is of importance, as 'GaI' is an often-used synthetic reagent whose exact composition and structure are unknown. Both ^{69}Ga and ^{71}Ga NMR measurements consistently indicate the presence of 'liquid-like' gallium metal, as evidenced by its lack of QI and very distinct chemical shift value. In addition, a second $^{69/71}$Ga site is observed for this sample, which is attributed to a $[GaI_4]^-$ fragment that is slightly distorted from perfect tetrahedral symmetry about the central Ga(III). Using ^{127}I NQR, it is conclusively seen that a significant portion of 'GaI' is actually GaI_2, which is present as $[Ga]^+[GaI_4]^-$. In addition, the presence of GaI_3 (and therefore also Ga_2I_3) could not be verified, which casts significant doubt on the earlier conclusions reached using Raman spectroscopy.

7.5   References

1   S. T. Haubrich and P. P. Power, *J. Am. Chem. Soc.*, **1998**, *120*, 2202-2203.

2   R. J. Wright, A. D. Phillips, N. J. Hardman and P. P. Power, *J. Am. Chem. Soc.*, **2002**, *124*, 8538-8539.

3   H. V. R. Dias, S. Singh and T. R. Cundari, *Angew. Chem. Int. Ed.*, **2005**, *44*, 4907-4910.

4   C. G. Andrews and C. L. B. Macdonald, *Angew. Chem. Int. Ed*, **2005**, *44*, 7453-7456.

5   T. Jurca, J. Lummiss, T. J. Burchell, S. I. Gorelsky and D. S. Richeson, *J. Am. Chem. Soc.*, **2009**, *131*, 4608-4609.

6   H. Schnöckel, *Dalton Trans.*, **2008**, 4344-4362.

7   M. L. H. Green, P. Mountford, G. J. Smout and S. R. Speel, *Polyhedron*, **1990**, *9*, 2763-2765.

8   S. Coban, Diplomarbeit Thesis, Universitat Karlsruhe, **1999**.

9   R. J. Baker, C. Jones, M. Kloth and D. P. Mills, *New J. Chem.*, **2004**, *28*, 207-213.

10   R. J. Baker and C. Jones, *Dalton Trans.*, **2005**, 1341-1348.

11   L. G. Waterworth and I. J. Worrall, *J. Inorg. Nucl. Chem.*, **1973**, *35*, 1535-1537.

12   T. Jurca and D. S. Richeson, private communication, **2008**.

13   R. K. Harris, E. D. Becker, S. M. Cabral De Menezes, P. Granger, R. E. Hoffman and K. W. Zilm, *Pure Appl. Chem.*, **2008**, *80*, 59-84.

14   I. Solomon, *Phys. Rev.*, **1958**, *110*, 61-65.

15   I. D. Weisman and L. H. Bennett, *Phys. Rev.*, **1969**, *181*, 1341-1350.

16   A. C. Kunwar, G. L. Turner and E. Oldfield, *J. Magn. Reson.*, **1986**, *69*, 124-127.

17   E. L. Hahn, *Phys. Rev.*, **1950**, *80*, 580-594.

18   K. Eichele and R. E. Wasylishen, *WSolids1: Solid-State NMR Spectrum Simulation Package*, v. 1.19.11, Universität Tübingen: Tübingen, **2009**.

19   M. I. Valič, S. N. Sharma and D. L. Williams, *Phys. Lett.*, **1968**, *26A*, 528-529.

20   D. W. Knight, *Phys. Rev.*, **1949**, *76*, 1259-1260.

21   J. W. Akitt, N. N. Greenwood and A. Storr, *J. Chem. Soc.*, **1965**, 4410-4416.

22   B. R. McGarvey, M. J. Taylor and D. G. Tuck, *Inorg. Chem.*, **1981**, *20*, 2010-2013.

23   R. P. Chapman and D. L. Bryce, *Phys. Chem. Chem. Phys.*, **2009**, *11*, 6987-6998.

24   T. Timofte, S. Bremm, A. V. Mudring and G. Meyer, *Z. Anorg. Allg. Chem.*, **2009**, *635*, 1890-1893.

25   G. Gerlach, W. Honle and A. Simon, *Z. Anorg. Allg. Chem.*, **1982**, *486*, 7-21.

26   R. G. Barnes, S. L. Segel, P. J. Bray and P. A. Casabella, *J. Chem. Phys.*, **1957**, *26*, 1345-1346.

27   C. M. Widdifield and D. L. Bryce, *J. Phys. Chem. A*, **2010**, *114*, 10810-10823.

28   S. L. Segel and R. G. Barnes, *J. Chem. Phys.*, **1956**, *25*, 578-579.

29   T. Okuda, H. Hamamoto, H. Ishihara and H. Negita, *Bull. Chem. Soc. Jpn.*, **1985**, *58*, 2731-2732.

General Conclusions

As enumerated in the individual conclusions to Chapters 3 – 7, it is clear that solid-state NMR experiments using quadrupolar nuclei as probes possess several distinct advantages over similar experiments performed upon spin-1/2 nuclei. Due in part to their relatively small Q values, quadrupolar nuclei such as ^{2}H, $^{6/7}$Li, ^{11}B, and ^{27}Al have been used for decades to probe solid state structures and dynamic processes in molecules. Because of the substantial developments in high-field magnet technology, SSNMR probe design, and the composition of efficient broadband pulse sequences, the sensitivity of SSNMR experiments is consistently being enhanced. As such, more advanced systems are being pursued for study using SSNMR experiments (e.g., surfaces and porous materials). As well, many nuclei which were thought to be far too 'exotic' for detection using SSNMR are now able to be studied.

In this dissertation, it has been clearly demonstrated that all of the quadrupolar halogen nuclei (i.e., $^{35/37}$Cl, $^{79/81}$Br, and ^{127}I) are reasonably amenable to the SSNMR experiment, if one makes intelligent choices about the applied field strength, the pulse sequence used, and the system under study. There does not appear to be any restriction for the study of all the above nuclei using SSNMR experiments, if the bonding environment at the halogen is known to be sufficiently ionic. Although recently-developed pulse sequences, such as WURST-QCPMG, should enable the detection of even covalently-bound chlorine environments using SSNMR, it does not appear that the same statement can be made for the heavier members of this chemical group. The primary reason for this lies in the larger nuclear electric quadrupole moments for the $^{79/81}$Br and ^{127}I nuclides. With that said, it is clear that SSNMR experiments upon these

probe nuclei still have much to offer. For example, these nuclei have been demonstrated to be effective probes of sample hydration, as well as local lattice symmetry. The sensitivity of the quadrupolar interaction as a function of the atomic/ionic positions in the lattice is pronounced to such an extent that for simple systems (e.g., $MgBr_2$, CaI_2, and MgI_2), ionic displacements of less than 0.05 Å may lead to drastic augmentations in the observed halide C_Q values. These types of experiments may also be used to provide evidence that compounds are isostructural (e.g., the BaX_2 series, where X = Cl, Br, I). The ability to complement several experimental techniques, such as SSNMR and pXRD, with advanced quantum chemical calculations (e.g., GIPAW DFT) has allowed for some basic structural refinements to be performed (i.e., $MgBr_2$) and for the correction of prior errors in the literature (i.e., ^{35}Cl SSNMR data for $CaCl_2$). Nuclear quadrupole resonance experiments have proven to be very useful in providing independent measures of the quadrupolar interactions, and clearly demonstrated that a major component of 'GaI' is indeed GaI_2, in contrast with earlier findings based upon rather complex Raman datasets.

During the course of this work, it was found that high-order quadrupole-induced effects (i.e., HOQIE) were present in several of the ^{127}I SSNMR spectra, and persisted even at the highest available applied magnetic field of 21.1 T. Subsequent studies using the $^{185/187}Re$ nuclides (which possess some of the largest Q values known) allowed for the observation of additional spectral fine structure which had never been observed before previously, and which was attributed to HOQIE. It is clear that the inclusion of these effects will be necessary as other research groups pursue the SSNMR study of systems containing nuclei which experience very large quadrupolar interactions (e.g., systems which contain $^{63/65}Cu$, ^{75}As, ^{93}Nb, ^{181}Ta, ^{209}Bi, etc.).

In closing, based on these many successes, a substantial amount of follow-up work is ongoing within the Bryce lab. One particular area of research involves studying the effects of

halogen bonding interactions upon halogen nuclide NMR observables. As such, collaborations have been established with world-leaders in halogen bonding to study these halogen bonding interaction effects in important industrial materials (see Chapter 9). Additional experiments are being performed to probe HOQIE in a more general sense (i.e., any spin quantum number and no restrictions on the EFG tensor symmetry, see Chapter 9). Others in the group are authoring efficient SSNMR line shape simulation software which will be able to treat any combination of Zeeman and QI simultaneously. It is expected that over the course of the next several years, many of these quadrupolar nuclei will lose their 'exotic' labels and join the many others already within the ever-expanding SSNMR toolkit.

Chapter Nine

Ongoing and Future Research Directions

9.1 Further Comments on the Utility of $^{185/187}$Re SSNMR

As briefly mentioned in Chapter 5, if rhenium chemical shift information could be reliably extracted, it would potentially offer insight into the Re oxidation state. Indeed, liquid-state rhenium NMR studies document a chemical shift range of about 6 800 ppm.[1,2] As part of an ongoing study, several different rhenium-containing compounds have been chosen in order to comment upon the ability of $^{185/187}$Re SSNMR to probe Re oxidation states. A selection of these systems is briefly discussed at this time.

9.1.1 ReO₃: Suggested Rhenium Chemical Shift Reference

As demonstrated previously (i.e., Chapters 3 – 7), methods which probe the EFG tensor can offer insight into the local molecular/lattice symmetry. Unfortunately, this tensor cannot be used to infer Re oxidation states. NMR experiments using metal nuclei such as ^{59}Co are known to potentially probe the metal oxidation state via substantial differences in δ_{iso} values.[3-6] However, one of the first challenges one faces when performing any $^{185/187}$Re SSNMR experiment is the poor sensitivity associated with the accepted chemical shift reference material. According to a recent IUPAC publication, a 0.1 mol/dm^3 solution containing the ReO_4^- group in D_2O is to be taken as the chemical shift reference.[7] It is perhaps counterintuitive that the observation of this NMR reference signal is somewhat time-consuming (often needing on the order of 1 000 transients to be obtained to arrive at a modest S/N). Keeping this in mind, a search was initiated with the goal of finding a new reference material. A potential candidate

reference compound has been found in Re(VI)O$_3$. This material packs in a cubic lattice[8] and therefore it would be expected that the EFG at the Re nuclei would be negligible. By removing QI line shape broadening effects, a sharp signal could be rapidly obtained, as Re T_1 values are necessarily very small (although not to the extent that lifetime broadening effects are important) due to the excessively large Q associated with each Re nuclide. Indeed, initial observations bear this out (Figure 9.1). Very high S/N spectra can be obtained using ~512 scans (~2 minutes experimental time). The measured rhenium isotropic chemical shifts at both $B_0 = 11.75$ and 21.1 T have been calibrated relative to the accepted solution standard as −2940(8) ppm (Table 9.1). This δ_{iso} value appears to be field independent, and tests of its temperature dependence are ongoing.
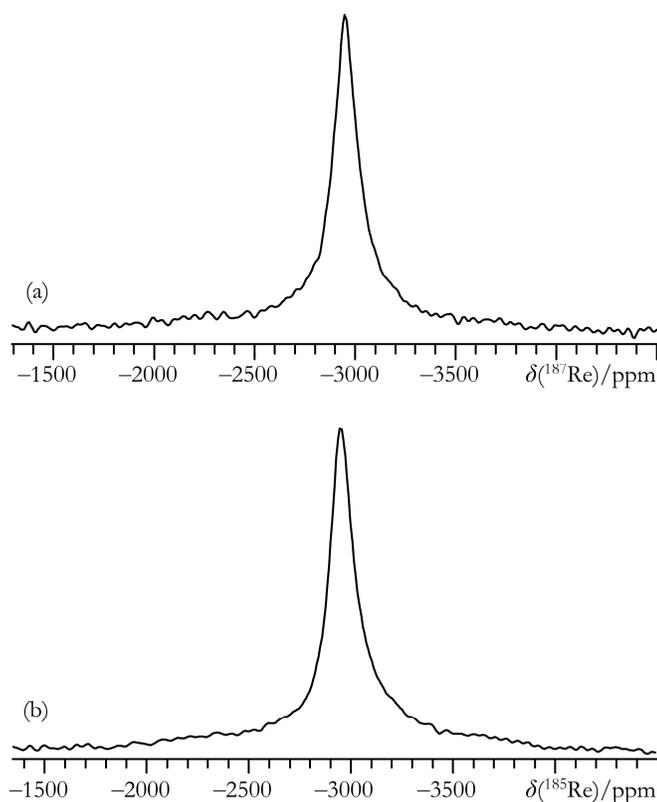
Figure 9.1 Experimental static Solomon echo [187]Re (a) and [185]Re (b) SSNMR spectra of powdered ReO$_3$ acquired at $B_0 = 11.75$ T. Analogous results have been obtained at $B_0 = 21.1$ T.

9.1.2 KReO₄: New and Useful HOQIE

The local rhenium environment in $KRe(VII)O_4$ is that of a distorted tetrahedron, and as such it is similar to that of NH_4ReO_4 and $NaReO_4$. Prior rhenium NQR experiments have been performed upon $KReO_4$, and established the following EFG tensor parameters near room temperature: $C_Q(^{185}Re) = 188.68$ MHz; $C_Q(^{187}Re) = 178.76$ MHz; and $\eta_Q < 0.02$.[9] The present $^{185/187}Re$ NQR measurements confirm these findings (see Figure 9.2 and Table 9.1), with the slight discrepancy being attributed to the differences in the respective measurement temperatures.
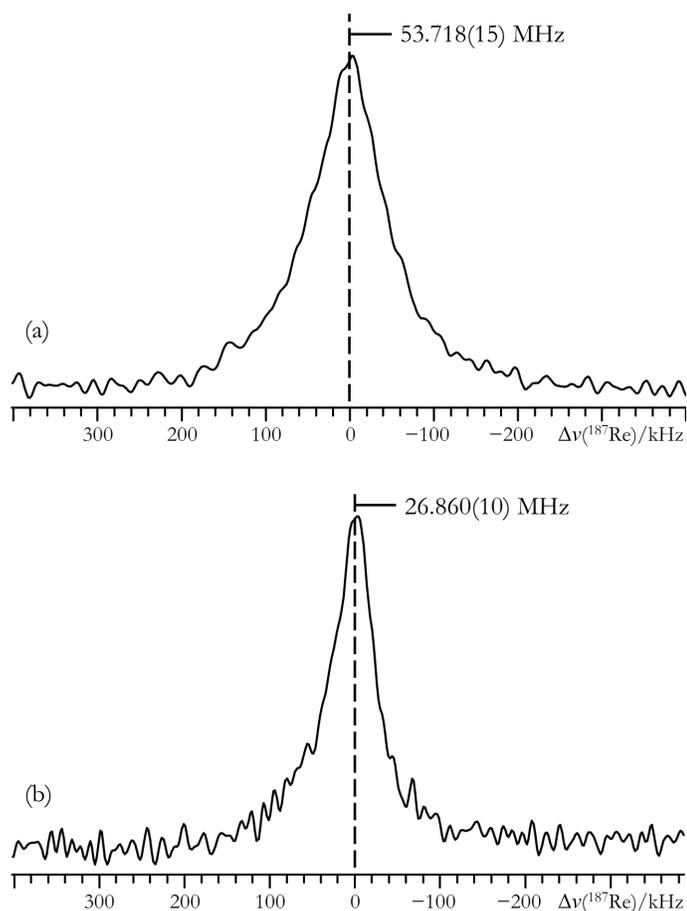
Figure 9.2 Experimental Hahn echo ^{187}Re (a, b) NQR spectra of powdered $KReO_4$ acquired at $T = 291.8$ K. The transition frequencies are specified in the Figure. (a) $m = \pm 3/2 \leftrightarrow \pm 5/2$; (b) $m = \pm 1/2 \leftrightarrow \pm 3/2$, where for all transitions $|\Delta m| = 1$. Analogous ^{185}Re NQR spectra have been acquired.

Table 9.1 Experimental $^{185/187}$Re EFG tensor parameters and δ_{iso} values[a]

compound	$\nu_{Q1}/\nu_{Q2}(^{185}\text{Re})$ / MHz	$\nu_{Q1}/\nu_{Q2}(^{187}\text{Re})$ / MHz	$|C_Q(^{185}\text{Re})|$ / MHz	$|C_Q(^{187}\text{Re})|$ / MHz	η_Q	δ_{iso}[b] / ppm
ReO$_3$	—	—	—	—	—	−2940(8)
KReO$_4$	28.380(10)/56.754(15)	26.860(10)/53.718(15)	189.18(6)	179.06(6)	<0.003[c]	0(50)
Re$_2$(CO)$_{10}$	29.287(15)/39.876(12)	27.720(12)/37.742(12)	142.06(6)	134.46(6)	0.642(2)	−4375(75)

[a] All values are extracted via exact modeling of the QI. Measurement errors are within parentheses. All measurements were carried out at T = 291.8(2) K, except for ReO$_3$, which was at room temperature.
[b] With respect to 0.1 mol/dm^3 NaReO$_4$ in D$_2$O ($\delta_{iso}(^{185/187}\text{Re})$ = 0 ppm).
[c] Value constrained as a result of modeling the $^{185/187}$Re $m = 1/2 \leftrightarrow 3/2$ SSNMR signals.

After precisely measuring the $^{185/187}$Re $\ddot{V}$ tensor parameters, rhenium SSNMR experiments were performed at B_0 = 11.75 and 21.1 T (see Figures 9.3 and 9.4) in order to establish the isotropic rhenium chemical shift value for this compound, and to comment upon the presence of any rhenium CSA effects (something which has never been conclusively measured). The $^{185/187}$Re CT SSNMR spectra at both 11.75 and 21.1 T are well-described using exact QI simulation software ('Quadrupolar Exact Software' (QUEST), generated in-house,[10] as opposed to the software used in prior Chapters) that utilizes the EFG tensor parameters in Table 9.1, and δ_{iso} = 0(50) ppm.
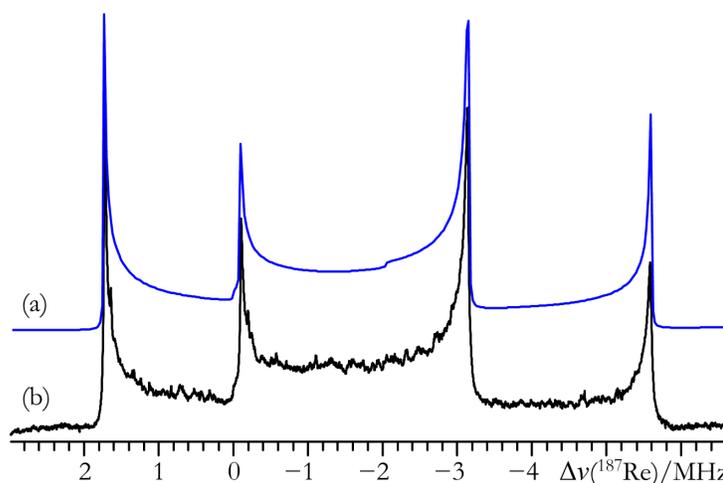
Figure 9.3 Best-fit QUEST exact simulation (a), and experimental static VOCS Solomon echo (b) $^{185/187}$Re CT SSNMR spectrum of powdered KReO$_4$ acquired at B_0 = 21.1 T and T = 291.8 K.
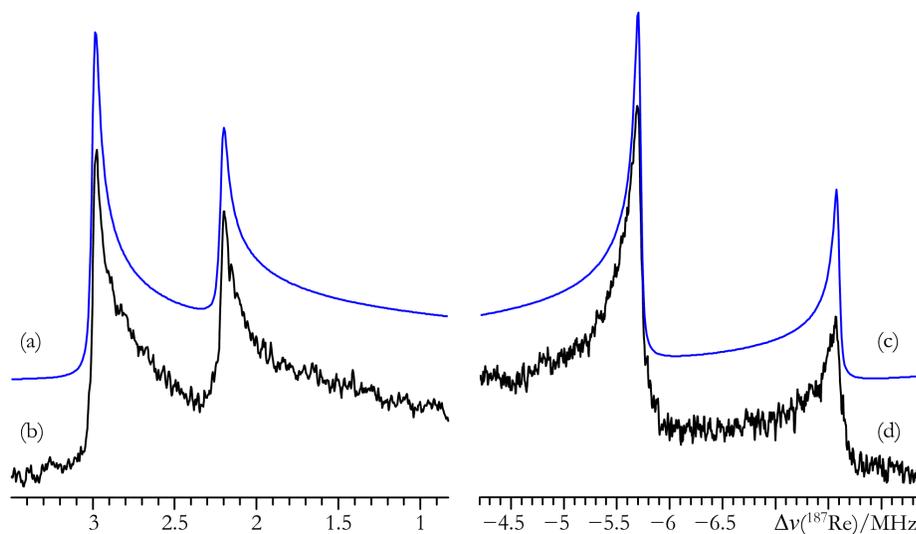
Figure 9.4 Best-fit QUEST exact simulations (a, c), and experimental static VOCS Hahn echo (b, d) $^{185/187}$Re CT SSNMR spectra of powdered KReO$_4$ acquired at $B_0 = 11.75$ T and $T = 291.8$ K. In (a, b) the high-frequency CT discontinuities are depicted, while in (c, d) the low-frequency CT discontinuities are shown. Please note that the horizontal scaling is not equivalent between (a, b) and (c, d), but the vertical scaling has been maintained.

While there is little evidence of HOQIE at 21.1 T, a very striking observation is made at the lower applied field if one includes one of the ST. Typically, for cases where η_Q is near zero, it is well known that the CT discontinuities are of significantly higher intensity than the individual satellite transition discontinuities. Hence, it was rather surprising to find that the discontinuities associated with the $m = 1/2 \leftrightarrow 3/2$ ST were of comparable intensity to the CT discontinuities at 11.75 T. At 21.1 T, partial observation of the same ST discontinuities lead to the expected result (i.e., much lower relative intensity for the ST) and is hence not discussed further. Due to this effect only being present at the lower applied field, it can be reasonably stated to be due to a HOQIE. It is also noted that these ST discontinuities are exceptionally sensitive to even small deviations in the η_Q value from zero (Figure 9.5). This allowed for a very precise determination of $\eta_Q(^{185/187}$Re) for KReO$_4$ (i.e., $\eta_Q < 0.003$). It is also established that

SSNMR observations allow for the η_Q value to be determined even more precisely than if only

[185/187]Re NQR experimental data were used. When using only the [185/187]Re NQR data for

$KReO_4$, the η_Q value can only be constrained to < 0.02. Proper line shape modeling of the

[185/187]Re ST SSNMR spectra under these conditions thus offers nearly an order of magnitude

gain in the measurement precision for η_Q relative to analogous NQR measurements.
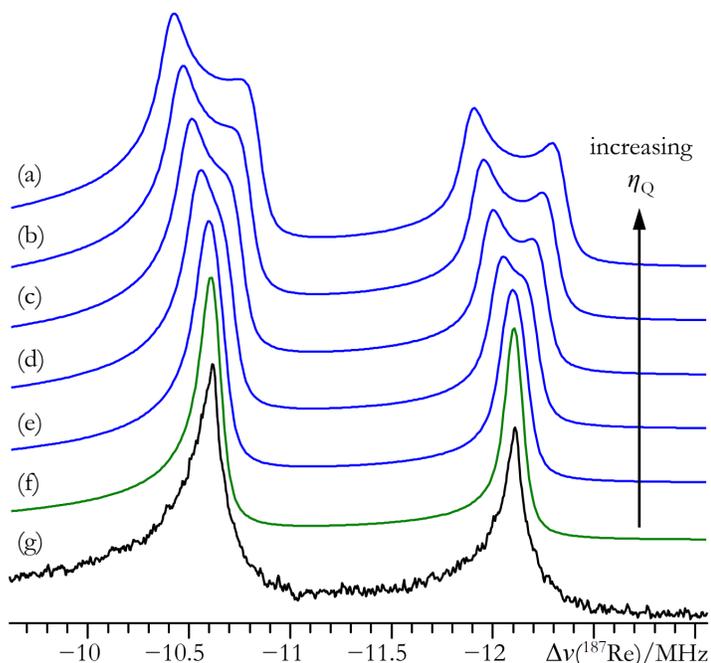
Figure 9.5 QUEST exact simulations (a – f), and experimental static VOCS Hahn echo [185/187]Re SSNMR spectrum ($m = 1/2 \leftrightarrow 3/2$ transition) of powdered KReO₄ acquired at $B_0 = 11.75$ T and $T = 291.8$ K (g), which highlight the effect of η_Q variation upon the [185/187]Re SSNMR line shape. The following values are used for η_Q, while all other parameters remain as reported in Table 9.1: (a) $\eta_Q = 0.015$; (b) $\eta_Q = 0.012$; (c) $\eta_Q = 0.009$; (d) $\eta_Q = 0.006$; (e) $\eta_Q = 0.003$; (f) $\eta_Q = 0$.

9.1.3   Re₂(CO)₁₀: Using [185/187]Re SSNMR to Probe Metal-Metal Bonds

The above two examples demonstrate the potential existence of a relationship between

the rhenium chemical shift value and the Re oxidation state. In order to further assess this

possibility, a Re(0) compound was chosen, which also possesses a Re-Re bond. This second

characteristic is rather interesting from both a chemical bonding perspective, as well as an SSNMR perspective.
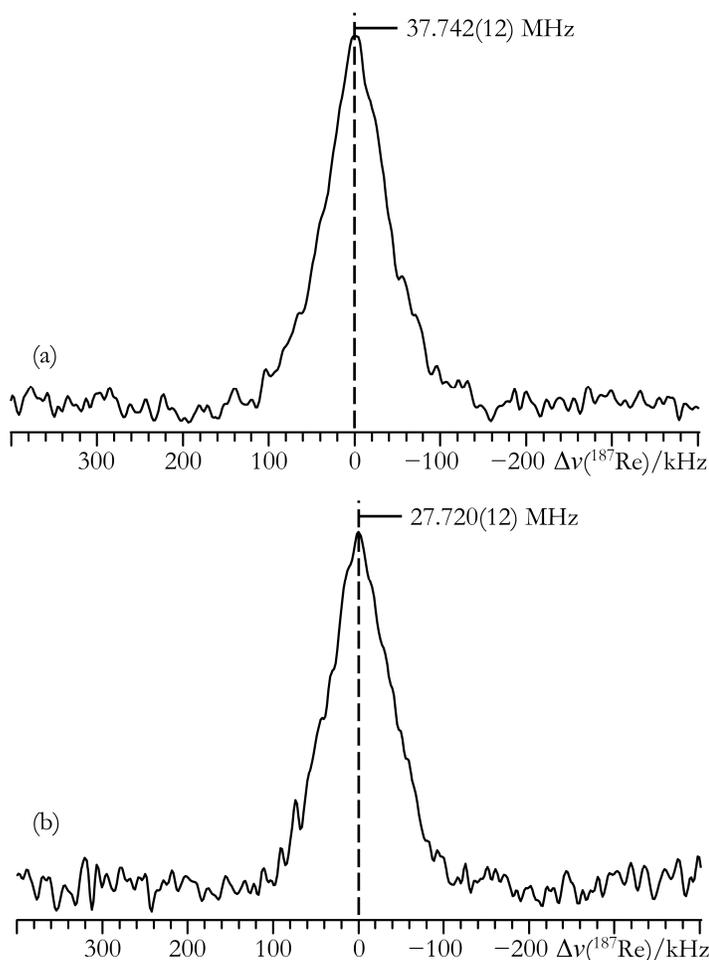
Figure 9.6 Experimental Hahn echo ^{187}Re (a, b) NQR spectra of powdered Re$_2$(CO)$_{10}$ acquired at T = 291.8 K. The transition frequencies are specified in the Figure. (a) m = ±3/2 ↔ ±5/2; (b) m = ±1/2 ↔ ±3/2, where for all transitions $|\Delta m|$ = 1. Analogous NQR spectra have also been acquired using the ^{185}Re nuclide.

As with KReO$_4$, $^{185/187}$Re NQR measurements have previously been carried out on Re$_2$(CO)$_{10}$,[11] and the rhenium NQR parameters isolated here are complementary to this earlier report (Figure 9.6 and Table 9.1). Preliminary $^{185/187}$Re SSNMR data have been acquired at B_0 = 21.1 T and

modeled with exact theory using the EFG tensor parameters arrived at from the NQR measurements (Figure 9.7).
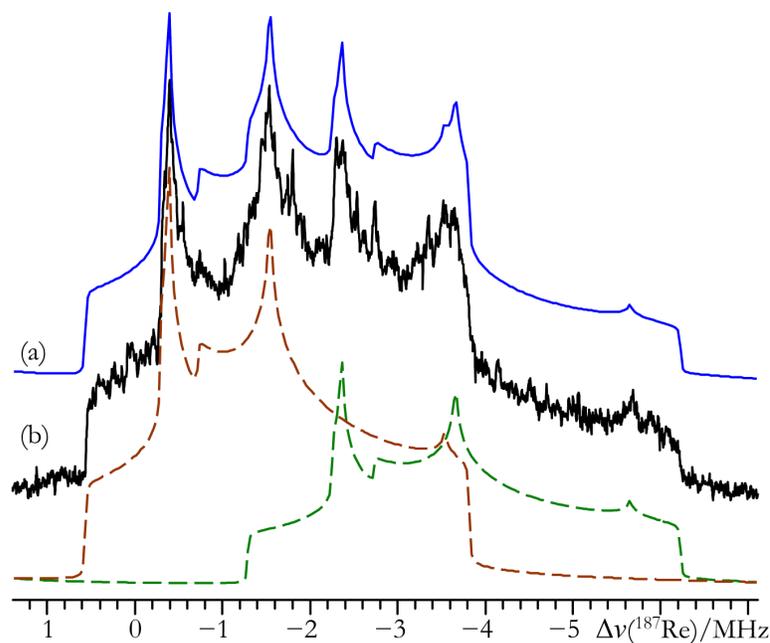
Figure 9.7 Tentative best-fit QUEST exact simulation (a), and experimental static VOCS Solomon echo (b) $^{185/187}$Re SSNMR spectrum of powdered Re$_2$(CO)$_{10}$ acquired at B_0 = 21.1 T and T = 291.8 K. A deconvolution is provided below (b): brown = ^{187}Re signal; green = ^{185}Re signal.

The best-fit exact QI simulation requires the inclusion of a substantial amount of MS, leading to the very low observed δ_{iso} value of −4 375(75) ppm. This observed δ_{iso} value is over 1 400 ppm more shielded than that in ReO$_3$. Overall, it can be stated that there appears to be a relationship between the rhenium isotropic chemical shift value and the oxidation state of the Re atom, but further examples would be required to make definitive statements of this sort. Attempts to acquire $^{185/187}$Re SSNMR spectra of higher quality, which might allow for the measurement of rhenium CSA, are ongoing.

9.2   Attempts to Detect HOQIE for I = 3/2 and I = 7/2

All prior HOQIE discussions pertained to cases where $I = 5/2$ (Chapters 4 and 5). Of course, it would be of greater utility to characterize these effects in a more general fashion, and hence extensions to other values of I must be made. At this time, some preliminary accounts for $I = 3/2$ and $I = 7/2$ are given.

9.2.1   Moderate-Field ^{81}Br SSNMR and ^{81}Br NQR on CaBr$_2$ (I = 3/2)

In Chapter 3, it was observed that for the bromide-containing materials studied, CaBr$_2$ possessed the largest bromine C_Q values. As such, this material was chosen in an attempt to observe HOQIE for $I = 3/2$. To enhance the chances of observing HOQIE, ^{81}Br SSNMR experiments were conducted in a relatively low magnetic field (i.e., $B_0 = 9.4$ T), as compared to the prior study. To begin, ^{81}Br NQR experiments were used to confirm the EFG tensor parameters at the Br nuclei (i.e., $\nu_Q(^{81}\text{Br}) = 32.39(1)$ MHz, Figure 9.8a), and indeed the NQR observations are fully consistent with $C_Q(^{81}\text{Br}) = 62.8(4)$ MHz and $\eta_Q = 0.445(20)$ after the application of **(3.1)**. Second, a ^{81}Br SSNMR line shape using the known ^{81}Br EFG and CS tensor parameters was generated using second-order perturbation theory and compared to the observed ^{81}Br SSNMR spectrum at 9.4 T (Figure 9.8b). It can be immediately stated that the second-order perturbation theory simulation using the known correct parameters from Tables 3.1 and 3.2 is slightly broader than the experimental spectrum, and is also nonuniformly shifted to a lower frequency. When attempting to fit the data using second-order perturbation theory, it is seen that the $C_Q(^{81}\text{Br})$ value is somewhat underestimated (just below the lower boundary of the measurement error), while the chemical shift is actually overestimated by nearly 200 ppm (Table 9.2). While the former observation is consistent with that observed for the $I = 5/2$ cases considered earlier, the later observation is opposite to what is normally seen for modest HOQIE

on the spectra for $I = 5/2$. Line shape modeling using exact theory (Figure 9.8c) yields a spectrum that is in quantitative agreement with the observed spectrum at $B_0 = 9.4$ T (Figure 9.8d) when one uses the known correct SSNMR parameters (i.e., within the experimental measurement errors reported in Tables 3.1 and 3.2).
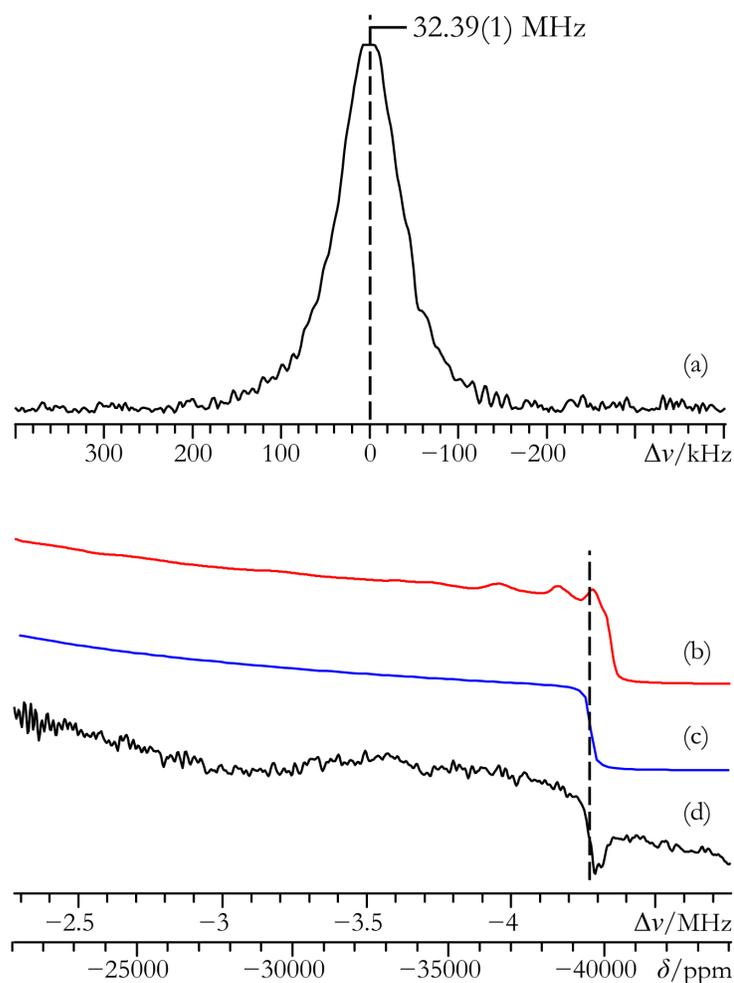
Figure 9.8 Experimental ^{81}Br NQR spectrum of CaBr$_2$ (a). The transition frequency is listed above the spectrum. Analytical simulation (b), best-fit QUEST exact simulation (c), and experimental static VOCS Solomon echo (d) ^{81}Br SSNMR spectrum of powdered CaBr$_2$ at $B_0 = 9.4$ T. Please note in (b – d) that only the low-frequency portion of the total VOCS spectrum is shown, in order to highlight the modest HOQIE for $I = 3/2$ at this applied field (i.e., the deviation from the dashed guide line).

Table 9.2 Experimental ^{81}Br EFG tensor and δ_{iso} values for CaBr$_2$ at B_0 = 9.4 T^a

method	$|C_Q(^{81}Br)|$ / MHz	η_Q	δ_{iso} ^{b} / ppm
2nd-order perturbation	62.35(30)	0.445	470(100)
exact theory	62.75(30)	0.445	280(100)
known correct values^c	62.8(4)	0.445(20)	280(50)

^{a} Error bounds are in parentheses. Values correspond to the *best-fit* parameters extracted from line shape modeling using the method specified in column 1. All parameters not specified here remain as disclosed originally in Tables 3.1 and 3.2.
^{b} With respect to solid KBr ($\delta_{iso}(^{81}Br)$ = 0.00 ppm).
^{c} As reported in Chapter 3 and consistent with ^{81}Br NQR measurements.

9.2.2 Tantalum-181 SSNMR (I = 7/2)

Examples of ^{181}Ta SSNMR are very few, even when compared to the scant prior literature on the $^{185/187}Re$ nuclides.[12] It can be reasonably assumed that this is due to the very large Q value for tantalum-181 ($Q(^{181}Ta)$ = 3170(20) mb),[13] as well as the somewhat low γ value,[14] although fortunately the ^{181}Ta nuclide is nearly 100 % naturally abundant. Indeed, ^{181}Ta SSNMR experiments are expected to remain highly challenging at even very high applied fields. However, perhaps with carefully selected samples, important observations and insights may be made.

Presently, the only ^{181}Ta SSNMR spectrum with reasonable S/N has been acquired on KTaO$_3$ (Figure 9.9), which is known to possess a cubic structure. Additional ^{181}Ta SSNMR experiments have been performed on LiTaO$_3$ (not shown), but the line shape associated with the latter species was rather featureless and therefore could not be interpreted. According to some literature reports,[15] LiTaO$_3$ is substantially disordered, which would lead to a distribution of C_Q values and greatly aids in the rationalization of the observed ^{181}Ta SSNMR line shape. Additional tantalum-containing oxide materials are being considered for study using ^{181}Ta SSNMR experiments.
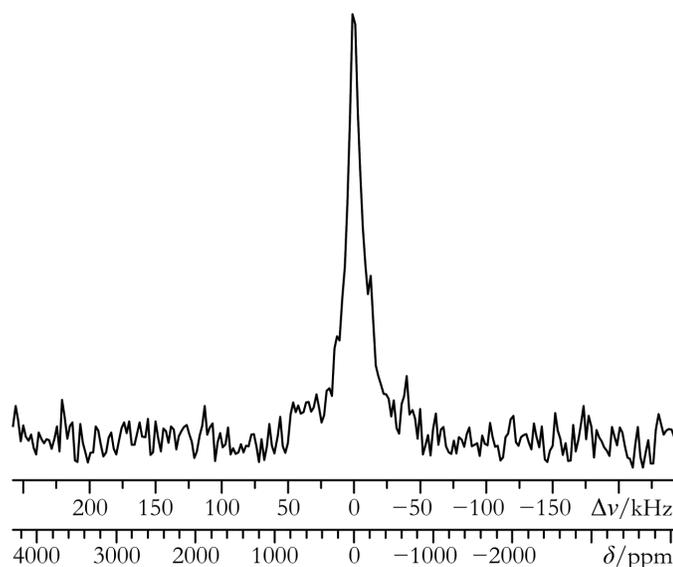
Figure 9.9 Experimental static Hahn echo ^{181}Ta SSNMR spectrum of powdered KTaO$_3$ acquired at B_0 = 11.75 T.

9.3 Probing Important Supramolecular Structures via ^{127}I SSNMR

As enumerated in Chapter 7, while rather simple systems are used during the initial development phases of a particular nuclides' SSNMR spectroscopy methods, it would be very interesting to perform SSNMR experiments upon systems which are of commercial/industrial importance. A recent area of much interest has been that of halogen bonding,[16,17] which is loosely defined as the intermolecular interaction between a halogen atom and some electron donating species. One particular example of an electron donating species is a halide anion. Early evidence of the importance of halide-halogen interactions was provided by Metrangolo *et al.* in a very high-impact publication.[18] They demonstrated that bis(trimethylammonium) alkane diiodides could encapsulate certain types of diiodoperfluoroalkanes and that the organization of the resulting product material was driven by the formation of a "I$^-$···I(CF$_2$)$_n$I···I$^-$ superanion" which involves halogen bonding interactions.[18]

As part of a more general study in the Bryce lab on the importance of these halogen bonding interactions in directing supramolecular structures,[19] a collaboration has been established with the group of Metrangolo and co-workers. They have provided several samples for study, and very preliminary findings are presented, which clearly establish that the observation of the iodide anions involved in these halogen bonding interactions is possible via [127]I SSNMR experiments (Figure 9.10 and Table 9.3).
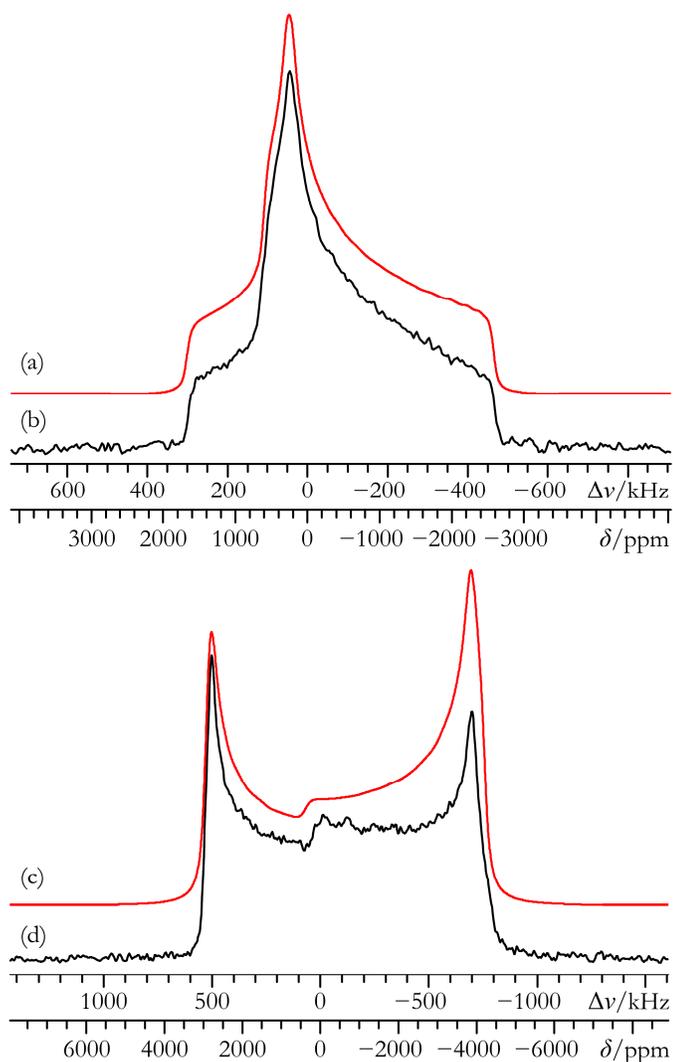
Figure 9.10 Tentative best-fit analytical simulations (a, c), and experimental static VOCS Solomon echo [127]I{^{1}H} SSNMR spectra of the supramolecular complexes **(1)** (b) and **(2)** (d) acquired at B_0 = 21.1 T. Complex specifications can be found in Table 9.3.

Table 9.3 Experimental ^{127}I EFG tensor parameters and δ_{iso} values for iodide-containing supramolecular materials[a]

compound[b]	$\|C_Q(^{127}I)\|$ / MHz	η_Q	δ_{iso}[c] / ppm
[IN(CH$_3$)$_3$(C$_{10}$H$_{20}$)(CH$_3$)$_3$NI][C$_6$F$_4$Br$_2$], **(1)**	48.3(5)	0.98(2)	250(25)
[IN(CH$_3$)$_3$(C$_{10}$H$_{20}$)(CH$_3$)$_3$NI][C$_6$H$_4$I$_2$], **(2)**	84.8(6)	0.04(2)	380(40)

[a] Error bounds are in parentheses.
[b] The observed species are denoted in italics.
[c] With respect to 0.1 mol/dm^3 KI in D$_2$O ($\delta_{iso}(^{127}I) = 0.0$ ppm).

Briefly, the availability of a very high B_0 (i.e., 21.1 T) has greatly facilitated the observation of the ^{127}I SSNMR spectra where iodide anions are involved in important halogen bonding interactions. Although not fully understood at the present time, it is highly interesting to note the drastic change in the value of η_Q between the two examples provided, especially as the structural changes should be somewhat modest (i.e., in both cases there is a bis(trimethylammonium) alkane diiodide and a C$_6$X$_4$Y$_2$ (X = H, F; Y = Br, I) unit assembled in a 1:1 stoichiometry, see Figure 9.11 for the unit cell and local iodide environment of **(2)**).[20] Clearly, the identity of the halogen involved in the halogen-halide bonding interaction is of critical importance (i.e., I vs. Br). In addition, as some of the X atoms of the C$_6$X$_4$Y$_2$ ring and the iodide are nearby, it is fully possible that the augmentation in the observed ^{127}I EFG tensor parameters between these two compounds is due to the exchanging of F atoms for H atoms, which would allow for the presence of hydrogen bonding interactions in the latter. This delicate balance between halogen and hydrogen bonding is of substantial significance in the organization of many supramolecular structures;[21] however, the ability of SSNMR experiments to make clear distinctions between the two (if it is even possible?) remains a tremendous challenge and is of ongoing interest in the Bryce group.
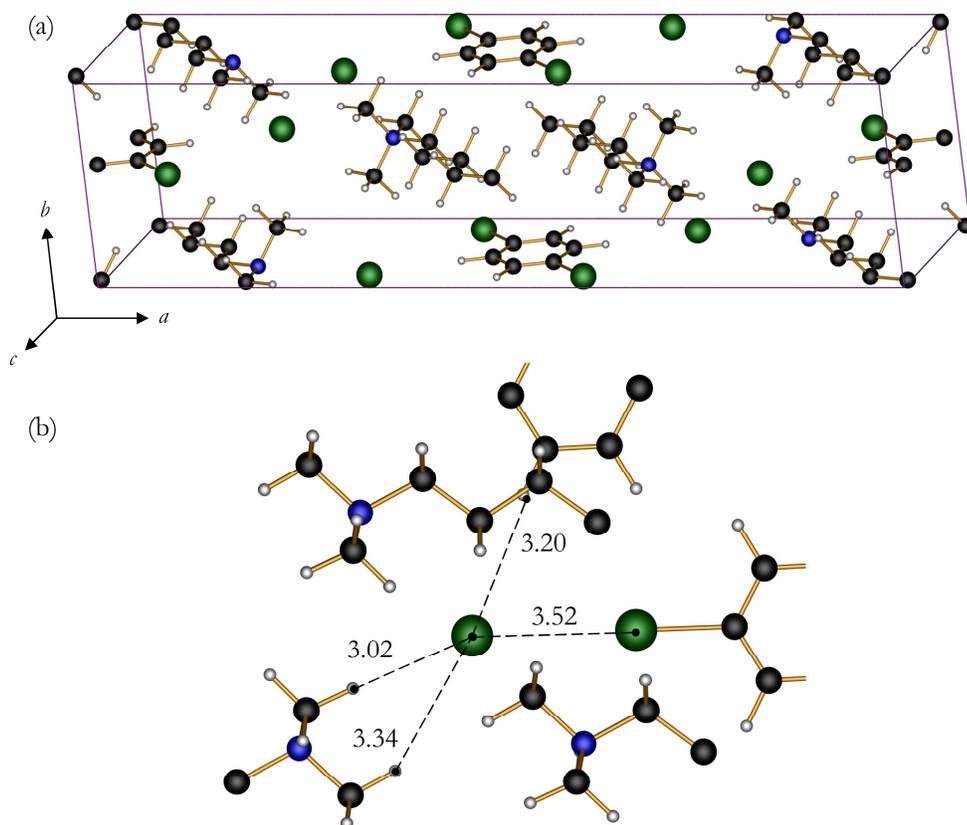
Figure 9.11 POV-ray renderings of (a) the unit cell of **(2)**, and (b) the local structure about the iodide anions in **(2)**. The following colour and labeling scheme is used: I = green; N = blue; C = black; H = white. In (b), the black dashed lines highlight some of the important interactions within 3.52 Å of the iodide anion (internuclear distances are specified near the dashed lines, in Å). Within this distance, there are 10 H contacts (3 are shown) and 1 halogen bonding interaction with the iodine atom from the diiodobenzene molecule. The crystal structure for **(1)** is currently unknown.

9.4 References

1 Y. Do, E. D. Simhon and R. H. Holm, *Inorg. Chem.*, **1985**, *24*, 4635-4642.

2 A. Müller, E. Krickemeyer, H. Bögge, M. Penk and D. Rehder, *Chimia*, **1986**, *40*, 50-52.

3 R. Benn, K. Cibura, P. Hofmann, K. Jonas and A. Rufińska, *Organometallics*, **1985**, *4*, 2214-2221.

4 K. J. Ooms, V. V. Terskikh and R. E. Wasylishen, *J. Am. Chem. Soc.*, **2007**, *129*, 6704-6705.

5   P. Crewdson, D. L. Bryce, F. Rominger and P. Hofmann, *Angew. Chem. Int. Ed.*, **2008**, *47*, 3454-3457.

6   K. J. Ooms, G. M. Bernard, A. Kadziola, P. Kofod and R. E. Wasylishen, *Phys. Chem. Chem. Phys.*, **2009**, *11*, 2690-2699.

7   R. K. Harris, E. D. Becker, S. M. Cabral De Menezes, P. Granger, R. E. Hoffman and K. W. Zilm, *Pure Appl. Chem.*, **2008**, *80*, 59-84.

8   A. Narath and D. C. Barham, *Phys. Rev.*, **1968**, *176*, 479-483.

9   M. T. Rogers and K. V. S. R. Rao, *J. Chem. Phys.*, **1968**, *49*, 1229-1231.

10   F. P. Perras, private communication, **2011**.

11   C. B. Harris, *Inorg. Chem.*, **1968**, *7*, 1691-1692.

12   O. B. Lapina, D. F. Khabibulin, A. A. Shubin and V. V. Terskikh, *Prog. Nucl. Magn. Reson. Spectrosc.*, **2008**, *53*, 128-191.

13   P. Pyykkö, *Mol. Phys.*, **2008**, *106*, 1965-1974.

14   R. K. Harris, E. D. Becker, S. M. Cabral De Menezes, R. Goodfellow and P. Granger, *Pure Appl. Chem.*, **2001**, *73*, 1795-1818.

15   A. P. Zhukov, L. V. Soboleva, L. M. Belyaev and A. F. Volkov, *Ferroelectrics*, **1978**, *21*, 601-604.

16   P. Metrangolo and G. Resnati, *Chem. Eur. J.*, **2001**, *1*, 2511-2519.

17   P. Metrangolo, F. Meyer, T. Pilati, G. Resnati and G. Terraneo, *Angew. Chem. Int. Ed.*, **2008**, *47*, 6114-6127.

18   P. Metrangolo, Y. Carcenac, M. Lahtinen, T. Pilati, K. Rissanen, A. Vij and G. Resnati, *Science*, **2009**, *323*, 1461-1464.

19   J. Viger-Gravel, I. Korobkov and D. L. Bryce, *Cryst. Growth Des.*, **2011**, *11*, 4984-4995.

20   P. Metrangolo, private communication, **2010**.

21   A. R. Voth, P. Khuu, K. Oishi and P. S. Ho, *Nature Chem.*, **1**, *2009*, 74-79.

Appendix A

Appendix to Chapter Three

Table A.1 Detailed $^{79/81}$Br SSNMR experimental acquisition parameters[a]

B_0 / T	^AX	window[b] / kHz	points[c]	$\pi/2$[d] / μs	scans	recycle delay / s	$\tau_1;\tau_2$[e] / μs	details
					CaBr$_2$			
11.75	^{81}Br	625	26 598	1.7	2 176	0.3	60;60;60;60	static; VOCS QCPMG; 201 MG loops; 74 pieces; offset = 86.31 kHz
21.1	^{79}Br	2 000	2 048	1.2	4 000	0.5	150;10	static; VOCS Solomon whole echo; 20 pieces; offset = 250 kHz
21.1	^{81}Br	2 000	2 048	1.0	4 096	0.5	100;10	static; VOCS Solomon whole echo; 14 pieces; offset = 300 kHz
					SrBr$_2$			
11.75	^{79}Br	2 000	2 048	1.0	16 384	0.3	150;10	static; VOCS Solomon whole echo; broadest signal not acquired; 8 pieces; offset = 300 kHz
11.75	^{81}Br	2 000	2 048	1.1	14 400	0.3	150;10	static; VOCS Solomon whole echo; broadest signal not acquired; 8 pieces; offset = 200 kHz
21.1	^{79}Br	2 000	2 048	1.2	4 096	0.4	250;10	static; VOCS Solomon whole echo; 16 pieces; offset = 250 kHz
21.1	^{81}Br	2 000	2 048	1.0	4 096	0.4	250;10	static; VOCS Solomon whole echo; 9 pieces; offset = 300 kHz
					BaBr$_2$			
11.75	^{79}Br	2 000	2 048	1.0	52 000	0.4	250;10	static; VOCS Solomon whole echo; 5 pieces; offset = 300 kHz
11.75	^{81}Br	2 000	2 048	1.2	32 768	0.4	250;10	static; VOCS Solomon whole echo; 4 pieces; offset = 325 kHz
21.1	^{79}Br	2 000	4 096	1.2	4 096	0.5	500;1	static; VOCS Solomon whole echo; 2 pieces; offset = 250 kHz
21.1	^{81}Br	1 000	2 048	1.0	32 768	0.5	500;1	static; Solomon whole echo
					MgBr$_2$·6H$_2$O			
11.75	^{79}Br	2 000	2 048	1.1	65 536	0.7	250;10	static; VOCS Solomon whole echo; 2 pieces; offset = 400 kHz; ν_1(^{1}H) = 40 kHz
11.75	^{81}Br	2 000	4 096	1.1	53 400	0.7	400;10	static; Solomon whole echo; ν_1(^{1}H) = 40 kHz
21.1	^{79}Br	2 000	2 048	1.0	2 048	0.4	200;10	static; Solomon whole echo
21.1	^{81}Br	2 000	2 048	1.0	2 000	0.8	200;10	static; Solomon whole echo; ν_1(^{1}H) = 100 kHz

B_0 / T	^AX	window[b] / kHz	points[c]	$\pi/2$[d] / μs	scans	recycle delay / s	$\tau_1;\tau_2$[e] / μs	details
					SrBr$_2$·6H$_2$O				
11.75	^{79}Br	2 000	2 048	1.1	16 384	0.4	40;20	static; VOCS Solomon half echo; 5 pieces; offset = 300 kHz
11.75	^{81}Br	2 000	1 024	1.2	14 400	0.5	40;20	static; VOCS Solomon half echo; 5 pieces; offset = 300 kHz
21.1	^{79}Br	2 000	2 048	1.2	4 096	0.5	100;10	static; VOCS Solomon half echo; 2 pieces; offset = 280 kHz
21.1	^{81}Br	2 000	2 048	1.0	1 024	0.5	100;0	static; Solomon half echo; $\nu_1(^1$H) = 100 kHz
					BaBr$_2$·2H$_2$O				
11.75	^{79}Br	400	1 024	2.1	8 192	0.4	60;50	static; Solomon half echo; $\nu_1(^1$H) = 40 kHz
11.75	^{81}Br	400	1 024	3.0	4 096	0.4	50;40	static; Solomon half echo; $\nu_1(^1$H) = 40 kHz
21.1	^{79}Br	500	1 024	1.9	2 048	0.5	26;0	static; Solomon half echo; $\nu_1(^1$H) = 100 kHz
21.1	^{79}Br	250	2 048	1.6	4 096	0.75	36.4;6.4	MAS; Solomon half echo; ν_{MAS} = 26.318 kHz; $\nu_1(^1$H) = 100 kHz
21.1	^{81}Br	500	1 024	2.0	1 000	0.5	26;0	static; Solomon half echo; $\nu_1(^1$H) = 100 kHz
21.1	^{81}Br	200	2 048	1.5	1 024	0.5	48.5;0	MAS; Solomon half echo; ν_{MAS} = 20.000 kHz; $\nu_1(^1$H) = 100 kHz
					CaBr$_2$·xH$_2$O				
11.75	^{79}Br	2 000	2 048	1.0	18 700	0.5	250;10	static; VOCS Solomon whole echo; broadest signal not acquired; 5 pieces; offset = 350 kHz
11.75	^{81}Br	625	19 866	1.7	800	0.8	45;45;45;45	static; VOCS QCPMG; 150 MG loops; 52 pieces; offset = 95.90 kHz
11.75	^{81}Br	2 000	2 048	1.2	15 028	0.5	250;10	static; VOCS Solomon whole echo; broadest signal not acquired; 3 pieces; offset = 350 kHz
21.1	^{79}Br	2 000	2 048	1.2	2 048	0.5	250;10	static; VOCS Solomon whole echo; broadest signal not acquired; 2 pieces; offset = 250 kHz
21.1	^{81}Br	2 000	4 096	1.0	4 000	0.5	300;10	static; VOCS Solomon whole echo; 12 pieces; offset = 300 kHz

[a] All static experiments were carried out at room temperature. For MAS experiments, cooled N$_2$ gas was passed through the probe to compensate for the frictional heating due to sample rotation.
[b] Acquisition parameters are for each sub-spectrum, where applicable.
[c] Number of complex time-domain data points acquired.
[d] CT selective pulses.
[e] For QCPMG experiments, this column corresponds to τ_1; τ_2; τ_3; τ_4.

Table A.2 GIPAW DFT computations: computed energies and structure references[a]

compound	functional	energy / eV	structure references and notes
$CaBr_2$	PBE	−3970.290480	Brackett *et al.*[1]
	PW91	−3980.612732	
$SrBr_2$	PBE	−18201.749028	Smeggil & Eick.[2]
	PW91	−18265.265086	
$BaBr_2$	PBE	−6733.787958	Brackett *et al.*[3]
	PW91	−6759.176405	
$MgBr_2 \cdot 6H_2O$	PBE	−9670.271689	Model A: heavy atom positions taken from Andress and Gundermann;[4] unit cell taken from Sorrell and Ramey;[5] H positions optimized computationally.
	PW91	−9683.751346	
	PBE	−9670.128969	Model B: heavy atom positions adjusted slightly (but within measurement errors) from Andress and Gundermann;[4] unit cell taken from Sorrell and Ramey;[5] H positions optimized computationally.
	PW91	−9683.603160	
$CaBr_2 \cdot 6H_2O$	PBE	−4810.061381	LeClaire & Borel.[6]
	PW91	−4816.525411	
$SrBr_2 \cdot 6H_2O$	PBE	−4645.028833	Model A: heavy atom positions and unit cell taken from Abrahams and Vordemvenne;[7] H positions optimized computationally, starting from those in $SrCl_2 \cdot 6H_2O$, as reported by Agron and Busing.[8]
	PW91	−4654.985229	
	PBE	−4645.330842	Model B: heavy atom positions and unit cell taken from Abrahams and Vordemvenne,[7] except the *c* value for the bromide is altered to −*c*; H positions optimized computationally, starting from those in $SrCl_2 \cdot 6H_2O$, as reported by Agron and Busing.[8]
	PW91	−4655.291209	
$BaBr_2 \cdot 2H_2O$	PBE	−10500.220328	Kellersohn *et al.*[9]
	PW91	−10530.421271	

[a] Crystal structure parameters used for GIPAW DFT NMR computations can be found in Table A.3. Information on the bromine otfg pseudopotential: (i) core states include $1s^2 2s^2 2p^6 3s^2 3p^6 3d^{10}$; valence states include $4s^2 4p^5$; (ii) the local channel is chosen to be *d*; (iii) the pseudisation radius for local and non-local channels is 2.0 a.u.; (iv) the pseudisation radius for augmentation functions is 1.4 a.u.; (v) augmentation charge and partial core correction are 1.401 a.u.; (vi) the string used for the generation of the pseudopotential, in the format used by Materials Studio is "2|2.0|2.0|1.4|3|4|5|40:41(qc=4)#[]" (see http://www.tcm.phy.cam.ac.uk/castep/usp-string-notes.txt and http://www.tcm.phy.cam.ac.uk/castep/otfg.pdf for further explanation).

Table A.3 GIPAW DFT computations: crystal structure parameters used for NMR parameter computations

compound	atom	Wyckoff site	local symmetry	$v_a{}^a$	$v_b{}^a$	$v_c{}^a$
CaBr$_2$[b]	Ca	2a	..2/m	0.0000	0.0000	0.0000
	Br	4g	..m	0.2636	0.3417	0.0000
	Br	4g	..m	0.7364	0.6583	0.0000
SrBr$_2$[c]	Sr	8g	1	0.8545	0.8356	0.2476
	Sr	2c	4..	0.0000	0.5000	0.8483
	Br(1)	2b	$\overline{4}$..	0.0000	0.0000	0.5000
	Br(2)	2a	$\overline{4}$..	0.0000	0.0000	0.0000
	Br(3)	8g	1	0.0888	0.7072	0.0963
	Br(4)	8g	1	0.9031	0.7090	0.6258
BaBr$_2$[d]	Ba	4c	.m.	0.2447	0.2500	0.1149
	Br(1)	4c	.m.	0.0284	0.2500	0.8401
	Br(2)	4c	.m.	0.1422	0.2500	0.4272
MgBr$_2$·6H$_2$O[e]	Mg	2a	2/m	0.0000	0.0000	0.0000
(model A)	Br	4i	m	0.3180	0.0000	0.6150
	O	4i	m	0.2000	0.0000	0.1100
	O	8j	1	0.9600	0.2000	0.2250
	H	8j	1	0.5222	0.7943	0.2807
	H	8j	1	0.3861	0.6956	0.3183
	H	4i	m	0.7695	0.5000	0.0078
	H	4i	m	0.7397	0.5000	0.2588
MgBr$_2$·6H$_2$O[e]	Mg	2a	2/m	0.0000	0.0000	0.0000
(model B)	Br	4i	m	0.3200	0.0000	0.6150
	O	4i	m	0.2000	0.0000	0.1150
	O	8j	1	0.9600	0.2050	0.2300
	H	8j	1	0.5230	0.7986	0.2853
	H	8j	1	0.3868	0.7007	0.3245
	H	4i	m	0.7697	0.5000	0.0112
	H	4i	m	0.7395	0.5000	0.2620
CaBr$_2$·6H$_2$O[f]	Ca	1a	32.	0.0000	0.0000	0.0000
	Br	2d	3..	0.3333	0.6667	0.4435
	O	3f	.2.	−0.2065	0.0000	0.5000
	O	3e	.2.	0.3021	0.0000	0.0000
	H	6g	1	−0.2192	0.1131	0.4925
	H	6g	1	0.4233	0.1039	−0.0791
SrBr$_2$·6H$_2$O[g]	Sr	1a	32.	0.0000	0.0000	0.0000

compound	atom	Wyckoff site	local symmetry	$v_a{}^a$	$v_b{}^a$	$v_c{}^a$
(model A)	Br	2d	3..	0.3333	0.6667	−0.4405
	O	3f	.2.	0.7874	0.0000	0.5000
	O	3e	.2.	0.3112	0.0000	0.0000
	H	6g	1	0.4324	0.0974	−0.0884
	H	6g	1	−0.2326	0.1090	0.4699
$SrBr_2 \cdot 6H_2O^g$	Sr	1a	32.	0.0000	0.0000	0.0000
(model B)	Br	2d	3..	0.3333	0.6667	0.4405
	O	3f	.2.	0.7874	0.0000	0.5000
	O	3e	.2.	0.3112	0.0000	0.0000
	H	6g	1	0.4310	0.0954	-0.0987
	H	6g	1	−0.2320	0.1097	0.4822
$BaBr_2 \cdot 2H_2O^b$	Ba	4e	2	0.0000	0.1009	0.2500
	Br	8f	1	0.2171	0.4710	0.3492
	O	8f	1	0.0098	0.7608	0.4428
	H	8f	1	0.0880	0.6855	0.4552
	H	8f	1	0.9302	0.6871	0.3739

[a] The values within these columns are in fractional unit cell coordinates.

[b] $Pnnm$ (№. 58); orthorhombic; a = 6.584 Å; b = 6.871 Å; c = 4.342 Å; $\alpha_C = \beta_C = \gamma_C = 90°$.

[c] $P4/n$ (№. 85); tetragonal; $a = b$ = 11.630 Å; c = 7.146 Å; $\alpha_C = \beta_C = \gamma_C = 90°$.

[d] $Pnma$ (№. 62); orthorhombic; a = 8.276 Å; b = 4.956 Å; c = 9.919 Å; $\alpha_C = \beta_C = \gamma_C = 90°$.

[e] $C2/m$ (№. 12); monoclinic; a = 10.290 Å; b = 7.334 Å; c = 6.211 Å; $\alpha_C = \gamma_C = 90°$; $\beta_C = 93.25°$. H positions are computationally optimized.

[f] $P321$ (№. 150); trigonal; $a = b$ = 8.164 Å; c = 4.016 Å; $\alpha_C = \beta_C = 90°$; $\gamma_C = 120°$.

[g] $P321$ (№. 150); trigonal; $a = b$ = 8.204 Å; c = 4.159 Å; $\alpha_C = \beta_C = 90°$; $\gamma_C = 120°$. H positions are computationally optimized.

[h] $C2/c$ (№. 15); monoclinic; a = 10.429 Å; b = 7.195 Å; c = 8.375 Å; $\alpha_C = \gamma_C = 90°$; $\beta_C = 113.60°$.
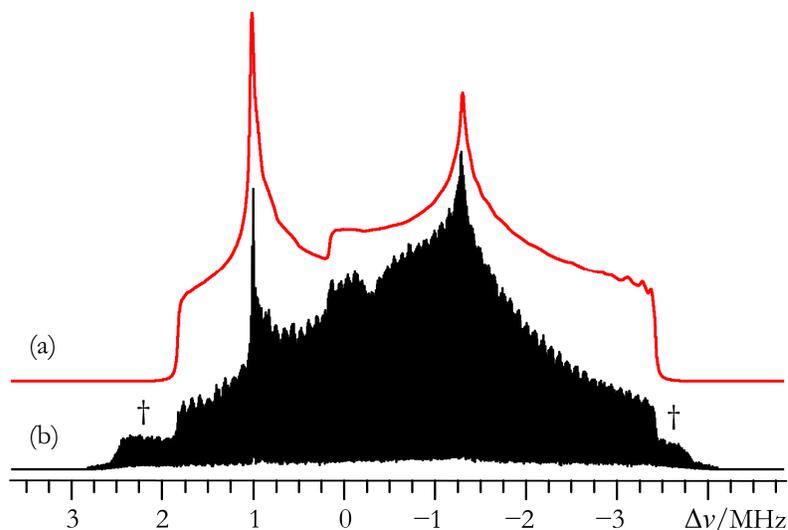
Figure A.1 Best-fit analytical simulation (a), and experimental static VOCS QCPMG ^{81}Br SSNMR spectrum of powdered CaBr$_2$ acquired at B_0 = 11.75 T (b). Partially excited ST are denoted using "†". CSA was neglected in the line shape simulation, but the $\ddot{V}$ tensor parameters agree quantitatively with those measured at B_0 = 21.1 T.

Table A.4 Input parameters for calculations involving isomorphic bromides and chlorides

compound A	compound B	$Q(^{35}Cl)$ / $\times 10^{-29}$ m²	$Q(^{81}Br)$ / $\times 10^{-29}$ m²	$(1 - \gamma_\infty)$ (^{35}Cl)	$(1 - \gamma_\infty)$ (^{81}Br)	V_A / Å³	V_B / Å³
CaCl$_2$	CaBr$_2$	-0.8165^a	2.62	43.0^b	81	168.52^c	196.43
BaCl$_2$	BaBr$_2$	-0.8165	2.62	43.0	81	350.55^d	406.84
MgCl$_2$·6H$_2$O	MgBr$_2$·6H$_2$O	-0.8165	2.62	43.0	81	424.74^e	467.97
SrCl$_2$·6H$_2$O	SrBr$_2$·6H$_2$O	-0.8165	2.62	43.0	81	226.29^f	242.42

[a] All Q values are from ref. 10.
[b] All $(1 - \gamma_\infty)$ values are from ref. 11.
[c] From ref. 12.
[d] From ref. 3.
[e] From ref. 13.
[f] From ref. 8.
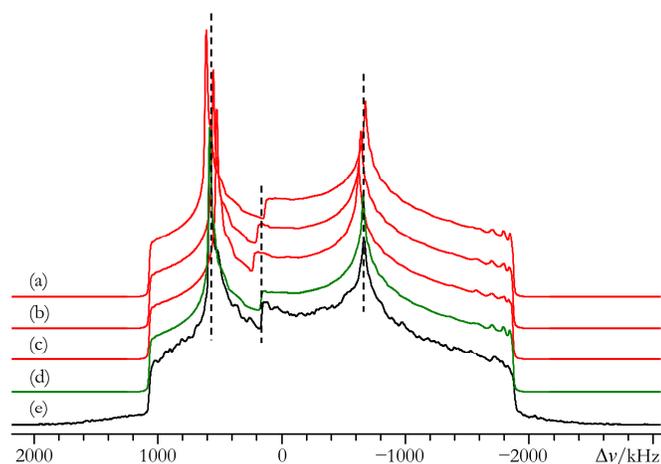
Figure A.2 Analytical simulations (a – d), and experimental static VOCS Solomon echo ^{81}Br SSNMR spectrum of powdered CaBr$_2$ acquired at B_0 = 21.1 T (e), which highlight the effect of Ω variation upon the ^{81}Br SSNMR line shape. The following values are used for Ω, while all other parameters remain as reported in Tables 3.1 and 3.2: (a) Ω = 0 ppm; (b) Ω = 500 ppm; (c) Ω = 750 ppm; (d) Ω = 250 ppm. Dashed lines highlight key line shape features which are dependent upon the Ω value.
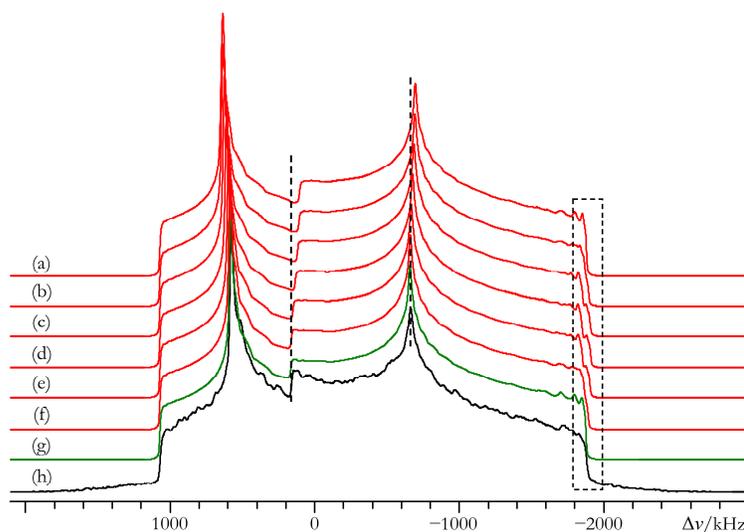
Figure A.3 Analytical simulations (a – g), and experimental static VOCS Solomon echo ^{81}Br SSNMR spectrum of powdered CaBr$_2$ acquired at B_0 = 21.1 T (h), which highlight selected effects of β variation upon the ^{81}Br SSNMR line shape. The following β values are used, while all other parameters remain as in Tables 3.1 and 3.2: (a) β = 0°; (b) β = 15°; (c) β = 30°; (d) β = 45°; (e) β = 60°; (f) β = 75°; (g) β = 90°. The dashed lines and boxed region highlight line shape features which depend upon the β value.
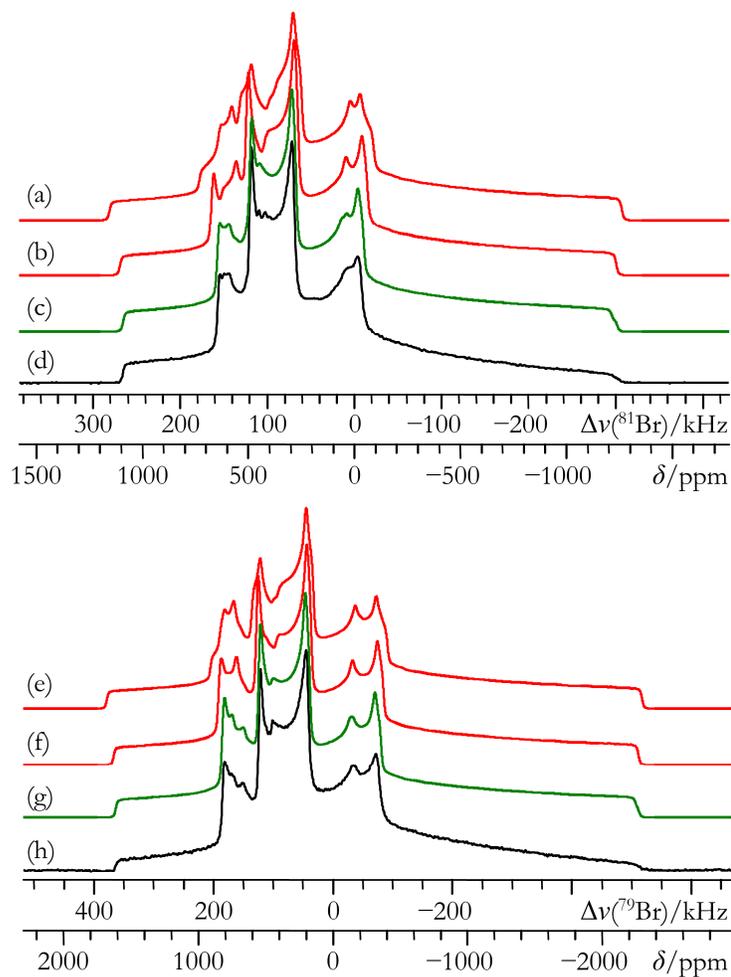
Figure A.4 Analytical simulations (a – c; e – g), and experimental static VOCS Solomon echo (d, h) $^{79/81}$Br SSNMR spectra of three of the four magnetically unique bromine sites in powdered SrBr$_2$ acquired at B_0 = 21.1 T. To highlight the importance of including both CSA and nonzero Euler angles within the line shape fitting analysis, (a) and (e) set $\alpha = \beta = \gamma = 0°$, (b) and (f) neglect CSA entirely (Ω = 0 ppm), while (c) and (g) include both CSA and nonzero Euler angle effects.
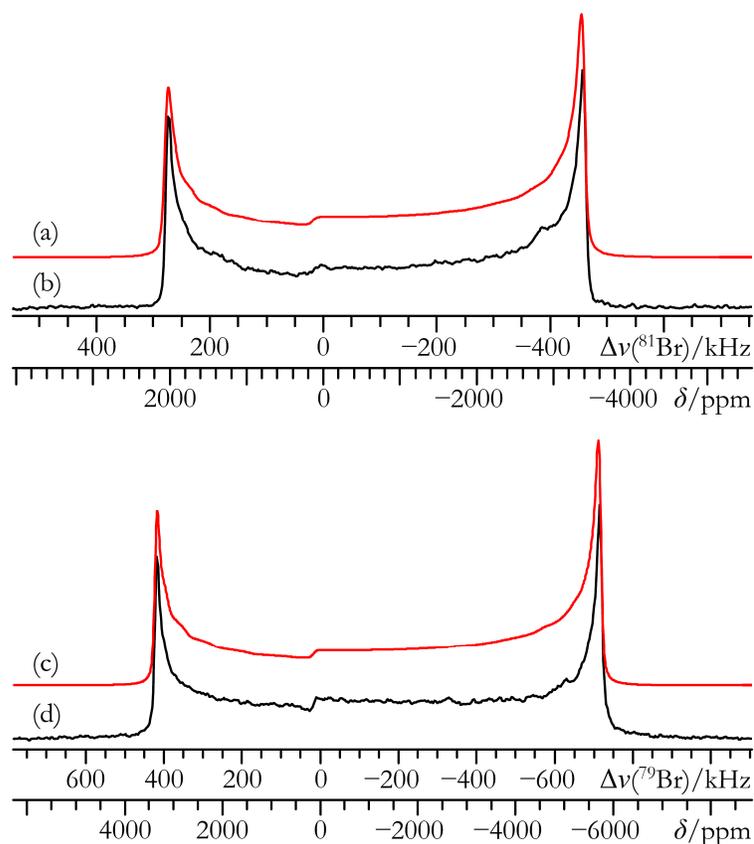
Figure A.5 Best-fit analytical simulations (a, c), and experimental static VOCS Solomon echo (b, d) $^{79/81}$Br SSNMR spectra of powdered $SrBr_2 \cdot 6H_2O$ acquired at $B_0 = 11.75$ T. As a test, the experimental spectra were acquired without ^{1}H decoupling and therefore 2 100 Hz of dipolar broadening has been applied to the simulated spectra (since $r_{H\text{-}Br}$ = ca. 2.5 Å). The differences between simulations including dipolar broadening, versus those which did not, are within measurement errors.
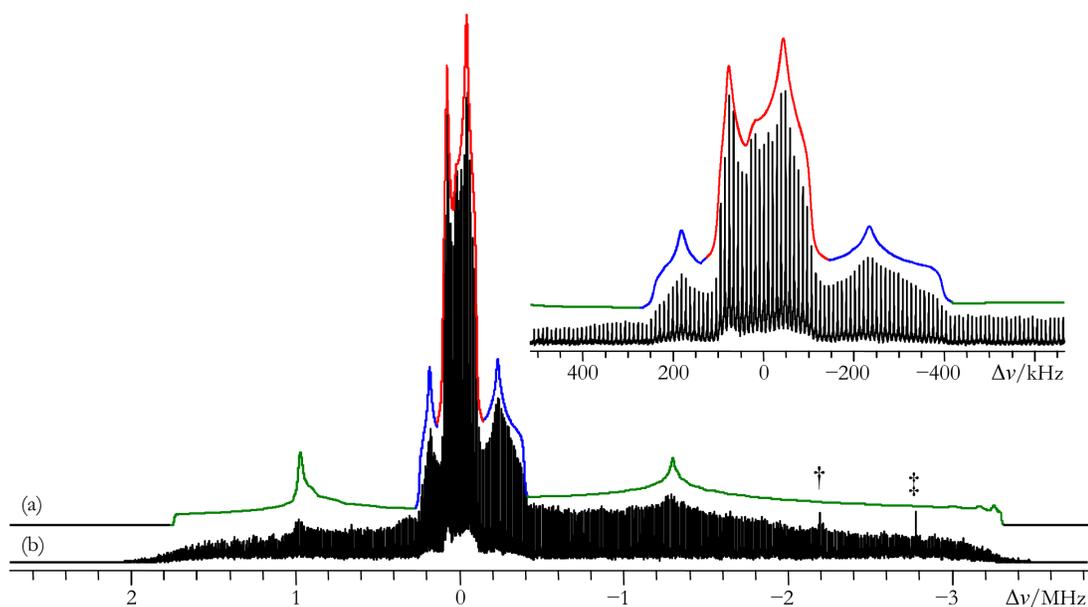
Figure A.6 Analytical simulation (a), and experimental static VOCS QCPMG (b) ^{81}Br SSNMR spectrum of powdered CaBr$_2\cdot x$H$_2$O acquired at B_0 = 11.75 T. The † and ‡ symbols denote NMR signals from ^{63}Cu within the receiving coil, and from ^{23}Na from NaBr, respectively. Inset: central region of the spectrum, highlighting the loss in resolution relative to the VOCS Solomon echo ^{81}Br SSNMR spectrum of the same mixture (see Figure 3.16).
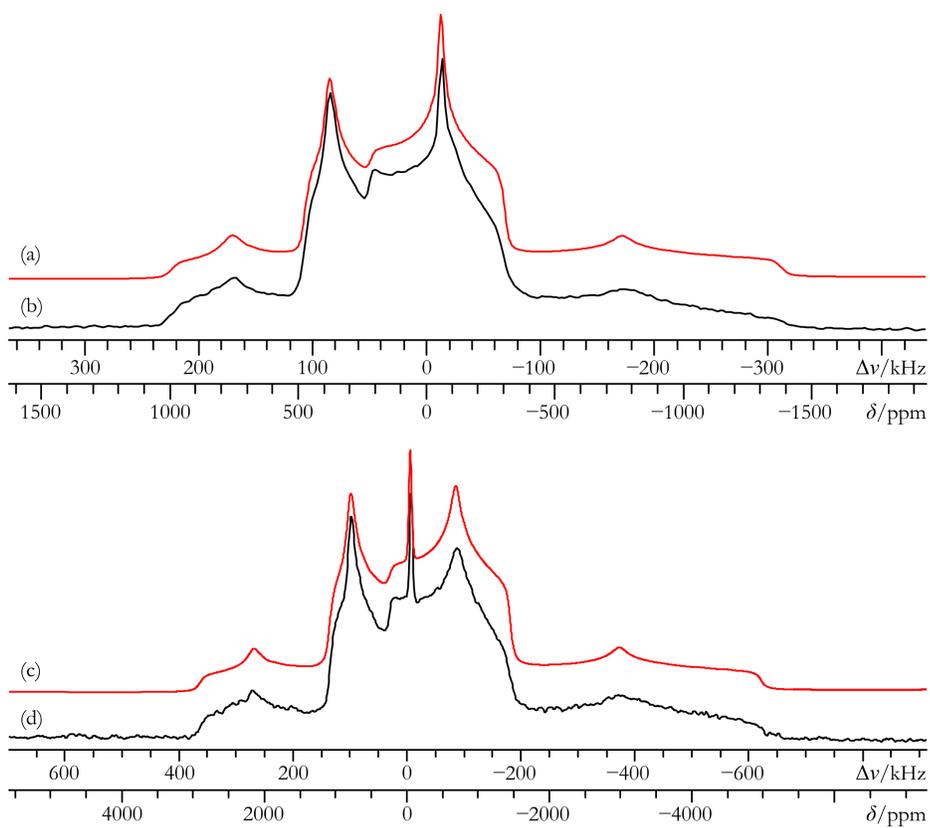
Figure A.7 Analytical simulations (a, c), and experimental static VOCS Solomon echo (b, d) [79]Br SSNMR spectra of the three central signals in powdered $CaBr_2 \cdot xH_2O$. Spectra were acquired at (b) $B_0 = 21.1$ T and (d) $B_0 = 11.75$ T.

Table A.5 GIPAW DFT ^{81}Br EFG tensor parameters: MBr$_2$ systems, additional information[a]

compound	functional	site label	V_{11} / a.u.	V_{22} / a.u.	V_{33} / a.u.	$C_Q(^{81}Br)$ / MHz	η_Q
CaBr$_2$	PBE	—	0.2829	0.8403	−1.1232	−69.15	0.496
	PW91	—	0.2837	0.8458	−1.1295	−69.53	0.498
SrBr$_2$	PBE	Br(1)	0.0796	0.0796	−0.1592	−9.80	0.000
		Br(2)	0.1439	0.1439	−0.2878	−17.72	0.000
		Br(3)	0.0381	0.4031	−0.4412	−27.16	0.827
		Br(4)	0.3453	0.6364	−0.9817	−60.43	0.297
	PW91	Br(1)	0.0799	0.0799	−0.1597	−9.83	0.000
		Br(2)	0.1448	0.1448	−0.2895	−17.82	0.000
		Br(3)	0.0360	0.4062	−0.4422	−27.22	0.837
		Br(4)	0.3471	0.6415	−0.9886	−60.86	0.298
BaBr$_2$	PBE	Br(1)	0.1509	0.1819	−0.3329	−20.49	0.093
		Br(2)	−0.2350	−0.2770	0.5120	31.52	0.082
	PW91	Br(1)	0.1509	0.1837	−0.3346	−20.60	0.098
		Br(2)	−0.2365	−0.2786	0.5151	31.71	0.082

[a] Parameter definitions are in Section 2.3.3.2. Additional details may be found in Table 3.5.

Table A.6 GIPAW DFT bromine CS tensor parameters: MBr$_2$ systems, additional information[a]

compound	functional	site label	σ_{11} / ppm	σ_{22} / ppm	σ_{33} / ppm	δ_{iso} / ppm	Ω / ppm	κ	α, β, γ / °
CaBr$_2$	PBE	—	2065.77	2229.95	2416.84	390.4	351.1	0.06	270.0, 89.5, 180.0
	PW91	—	2055.78	2220.68	2409.78	398.4	354.1	0.07	270.0, 89.5, 180.0
SrBr$_2$	PBE	Br(1)	2102.24	2160.20	2160.20	487.3	58.0	−1.00	90.0, 90.0, 180.0
		Br(2)	2091.93	2202.13	2202.13	462.7	110.2	−1.00	90.0, 90.0, 180.0
		Br(3)	2197.55	2256.57	2330.15	366.4	132.6	0.11	43.3, 88.4, 231.9
		Br(4)	2178.37	2287.01	2360.85	352.4	182.5	−0.19	242.4, 72.5, 214.5
	PW91	Br(1)	2103.62	2160.34	2160.34	486.0	56.7	−1.00	90.0, 90.0, 180.0
		Br(2)	2095.06	2202.52	2202.52	460.7	107.5	−1.00	90.0, 90.0, 180.0
		Br(3)	2201.35	2257.40	2330.10	364.2	128.8	0.13	44.3, 88.3, 233.3
		Br(4)	2182.08	2288.69	2363.12	349.1	181.0	−0.18	242.4, 72.5, 213.8
BaBr$_2$	PBE	Br(1)	2148.09	2334.74	2400.42	333.3	252.3	−0.48	0.0, 49.6, 180.0
		Br(2)	1997.72	2082.59	2206.05	532.8	208.3	0.18	180.0, 19.2, 180.0
	PW91	Br(1)	2144.34	2330.55	2397.37	336.3	253.0	−0.47	0.0, 49.6, 180.0
		Br(2)	1991.99	2077.10	2201.30	537.4	209.3	0.19	180.0, 19.4, 180.0

[a] Parameter definitions are in Sections 2.3.2.4, 2.3.3.1 and 2.3.3.3. Additional details may be found in Table 3.6.

Table A.7 GIPAW DFT ^{81}Br EFG tensor parameters: MBr_2 hydrates, additional information[a]

compound	functional	model label	V_{11} / a.u.	V_{22} / a.u.	V_{33} / a.u.	$C_Q(^{81}Br)$ / MHz	η_Q
$MgBr_2 \cdot 6H_2O$	PBE	A	−0.2112	−0.2171	0.4283	26.37	0.014
	PW91	A	−0.2075	−0.2152	0.4227	26.02	0.018
	PBE	B	−0.1800	−0.2372	0.4172	25.68	0.137
	PW91	B	−0.1784	−0.2332	0.4116	25.34	0.133
$CaBr_2 \cdot 6H_2O$	PBE	—	0.2797	0.2797	−0.5594	−34.44	0.000
	PW91	—	0.2792	0.2793	−0.5584	−34.38	0.000
$SrBr_2 \cdot 6H_2O$	PBE	A	0.1496	0.1496	−0.2992	−18.42	0.000
	PW91	A	0.1494	0.1494	−0.2988	−18.39	0.000
	PBE	B	0.3327	0.3327	−0.6655	−40.97	0.000
	PW91	B	0.3331	0.3331	−0.6662	−41.01	0.000
$BaBr_2 \cdot 2H_2O$	PBE	—	0.0429	0.0989	−0.1418	−8.73	0.395
	PW91	—	0.0435	0.1042	−0.1477	−9.09	0.411

[a] Parameter definitions are in Sections 2.3.3.2. Additional details may be found in Table 3.7.

Table A.8 GIPAW DFT bromine CS tensor parameters: MBr_2 hydrates, additional information[a]

compound	funct-ional	model label	σ_{11} / ppm	σ_{22} / ppm	σ_{33} / ppm	δ_{iso} / ppm	Ω / ppm	κ	α, β, γ / °
$MgBr_2 \cdot 6H_2O$	PBE	A	2598.85	2614.76	2658.22	3.0	59.4	0.46	0.0, 58.1, 0.0
	PW91	A	2596.80	2613.57	2657.01	3.7	60.2	0.44	0.0, 57.9, 0.0
	PBE	B	2589.62	2611.83	2653.60	8.6	64.0	0.31	270.0, 55.2, 180.0
	PW91	B	2587.46	2610.54	2652.26	9.4	64.8	0.29	270.0, 55.1, 180.0
$CaBr_2 \cdot 6H_2O$	PBE	—	2537.60	2578.57	2578.58	62.1	41.0	−1.00	247.2, 89.8, 180.2
	PW91	—	2537.11	2577.88	2577.90	62.0	40.8	−1.00	223.1, 89.9, 180.3
$SrBr_2 \cdot 6H_2O$	PBE	A	2537.94	2569.36	2569.36	68.2	31.5	−1.00	224.3, 89.9, 180.4
	PW91	A	2538.28	2569.50	2569.53	67.2	31.2	−1.00	226.6, 89.9, 180.4
	PBE	B	2532.15	2612.80	2612.83	41.1	80.7	−1.00	210.9, 90.0, 180.2
	PW91	B	2532.29	2612.85	2612.88	40.3	80.6	−1.00	212.2, 90.0, 180.2
$BaBr_2 \cdot 2H_2O$	PBE	—	2377.13	2435.31	2471.25	199.5	94.1	−0.24	61.0, 84.1, 240.7
	PW91	—	2373.36	2431.53	2467.77	202.5	94.4	−0.23	64.0, 84.5, 240.6

[a] Parameter definitions are in Sections 2.3.2.4, 2.3.3.1 and 2.3.3.3. Additional details may be found in Table 3.8.
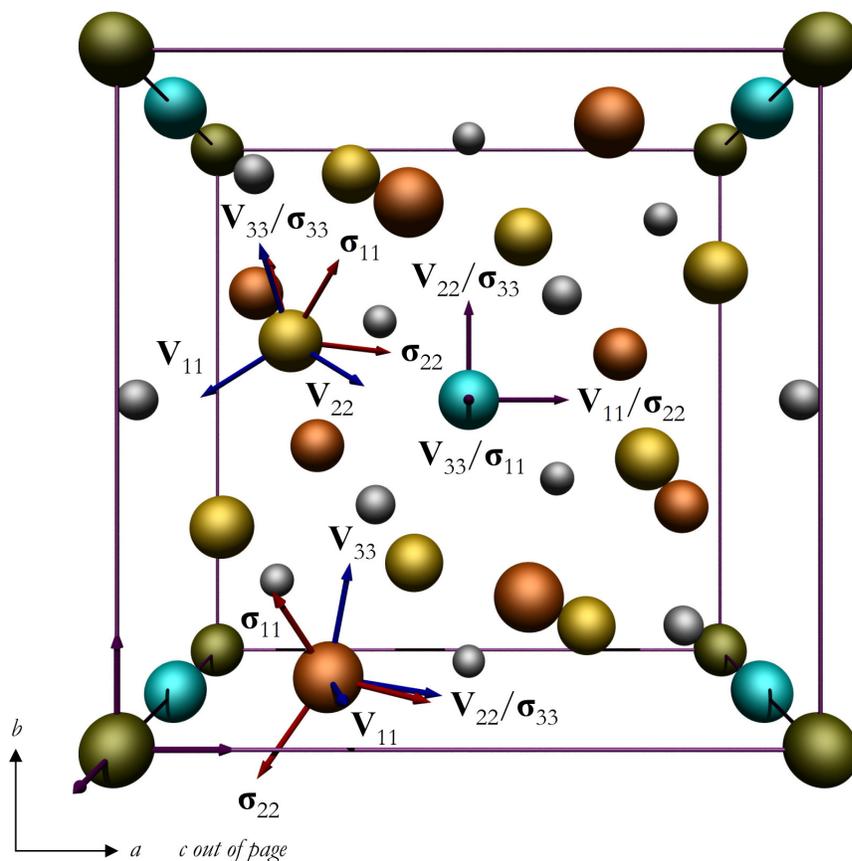
Figure A.8 POV-Ray rendering of the computed bromine $\ddot{V}$ (V_{ii}, i = 1, 2, 3, in blue) and symmetric $\ddot{\sigma}$ (σ_{ii}, red) tensor eigenvectors in the crystal frame of SrBr$_2$. Sr ions are in grey. The computations used E_{cut} = 500 eV, a 3 × 3 × 5 k-point grid, and the PBE XC functional. Where the $\ddot{V}$ and $\ddot{\sigma}$ tensor eigenvectors are coincident, a purple vector represents both. The unique bromine sites are Br(1) (turquoise), Br(2) (green), Br(3) (orange), and Br(4) (gold). Eigenvectors are displayed once per unique Br and were placed using Diamond 3.2. The Br(2) ion located at (1/2, 1/2, 1) has been removed to better show the tensor orientations for Br(1). The tensor orientations are identical for Br(1) and Br(2); hence, labels have been omitted for Br(2) to enhance clarity.
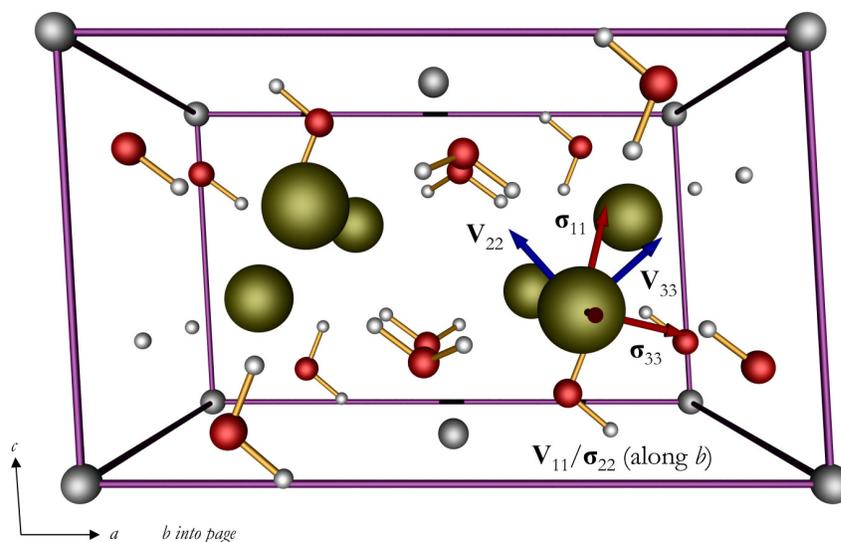
Figure A.9 POV-Ray rendering of the computed bromine $\ddot{V}$ (blue) and symmetric $\ddot{\sigma}$ (red) tensor eigenvectors in the crystal frame of $MgBr_2 \cdot 6H_2O$ (model B). The computation used $E_{cut} = 750$ eV, a $2 \times 3 \times 4$ k-point grid, and the PBE XC functional. Eigenvectors were placed using Diamond 3.2.
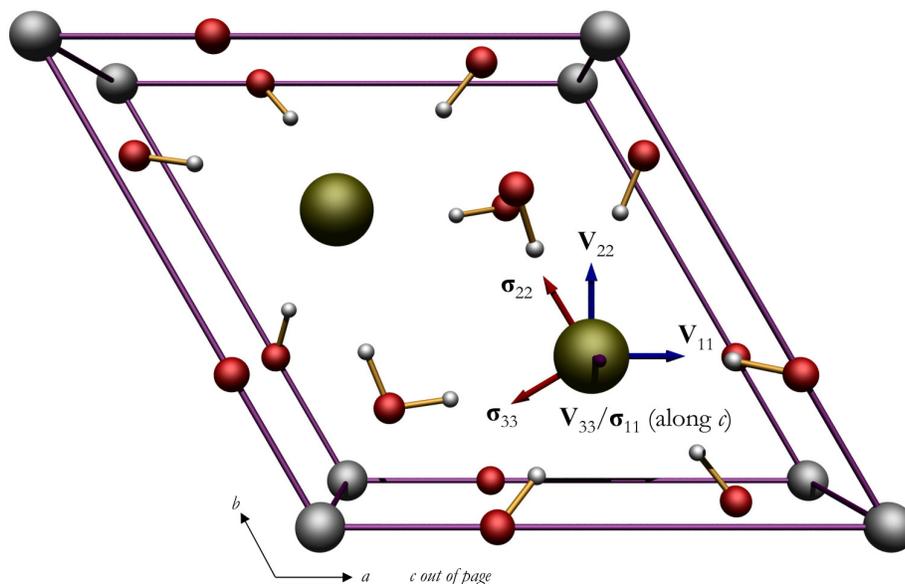
Figure A.10 POV-ray rendering of the computed bromine $\ddot{V}$ (blue) and symmetric $\ddot{\sigma}$ (red) tensor eigenvectors in the crystal frame of $SrBr_2 \cdot 6H_2O$ (model B). The computation used $E_{cut} = 800$ eV, a $4 \times 4 \times 6$ k-point grid, and the PBE XC functional. Where the $\ddot{V}$ and $\ddot{\sigma}$ eigenvectors are coincident, a purple vector represents both. Eigenvectors were placed using Diamond 3.2.
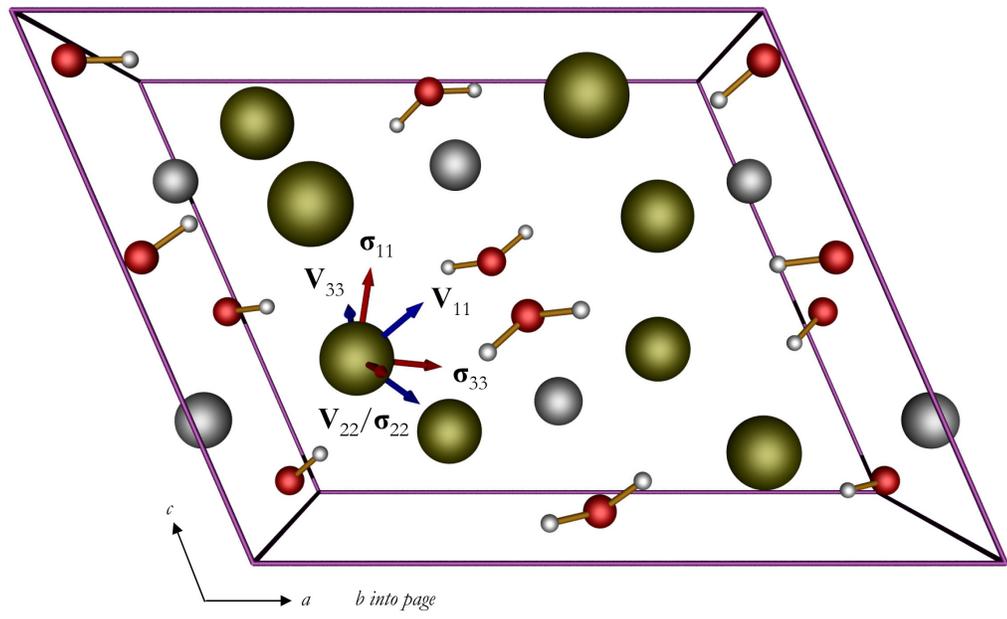
Figure A.11 POV-ray rendering of the computed bromine $\ddot{V}$ (blue) and symmetric $\ddot{\sigma}$ (red) tensor eigenvectors in the crystal frame of $BaBr_2 \cdot 2H_2O$. The computation used $E_{cut} = 800$ eV, a $3 \times 3 \times 3$ k-point grid, and the PBE XC functional. Eigenvectors were placed using Diamond 3.2.

Table A.9 Bromine-79/81 $\ddot{V}$ and $\ddot{\sigma}$ tensor eigenvectors, normalized and in their respective crystal frames[a]

compound	site label	eigenvector label	$v_a{}^b$	$v_b{}^b$	$v_c{}^b$
CaBr$_2$	—	$\mathbf{V}_{11}$	0.0000	0.0000	1.0000
		$\mathbf{V}_{22}$	0.7071	0.7071	0.0000
		$\mathbf{V}_{33}$	−0.7071	0.7071	0.0000
		$\boldsymbol{\sigma}_{11}$	−0.7011	0.7130	0.0000
		$\boldsymbol{\sigma}_{22}$	0.0000	0.0000	−1.0000
		$\boldsymbol{\sigma}_{33}$	0.7130	−0.7011	0.0000
SrBr$_2$	Br(1)	$\mathbf{V}_{11}$	1.0000	0.0000	0.0000
		$\mathbf{V}_{22}$	0.0000	1.0000	0.0000
		$\mathbf{V}_{33}$	0.0000	0.0000	1.0000
		$\boldsymbol{\sigma}_{11}$	0.0000	0.0000	1.0000
		$\boldsymbol{\sigma}_{22}$	1.0000	0.0000	0.0000
		$\boldsymbol{\sigma}_{33}$	0.0000	1.0000	0.0000
	Br(2)	$\mathbf{V}_{11}$	1.0000	0.0000	0.0000
		$\mathbf{V}_{22}$	0.0000	1.0000	0.0000
		$\mathbf{V}_{33}$	0.0000	0.0000	1.0000
		$\boldsymbol{\sigma}_{11}$	0.0000	0.0000	1.0000
		$\boldsymbol{\sigma}_{22}$	1.0000	0.0000	0.0000
		$\boldsymbol{\sigma}_{33}$	0.0000	1.0000	0.0000
	Br(3)	$\mathbf{V}_{11}$	0.1623	0.0186	0.9866
		$\mathbf{V}_{22}$	0.9698	−0.1874	−0.1561
		$\mathbf{V}_{33}$	0.1820	0.9821	−0.0485
		$\boldsymbol{\sigma}_{11}$	−0.3683	0.7253	0.5816
		$\boldsymbol{\sigma}_{22}$	−0.4927	−0.6828	0.5395
		$\boldsymbol{\sigma}_{33}$	0.7884	−0.0879	0.6088
	Br(4)	$\mathbf{V}_{11}$	−0.7485	−0.5131	0.4201
		$\mathbf{V}_{22}$	0.6353	−0.3733	0.6760
		$\mathbf{V}_{33}$	−0.1901	0.7729	0.6054
		$\boldsymbol{\sigma}_{11}$	0.4466	0.6265	0.6388
		$\boldsymbol{\sigma}_{22}$	0.8550	−0.0885	−0.5110
		$\boldsymbol{\sigma}_{33}$	−0.2636	0.7744	−0.5752
BaBr$_2$	Br(1)	$\mathbf{V}_{11}$	0.8873	0.0000	−0.4613
		$\mathbf{V}_{22}$	0.0000	1.0000	0.0000
		$\mathbf{V}_{33}$	0.4613	0.0000	0.8873
		$\boldsymbol{\sigma}_{11}$	−0.2246	0.0000	0.9745
		$\boldsymbol{\sigma}_{22}$	0.0000	−1.0000	0.0000
		$\boldsymbol{\sigma}_{33}$	0.9745	0.0000	0.2246

compound	site label	eigenvector label	$v_a{}^b$	$v_b{}^b$	$v_c{}^b$
	Br(2)	$\mathbf{V}_{11}$	0.9088	0.0000	−0.4172
		$\mathbf{V}_{22}$	0.0000	1.0000	0.0000
		$\mathbf{V}_{33}$	0.4172	0.0000	0.9088
		$\boldsymbol{\sigma}_{11}$	0.9955	0.0000	−0.0942
		$\boldsymbol{\sigma}_{22}$	0.0000	1.0000	0.0000
		$\boldsymbol{\sigma}_{33}$	0.0942	0.0000	0.9955
MgBr$_2$·6H$_2$O^c	—	$\mathbf{V}_{11}$	0.0000	0.1364	0.0000
(model B)		$\mathbf{V}_{22}$	−0.0608	0.0000	0.1200
		$\mathbf{V}_{33}$	0.0760	0.0000	0.1077
		$\boldsymbol{\sigma}_{11}$	0.0278	0.0000	0.1569
		$\boldsymbol{\sigma}_{22}$	0.0000	−0.1364	0.0000
		$\boldsymbol{\sigma}_{33}$	0.0933	0.0000	−0.0372
SrBr$_2$·6H$_2$O^c	—	$\mathbf{V}_{11}$	0.1218	0.0000	0.0000
(model B)		$\mathbf{V}_{22}$	0.0703	0.1407	0.0000
		$\mathbf{V}_{33}$	0.0000	0.0000	0.2404
		$\boldsymbol{\sigma}_{11}$	0.0000	0.0003	0.2404
		$\boldsymbol{\sigma}_{22}$	−0.0023	0.1207	−0.0007
		$\boldsymbol{\sigma}_{33}$	−0.1408	−0.0724	0.0001
BaBr$_2$·2H$_2$O^c	—	$\mathbf{V}_{11}$	0.0965	−0.0391	0.0798
		$\mathbf{V}_{22}$	0.0398	0.0747	−0.0700
		$\mathbf{V}_{33}$	0.0072	0.1105	0.0755
		$\boldsymbol{\sigma}_{11}$	0.0562	−0.0098	0.1284
		$\boldsymbol{\sigma}_{22}$	0.0329	−0.1262	−0.0167
		$\boldsymbol{\sigma}_{33}$	0.0819	0.0574	−0.0148

^{a} Orientations were determined from GIPAW DFT computations using the PBE XC functional.
^{b} The values within these columns are fractional unit cell coordinates.
^{c} Belongs to a lattice which requires the use of the general form of the vector norm (i.e., for non-orthogonal, non-Cartesian basis

vectors). Hence, $\|\mathbf{v}\| = \sqrt{v_a^2\,|\mathbf{a}|^2 + v_b^2\,|\mathbf{b}|^2 + v_c^2\,|\mathbf{c}|^2 + 2v_a v_b\,|\mathbf{a}||\mathbf{b}|\cos\gamma_C + 2v_a v_c\,|\mathbf{a}||\mathbf{c}|\cos\beta_C + 2v_b v_c\,|\mathbf{b}||\mathbf{c}|\cos\alpha_C}$.

The input parameters used can be found in the footnotes to Table A.3.
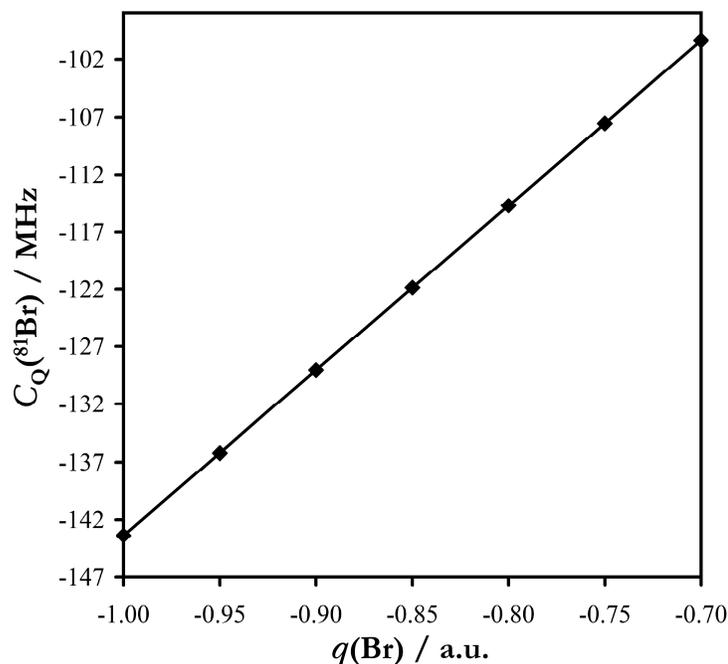
Figure A.12 Plot of $C_Q(^{81}Br)$ versus $q(Br)$ for CaBr$_2$ using the point charge model described in the main text of Chapter 3. Linear equation of best fit: $C_Q(^{81}Br) = 143.37q(Br)$, $R^2 = 1.00$.

A.1   References

1   E. B. Brackett, T. E. Brackett and R. L. Sass, *J. Inorg. Nucl. Chem.*, **1963**, *25*, 1295-1296.

2   J. G. Smeggil and H. A. Eick, *Inorg. Chem.*, **1971**, *10*, 1458-1460.

3   E. B. Brackett, T. E. Brackett and R. L. Sass, *J. Phys. Chem.*, **1963**, *67*, 2132-2135.

4   K. R. Andress and J. Gundermann, *Z. Kristallogr.*, **1934**, *87*, 345-369.

5   C. A. Sorrell and R. R. Ramey, *J. Chem. Eng. Data*, **1974**, *19*, 307-308.

6   A. LeClaire and M. M. Borel, *Acta Cryst. B*, **1977**, *B33*, 2938-2940.

7   I. Abrahams and E. Vordemvenne, *Acta Cryst. C*, **1995**, *C51*, 183-185.

8   P. A. Agron and W. R. Busing, *Acta Cryst. C*, **1986**, *C42*, 141-143.

9   T. Kellersohn, B. Engelen, H. D. Lutz, H. Bartl, B. P. Schweiss and H. Fuess, *Z. Kristallogr.*, **1991**, *197*, 175-184.

10   P. Pyykkö, *Mol. Phys.*, **2008**, *106*, 1965-1974.

11   K. J. D. MacKenzie and M. E. Smith, *Multinuclear Solid-State NMR of Inorganic Materials*, Pergamon: Amsterdam, **2002**.

12   A. K. van Bever and W. Nieuwenkamp, *Z. Kristallogr.*, **1935**, *90*, 374-376.

13   P. A. Agron and W. R. Busing, *Acta Cryst. C*, **1985**, *C41*, 8-10.

Appendix B

Appendix to Chapter Four

B.1   Additional Experimental Details

B.1.1   Confirmation of Sample Purity

Sample purity was confirmed for each compound by the manufacturer based primarily on trace metal analysis using inductively coupled plasma mass spectrometry (ICP-MS), except $BaI_2 \cdot 2H_2O$, which was confirmed via titration with $AgNO_3$. Detailed results of the ICP-MS experiments may be obtained by visiting www.sigmaaldrich.com and noting the appropriate lot number: MgI_2 (19170LH); CaI_2 (06459HE); BaI_2 (10754CE); CdI_2 (07335HD); $SrI_2 \cdot 6H_2O$ (MKAA0436); $BaI_2 \cdot 2H_2O$ (02211HH).

B.1.2   Choice of Hahn Echo or Solomon Echo Pulse Sequence

Relative to the Hahn echo pulse sequence, and assuming adequate probe bandwidth, the Solomon echo pulse sequence allows for more uniform excitation of a static SSNMR spectrum for a half-integer quadrupolar nucleus.[1]   This comes at the expense of signal intensity, where the Hahn echo sequence is superior by a factor of 2. Hence, as sufficient ^{127}I signal was often available at 21.1 T, the Solomon echo was used. At 11.75 T, it was deemed in certain cases that the increased signal would be preferred; hence, the Hahn echo pulse sequence was chosen.

B.1.3   Quantum Chemical Calculations – Additional Information

The 'precise' setting, as defined by Materials Studio, was used for the FFT grid, except NMR tensor calculations for SrI_2 and $BaI_2 \cdot 2H_2O$, where the 'fine' setting was used due to computational resource limitations.

Table B.1 Detailed ^{127}I SSNMR/NQR experimental acquisition parameters[a]

B_0 / T	window[b] / kHz	points[c]	$\pi/2$[d] / µs	scans	recycle delay / s	$\tau_1;\tau_2$ / µs	details
				MgI$_2$			
11.75	2 000	1 024	1.0	18 800	0.25	30;10	Solomon echo; 8 pieces; offset = 300 kHz; 4 mm probe
21.1	2 000	512	1.0	8 192	0.25	30;10	Solomon echo; 7 pieces; offset = 300 kHz; 3.2 mm probe
				CaI$_2$			
11.75	2 000	512	1.0	4 992	0.25	30;10	Hahn echo; 50 pieces; offset = 300 kHz; 4 mm probe
21.1	2 000	1 024	1.0	6 000	0.25	30;10	Solomon echo; 3.2 mm probe
				BaI$_2$			
11.75	2 000	1 024	1.0	14 400	0.25	30;10	Solomon echo; 17 pieces; offset = 300 kHz; 4 mm probe
21.1	2 000	512	1.0	6 000	0.25	30;10	Solomon echo; 11 pieces; offset = 300 kHz; 3.2 mm probe
0.0	2 000	512	2.0	1 500	0.35	30;25	site I(2); Hahn echo; 7 mm probe; m = ±1/2 ↔ ±3/2 transition
0.0	2 000	512	2.0	1 500	0.35	30;25	site I(2); Hahn echo; 7 mm probe; m = ±3/2 ↔ ±5/2 transition
				CdI$_2$ (4H)			
11.75	2 000	512	1.0	18 000	0.3	30;20	Solomon echo; 11 pieces; offset = 300 kHz; 4 mm probe
21.1	2 000	1 024	1.0	8 192	0.4	30;10	Solomon echo; 7 pieces; offset = 300 kHz; 3.2 mm probe
				BaI$_2$·2H$_2$O			
11.75	2 000	1 024	1.0	8 000	0.25	28.5;10	Hahn echo; 11 pieces; offset = 200 kHz; 4 mm probe; T = 295
11.75	2 000	1 024	1.0	3 000	0.25	28.5;10	Hahn echo; 8 pieces; offset = 250 kHz; 4 mm probe; T ≈ 243 K
21.1	2 000	1 024	1.0	3 000	0.25	30;5	Solomon echo; 5 pieces; offset = 300 kHz; 3.2 mm probe
21.1	2 000	1 024	1.4	4 000[e]	0.25	18.6;4.3	Solomon echo; 6 pieces; offset = 300 kHz; v_1(^{1}H) ~ 85 kHz; 4 mm probe
				SrI$_2$·6H$_2$O			
21.1	2 000	1 024	1.4	5 000	0.25	18.6;4.3	Solomon echo; 16 pieces; offset = 250 kHz; 4 mm probe
0.0	2 000	512	3.0	512	0.2	30;20	Hahn echo; 7 mm probe; m = ±1/2 ↔ ±3/2 transition
0.0	2 000	512	2.5	1 000	0.2	30;20	Hahn echo; 7 mm probe; m = ±1/2 ↔ ±3/2 transition

[a] All experiments were carried out at room temperature. [b] Acquisition parameters are for each sub-spectrum, where applicable. [c] Number of complex time-domain data points acquired. [d] CT selective pulses. [e] The spectrum in Figure B.6b was acquired using similar parameters as that in Figure 4.9b, except that it used 4 096 scans, 9 pieces, and offset = 200 kHz.

Table B.2 GIPAW DFT computations: pseudopotentials, energies and structure references[a]

compound	functional	pseudopotential files used[b]	energy / eV	structure references and notes
MgI_2	PBE	Mg_00.otfg, I_00.otfg	−2369.392311	Brogan et al.[2]
	PW91	Mg_00.otfg, I_00.otfg	−2374.230972	
CaI_2	PBE	Ca_00PBE.usp, I_00.otfg	−2345.200635	Blum[3]
	PW91	Ca_00.usp, I_00.otfg	−2352.075263	
SrI_2	PBE	Sr_00PBE.usp, I_00.otfg	−17441.069319	Rietschel & Bärnighausen[4]
	PW91	Sr_00.usp, I_00.otfg	−17505.568054	
BaI_2	PBE	Ba_00PBE.usp, I_00.otfg	−8173.788719	Brackett et al.[5]
	PW91	Ba_00.usp, I_00.otfg	−8205.999024	
CdI_2 (4H)	PBE	Cd_00PBE.usp, I_00.otfg	−5248.652457	Mitchell[6]
	PW91	Cd_00.usp, I_00.otfg	−5265.218784	
$BaI_2 \cdot 2H_2O$	PBE	H_00.otfg, O_00.otfg, Ba_00PBE.usp, I_00.otfg	−11940.988506	Unit cell and all atomic positions were optimized computationally, starting from the known structure of $BaBr_2 \cdot 2H_2O$, as determined by Kellersohn et al.,[7] and under the initial assumption that $BaBr_2 \cdot 2H_2O$ and $BaI_2 \cdot 2H_2O$ are isostructural.
	PW91	H_00.otfg, O_00.otfg, Ba_00.usp, I_00.otfg	−11977.973431	
$SrI_2 \cdot 6H_2O$	PBE	H_00.otfg, O_00.otfg, Sr_00PBE.usp, I_00.otfg	−5005.464730	Using the unit cell parameters of Herrmann,[8] the H, O, and I atomic positions were optimized computationally. The initial placement of the atoms was at the corresponding positions in the known structure of $SrCl_2 \cdot 6H_2O$, as determined by Agron and Busing,[9] and under the initial assumption that $SrCl_2 \cdot 6H_2O$ and $SrI_2 \cdot 6H_2O$ are isostructural.
	PW91	H_00.otfg, O_00.otfg, Sr_00.usp, I_00.otfg	−5017.135767	

[a] Crystal structure parameters used for GIPAW DFT NMR computations can be found in Table B.3.

[b] File extensions identify the type of pseudopotential used: .otfg = on-the-fly generation; .usp = ultrasoft. The .usp pseudopotentials were used for atoms containing nuclei that were not directly probed using SSNMR, while the .otfg pseudopotentials were used on the relevant NMR-active nuclei, and were generated during each calculation starting from the input string specified below. File names are as specified in Materials Studio 3.2.0.0. Information on the iodine otfg pseudopotential: (i) core states include $1s^2 2s^2 2p^6 3s^2 3p^6 3d^{10} 4s^2 4p^6 4d^{10}$; valence states include $5s^2 5p^5$; (ii) the local channel is chosen to be *d*; (iii) the pseudisation radius for local and non-local channels is 2.0 a.u.; (iv) the pseudisation radius for augmentation functions is 1.6 a.u.; (v) augmentation charge and partial core correction are 1.602 a.u.; (vi) the string used for the generation of the pseudopotential, in the format used by Materials Studio is "2|2|2|1.6|6|7.3|9.9|50U=-0.65U=+0:51U=-0.265U=+0[]"
(see http://www.tcm.phy.cam.ac.uk/castep/usp-string-notes.txt and http://www.tcm.phy.cam.ac.uk/castep/otfg.pdf for further explanation).

Table B.3 GIPAW DFT computations: crystal structure parameters used for NMR parameter computations

compound	atom	Wyckoff site	local symmetry	$v_a{}^a$	$v_b{}^a$	$v_c{}^a$
MgI$_2{}^b$	Mg	1a	$\overline{3}m$	0.0000	0.0000	0.0000
	I	2d	$3m$	0.3333	0.6667	0.2424
CaI$_2{}^c$	Ca	1a	$\overline{3}m$	0.0000	0.0000	0.0000
	I	2d	$3m$	0.3333	0.6667	0.2500
SrI$_2{}^d$	Sr	8c	1	0.1105	0.4505	0.2764
	I(1)	8c	1	−0.0341	0.2682	0.0054
	I(2)	8c	1	0.2020	0.1077	0.1630
BaI$_2{}^e$	Ba	4c	m	0.2366	0.2500	0.1215
	I(1)	4c	m	0.0290	0.2500	0.8387
	I(2)	4c	m	0.1393	0.2500	0.4265
CdI$_2$ (4H)^f	Cd	2b	$3m$	0.3333	0.6667	0.0000
	I(1)	2b	$3m$	0.3333	0.6667	0.3750
	I(2)	2a	$3m$	0.0000	0.0000	0.6250
BaI$_2$·2H$_2$O^g	Ba	4e	2	0.0000^b	0.0992^b	0.2500^b
	I	8f	1	0.2108^b	0.4841^b	0.3474^b
	O	8f	1	0.0052^b	0.7808^b	0.4418^b
	H	8f	1	0.0804^b	0.7072^b	0.4508^b
	H	8f	1	0.9304^b	0.7071^b	0.3764^b
SrI$_2$·6H$_2$O^i	Sr	1a	32.	0.0000	0.0000	0.0000
	I	2d	3	0.3333	0.6667	0.4411^b
	O	3f	2	−0.2036^b	0.0000^b	0.5000^b
	O	3e	2	0.3008^b	0.0000^b	0.0000^b
	H	6g	1	0.4164^b	0.0914^b	−0.0964^b
	H	6g	1	−0.2228^b	0.1054^b	0.4815^b

^{a} The values within these columns are in fractional unit cell coordinates.

^{b} $P\overline{3}m1$ (№. 164); trigonal; $a = b = 4.1537$ Å; $c = 6.862$ Å; $\alpha_C = \beta_C = 90°$; $\gamma_C = 120°$.

^{c} $P\overline{3}m1$ (№. 164); trigonal; $a = b = 4.48$ Å; $c = 6.96$ Å; $\alpha_C = \beta_C = 90°$; $\gamma_C = 120°$.

^{d} $Pbca$ (№. 61); orthorhombic; $a = 15.22$ Å; $b = 8.22$ Å; $c = 7.90$ Å; $\alpha_C = \beta_C = \gamma_C = 90°$.

^{e} $Pnma$ (№. 62); orthorhombic; $a = 8.922$ Å; $b = 5.304$ Å; $c = 10.695$ Å; $\alpha_C = \beta_C = \gamma_C = 90°$.

^{f} $P6_3mc$ (№. 186); hexagonal; $a = b = 4.24$ Å; $c = 13.67$ Å; $\alpha_C = \beta_C = 90°$; $\gamma_C = 120°$.

^{g} $C2/c$ (№. 15); monoclinic; $a = 11.260$ Å; $b = 7.642$ Å; $c = 8.734$ Å; $\alpha_C = \gamma_C = 90°$; $\beta_C = 112.32°$.

^{h} Position optimized computationally, as described in Section 4.2.4 and Table B.2.

^{i} $P321$ (№. 150); trigonal; $a = b = 8.51$ Å; $c = 4.29$ Å; $\alpha_C = \beta_C = 90°$; $\gamma_C = 120°$.
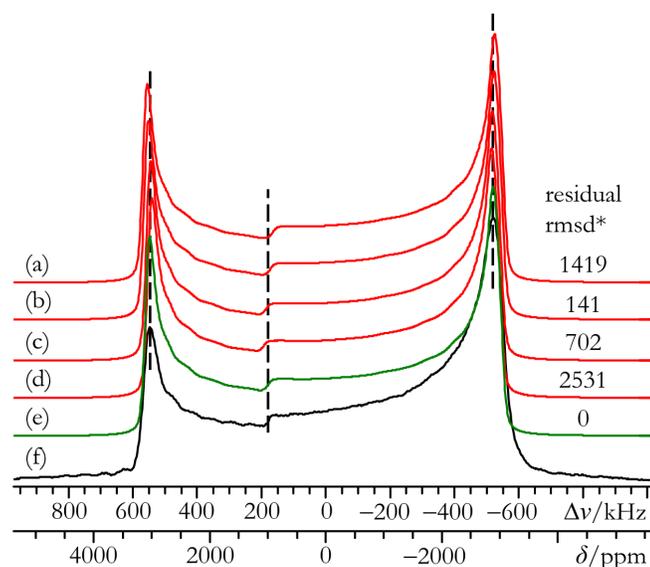
Figure B.1 In (a – e), analytical simulations highlight the importance of including iodine CSA in the line shape fits for powdered MgI$_2$ at B_0 = 21.1 T. The following Ω values were used in the simulations, while all other parameters remain as listed in Tables 4.1 and 4.2: (a) 0 ppm; (b) 60 ppm; (c) 180 ppm; (d) 240 ppm; (e) 120 ppm. The experimental static VOCS Solomon echo ^{127}I CT SSNMR spectrum is in (f). *Values in this column represent the residuals extracted from rmsd calculations using all points depicted in the above spectral regions, and are in ppm. The rmsd values were calculated for each simulation by taking the difference between the experimental spectrum and each simulation in a point-by-point fashion, followed by an rms calculation. The rmsd values were then normalized to (e), which is the best-fit spectrum (this yields normalized rmsd values for each simulation equal to 1.001419, 1.000141, 1.000702, 1.002531 and 1 for (a – e), respectively). Residual rmsd values were determined by taking the positive difference between the normalized rmsd of the best-fit spectrum in (e), and those of the other simulations in (a – d).
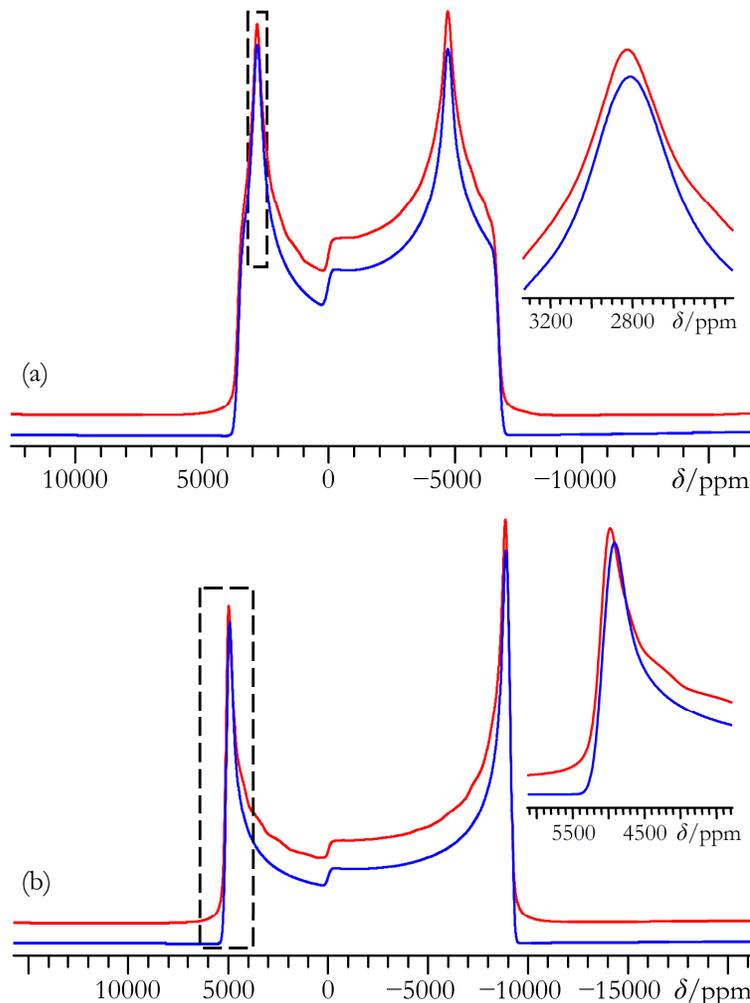
Figure B.2 Comparison of [127]I SSNMR powder patterns generated using second-order perturbation theory (red traces), with those calculated using exact theory (blue traces). The [127]I $\ddot{V}$ parameters used in these simulations correspond to those for (a) site I(1), and (b) site I(2) of BaI$_2$ at $B_0 = 21.1$ T. Chemical shift effects are ignored. The insets are horizontal expansions of the regions contained within the dashed boxes. In both cases, any HOQIE are less than the reported δ_{iso} measurement errors.
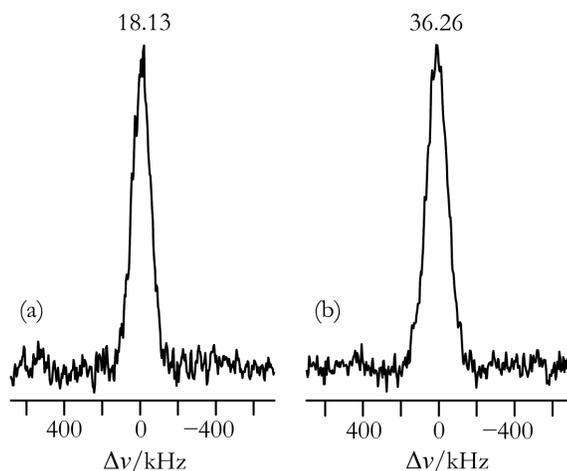
Figure B.3 Experimental ^{127}I NQR spectra of site I(2) in BaI$_2$. (a) $m = \pm 1/2 \leftrightarrow \pm 3/2$ transition; (b) $m = \pm 3/2 \leftrightarrow \pm 5/2$ transition. The transition frequencies (in MHz) are listed at the top of each signal.
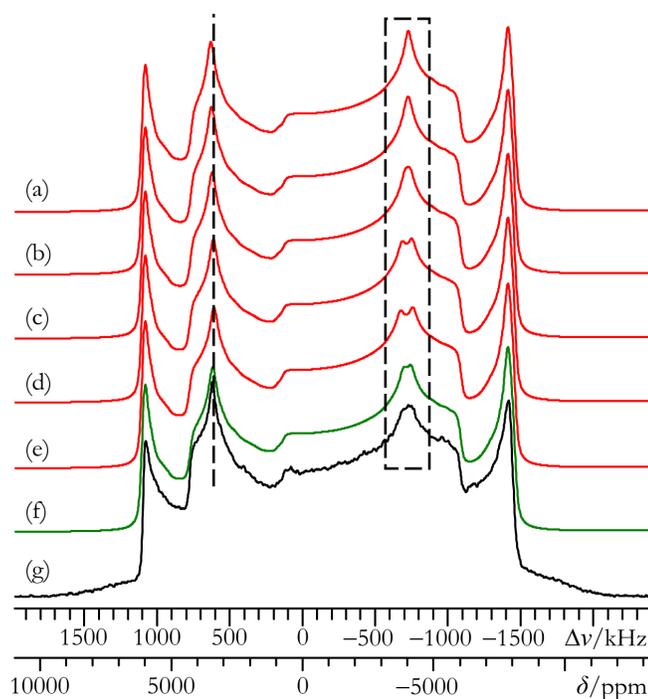
Figure B.4 In (a – f), analytical simulations highlight the importance of including CSA in the line shape fits for powdered BaI$_2$ at $B_0 = 21.1$ T. The following Ω values were used in the simulations, while all other parameters remain as listed in Tables 4.1 and 4.2: (a) 0 ppm; (b) 100 ppm; (c) 200 ppm; (d) 400 ppm; (e) 500 ppm; (f) 300 ppm. The experimental static VOCS Solomon echo ^{127}I CT SSNMR spectrum is provided in (g).
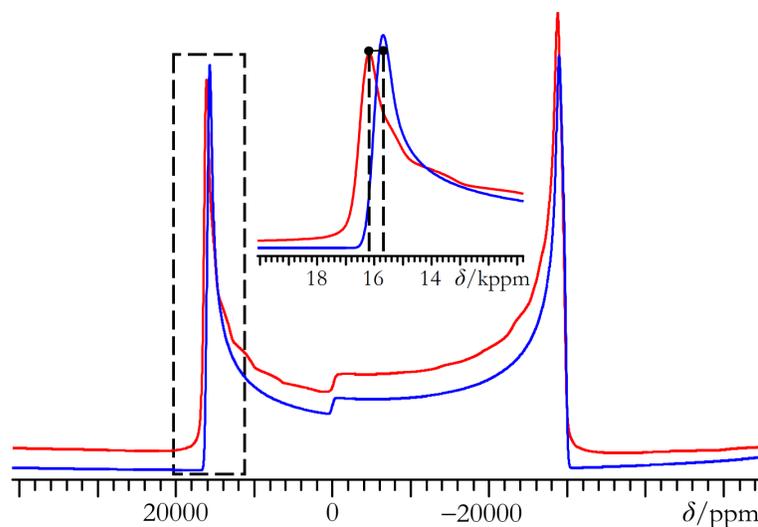
Figure B.5 Comparison of a ^{127}I SSNMR powder pattern generated using second-order perturbation theory (red trace), with one calculated using exact theory (blue trace). The ^{127}I $\ddot{V}$ parameters used in these simulations correspond to those for site I(2) in BaI$_2$ at B_0 = 11.75 T. Chemical shift effects are ignored. Relative to the second-order perturbation theory simulation, the exact simulation is shifted in a slightly orientation-dependent manner to a lower frequency, which is attributed to HOQIE at 11.75 T. The inset is a horizontal expansion of the region contained within the dashed box.
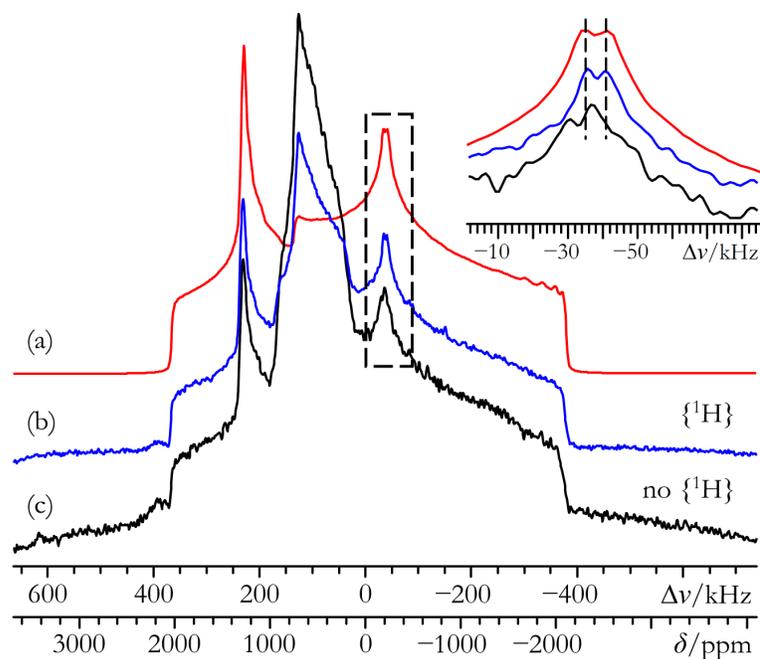
Figure B.6 Analytical simulation (a), and experimental static VOCS Solomon echo (b, c) [127]I CT SSNMR spectra of powdered $BaI_2 \cdot 2H_2O$ acquired at B_0 = 21.1 T after sample grinding. Spectrum (b) was acquired with ^{1}H decoupling, while (c) was acquired without ^{1}H decoupling. The inset highlights a change in the spectral region contained within the dashed box, which is dependent upon ^{1}H decoupling, and aids in the accurate measurement of $\ddot{V} / \ddot{\sigma}$ noncoincidence.
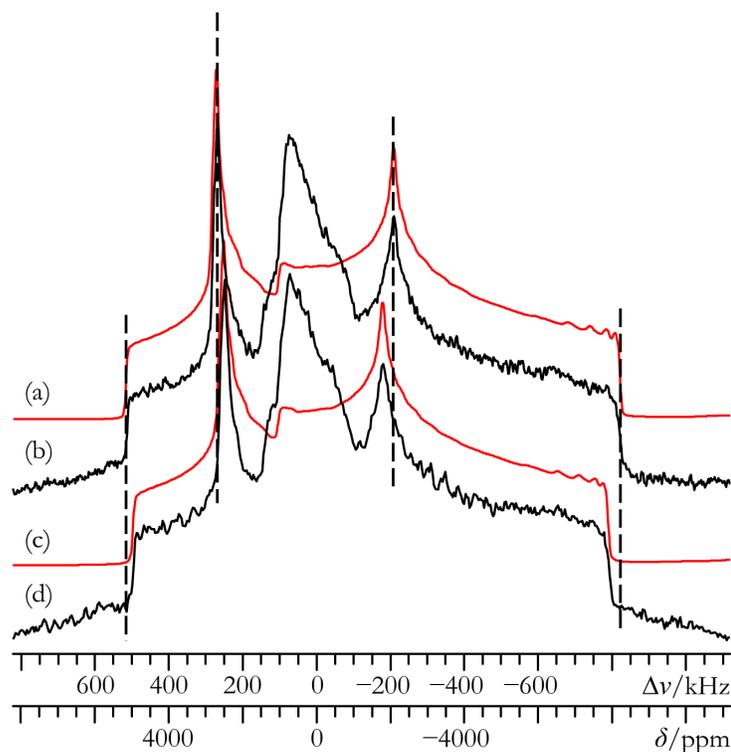
Figure B.7 Analytical simulations (a, c), and experimental static VOCS Hahn echo (b, d) [127]I CT SSNMR spectra of powdered $BaI_2·2H_2O$ acquired at $B_0 = 11.75$ T after sample grinding. Spectrum (b) was acquired at $T = 295$ K, while (d) was acquired at $T ≈ 243$ K. The dashed lines highlight key temperature-dependent spectral features. Note that the line shape associated with the impurity phase does not significantly change in this temperature interval.
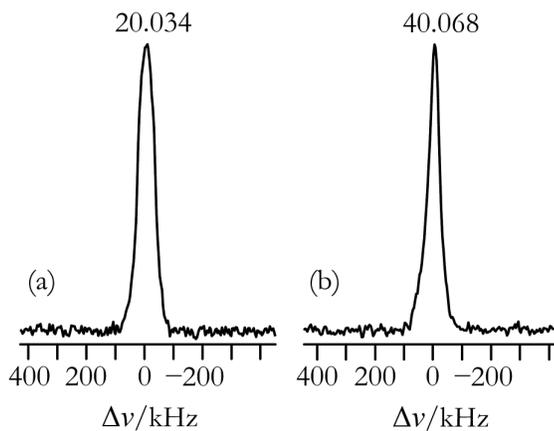
Figure B.8 Experimental [127]I NQR spectra of $SrI_2·6H_2O$. (a) $m = ±1/2 ↔ ±3/2$ transition; (b) $m = ±3/2 ↔ ±5/2$ transition. The transition frequencies (in MHz) are listed at the top of each signal.
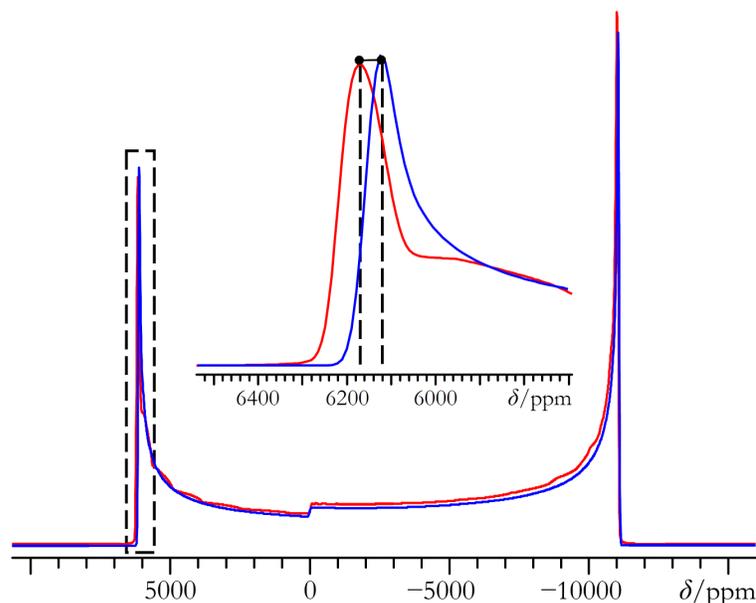
Figure B.9 Comparison of a ^{127}I SSNMR powder pattern generated using second-order perturbation theory (red trace), with one calculated using exact theory (blue trace). The ^{127}I $\ddot{V}$ parameters used in these simulations correspond to those for SrI$_2$·6H$_2$O at B_0 = 21.1 T. Chemical shift effects are ignored. The inset is a horizontal expansion of the region contained within the dashed box.

Table B.4 Input parameters for calculations involving isostructural halides[a]

Cl-containing compound	Br-containing compound	I-containing compound	$C_Q(^{35/37}Cl)$ / MHz	$C_Q(^{79/81}Br)$[b] / MHz	$C_Q(^{127}I)$[c] / MHz	V_{Cl} / Å³	V_{Br} / Å³	V_I / Å³
—	MgBr$_2$	MgI$_2$	—	26.25/21.93	79.8	—	78.70[d]	102.52[e]
CaCl$_2$	CaBr$_2$	—	8.8/6.95[f]	75.1/62.8	—	168.52[g]	196.43[h]	—
BaCl$_2$/site 1	BaBr$_2$/site 1	BaI$_2$/site 1	3.5[i]	28.1/23.5	96.2	350.55[j]	406.84[j]	506.11[j]
BaCl$_2$/site 2	BaBr$_2$/site 2	BaI$_2$/site 2	3.95[i]	32.5/27.2	120.9			
MgCl$_2$·6H$_2$O	MgBr$_2$·6H$_2$O	—	3.02/2.36[k]	22.7/19.0	—	424.74[l]	467.97[m]	—
SrCl$_2$·6H$_2$O	SrBr$_2$·6H$_2$O	SrI$_2$·6H$_2$O[n]	3.91/3.05[k]	33.2/27.7	133.6	226.29[o]	242.42[p]	269.06[q]
—	BaBr$_2$·2H$_2$O	BaI$_2$·2H$_2$O[n]	—	8.74/7.32	53.8	—	575.87[r]	695.24[s]

[a] $Q(^{35}Cl)$ = −0.8165 × 10^{-29} m², $Q(^{37}Cl)$ = −0.6435 × 10^{-29} m², $(1 − \gamma_\infty(Cl))$ = 43.0, $Q(^{79}Br)$ = 3.13 × 10^{-29} m², $Q(^{81}Br)$ = 2.62 × 10^{-29} m², $(1 − \gamma_\infty(Br))$ = 81, $Q(^{127}I)$ = −6.96 × 10^{-29} m², $(1 − \gamma_\infty(I))$ = 163. All Q values are from ref. 10, and $(1 − \gamma_\infty(X))$ values are from ref. 11. [b] Within this column, data are from Chapters 3 or 6. [c] Within this column, data are from Chapter 4. [d] From ref. 12. [e] From ref. 2. [f] Data are from Chapter 6. [g] From ref. 13. [h] From ref. 14. [i] From ref. 15. [j] From ref. 5. [k] From ref. 16. [l] From ref. 17. [m] From ref. 18. [n] Suspected member of an isostructural series. [o] From ref. 9. [p] From ref. 19. [q] From ref. 8. [r] From ref. 7. [s] Optimized as part of Chapter 4.

Table B.5 Observed halogen C_Q ratios and calculated $Q(1 - \gamma_\infty)/V$ ratios for known isostructural compounds[a]

isostructural compounds	nuclei considered	observed C_Q ratio	calculated $Q(1 – \gamma_\infty)/V$ ratio	% difference
MgI$_2$/MgBr$_2$	^{127}I / ^{79}Br	3.04	3.43	12.1
CaBr$_2$/CaCl$_2$	^{79}Br / ^{35}Cl	8.53	6.20	31.6
MgBr$_2$·6H$_2$O/MgCl$_2$·6H$_2$O	^{79}Br / ^{35}Cl	7.52	6.55	13.8
SrBr$_2$·6H$_2$O/SrCl$_2$·6H$_2$O	^{79}Br / ^{35}Cl	8.49	6.74	23.0

[a] The input values used for these calculations are taken from Table B.4.

Table B.6 GIPAW DFT ^{127}I EFG tensor parameters: MI$_2$ systems, additional information[a]

compound	functional	site label	V_{11} / a.u.	V_{22} / a.u.	V_{33} / a.u.	$C_Q(^{127}I)$ / MHz	η_Q
MgI$_2$	PBE	—	0.2475	0.2475	−0.4951	80.97	0.000
	PW91	—	0.2489	0.2489	−0.4979	81.42	0.000
CaI$_2$	PBE	—	0.1291	0.1291	−0.2581	42.21	0.000
	PW91	—	0.1320	0.1320	−0.2641	43.19	0.000
SrI$_2$	PBE	I(1)	−0.2223	−0.4377	0.6599	−107.92	0.326
		I(2)	0.4805	0.9341	−1.4146	231.34	0.321
	PW91	I(1)	−0.2240	−0.4400	0.6640	−108.59	0.325
		I(2)	0.4848	0.9390	−1.4237	232.83	0.319
BaI$_2$	PBE	I(1)	0.2132	0.3041	−0.5173	84.60	0.176
		I(2)	−0.4263	−0.4962	0.9245	−151.19	0.078
	PW91	I(1)	0.2123	0.3058	−0.5181	84.73	0.180
		I(2)	−0.4285	−0.5001	0.9286	−151.86	0.077
CdI$_2$ (4H)	PBE	I(1)	0.2754	0.2754	−0.5509	90.09	0.000
		I(2)	0.2852	0.2852	−0.5705	93.30	0.000
	PW91	I(1)	0.2815	0.2815	−0.5629	92.05	0.000
		I(2)	0.2916	0.2916	−0.5832	95.37	0.000

[a] Parameter definitions are in Section 2.3.3.2. Additional details may be found in Table 4.5.

Table B.7 GIPAW DFT iodine CS tensor parameters: MI$_2$ systems, additional information[a]

compound	functional	site label	σ_{11} / ppm	σ_{22} / ppm	σ_{33} / ppm	δ_{iso} / ppm	Ω / ppm	κ	α, β, γ / °
MgI$_2$	PBE	—	3756.08	3901.05	3901.19	1189.8	145.1	−0.998	89.3, 90.0, 90.0
	PW91	—	3763.39	3907.21	3907.34	1192.8	144.0	−0.998	89.3, 90.0, 90.0
CaI$_2$	PBE	—	3963.28	3963.29	3969.10	1076.8	5.8	1.00	90.0, 0.0, 90.0
	PW91	—	3950.00	3950.01	3956.02	1099.6	6.0	1.00	90.0, 0.0, 90.0
SrI$_2$	PBE	I(1)	3911.25	3979.19	4132.56	1034.1	221.3	0.386	138.7, 36.3, 259.1
		I(2)	3912.08	3996.46	4372.58	947.6	460.5	0.634	104.6, 89.8, 333.7
	PW91	I(1)	3914.00	3978.57	4131.00	1043.5	217.0	0.405	137.1, 35.5, 257.7
		I(2)	3915.80	4000.97	4097.00	953.9	458.4	0.628	104.2, 89.7, 333.2
BaI$_2$	PBE	I(1)	3852.62	4255.95	4346.45	889.4	493.8	−0.633	0.0, 47.1, 180.0
		I(2)	3711.80	3773.54	3951.15	1230.6	239.4	0.484	180.0, 36.4, 180.0
	PW91	I(1)	3844.61	4248.52	4340.99	906.0	496.4	−0.627	0.0, 47.2, 180.0
		I(2)	3700.10	3762.31	3942.75	1250.7	242.6	0.487	180.0, 36.5, 180.0
CdI$_2$ (4H)	PBE	I(1)	2854.60	3025.67	3026.37	2078.2	171.8	−0.992	273.1, 90.0, 180.0
		I(2)	2823.75	3251.00	3251.77	1937.5	428.0	−0.996	273.0, 90.0, 180.0
	PW91	I(1)	2766.62	2947.59	2948.32	2169.6	181.7	−0.992	273.0, 90.0, 180.0
		I(2)	2733.34	3181.66	3182.46	2023.8	449.1	−0.996	273.0, 90.0, 180.0

[a] Parameter definitions are in Sections 2.3.2.4, 2.3.3.1 and 2.3.3.3. Additional details may be found in Table 4.6.

Table B.8 GIPAW DFT ^{127}I EFG tensor parameters: MI$_2$ hydrates, additional information[a]

compound	functional	V_{11} / a.u.	V_{22} / a.u.	V_{33} / a.u.	$C_Q(^{127}I)$ / MHz	η_Q
SrI$_2$·6H$_2$O	PBE	0.5851	0.5851	−1.1702	191.37	0.000
	PW91	0.5845	0.5845	−1.1690	191.17	0.000
BaI$_2$·2H$_2$O	PBE	0.1192	0.2835	−0.4027	65.86	0.408
	PW91	0.1165	0.2912	−0.4077	66.67	0.429

[a] Parameter definitions are in Section 2.3.3.2. Additional details may be found in Table 4.7.

Table B.9 GIPAW DFT iodine CS tensor parameters: MI_2 hydrates, additional information[a]

compound	functional	σ_{11} / ppm	σ_{22} / ppm	σ_{33} / ppm	δ_{iso} / ppm	Ω / ppm	κ	α, β, γ / °
$SrI_2 \cdot 6H_2O$	PBE	4675.98	4690.16	4690.25	352.9	14.3	−0.988	357.7, 90.0, 180.1
	PW91	4675.15	4689.94	4690.02	362.9	14.9	−0.988	358.8, 90.0, 180.1
$BaI_2 \cdot 2H_2O$	PBE	4329.91	4386.80	4412.43	663.6	82.5	−0.379	250.4, 86.4, 325.0
	PW91	4321.43	4378.83	4405.52	681.0	84.1	−0.365	251.7, 86.4, 324.7

[a] Parameter definitions are in Sections 2.3.2.4, 2.3.3.1 and 2.3.3.3. Additional details may be found in Table 4.8.
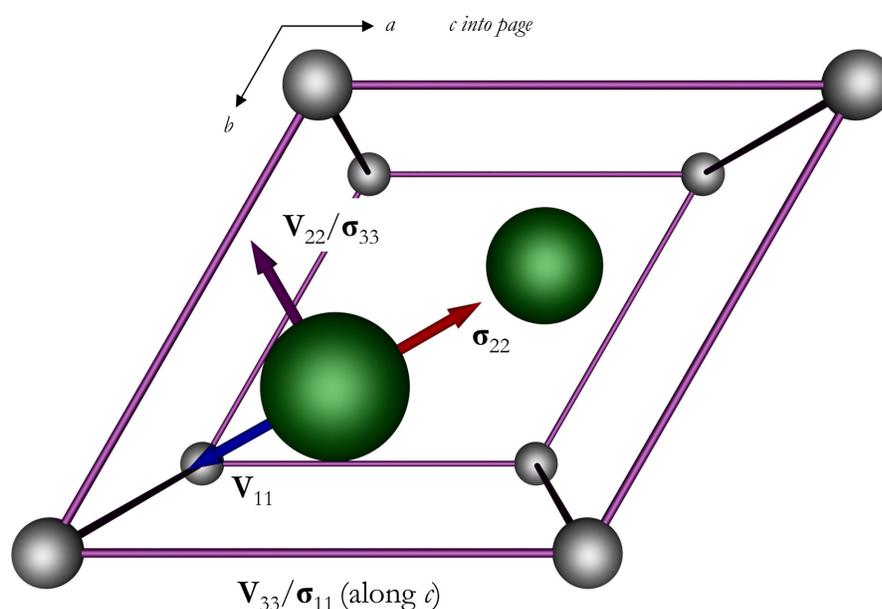
Figure B.10 POV-Ray rendering of the computed iodine $\ddot{V}$ ($\mathbf{V}_{ii}$, i = 1, 2, 3, in blue) and symmetric $\ddot{\sigma}$ ($\boldsymbol{\sigma}_{ii}$, red) tensor eigenvectors in the crystal frame of MgI_2. For all eigenvector figures in this Appendix, the metal cation is in grey, the eigenvectors are displayed once for each unique I, and were placed using Diamond v. 3.2d. When a $\ddot{V}$ eigenvector overlaps with a $\ddot{\sigma}$ eigenvector, they are displayed in purple. This calculation used E_{cut} = 1000 eV, a 9 × 9 × 6 k-point grid, and the PBE XC functional. **Note:** as η_Q = 0, $\mathbf{V}_{11}$ and $\mathbf{V}_{22}$ are interchangeable; indeed, these eigenvectors span a plane of equivalent EFG.
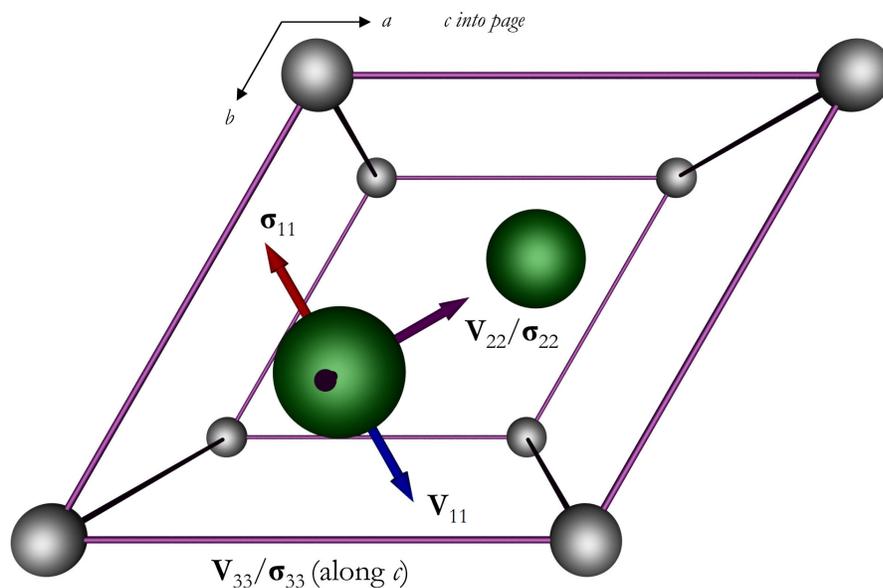
Figure B.11 POV-Ray rendering of the computed iodine $\overset{..}{V}$ (blue) and $\overset{..}{\sigma}$ (red) tensor eigenvectors in the crystal frame of CaI_2. When a $\overset{..}{V}$ eigenvector overlaps with a $\overset{..}{\sigma}$ eigenvector, they are displayed in purple. This calculation used $E_{cut} = 1200$ eV, a $9 \times 9 \times 6$ k-point grid, and the PBE XC functional. **Notes:** as $\eta_Q = 0$, V_{11} and V_{22} are interchangeable; as $\kappa = 1$, σ_{11} and σ_{22} are interchangeable.
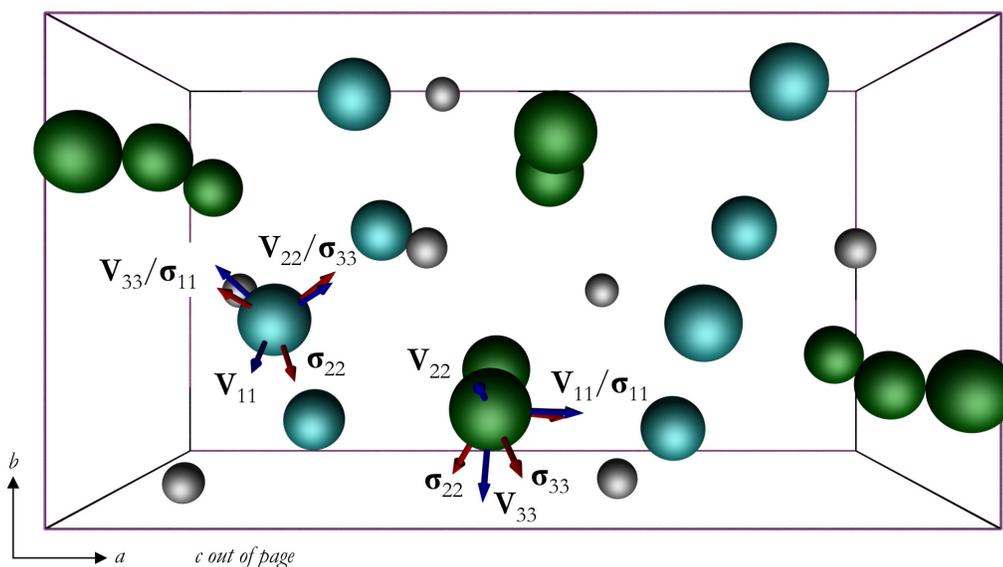
Figure B.12 POV-Ray rendering of the computed iodine $\overset{..}{V}$ (blue) and $\overset{..}{\sigma}$ (red) tensor eigenvectors in the crystal frame of SrI_2. This calculation used $E_{cut} = 550$ eV, a $2 \times 4 \times 4$ k-point grid, and the PBE XC functional. The colour and labeling scheme for the iodine atoms remains as in Figure 5.3.
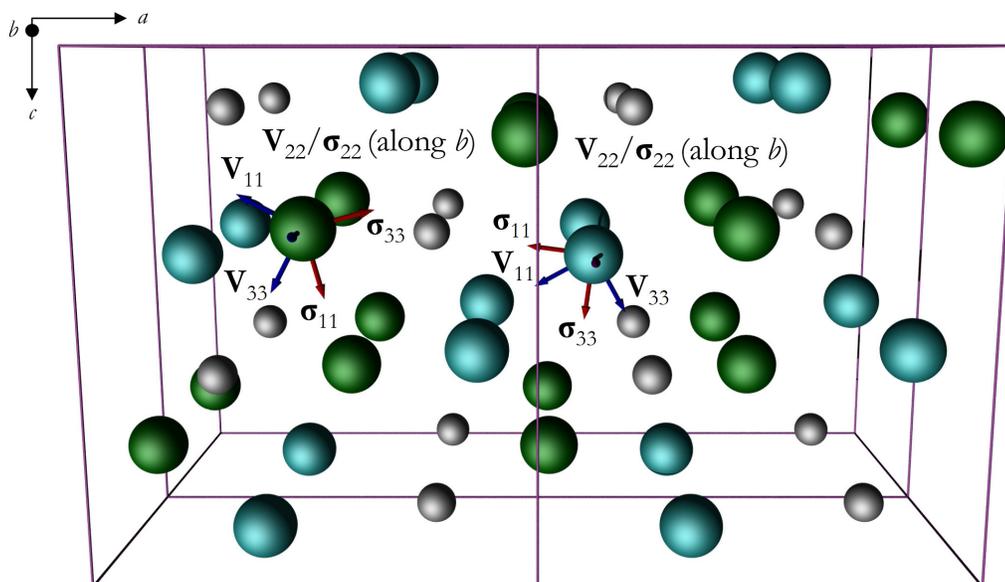
Figure B.13 POV-Ray rendering of the computed iodine $\ddot{V}$ (blue) and $\ddot{\sigma}$ (red) tensor eigenvectors in the crystal frame of BaI_2. This calculation used $E_{cut} = 600$ eV, a $4 \times 6 \times 3$ k-point grid, and the PBE XC functional. The colour and labeling scheme for the iodine atoms remains as in Figure 4.6.
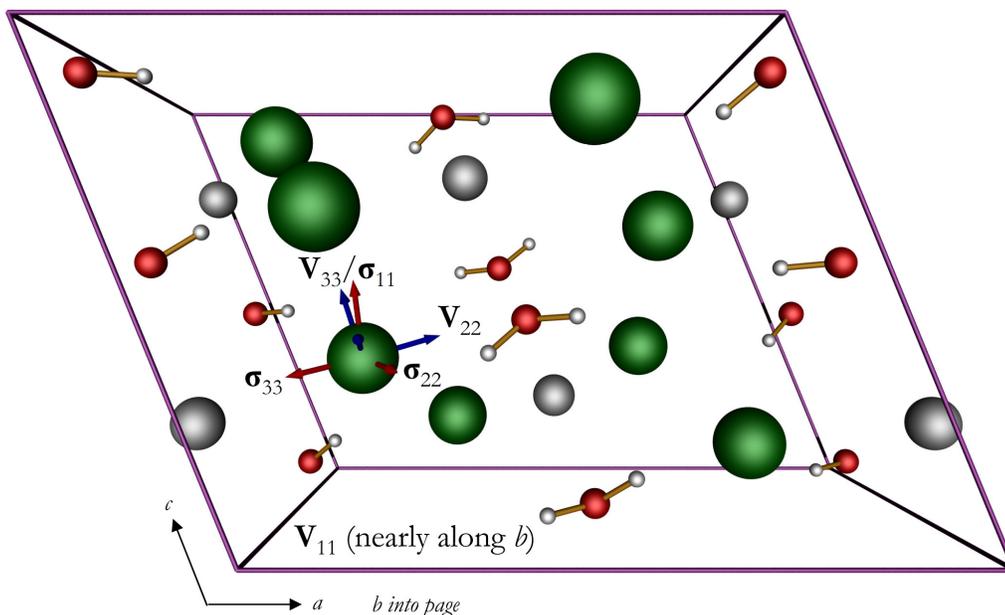
Figure B.14 POV-Ray rendering of the computed iodine $\ddot{V}$ (blue) and $\ddot{\sigma}$ (red) tensor eigenvectors in the crystal frame of $BaI_2 \cdot 2H_2O$. This calculation used $E_{cut} = 650$ eV, a $2 \times 3 \times 3$ k-point grid, and the PBE XC functional.
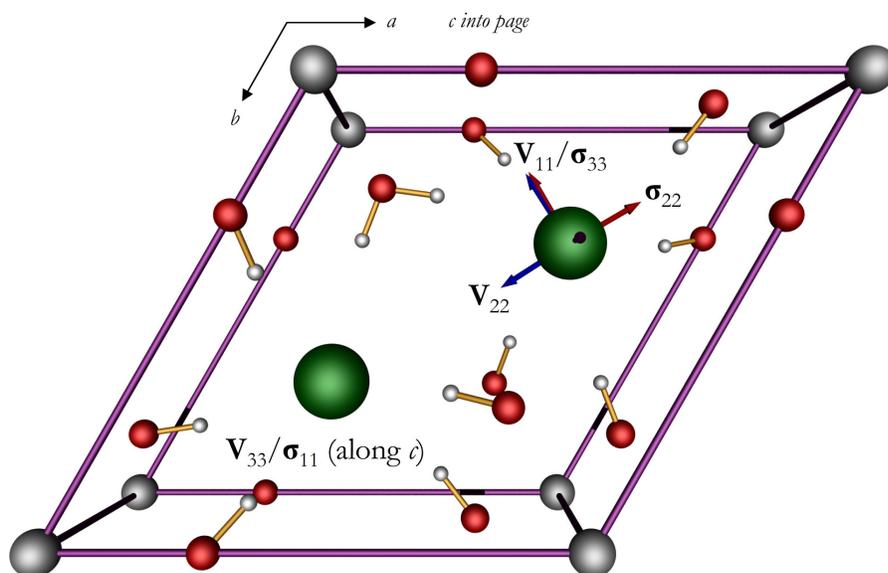
Figure B.15 POV-Ray rendering of the computed iodine $\ddot{V}$ (blue) and $\ddot{\sigma}$ (red) tensor eigenvectors in the crystal frame of $SrI_2 \cdot 6H_2O$. When a $\ddot{V}$ eigenvector overlaps with a $\ddot{\sigma}$ eigenvector, they are displayed in purple. This calculation used $E_{cut} = 800$ eV, a $5 \times 5 \times 8$ k-point grid, and the PBE XC functional. **Note:** as $\eta_Q = 0$, V_{11} and V_{22} are interchangeable.
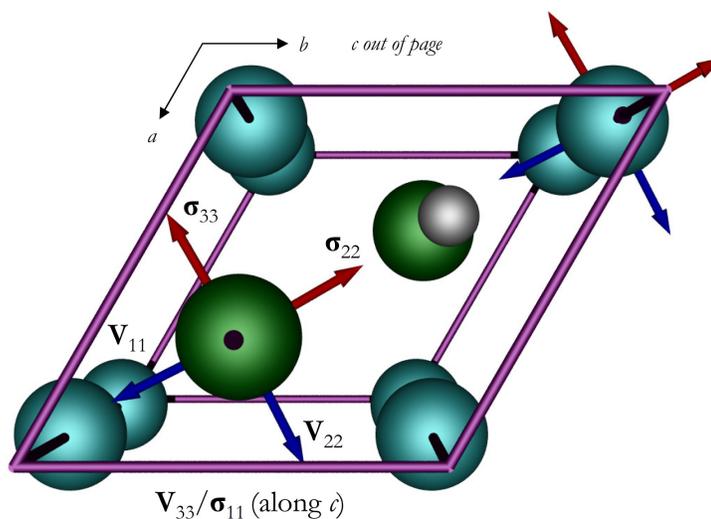
Figure B.16 POV-Ray rendering of the computed iodine $\ddot{V}$ (blue) and $\ddot{\sigma}$ (red) tensor eigenvectors in the crystal frame of CdI_2 (4H). When a $\ddot{V}$ eigenvector overlaps with a $\ddot{\sigma}$ eigenvector, they are displayed in purple. This calculation used $E_{cut} = 1000$ eV, a $9 \times 9 \times 2$ k-point grid, and the PBE XC functional. **Notes:** the eigenvector orientations are equivalent for both the I(1) (green) and I(2) (aqua) sites, and as $\eta_Q = 0$, V_{11} and V_{22} are interchangeable.

Table B.10 Iodine-127 $\ddot{V}$ and $\ddot{\sigma}$ tensor eigenvectors, normalized and in their respective crystal frames[a]

compound	site label	eigenvector label	$v_a{}^b$	$v_b{}^b$	$v_c{}^b$
MgI$_2$[c]	—	$\mathbf{V}_{11}$	−0.1419	0.1361	0.0000
		$\mathbf{V}_{22}$	−0.2390	−0.2424	0.0000
		$\mathbf{V}_{33}$	0.0000	0.0000	0.1457
		σ_{11}	0.0000	0.0000	0.1457
		σ_{22}	0.1390	−0.1390	0.0002
		σ_{33}	−0.2408	−0.2407	0.0000
CaI$_2$[c]	—	$\mathbf{V}_{11}$	0.2223	0.2242	0.0000
		$\mathbf{V}_{22}$	0.1305	−0.1272	0.0000
		$\mathbf{V}_{33}$	0.0000	0.0000	−0.1437
		σ_{11}	0.2232	0.2232	0.0000
		σ_{22}	0.1289	−0.1289	−0.0004
		σ_{33}	−0.0001	0.0001	−0.1437
SrI$_2$	I(1)	$\mathbf{V}_{11}$	0.9914	−0.0233	0.1291
		$\mathbf{V}_{22}$	−0.1107	0.3791	0.9187
		$\mathbf{V}_{33}$	−0.0703	−0.9251	0.3732
		σ_{11}	0.8343	−0.1562	−0.5287
		σ_{22}	−0.4335	−0.7783	−0.4542
		σ_{33}	0.3405	−0.6081	0.7171
	I(2)	$\mathbf{V}_{11}$	−0.0908	−0.5853	0.8057
		$\mathbf{V}_{22}$	0.7823	0.4587	0.4214
		$\mathbf{V}_{33}$	−0.6162	0.6686	0.4162
		σ_{11}	−0.5015	0.4007	0.7667
		σ_{22}	0.3699	−0.7018	0.6088
		σ_{33}	0.7821	0.5889	0.2038
BaI$_2$	I(1)	$\mathbf{V}_{11}$	−0.8829	0.0000	−0.4695
		$\mathbf{V}_{22}$	0.0000	1.0000	0.0000
		$\mathbf{V}_{33}$	−0.4695	0.0000	0.8829
		σ_{11}	0.2575	0.0000	0.9663
		σ_{22}	0.0000	−1.0000	0.0000
		σ_{33}	0.9663	0.0000	−0.2575
	I(2)	$\mathbf{V}_{11}$	−0.8765	0.0000	0.4814
		$\mathbf{V}_{22}$	0.0000	1.0000	0.0000
		$\mathbf{V}_{33}$	0.4814	0.0000	0.8765
		σ_{11}	−0.9910	0.0000	−0.1336
		σ_{22}	0.0000	1.0000	0.0000
		σ_{33}	−0.1336	0.0000	0.9910

compound	site label	eigenvector label	$v_a{}^b$	$v_b{}^b$	$v_c{}^b$
CdI_2 (4H)^c	I(1)	$\mathbf{V}_{11}$	0.1235	−0.1484	0.0000
		$\mathbf{V}_{22}$	0.2425	0.2286	0.0000
		$\mathbf{V}_{33}$	0.0000	0.0000	0.0732
		$\boldsymbol{\sigma}_{11}$	0.0000	0.0000	0.0732
		$\boldsymbol{\sigma}_{22}$	−0.1364	0.1359	0.0001
		$\boldsymbol{\sigma}_{33}$	−0.2354	−0.2363	0.0000
	I(2)	$\mathbf{V}_{11}$	0.1240	−0.1480	0.0000
		$\mathbf{V}_{22}$	0.2423	0.2288	0.0000
		$\mathbf{V}_{33}$	0.0000	0.0000	0.0732
		$\boldsymbol{\sigma}_{11}$	0.0000	0.0000	0.0732
		$\boldsymbol{\sigma}_{22}$	−0.1364	0.1359	0.0001
		$\boldsymbol{\sigma}_{33}$	−0.2354	−0.2363	0.0000
$BaI_2{\cdot}2H_2O^c$	—	$\mathbf{V}_{11}$	0.0275	−0.1175	0.0516
		$\mathbf{V}_{22}$	0.0942	0.0166	0.0295
		$\mathbf{V}_{33}$	0.0006	0.0385	0.1097
		$\boldsymbol{\sigma}_{11}$	0.0322	−0.0253	0.1213
		$\boldsymbol{\sigma}_{22}$	0.0556	−0.0952	−0.0149
		$\boldsymbol{\sigma}_{33}$	−0.0876	−0.0480	−0.0223
$SrI_2{\cdot}6H_2O^c$	—	$\mathbf{V}_{11}$	−0.1205	−0.1143	0.0000
		$\mathbf{V}_{22}$	−0.0624	0.0731	0.0000
		$\mathbf{V}_{33}$	0.0000	0.0000	−0.2331
		$\boldsymbol{\sigma}_{11}$	0.0005	−0.0001	−0.2331
		$\boldsymbol{\sigma}_{22}$	0.0673	−0.0684	0.0003
		$\boldsymbol{\sigma}_{33}$	−0.1178	−0.1172	−0.0001

[a] Orientations were determined from GIPAW DFT computations using the PBE XC functional.

[b] The values within these columns are fractional unit cell coordinates.

[c] Belongs to a lattice which requires the use of the general form of the vector norm (i.e., for non-orthogonal, non-Cartesian basis vectors). Hence, $\|\mathbf{v}\| = \sqrt{v_a^2|\mathbf{a}|^2 + v_b^2|\mathbf{b}|^2 + v_c^2|\mathbf{c}|^2 + 2v_a v_b|\mathbf{a}||\mathbf{b}|\cos\gamma_C + 2v_a v_c|\mathbf{a}||\mathbf{c}|\cos\beta_C + 2v_b v_c|\mathbf{b}||\mathbf{c}|\cos\alpha_C}$.

The input parameters used can be found in the footnotes to Table B.3.

B.2 References

1   P. R. Bodart, J.-P. Amoureux, Y. Dumazy and R. Lefort, *Mol. Phys.*, **2000**, *98*, 1545-1551.

2   M. A. Brogan, A. J. Blake, C. Wilson and D. H. Gregory, *Acta Cryst. C*, **2003**, *C59*, i136-i138.

3   H. Blum, *Z. Physik. Chem. B*, **1933**, *B22*, 298-304.

4   E. T. Rietschel and H. Bärnighausen, *Z. Anorg. Allg. Chem.*, **1969**, *368*, 62-72.

5   E. B. Brackett, T. E. Brackett and R. L. Sass, *J. Phys. Chem.*, **1963**, *67*, 2132-2135.

6   R. S. Mitchell, *Z. Kristallogr.*, **1956**, *108*, 296-315.

7   T. Kellersohn, B. Engelen, H. D. Lutz, H. Bartl, B. P. Schweiss and H. Fuess, *Z. Kristallogr.*, **1991**, *197*, 175-184.

8   Z. Herrmann, *Z. Anorg. Allg. Chem.*, **1931**, *197*, 212-218.

9   P. A. Agron and W. R. Busing, *Acta Cryst. C*, **1986**, *C42*, 141-143.

10 P. Pyykkö, *Mol. Phys.*, **2008**, *106*, 1965-1974.

11 K. J. D. MacKenzie and M. E. Smith, *Multinuclear Solid-State NMR of Inorganic Materials*, Pergamon: Amsterdam, **2002**.

12 A. Ferrari and F. Giorgi, *Atti della Accademia Nazionale dei Lincei, Classe di Scienze Fisiche, Matematiche e Naturali, Rendiconti*, **1929**, *9*, 1134-1140.

13 A. K. van Bever and W. Nieuwenkamp, *Z. Kristallogr.*, **1935**, *90*, 374-376.

14 E. B. Brackett, T. E. Brackett and R. L. Sass, *J. Inorg. Nucl. Chem.*, **1963**, *25*, 1295-1296.

15 J. F. Stebbins and L. S. Du, *Am. Mineral.*, **2002**, *87*, 359-363.

16 D. L. Bryce and E. B. Bultz, *Chem. Eur. J.*, **2007**, *13*, 4786-4796.

17 P. A. Agron and W. R. Busing, *Acta Cryst. C*, **1985**, *C41*, 8-10.

18 C. A. Sorrell and R. R. Ramey, *J. Chem. Eng. Data*, **1974**, *19*, 307-308.

19 I. Abrahams and E. Vordemvenne, *Acta Cryst. C*, **1995**, *C51*, 183-185.

Appendix C

Appendix to Chapter Five

C.1   Additional Experimental Details

C.1.1   Confirmation of Sample Purity

In addition to the ^{127}I NQR and $^{185/187}$Re NQR experiments presented here, sample purity was confirmed for each compound by the manufacturer based primarily on trace metal analysis using ICP-MS.   Purity was also confirmed for the Re-containing materials using gravimetric analysis (with tetraphenylarsonium chloride) and pXRD (NH_4ReO_4 only).   Detailed results of the pXRD and ICP-MS experiments may be obtained by visiting www.sigmaaldrich.com and noting the appropriate lot numbers: SrI_2 (04453JJ); NH_4ReO_4 (MKBB7440); $NaReO_4$ (17920CH).

C.1.2   Regarding the WURST Pulse Bandwidth

The WURST pulse sweep bandwidth used was not fully optimized, but it was observed that more severe line shape distortions resulted when using larger sweeps (i.e., 2 MHz versus 1 MHz).   A smaller WURST sweep bandwidth would minimize the line shape distortions due to having a finite probe bandwidth, but would also reduce the benefit of rapid data acquisition afforded by the WURST pulses, as compared to traditional echo experiments.

Table C.1 Detailed ^{127}I and $^{185/187}$Re SSNMR/NQR experimental acquisition parameters[a]

B_0 / T	^AX	window[b] / kHz	points[c]	$\pi/2$[d] / μs	scans	recycle delay / s	$\tau_1;\tau_2$ / μs	details
					SrI$_2$			
21.1	^{127}I	2 000	512	1.0	7 000	0.25	30;10	site I(1); VOCS Solomon echo; 11 pieces; offset = 300 kHz; 3.2 mm probe
21.1	^{127}I	2 000	512	50.0	4 000	0.25	—	VOCS WURST echo; 1 MHz bandwidth sweep from high to low frequency; 16 pieces; offset = 848 kHz; 4 mm probe
0.0	^{127}I	2 000	512	1.5	2 000	0.2	30;20	site I(2); Hahn echo; 4 mm probe; $m = \pm1/2 \leftrightarrow \pm3/2$ transition
0.0	^{127}I	2 000	512	1.2	2 000	0.2	30;20	site I(2); Hahn echo; 4 mm probe; $m = \pm3/2 \leftrightarrow \pm5/2$ transition
					NH$_4$ReO$_4$			
21.1	$^{185/187}$Re	2 000	1 024	1.2	8 192	0.1	13.8;9.4	VOCS Solomon echo; 20 pieces; offset = 300 kHz; 4 mm probe
11.75	$^{185/187}$Re	2 000	1 024	1.2	17 500	0.1	13.2;5.0	VOCS Hahn echo; 31 pieces; offset = 200 kHz; 4 mm probe
0.0	^{185}Re	1 000	512	1.6	4 096	0.1	12.6;10.0	Hahn echo; 4 mm probe; $m = \pm3/2 \leftrightarrow \pm5/2$ transition
0.0	^{187}Re	1 000	512	1.6	4 096	0.1	12.6;10.0	Hahn echo; 4 mm probe; $m = \pm3/2 \leftrightarrow \pm5/2$ transition
					NaReO$_4$			
21.1	$^{185/187}$Re	2 000	1 024	e	8 192	0.09	e	VOCS Solomon echo; 56 pieces; offset = 300 kHz; 4 mm probe
11.75	$^{185/187}$Re	2 000	512	f	17 500	0.09	f	VOCS Hahn echo; 71 pieces; offset = 200 kHz; 4 mm probe
0.0	^{185}Re	1 000	512	1.1	256	0.1	13.35;4.5	Hahn echo; 4 mm probe; $m = \pm1/2 \leftrightarrow \pm3/2$ transition
0.0	^{185}Re	1 000	512	1.1	256	0.1	13.35;4.5	Hahn echo; 4 mm probe; $m = \pm3/2 \leftrightarrow \pm5/2$ transition
0.0	^{187}Re	1 000	512	1.5	256	0.1	12.75;4.5	Hahn echo; 4 mm probe; $m = \pm1/2 \leftrightarrow \pm3/2$ transition
0.0	^{187}Re	1 000	512	1.1	256	0.1	13.35;5.0	Hahn echo; 4 mm probe; $m = \pm3/2 \leftrightarrow \pm5/2$ transition

[a] All ^{127}I experiments were carried out at room temperature, while all $^{185/187}$Re experiments were at $T = 291.8(2)$ K.
[b] Acquisition parameters are for each sub-spectrum, where applicable.
[c] Number of complex time-domain data points.
[d] CT selective pulses were used for NMR experiments.
[e] Experiments used a variety of pulse lengths and delays, which were optimized at several different transmitter frequencies, as follows: for 207.483 – 209.583 MHz sub-spectra, $\pi/2 = 1.7$ μs and $\tau_1 = 13.3$ μs; for 205.983 – 207.183 MHz sub-spectra, $\pi/2 = 1.5$ μs and $\tau_1 = 13.5$ μs; for 202.383 – 205.683 MHz sub-spectra, $\pi/2 = 1.3$ μs and $\tau_1 = 13.7$ μs; for 199.983 – 202.083 MHz sub-spectra, $\pi/2 = 1.4$ μs and $\tau_1 = 13.6$ μs; for 193.083 – 199.683 MHz sub-spectra, $\pi/2 = 1.5$ μs and $\tau_1 = 13.5$ μs.
[f] Experiments used a variety of pulse lengths and delays, which were optimized as above: for high frequency (117.687 – 121.287 MHz) sub-spectra, $\pi/2 = 1.2$ μs and $\tau_1 = 13.2$ μs; for low frequency (93.887 – 104.087 MHz) sub-spectra, $\pi/2 = 0.8$ μs and $\tau_1 = 13.8$ μs.
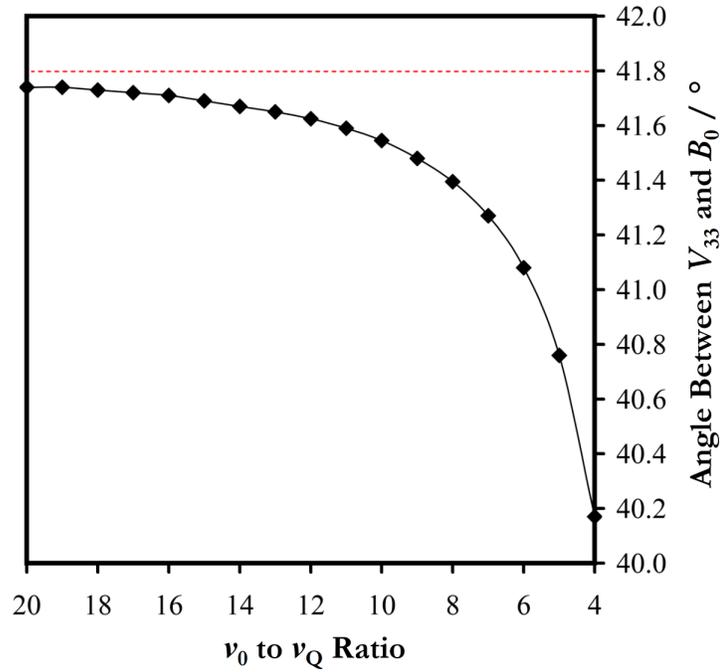
Figure C.1 Angle between $\mathbf{V}_{33}$ and B_0, which corresponds to the low-frequency CT discontinuity, as a function of the ν_0 to ν_Q ratio using exact QI simulations. The dashed red line highlights the constant value (i.e., independent of the ν_0 to ν_Q ratio) of 41.81° arrived at using second-order perturbation theory. The points in the graph are connected using a line that is meant to serve as a guide for the eyes only.

Table C.2 Table of values used to construct Figure 5.11[a]

ν_0/ν_Q	C_Q / MHz	ν_Q / MHz	ΔC_Q[b] / MHz	ΔC_Q / %	$\Delta\delta_{iso}$[c] / kHz	$\Delta\delta_{iso}$ / ppm
20	37.929	5.6894	−0.0095	−0.0250	−0.28444	−2.4998
19	39.927	5.9890	−0.0111	−0.0278	−0.34929	−3.0697
18	42.143	6.3215	−0.0130	−0.0309	−0.43354	−3.8101
17	44.620	6.6934	−0.0155	−0.0347	−0.54480	−4.7879
16	47.413	7.1117	−0.0186	−0.0392	−0.69454	−6.1039
15	50.573	7.5860	−0.0225	−0.0446	−0.89907	−7.9013
14	54.187	8.1280	−0.0277	−0.0512	−1.1849	−10.413
13	58.353	8.7530	−0.0347	−0.0594	−1.5935	−14.004
12	63.213	9.4820	−0.0441	−0.0698	−2.1944	−19.285
11	68.960	10.344	−0.0573	−0.0831	−3.1079	−27.313
10	75.860	11.379	−0.0764	−0.1007	−4.5510	−39.996
9	84.287	12.643	−0.1049	−0.1245	−6.9353	−60.950
8	94.820	14.223	−0.1497	−0.1579	−11.107	−97.610
7	108.367	16.255	−0.2241	−0.2068	−18.946	−166.50
6	126.430	18.964	−0.3576	−0.2828	−35.092	−308.40
5	151.713	22.757	−0.6225	−0.4103	−72.724	−639.13
4	189.647	28.447	−1.2320	−0.6496	−177.36	−1558.7

[a] For these calculations, the ν_0 value was kept constant at 113.787 MHz. Any set of values for ν_0 and ν_Q could have been chosen, as the important quantity is their ratio with respect to one another.
[b] Error in the C_Q value obtained if using second-order perturbation theory. Details are given in Section 5.2.4.
[c] Error in the δ_{iso} value obtained if using second-order perturbation theory. Details are given in Section 5.2.4.
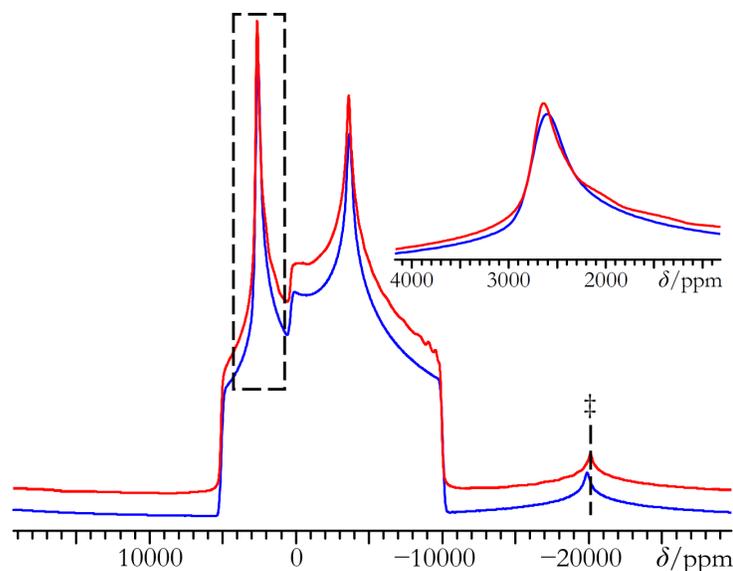
Figure C.2 Comparison of a ^{127}I SSNMR powder pattern generated using second-order perturbation theory (red trace), with one calculated using exact theory (blue trace). The ^{127}I $\ddot{V}$ parameters used in these simulations correspond to those for site I(1) in powdered SrI$_2$ at B_0 = 21.1 T. Chemical shift effects are ignored. The second-order perturbation theory simulation is essentially identical to the exact simulation, and there is no clear evidence of HOQIE on the CT. The inset is a horizontal expansion of the region within the dashed box. Low-frequency features (‡) are from the ST, and highlight the slight breakdown of the high-field approximation for these transitions, where third-order QIE are known to be nonzero.
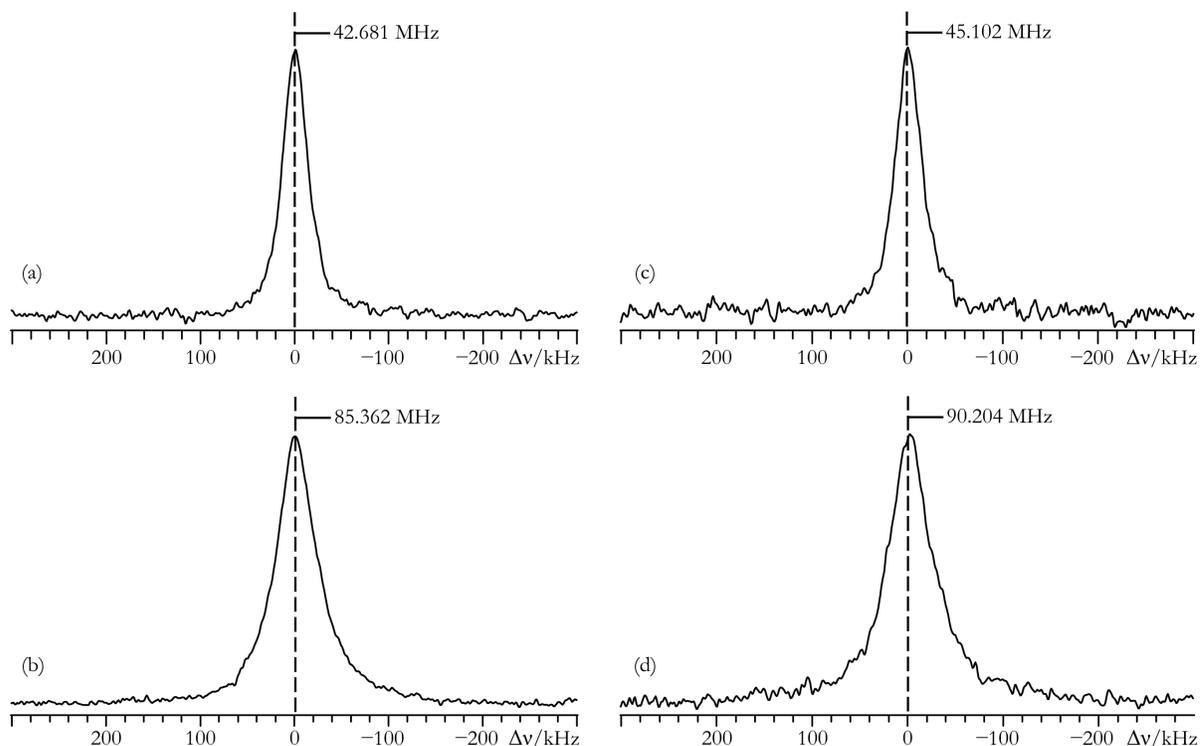
Figure C.3 Experimental ^{187}Re (a, b) and ^{185}Re (c, d) NQR spectra of powdered NaReO$_4$ acquired at $T =$ 291.8 K. The transition frequencies are specified in the Figure. (a, c) $m = \pm1/2 \leftrightarrow \pm3/2$; (b, d) $m = \pm3/2 \leftrightarrow \pm5/2$, where for all transitions $|\Delta m| = 1$.
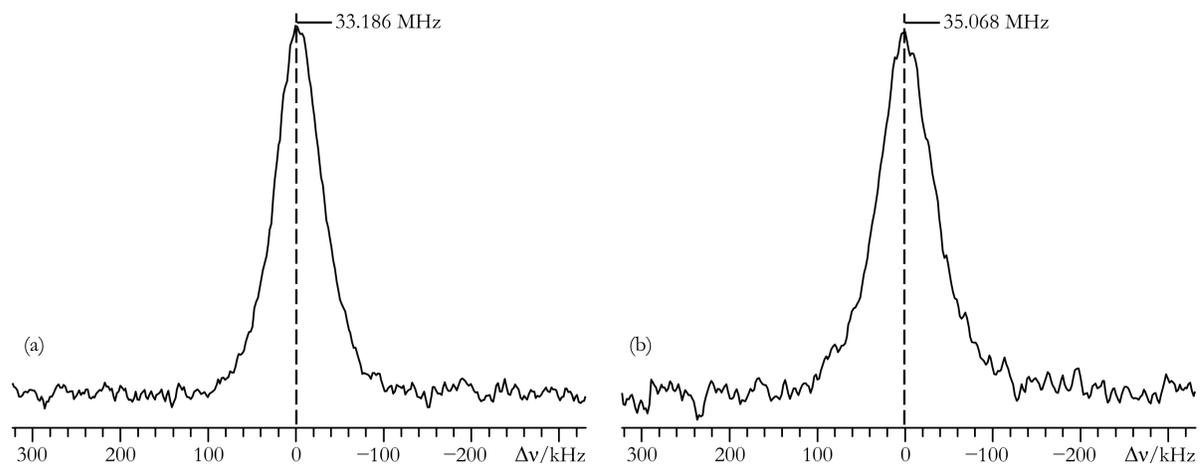
Figure C.4 Experimental ^{187}Re (a) and ^{185}Re (b) NQR spectra ($m = \pm3/2 \leftrightarrow \pm5/2$, where $|\Delta m| = 1$) of powdered NH$_4$ReO$_4$ acquired at $T =$ 291.8 K. The transition frequencies are specified in the Figure.

Table C.3 Experimental $^{185/187}$Re EFG tensor parameters and δ_{iso} values obtained via second-order perturbation theory modeling of the QI[a]

compound	B_0 / T	$|C_Q(^{185}\text{Re})|$[b] / MHz	$|C_Q(^{187}\text{Re})|$ / MHz	η_Q	$\delta_{\text{iso}}(^{185}\text{Re})$[c] / ppm	$\delta_{\text{iso}}(^{187}\text{Re})$[c] / ppm
NaReO$_4$	21.1	299.8(4)	283.9(4)	~0	−870(50)	−650(50)
NH$_4$ReO$_4$	11.75	116.8(4)	110.6(3)	~0	−210(50)	−170(50)

[a] Note that this table is for comparison purposes only (i.e., with Table 5.1). These values are not the correct parameters for the systems under study. They serve to highlight the *errors* associated with using second-order perturbation theory to model the SSNMR line shapes when there is a very large QI. Error bounds are in parentheses and parameter definitions are in Section 2.3. All measurements were carried out at T = 291.8(2) K. Second-order perturbation theory line shape simulations were performed using WSolids1.[1]
[b] While C_Q may take any real value, $|C_Q|$ is measured using conventional SSNMR experiments.
[c] Rhenium chemical shifts are reported relative to 0.1 mol/dm³ NaReO$_4$ in D$_2$O ($\delta_{\text{iso}}(^{185/187}\text{Re})$ = 0 ppm).

C.2   Reference

1   K. Eichele and R. E. Wasylishen, *WSolids1: Solid-State NMR Spectrum Simulation Package*, v. 1.19.11, Universität Tübingen: Tübingen, **2009**.

Appendix D

Appendix to Chapter Six

D.1 Additional Experimental Details

D.1.1 Confirmation of Sample Purity

Sample purity for $CaCl_2$ and $CaCl_2·6H_2O$ was confirmed by the manufacturer based primarily on trace metal analysis using ICP-MS. Purity for $MgBr_2$ was confirmed using pXRD (Figure 6.5). Detailed results of the ICP-MS experiments may be obtained by visiting www.sigmaaldrich.com and noting the appropriate lot number: $CaCl_2$ (12370DH).

Table D.1 Detailed ^{25}Mg, $^{35/37}Cl$, ^{43}Ca, and $^{79/81}Br$ SSNMR experimental acquisition parameters[a]

B_0 / T	^AX	window[b] / kHz	points[c]	$\pi/2$[d] / μs	scans	recycle delay / s	$\tau_1;\tau_2$ / μs	details
					$MgBr_2$			
11.75	^{81}Br	625	26 598	1.7	1 152	0.4	60[e]	static; VOCS QCPMG; 201 MG loops; 11 pieces; offset = 95.9 kHz
11.75	^{81}Br	2 000	2 048	1.2	12 000	0.4	250;10	static; VOCS Solomon whole echo; 3 pieces; offset = 300 kHz
11.75	^{79}Br	714.286	30 118	1.8	1 920	0.45	60[e]	static; VOCS QCPMG; 203 MG loops; 11 pieces; offset = 87.8 kHz
11.75	^{79}Br	2 000	2 048	1.1	12 000	0.4	250;10	static; VOCS Solomon whole echo; 3 pieces; offset = 300 kHz
11.75	^{25}Mg	10	2 048	4.5	560	90	—	MAS; pulse-acq; ν_{MAS} = 5 kHz
21.1	^{81}Br	1 000	2 048	1.0	2 048	0.6	300;10	static; Solomon whole echo
21.1	^{79}Br	2 000	4 096	1.2	2 048	0.6	300;10	static; Solomon whole echo
21.1	^{25}Mg	10	4 096	4.2	104	60	—	MAS; pulse-acq; ν_{MAS} = 5 kHz
					$CaCl_2$			
11.75	^{35}Cl	1 000	1 024	2.4	40 000	1.0	50;20	static; VOCS Solomon echo; 6 pieces; offset = 110 kHz
21.1	^{43}Ca	20	512	0.9	25 648	5.0	—	static; pulse-acq
21.1	^{43}Ca	20	1 024	1.0	4 313	5.0	—	MAS; pulse-acq; ν_{MAS} = 4 kHz
21.1	^{37}Cl	500	1 024	3.0	960	10.0	37.0;23.5	static; Solomon echo; 7 mm X static probe

B_0 / T	^AX	window[b] / kHz	points[c]	$\pi/2$[d] / μs	scans	recycle delay / s	$\tau_1;\tau_2$ / μs	details
21.1	^{35}Cl	500	1 024	3.2	400	10.0	36.8;23.4	static; Solomon echo; 7 mm X static probe
				CaCl$_2$·6H$_2$O				
11.75	^{35}Cl	250	1 024	2.4	16 000	3.0	78.8;37.4	static; Solomon echo
11.75	^{35}Cl	250	1 024	2.4	5 616	3.0	78.8;37.4	static; Solomon echo; $\nu_1(^1H) \sim 50$ kHz
21.1	^{35}Cl	200	2 048	2.5	272	5.0	27.5;3.75	static; Solomon echo; 4 mm HX static probe; $\nu_1(^1H) \sim 85$ kHz

[a] All experiments were carried out at room temperature.
[b] Acquisition parameters are for each sub-spectrum, where applicable.
[c] Number of complex time-domain data points acquired.
[d] CT selective pulses.
[e] All four τ values were set to 60 μs.

Table D.2 GIPAW DFT computations: pseudopotentials, energies and structure references[a]

compound	XC	pseudopotential files used[b]	energy / eV	structure references and notes
$MgBr_2$ (XRD)	PBE	Mg_00.otfg, Br_00.otfg	−2009.410406	Ferrari & Giorgi.[1] EFG/MS tensor calculations used the 'precise' setting, as defined by Materials Studio, for the FFT grid.
	PW91	Mg_00.otfg, Br_00.otfg	−2012.541456	
$MgBr_2$ (fixed cell)	PBE	Mg_00.otfg, Br_00.otfg	−2009.429912	Fixed unit cell geometry optimization. EFG/MS tensor calculations used a 'precise' FFT grid.
	PW91	Mg_00.otfg, Br_00.otfg	−2012.561001	
$MgBr_2$ (full opt.)	PBE	Mg_00.otfg, Br_00.otfg	−2009.481718	Fully-optimized structure. EFG/MS tensor calculations used a 'precise' FFT grid.
	PW91	Mg_00.otfg, Br_00.otfg	−2012.614200	
$CaCl_2$	PBE	Cl_00.otfg, Ca_00.otfg	−3739.393763	van Bever & Nieuwenkamp.[2] EFG/MS tensor calculations used a 'precise' FFT grid.
	PW91	Cl_00.otfg, Ca_00.otfg	−3742.799297	
$CaCl_2 \cdot 2H_2O$	PBE	H_00PBE.usp, O_00PBE.usp, Cl_00.otfg, Ca_00.otfg	−11234.737111	LeClaire & Borel.[3] Optimization of H atomic positions used a 'standard' FFT grid, while EFG/MS tensor calculations used a 'fine' FFT grid.
	PW91	H_00.usp, O_00.usp, Cl_00.otfg, Ca_00.otfg	−11258.718022	
α–$CaCl_2 \cdot 4H_2O$	PBE	H_00PBE.usp, O_00PBE.usp, Cl_00.otfg, Ca_00.otfg	−7495.075838	LeClaire & Borel.[4] Optimization of H atomic positions used a 'standard' FFT grid, while EFG/MS tensor calculations used a 'fine' FFT grid.
	PW91	H_00.usp, O_00.usp, Cl_00.otfg, Ca_00.otfg	−7515.610715	
β–$CaCl_2 \cdot 4H_2O$	PBE	H_00PBE.usp, O_00PBE.usp, Cl_00.otfg, Ca_00.otfg	−22483.877481	LeClaire & Borel.[5] Optimization of H atomic positions used a 'standard' FFT grid, while EFG/MS tensor calculations used a 'fine' FFT grid.
	PW91	H_00.usp, O_00.usp, Cl_00.otfg, Ca_00.otfg	−22545.390279	
γ–$CaCl_2 \cdot 4H_2O$	PBE	H_00PBE.usp, O_00PBE.usp, Cl_00.otfg, Ca_00.otfg	−7495.399755	LeClaire et al.[6] Optimization of H atomic positions used a 'standard' FFT grid, while EFG/MS tensor calculations used a 'fine' FFT grid.
	PW91	H_00.usp, O_00.usp, Cl_00.otfg, Ca_00.otfg	−7515.969910	
$CaCl_2 \cdot 6H_2O$	PBE	H_00.otfg, O_00.otfg, Cl_00.otfg, Ca_00.otfg	−4694.442249	Agron & Busing.[7,8] EFG/MS tensor calculations used a 'precise' FFT grid.
	PW91	H_00.otfg, O_00.otfg, Cl_00.otfg, Ca_00.otfg	−4699.752940	

[a] Crystal structure parameters used for GIPAW DFT NMR computations can be found in Table D.3.
[b] File extensions identify the type of pseudopotential used (defined previously). File names are as specified in Materials Studio 3.2.0.0. Information on the magnesium otfg pseudopotential: (i) core states include $1s^2 2s^2$; valence states include $2p^6 3s^2$; (ii) the local channel is d, (iii) the pseudisation radii for the local, nonlocal, and the augmentation functions and pseudo-core charge are 1.601, 2.005, 1.401 a.u., respectively; (iv) the string used for the generation of the pseudopotential, in the format used by Materials Studio is "2|1.6|2|1.4|6|7|8|30NH:21U:31UU:32LGG{qc=4.5}[]". Information on the chlorine otfg pseudopotential: (i) core states include $1s^2 2s^2 2p^6$; valence states include $3s^2 3p^5$; (ii) the local channel is d; (iii) the pseudisation radii for the local, nonlocal, and the augmentation functions and pseudo-core charge are 1.705, 1.705, and 1.191 a.u., respectively; (iv) the string used for the generation of the pseudopotential is "2|1.7|5.88|7.35|9.187|30UU:31UU:32LGG[]". Information on the calcium otfg pseudopotential: (i) core states include $1s^2 2s^2 2p^6$; valence states include $3s^2 3p^6 4s^2$; (ii) the local channel is f; (iii) the pseudisation radii for the local, nonlocal, and the augmentation functions and pseudo-core charge are 1.601, 2.005, and 1.401 a.u., respectively; (iv) the string used for the generation of the pseudopotential is "3|1.6|2.0|1.4|7|9|10|30U:40U:31:32U=0U=1.0".

Table D.3 GIPAW DFT computations: crystal structure parameters used for NMR parameter computations

compound	atom	Wyckoff site	local symmetry	$v_a{}^a$	$v_b{}^a$	$v_c{}^a$
$MgBr_2{}^b$	Mg	1a	$\bar{3}m$	0.0000	0.0000	0.0000
(XRD)	Br	2d	$3m$	0.3333	0.6667	0.2500
$MgBr_2{}^b$	Mg	1a	$\bar{3}m$	0.0000^c	0.0000^c	0.0000^c
(fixed cell)	Br	2d	$3m$	0.3333^c	0.6667^c	0.2424^c
$MgBr_2{}^d$	Mg	1a	$\bar{3}m$	0.0000^c	0.0000^c	0.0000^c
(full opt.)	Br	2d	$3m$	0.3333^c	0.6667^c	0.2125^c
$CaCl_2{}^e$	Ca	2a	$2/m$	0.000	0.000	0.000
	Cl	4g	m	0.275	0.325	0.000
$CaCl_2 \cdot 2H_2O^f$	Ca	4c	2	0.0000	0.2157	0.2500
	Cl	8d	1	−0.2725	0.4509	0.1380
	O	8d	1	0.2645	0.2107	0.1082
	H	8d	1	0.4124^c	0.2713^c	0.1138^c
	H	8d	1	0.2606^c	0.1500^c	0.0358^c
$\alpha\text{–}CaCl_2 \cdot 4H_2O^g$	Ca	2i	1	0.1189	−0.0139	0.2614
	Cl(1)	2i	1	0.2909	−0.2776	0.0503
	Cl(2)	2i	1	−0.2496	−0.2394	0.4133
	O	2i	1	−0.1821	−0.1868	0.0440
	O	2i	1	−0.0153	0.2890	0.2718
	O	2i	1	0.4792	0.2413	0.2668
	O	2i	1	0.2482	−0.2529	0.4149
	H	2i	1	-0.3248^c	-0.1896^c	0.0738^c
	H	2i	1	-0.2070^c	-0.3487^c	0.0054^c
	H	2i	1	0.0789^c	0.4459^c	0.3217^c
	H	2i	1	-0.0918^c	0.3006^c	0.1723^c
	H	2i	1	0.5464^c	0.4014^c	0.3204^c
	H	2i	1	0.5468^c	0.2347^c	0.1675^c
	H	2i	1	0.4019^c	-0.2393^c	0.4117^c
	H	2i	1	0.2252^c	-0.2346^c	0.5276^c
$\beta\text{–}CaCl_2 \cdot 4H_2O^h$	Ca(1)	2a	$\bar{1}$	0.0000	0.0000	0.0000
	Ca(2)	4e	1	−0.2582	0.0468	0.3633
	Cl(1)	4e	1	0.1734	0.0036	0.2332
	Cl(2)	4e	1	0.2435	0.1410	−0.0272
	Cl(3)	4e	1	−0.1577	0.2266	0.0090
	O	4e	1	−0.1545	−0.1389	0.3016
	O	4e	1	−0.4568	−0.0293	0.1659

compound	atom	Wyckoff site	local symmetry	$v_a{}^a$	$v_b{}^a$	$v_c{}^a$
	O	4e	1	−0.4472	−0.0863	0.4091
	O	4e	1	−0.2015	0.1940	0.2407
	O	4e	1	−0.5018	0.1809	0.3141
	O	4e	1	−0.0897	−0.0661	0.5530
	H	4e	1	−0.1581^c	−0.1496^c	0.2243^c
	H	4e	1	−0.0566^c	−0.1869^c	0.3555^c
	H	4e	1	−0.5524^c	0.0256^c	0.1204^c
	H	4e	1	−0.4045^c	−0.0515^c	0.1140^c
	H	4e	1	−0.5666^c	−0.0746^c	0.3675^c
	H	4e	1	−0.4260^c	−0.1768^c	0.4361^c
	H	4e	1	−0.1945^c	0.1856^c	0.1662^c
	H	4e	1	−0.1897^c	0.2885^c	0.2579^c
	H	4e	1	−0.6160^c	0.1490^c	0.2812^c
	H	4e	1	−0.5059^c	0.2768^c	0.3152^c
	H	4e	1	−0.1088^c	−0.0372^c	0.6202^c
	H	4e	1	−0.1181^c	−0.1598^c	0.5465^c
γ–CaCl$_2$·4H$_2$O^i	Ca	2a	$\overline{1}$	0.0000	0.0000	0.0000
	Cl	4e	1	0.2990	0.2790	0.0738
	O	4e	1	0.3111	−0.1965	0.0766
	O	4e	1	0.0043	−0.0015	0.2622
	H	4e	1	0.4168^c	−0.2089^c	0.1895^c
	H	4e	1	0.4079^c	−0.2265^c	0.0128^c
	H	4e	1	0.1065^c	0.0684^c	0.3544^c
	H	4e	1	−0.0979^c	−0.0670^c	0.3047^c
CaCl$_2$·6H$_2$O^j	Ca	1a	32.	0.0000	0.0000	0.0000
	Cl	2d	3	0.3333	0.3333	0.4249
	O	3e	2	0.3114	0.0000	0.0000
	O	3f	2	−0.2132	0.0000	0.5000
	H	6g	1	0.4326	0.0988	−0.0926
	H	6g	1	−0.2330	0.1113	0.4835

^{a} The values within these columns are in fractional unit cell coordinates.

^{b} $P\overline{3}m1$ (№. 164); trigonal; $a = b = 3.81$ Å; $c = 6.26$ Å; $\alpha_C = \beta_C = 90°$; $\gamma_C = 120°$.

^{c} Position optimized computationally, as described in Section 6.2.5 and Table D.2.

^{d} $P\overline{3}m1$ (№. 164); trigonal; $a = b = 3.887$ Å; $c = 7.108$ Å; $\alpha_C = \beta_C = 90°$; $\gamma_C = 120°$.

^{e} $Pnnm$ (№. 58); orthorhombic; $a = 6.24$ Å; $b = 6.43$ Å; $c = 4.20$ Å; $\alpha_C = \beta_C = \gamma_C = 90°$.

^{f} $Pbcn$ (№. 60); orthorhombic; $a = 5.893$ Å; $b = 7.469$ Å; $c = 12.070$ Å; $\alpha_C = \beta_C = \gamma_C = 90°$.

^{g} $P\overline{1}$ (№. 2); triclinic; $a = 6.5932$ Å; $b = 6.3673$ Å; $c = 8.5606$ Å; $\alpha_C = 97.83°$; $\beta_C = 93.50°$; $\gamma_C = 110.58°$.

^{h} $P2_1/c$ (№. 14); monoclinic; $a = 8.923$ Å; $b = 10.221$ Å; $c = 12.787$ Å; $\alpha_C = \gamma_C = 90°$; $\beta_C = 114.68°$.

^{i} $P2_1/c$ (№. 14); monoclinic; $a = 6.1387$ Å; $b = 7.6669$ Å; $c = 8.9014$ Å; $\alpha_C = \gamma_C = 90°$; $\beta_C = 111.00°$.

^{j} $P321$ (№. 150); trigonal; $a = b = 7.8759$ Å; $c = 3.9545$ Å; $\alpha_C = \beta_C = 90°$; $\gamma_C = 120°$.
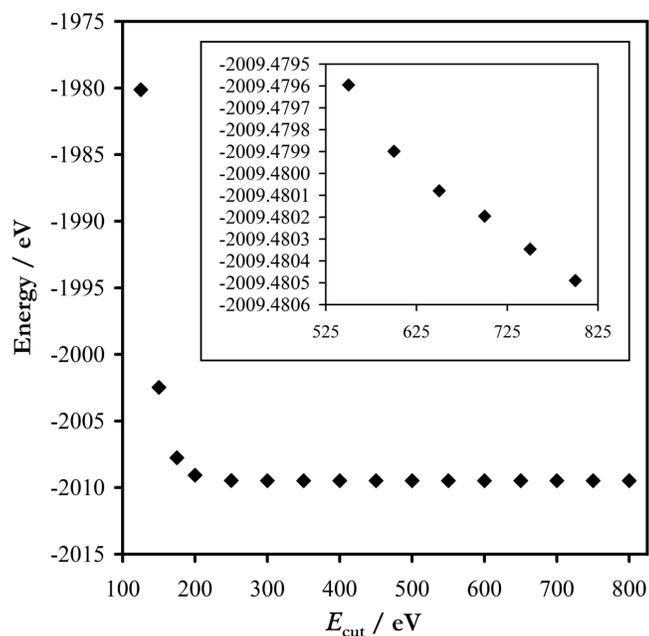
Figure D.1 MgBr$_2$ system energy versus E_{cut} demonstrates convergence of the computations with respect to energy. Calculations used the GIPAW DFT fully optimized geometry and the PBE XC functional. Inset: zoom of the higher E_{cut} region, highlighting the slow rate of further convergence.
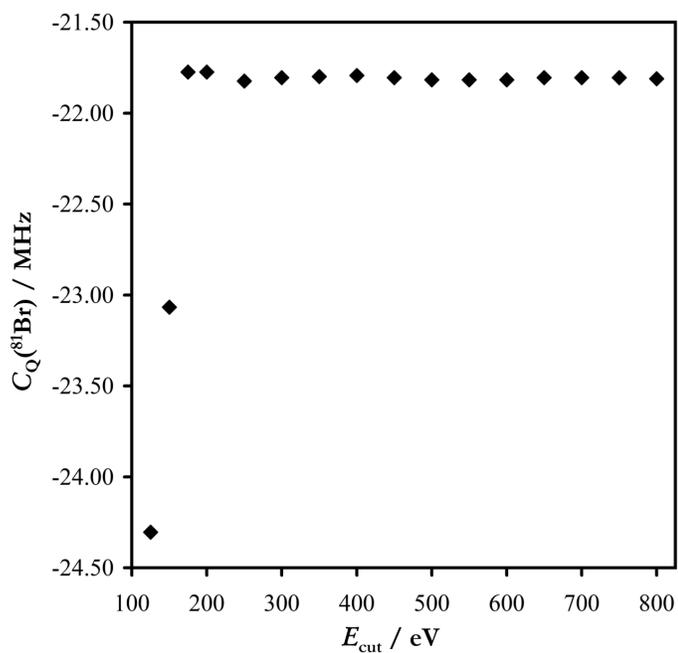
Figure D.2 $C_Q(^{81}Br)$ versus E_{cut} for MgBr$_2$ demonstrates convergence with respect to this parameter. Calculations used the GIPAW DFT fully optimized geometry and the PBE XC functional.
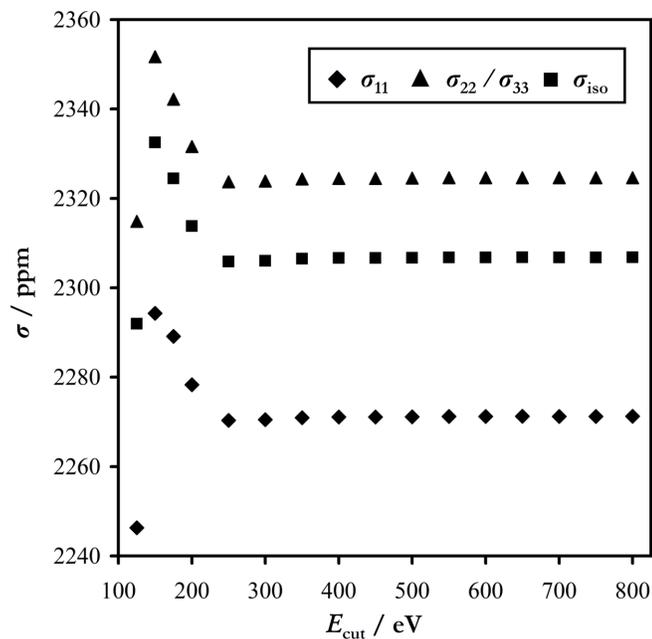
Figure D.3 Bromine magnetic shielding tensor parameters versus E_{cut} for $MgBr_2$ demonstrates convergence with respect to these parameters. Calculations used the GIPAW DFT fully optimized geometry and the PBE XC functional.

$$E \text{ / eV} = 5.6546(\Delta c)^2 + 0.0782(\Delta c) - 2009.5$$
$$R^2 = 0.9999$$
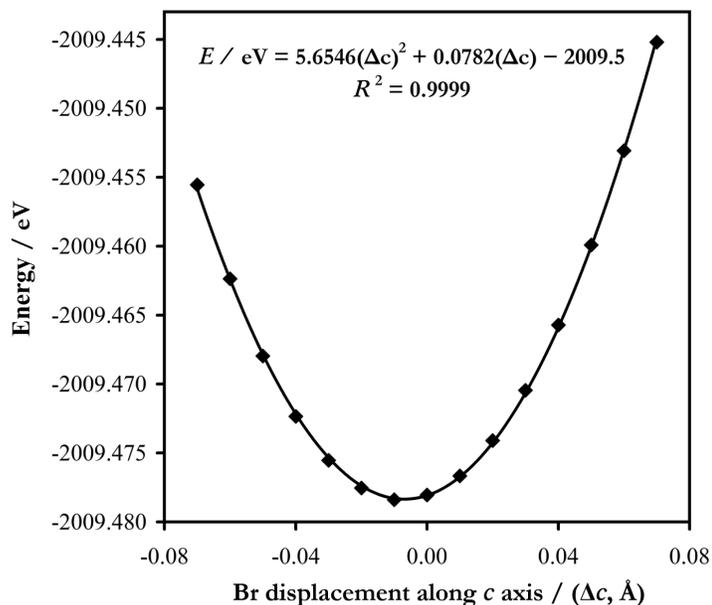
Figure D.4 $MgBr_2$ system energy versus the displacement of the bromide anion parallel to the c unit cell axis. The optimized zero position (i.e., $\Delta c = 0.00$ Å) is from the GIPAW DFT fully optimized geometry. Computations used the PBE XC functional.

Table D.4 GIPAW DFT ^{25}Mg and ^{81}Br EFG tensor parameters: MgBr$_2$, additional information[a]

nuclide	structure	functional	V_{11} / a.u.	V_{22} / a.u.	V_{33} / a.u.	$C_Q(X)$ / MHz	η_Q
^{25}Mg	XRD	PBE	0.0370	0.0370	−0.0741	−3.47	0.000
^{25}Mg	XRD	PW91	0.0373	0.0373	−0.0747	−3.50	0.000
^{81}Br	XRD	PBE	0.0316	0.0316	−0.0633	−3.90	0.000
^{81}Br	XRD	PW91	0.0335	0.0335	−0.0671	−4.13	0.000
^{25}Mg	fixed cell	PBE	0.0318	0.0318	−0.0635	−2.98	0.000
^{25}Mg	fixed cell	PW91	0.0321	0.0321	−0.0643	−3.01	0.000
^{81}Br	fixed cell	PBE	0.1209	0.1209	−0.2418	−14.89	0.000
^{81}Br	fixed cell	PW91	0.1229	0.1229	−0.2459	−15.14	0.000
^{25}Mg	full opt.	PBE	0.0292	0.0292	−0.0584	−2.74	0.000
^{25}Mg	full opt.	PW91	0.0296	0.0296	−0.0593	−2.78	0.000
^{81}Br	full opt.	PBE	0.1771	0.1771	−0.3543	−21.81	0.000
^{81}Br	full opt.	PW91	0.1823	0.1823	−0.3647	−22.45	0.000

[a] Parameter definitions are in Section 2.3.3.2. Additional details may be found in Table 6.1. $Q(^{25}$Mg$) = 1.994 \times 10^{-29}$ m²; $Q(^{81}$Br$) = 2.62 \times 10^{-29}$ m². To convert $V_{33}(^{81}$Br$)$ and $V_{33}(^{25}$Mg$)$ into frequency units, conversion factors of 61.56077 MHz/a.u. and 46.85197 MHz/a.u. were used for ^{81}Br and ^{25}Mg, respectively, and the unit EFG is $9.71736166 \times 10^{21}$ J C^{-1} m^{-2}.

Table D.5 GIPAW DFT magnesium and bromine CS tensor parameters: MgBr$_2$, additional information[a]

| nuclide	structure	functional	σ_{11} / ppm	σ_{22} / ppm	σ_{33} / ppm	δ_{iso} / ppm	Ω / ppm	κ
^{25}Mg	XRD	PBE	549.75	554.43	554.46	—	4.71	−0.987
^{25}Mg	XRD	PW91	550.38	555.05	555.07	—	4.69	−0.990
^{81}Br	XRD	PBE	2264.05	2279.96	2280.09	353.11	16.0	−0.985
^{81}Br	XRD	PW91	2265.97	2282.48	2282.60	350.06	16.6	−0.985
^{25}Mg	fixed cell	PBE	547.92	552.92	552.97	—	5.05	−0.983
^{25}Mg	fixed cell	PW91	548.52	553.48	553.52	—	5.00	−0.982
^{81}Br	fixed cell	PBE	2264.26	2293.54	2293.66	343.97	29.41	−0.992
^{81}Br	fixed cell	PW91	2266.09	2295.96	2296.09	341.01	30.00	−0.992
^{25}Mg	full opt.	PBE	549.97	555.78	555.84	—	5.86	−0.982
^{25}Mg	full opt.	PW91	550.74	556.49	556.53	—	5.78	−0.989
^{81}Br	full opt.	PBE	2271.29	2324.59	2324.69	320.88	53.40	−0.996
^{81}Br	full opt.	PW91	2273.93	2328.14	2328.24	316.89	54.31	−0.996

[a] Parameter definitions are in Sections 2.3.2.4, 2.3.3.1 and 2.3.3.3. Additional details may be found in Table 6.1.

Table D.6 GIPAW DFT ^{35}Cl EFG tensor parameters: $CaCl_2$ and hydrates, additional information[a]

compound	functional	site label	V_{11} / a.u.	V_{22} / a.u.	V_{33} / a.u.	$C_Q(^{35}Cl)$ / MHz	η_Q
$CaCl_2$	PBE	—	0.1463	0.3571	−0.5035	9.66	0.419
	PW91	—	0.1468	0.3597	−0.5065	9.72	0.420
$CaCl_2 \cdot 2H_2O$	PBE	—	0.0554	0.1755	−0.2309	4.43	0.520
	PW91	—	0.0524	0.1775	−0.2299	4.41	0.544
α–$CaCl_2 \cdot 4H_2O$	PBE	Cl(1)	−0.0574	−0.1354	0.1927	−3.70	0.405
		Cl(2)	0.0087	0.3024	−0.3111	5.97	0.944
	PW91	Cl(1)	−0.0567	−0.1360	0.1927	−3.70	0.412
		Cl(2)	0.0091	0.3054	−0.3145	6.03	0.942
β–$CaCl_2 \cdot 4H_2O$	PBE	Cl(1)	−0.0052	−0.1903	0.1955	−3.75	0.947
		Cl(2)	0.0097	0.1031	−0.1128	2.16	0.828
		Cl(3)	0.0231	0.1835	−0.2067	3.97	0.776
	PW91	Cl(1)	−0.0018	−0.1934	0.1952	−3.74	0.982
		Cl(2)	0.0103	0.1051	−0.1154	2.21	0.821
		Cl(3)	0.0273	0.1810	−0.2083	4.00	0.738
γ–$CaCl_2 \cdot 4H_2O$	PBE	—	0.0796	0.1074	−0.1870	3.59	0.149
	PW91	—	0.0825	0.1092	−0.1918	3.68	0.139
$CaCl_2 \cdot 6H_2O$	PBE	—	0.1429	0.1429	−0.2858	5.48	0.000
	PW91	—	0.1437	0.1437	−0.2873	5.51	0.000

[a] Parameter definitions are in Section 2.3.3.2. Additional details may be found in Table 6.4. $Q(^{35}Cl) = -8.165 \times 10^{-30}$ m^2.[9] To convert $V_{33}(^{35}Cl)$ into frequency units, a conversion factor of −19.1848743 MHz/a.u. was used, and the unit EFG is $9.71736166 \times 10^{21}$ J C^{-1} m^{-2}.

Table D.7 GIPAW DFT chlorine CS tensor parameters: $CaCl_2$ and hydrates, additional information[a]

compound	funct-ional	site label	σ_{11} / ppm	σ_{22} / ppm	σ_{33} / ppm	δ_{iso}[b] / ppm	Ω / ppm	κ	α, β, γ / °
$CaCl_2$	PBE	—	658.69	747.07	859.61	179.03	200.92	0.120	90.0, 89.7, 0.0
	PW91	—	656.36	745.11	858.44	181.87	202.07	0.122	90.0, 89.7, 0.0
$CaCl_2 \cdot 2H_2O$	PBE	—	765.95	801.71	906.66	109.32	140.71	0.492	118.3, 80.8, 2.7
	PW91	—	765.40	801.33	907.24	110.44	141.84	0.493	119.5, 80.8, 3.4
α–$CaCl_2 \cdot 4H_2O$	PBE	Cl(1)	825.85	848.44	899.49	76.12	73.64	0.386	15.4, 1.4, 18.8
		Cl(2)	810.27	867.46	888.21	78.74	77.94	−0.468	118.1, 77.3, 178.1
	PW91	Cl(1)	826.44	849.07	899.90	76.60	73.46	0.384	9.7, 1.6, 26.3
		Cl(2)	810.54	867.66	888.87	79.38	78.33	−0.458	118.3, 77.1, 178.9
β–$CaCl_2 \cdot 4H_2O$	PBE	Cl(1)	793.89	812.30	917.42	92.87	123.53	0.702	183.1, 3.2, 269.3
		Cl(2)	821.54	838.62	905.19	78.94	83.65	0.592	135.5, 73.6, 199.5
		Cl(3)	776.02	810.77	901.60	104.62	125.58	0.446	65.3, 82.6, 357.7
	PW91	Cl(1)	793.83	812.23	918.25	93.65	124.42	0.704	185.5, 3.4, 267.3
		Cl(2)	821.87	838.55	906.32	79.49	84.45	0.605	137.5, 73.3, 199.9
		Cl(3)	775.15	809.75	902.01	106.13	126.86	0.454	64.6, 82.4, 357.7
γ–$CaCl_2 \cdot 4H_2O$	PBE	—	848.47	882.59	925.58	48.48	77.11	0.115	111.1, 47.7, 190.6
	PW91	—	850.02	883.17	927.24	48.24	77.22	0.141	110.8, 46.7, 190.9
$CaCl_2 \cdot 6H_2O$	PBE	—	859.79	906.13	906.14	43.34	46.35	−1.000	N/A, 90.0, 0.3
	PW91	—	859.46	905.82	905.82	44.67	46.36	−1.000	N/A, 90.0, 0.3

[a] Parameter definitions are in Sections 2.3.2.4, 2.3.3.1 and 2.3.3.3. Additional details may be found in Table 6.4.
[b] Computed chlorine absolute shielding values, σ_{iso}, for NaCl(s) were 975.06 ppm ($4 \times 4 \times 4$ k-point grid and E_{cut} = 1200 eV) for PBE XC calculations and 976.07 ppm ($4 \times 4 \times 4$ k-point grid and E_{cut} = 1200 eV) for PW91 XC calculations. The absolute chlorine MS for 0.1 mol/dm³ NaCl in D_2O was found by solving: δ_{iso}(NaCl(s)) = −41.11 ppm = $[\sigma_{iso}$(NaCl(0.1 mol/dm³)) − σ_{iso}(NaCl(s))]/[1 − σ_{iso}(NaCl(0.1 mol/dm³))] using the σ_{iso} values for NaCl(s) noted directly above.

Table D.8 GIPAW DFT ^{43}Ca EFG tensor parameters: $CaCl_2$ and hydrates, additional information[a]

compound	functional	site label	V_{11} / a.u.	V_{22} / a.u.	V_{33} / a.u.	$C_Q(^{43}Ca)$ / MHz	η_Q
$CaCl_2$	PBE	—	−0.0235	−0.0788	0.1023	−0.98	0.541
	PW91	—	−0.0222	−0.0787	0.1008	−0.97	0.561
$CaCl_2 \cdot 2H_2O$	PBE	—	0.1297	0.1912	−0.3209	3.08	0.192
	PW91	—	0.1323	0.1942	−0.3265	3.13	0.190
α–$CaCl_2 \cdot 4H_2O$	PBE	—	−0.0237	−0.1798	0.2035	−1.95	0.767
	PW91	—	−0.0230	−0.1804	0.2035	−1.95	0.773
β–$CaCl_2 \cdot 4H_2O$	PBE	Ca(1)	−0.0296	−0.1316	0.1611	−1.54	0.633
		Ca(2)	−0.0018	−0.0308	0.0327	−0.31	0.887
	PW91	Ca(1)	−0.0299	−0.1330	0.1628	−1.56	0.633
		Ca(2)	−0.0032	−0.0296	0.0328	−0.31	0.805
γ–$CaCl_2 \cdot 4H_2O$	PBE	—	−0.1118	−0.1759	0.2877	−2.76	0.223
	PW91	—	−0.1168	−0.1766	0.2935	−2.81	0.204
$CaCl_2 \cdot 6H_2O$	PBE	—	−0.0178	−0.0178	0.0356	−0.34	0.000
	PW91	—	−0.0169	−0.0169	0.0338	−0.32	0.000

[a] Parameter definitions are in Section 2.3.3.2. Additional details may be found in Table 6.3. $Q(^{43}Ca) = -4.08 \times 10^{-30}$ m^2.[9] To convert $V_{33}(^{43}Ca)$ into frequency units, a conversion factor of −9.58656303 MHz/a.u. was used.

Table D.9 GIPAW DFT calcium CS tensor parameters: $CaCl_2$ and hydrates, additional information[a]

compound	funct-ional	site label	σ_{11} / ppm	σ_{22} / ppm	σ_{33} / ppm	δ_{iso}[b] / ppm	Ω / ppm	κ	α, β, γ / °
$CaCl_2$	PBE	—	1020.37	1053.07	1073.10	67.68	52.72	−0.240	90.0, 89.4, 0.0
	PW91	—	1018.81	1051.84	1072.00	68.78	53.19	−0.242	90.0, 89.3, 0.0
$CaCl_2{\cdot}2H_2O$	PBE	—	1042.09	1050.97	1067.98	63.61	25.89	0.314	180.0, 84.4, 180.0
	PW91	—	1041.30	1051.16	1068.34	63.67	27.05	0.270	180.0, 84.8, 180.0
α–$CaCl_2{\cdot}4H_2O$	PBE	—	1085.30	1111.91	1121.86	19.18	36.56	−0.456	60.1, 73.0, 18.7
	PW91	—	1087.14	1113.59	1123.91	17.62	36.77	−0.438	60.6, 72.2, 19.6
β–$CaCl_2{\cdot}4H_2O$	PBE	Ca(1)	1115.06	1140.07	1151.40	−5.41	36.34	−0.377	273.5, 70.1, 326.4
		Ca(2)	1017.32	1024.03	1029.54	88.95	12.22	−0.099	80.1, 89.2, 349.1
	PW91	Ca(1)	1117.21	1142.49	1153.91	−7.40	36.70	−0.377	273.5, 69.7, 326.7
		Ca(2)	1015.59	1022.74	1028.02	90.23	12.43	−0.150	80.7, 88.6, 349.2
γ–$CaCl_2{\cdot}4H_2O$	PBE	—	1058.07	1058.39	1087.24	51.62	29.17	0.978	325.6, 1.8, 162.7
	PW91	—	1058.95	1059.35	1088.87	50.64	29.92	0.974	316.6, 1.9, 164.6
$CaCl_2{\cdot}6H_2O$	PBE	—	1155.47	1164.67	1164.68	−27.42	9.20	−0.999	29.8, 90.0, 178.7
	PW91	—	1155.28	1164.49	1164.50	−27.26	9.22	−0.999	29.8, 90.0, 178.7

[a] Parameter definitions are in Sections 2.3.2.4, 2.3.3.1 and 2.3.3.3. Additional details may be found in Table 6.3.
[b] To convert computed MS values into chemical shift values, the procedure developed by Moudrakovski *et al.* was used. The presently calculated isotropic calcium MS values (i.e., σ_{iso}) were used as input into their empirically-determined formula: $\delta_{iso} = (1129.1 − \sigma_{iso})/1.1857$.[10]

D.2   References

1   A. Ferrari and F. Giorgi, *Atti della Accademia Nazionale dei Lincei, Classe di Scienze Fisiche, Matematiche e Naturali, Rendiconti*, **1929**, *9*, 1134-1140.

2   A. K. van Bever and W. Nieuwenkamp, *Z. Kristallogr.*, **1935**, *90*, 374-376.

3   A. LeClaire and M. M. Borel, *Acta. Cryst. B*, **1977**, *B33*, 1608-1610.

4   A. LeClaire and M. M. Borel, *Acta. Cryst. B*, **1979**, *B35*, 585-588.

5   A. LeClaire and M. M. Borel, *Acta. Cryst. B*, **1978**, *B34*, 900-902.

6   A. LeClaire, M. M. Borel and J. C. Monier, *Acta. Cryst. B*, **1980**, *B36*, 2757-2759.

7   P. A. Agron and W. R. Busing, *Acta Cryst. C*, **1986**, *C42*, 141-143.

8   A. LeClaire and M. M. Borel, *Acta Cryst. B*, **1977**, *B33*, 2938-2940.

9   P. Pyykkö, *Mol. Phys.*, **2008**, *106*, 1965-1974.

10   I. L. Moudrakovski, R. Alizadeh and J. J. Beaudoin, *Phys. Chem. Chem. Phys.*, **2010**, *12*, 6961-6969.

Appendix to Chapter Seven

Table E.1 Detailed $^{69/71}$Ga SSNMR and ^{127}I NQR experimental acquisition parameters[a]

B_0 / T	window / kHz	points[b]	$\pi/2^{c}$ / μs	scans	recycle delay / s	$\tau_1;\tau_2$ / μs	details
21.1	250	512	1.6	1 024	1.0	18.4;5.2	shielded site; ^{71}Ga NMR; Solomon echo; 4 mm HX probe
21.1	250	512	2.4	1 024	1.0	17.6;4.8	shielded site; ^{69}Ga NMR; Solomon echo; 4 mm HX probe
11.75	1 000	2 048	1.7	7 000	1.0	50;30	shielded site; ^{71}Ga NMR; Solomon echo; 4 mm HXY probe
11.75	50	1 024	11.0	1 024	0.35	50;35	deshielded site; ^{71}Ga NMR; Solomon echo; 4 mm HXY probe
0.0	1 000	1 024	1.0	512	0.5	40;20	^{127}I NQR; Hahn echo; 4 mm HXY probe; ν_{RF} = 132.0 MHz
0.0	1 000	1 024	1.0	512	0.5	40;20	^{127}I NQR; Hahn echo; 4 mm HXY probe; ν_{RF} = 134.37 MHz
0.0	1 000	1 024	1.0	512	0.5	40;20	^{127}I NQR; Hahn echo; 4 mm HXY probe; ν_{RF} = 113.75 MHz

[a] All experiments were carried out at room temperature, and under static conditions.
[b] Number of complex time-domain data points acquired.
[c] CT selective pulses were used for SSNMR experiments, where applicable.

Vita Auctoris

Cory M. Widdifield was born on October 8th, 1981 in Windsor, Ontario, Canada. He graduated from St. Thomas of Villanova Secondary School in June of 2000. He obtained B.Sc.[H] and M.Sc. degrees (both in chemistry) from the University of Windsor in June of 2004, and September of 2006, respectively, under the supervision of Prof. Robert W. Schurko. He also obtained a B.Ed. degree (chemistry & physics) in June of 2007 and was a chemistry instructor at St. Clair College (Windsor) in the fall of 2007. He is expecting to complete the requirements for his Ph.D. degree at the University of Ottawa during winter 2011-12, under the supervision of Prof. David L. Bryce. He is currently seeking a postdoctoral appointment.

Academic Honours and Awards

NSERC Alexander Graham Bell CGS D2 – 2008 to 2010

Poster Prize – OCCI Day – 2008

NSERC PGS M – 2004 to 2006

Ontario Graduate Scholarship (two times) – 2004, 2006

NSERC USRA (three times) – 2002, 2003, 2004

Poster Prize – 87th CSC Conference – 2004

Presentation Award – 32nd SOUSCC – 2003

Governor General Bronze Medal – 2000

University Entrance Award – 2000 to 2004

R. J. Attrell, C. M. Widdifield, I. Korobkov and D. L. Bryce. Weak Halogen Bonding in Solid Haloanilinium Halides Probed Directly via Chlorine-35, Bromine-81, and Iodine-127 NMR Spectroscopy. *Cryst. Growth Des.*, **2012**, *in press*.

C. M. Widdifield, T. Jurca, D. S. Richeson and D. L. Bryce. Using $^{69/71}$Ga Solid-State NMR and ^{127}I NQR as Probes to Elucidate the Composition of 'GaI'. *Polyhedron*, **2012**, *35*, 96 – 100.

C. M. Widdifield, A. D. Bain and D. L. Bryce. Definitive Solid-State $^{185/187}$Re NMR Spectral Evidence for and Analysis of the Origin of High-Order Quadrupole-Induced Effects for $I = 5/2$. *Phys. Chem. Chem. Phys.*, **2011**, *13*, 12413 – 12420. **Cover Article**.

D. L. Bryce, C. M. Widdifield, R. P. Chapman and R. J. Attrell. Chlorine, Bromine, and Iodine Solid-State NMR in *NMR of Quadrupolar Nuclei in Solid Materials*, R. E. Wasylishen, S. E. Ashbrook, and S. Wimperis, Eds. (*in press*). Invited Contribution.

C. M. Widdifield and D. L. Bryce. A Multinuclear Solid-State Magnetic Resonance and GIPAW DFT Study of Anhydrous Calcium Chloride and its Hydrates. *Can. J. Chem.*, **2011**, *89*, 754 – 763.

C. M. Widdifield and D. L. Bryce. Solid-State ^{127}I NMR and GIPAW DFT Study of Metal Iodides and Their Hydrates: Structure, Symmetry, and Higher-Order Quadrupole-Induced Effects. *J. Phys. Chem. A*, **2010**, *114*, 10810 – 10823.

C. M. Widdifield and D. L. Bryce. Solid-State $^{79/81}$Br NMR and Gauge-Including Projector-Augmented Wave Study of Structure, Symmetry, and Hydration State in Alkaline Earth Metal Bromides. *J. Phys. Chem. A*, **2010**, *114*, 2102 – 2116.

T. Pathmalingham, F. Habib, C. M. Widdifield, F. Loiseau, T. J. Burchell, S. I. Gorelsky, A. M. Beauchemin, D. L. Bryce and M. Murugesu. Combining Oximes with Azides to Create A Novel 1–D [NaCo$^{III}_2$] System: Synthesis, Structure and Solid-State NMR. *Dalton Trans.*, **2010**, *39*, 1504 – 1510.

R. P. Chapman, C. M. Widdifield and D. L. Bryce. Solid-State NMR of Quadrupolar Halogen Nuclei. *Prog. Nucl. Magn. Reson. Spectrosc.*, **2009**, *55*, 215 – 237. Invited Contribution.

C. M. Widdifield and D. L. Bryce. Crystallographic Structure Refinement with Quadrupolar Nuclei: A Combined Solid-State NMR and GIPAW DFT Example using MgBr$_2$. *Phys. Chem. Chem. Phys.*, **2009**, *11*, 7120 – 7122.

C. M. Widdifield, R. P. Chapman and D. L. Bryce. Chlorine, Bromine, and Iodine Solid-State NMR Spectroscopy in *Annual Reports on NMR Spectroscopy*, G. A. Webb, Ed., Chapter 5, **2009**, *66*, 195 – 326. Invited Contribution.

Oral Presentations at Conferences During Ph.D. Period

C. M. Widdifield, A. D. Bain and D. L. Bryce. High-Order Quadrupole-Induced Effects in Solid-State NMR Spectra for $I = 5/2$ via Iodine-127 and Rhenium-185/187 Nuclei. The 94th Conference of the Canadian Society for Chemistry, June 5th – 9th, 2011, Palais des Congrès de Montréal, Montréal, Québec, Canada.

C. M. Widdifield and D. L. Bryce. Solid-State ^{127}I NMR Spectroscopy and GIPAW DFT Calculations of Inorganic Iodide Systems: Structure, Symmetry, and 'Beyond Second-Order' Quadrupole-Induced Shifts. The 5th Annual Solid-State NMR Workshop, May 29th, 2010, Metro Toronto Convention Centre, Toronto, Ontario, Canada. Invited presentation.

C. M. Widdifield and D. L. Bryce. Applications of $^{79/81}$Br and ^{127}I Solid-State Nuclear Magnetic Resonance. The MOOT XXI NMR Symposium, October 4th – 5th, 2008, Canterbury College, Windsor, Ontario, Canada.

Poster Presentations at Conferences During Ph.D. Period

C. M. Widdifield and D. L. Bryce. Advances in the Acquisition of Solid-State ^{43}Ca NMR Spectra: Applications to Organic and Inorganic Systems. The 7th Alpine Conference on Solid-State NMR, September 11th – 15th, 2011, Chamonix-Mont Blanc, France.

C. M. Widdifield and D. L. Bryce. Solid-State Iodine-127 NMR Spectroscopy and GIPAW DFT Study of Inorganic Iodine-Containing Systems. The 93rd Conference of the Canadian Society for Chemistry, May 29th – June 2nd, 2010, Metro Toronto Convention Centre, Toronto, Ontario, Canada.

C. M. Widdifield and D. L. Bryce. Characterization of $^{79/81}$Br Magnetic Shielding and Electric Field Gradient Tensors in a Series of Alkaline Earth Metal Bromides and Hydrates Thereof. The 50th Rocky Mountain Conference on Analytical Chemistry, July 27th – 31st, 2008, Breckenridge, Colorado, USA.

C. M. Widdifield and D. L. Bryce. Characterization of $^{79/81}$Br Magnetic Shielding and Electric Field Gradient Tensors in a Series of Alkaline Earth Metal Bromides and Hydrates Thereof. Ottawa-Carleton Chemistry Institute (OCCI) Day, May 15th, 2008, Ottawa, Ontario, Canada. **Award: Poster Competition**